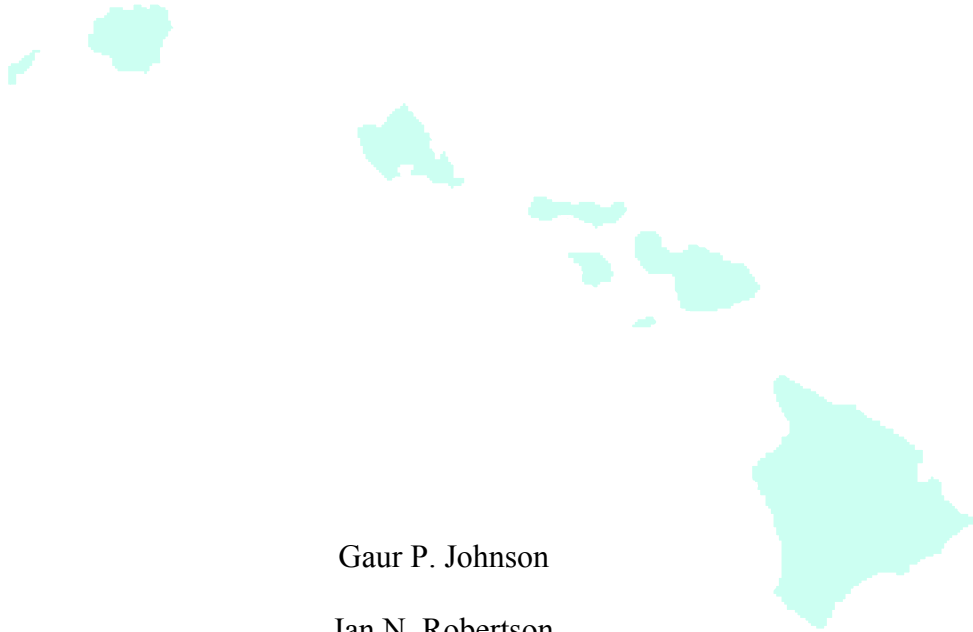


STRUCTURAL HEALTH MONITORING SYSTEMS
FOR CIVIL AND ARCHITECTURAL STRUCTURES:
LVDT-TAUT-WIRE BASELINES,
CRACK MONITORING DEVICES,
&
STRAIN BASED DEFLECTION MONITORING ALGORITHMS.



Gaur P. Johnson

Ian N. Robertson



UNIVERSITY OF HAWAII
COLLEGE OF ENGINEERING

DEPARTMENT OF CIVIL AND ENVIRONMENTAL ENGINEERING

Research Report UHM/CEE/07-02
February 2007

ACKNOWLEDGMENTS

This report is based on a Ph.D. Dissertation prepared by Gaur Johnson under the direction of Ian Robertson at the Department of Civil Engineering at the University of Hawaii at Manoa.

The authors would like to thank the following projects which helped to make this report possible:

- Robertson, I. (P.I.) "Instrumentation and Long-Term Monitoring of the H3 North Halawa Valley Viaduct", funded by FHWA and Hawaii State DOT, 94-04.
- Robertson, I. (P.I.) "Seismic Instrumentation and Monitoring of the Kealakaha Stream Bridge", funded by FHWA and Hawaii State DOT, 00-05.
- Robertson, I. (P.I.) "Testing of Prestressed Concrete Beams Repaired with Carbon Fiber Reinforced Polymers", funded by Hawaii State DOT, 00-01.
- Riggs, H.R. (P.I.), Ian Robertson (co-P.I.) Si-Hwan Park (co-P.I.), 'Instrumenting and Monitoring the Performance of the FRP Shear Strengthening of the Salt Lake Boulevard Bridge,' FHWA Innovative Bridge Research and Construction program, November 2003 - October 2008.

Thank you to all the faculty, staff, and fellow graduate students who have helped through the process, including but by no means limited to: Dr. Ian Robertson, Dr. H. Ronald Riggs, Dr. Si-Hwan Park, Dr. David Ma, Dr. Ronald Knapp, Dr. Craig Newton, Dr.

Arthur Chiu, Gary Chock, Miles Wagner, Andy Oshita, Janis Kusatsu, Bhavna Sharma, Huiping Cheng, Jiabao Chen, Jinghai Yang, Huiyun Zhang, Kainoa Aki, Derek Yonemura, Justin Nii, Wesley Furuya, Brian Enomoto, Martin & Chock, Nagamine Okawa Engineers, and Iwamoto & Associates.

ABSTRACT

In this age of computers and electronics, we become increasingly aware of all the new information we can collect about our surroundings. The medical industry has fully embraced the use of this technology to help diagnose problems with our health. The civil engineering profession is only now beginning the steps toward using structural health monitoring (SHM) for the purpose of extending the productive lives of our infrastructure. The ubiquitous use of SHM will reap the benefit of providing a rational method to prioritize expenditure allocation to maintain our deteriorating facilities. Since SHM is far from ubiquitous, the lessons learned during any instrumentation program provide a significant contribution to the SHM field.

This dissertation begins by showing structural engineers a few of the tools of the trade that can be used in a SHM program. To help open the instrumentation world to engineers and scientists, an example of the process by which to design an economical crack gauge is discussed. This dissertation also contributes new information to the SHM field. First, a simple design process for an LVDT-Taut-Wire baseline system that measures vertical deflections on long and short span beams is established. Second, a method by which to pre-determine the magnitude of expected error caused by real data for a strain based deflection monitoring algorithm is presented. Both of these contributions will help to more quickly design SHM systems and provide the user reasonable confidence of the systems performance before the system is installed. Finally, a brief discussion of how some of the key lessons learned will be incorporated into four SHM projects is presented.

TABLE OF CONTENTS

Acknowledgments.....	iii
Abstract.....	v
TABLE OF CONTENTS.....	vii
LIST OF TABLES.....	xvii
LIST OF FIGURES.....	xix
Chapter 1. INTRODUCTION TO STRUCTURAL HEALTH MONITORING.....	1
1.1 General Purpose.....	1
1.2 Literature Review.....	5
Chapter 2. AVAILABLE MEASUREMENT METHODOLOGIES.....	9
2.1 Overall Data Acquisition Systems.....	9
2.2 Linear Variable Differential Transformer (LVDT):.....	10
2.2.1 Ratiometric Wire Configuration.....	12
2.2.2 Open Wire Configuration.....	12
2.2.3 Influence of Cable Length.....	13
2.2.4 Sensitivity Correction Factor (SCF).....	14

2.2.5	Limitations for Structural Health Monitoring.....	17
2.3	Strain Gauges.....	18
2.3.1	Types of Strain Gauges.....	18
2.3.1.1	Electrical Resistance Strain Gauges.....	19
2.3.1.2	Fiber Optic Strain Gauges.....	28
2.3.1.3	Vibrating Wire Strain Gauges.....	35
2.3.2	Thermal Effects and Considerations for Strain Gauges.....	36
2.3.2.1	Thermal Output Compensation Techniques	39
2.3.3	Structural Health Monitoring Strain Gauge Comparison	46
2.3.3.1	Electrical Resistance Strain Gauges.....	46
2.3.3.2	Fiber Optic Strain Gauges.....	47
2.3.3.3	Vibrating Wire Strain Gauges.....	49
Chapter 3.	LVDT-TAUT-WIRE BASELINE DEFLECTION SYSTEM DESIGN..	51
3.1	Literature Review.....	51
3.2	University of Hawaii System Design Process	57
3.2.1	In Laboratory Prestressed Concrete T-Beam Testing.....	58

3.2.2	North Halawa Valley Viaduct (H3 Freeway) Field Installation	62
3.2.3	Hanapepe River Bridge Load Test Field Installation	65
3.3	System Sizing Considerations.....	68
3.3.1	Implemented System Comparisons.....	68
3.3.2	Suggested Design Process.....	73
Chapter 4.	WHEATSTONE BRIDGE DEVICE DESIGN	77
4.1	Background.....	77
4.2	Crack Gauge Device	78
4.2.1	Design Basis.....	79
4.2.2	Physical Specifications	80
4.2.3	Estimating Crack Mouth Opening Displacement (CMOD) Resolution ...	84
4.3	Rotation Monitoring by Deflection Device	87
4.3.1	Design Basis.....	87
4.3.2	Physical Specifications	88
4.3.3	Estimating Displacement Resolution.....	91
Chapter 5.	STRAIN GAUGE BASED DEFLECTED SHAPE CALCULATION	93

5.1	Literature Review.....	93
5.2	General Methodology	96
5.3	Curvature to Displacement (C2D) Derivation	97
5.4	C2D Method Matlab™ Implementation:.....	101
5.4.1	RISA-2D Strain Input	102
5.4.2	Evaluated Loading Scenarios.....	104
5.4.3	Matlab Implementation Scenario 1MoCS	106
5.4.4	Matlab Implementation Scenario 1MoAS	107
5.4.5	Matlab Implementation Scenario 1QPoCS.....	109
5.4.6	Matlab Implementation Scenario 1DLoM2	112
5.4.7	Matlab Implementation Scenario 1DLoNb.....	113
5.4.8	Small Scale Implimentation.....	115
5.4.8.1	Static Test.....	116
5.4.8.2	Dynamic Tests	119
5.5	Conclusions.....	121
5.5.1	Comments on Curvature Estimation.....	122

5.5.2	Comments on Deflected Shape.....	122
5.5.3	Comments on Real Data Implementation.....	123
Chapter 6. ANALYSIS OF STRAIN GAGE BASED DEFLECTED SHAPE		
CALCULATIONS.....		
6.1	Background.....	125
6.2	Error Sources in Real Data used in C2D Method.....	126
6.2.1	Measurement Round Off.....	127
6.2.1.1	Matlab Implementation Scenario 1MoCS	128
6.2.1.2	Matlab Implementation Scenario 1MoAS	130
6.2.1.3	Matlab Implementation Scenario 1QPoCS.....	133
6.2.1.4	Matlab Implementation Scenario 1DLom2.....	136
6.2.1.5	Matlab Implementation Scenario 1DLonb.....	138
6.2.2	Signal Noise Characteristics	141
6.2.3	Sample of Real Strain Data.....	143
6.3	Analysis of Error Propagation in C2D Method	144
6.3.1	Error at Individual Sensors	145

6.3.1.1	Single Beam Section.....	145
6.3.1.2	Entire Beam	148
6.3.2	Error at Multiple Sensors	151
6.3.2.1	Deflected Shape of the Entire Beam.....	152
6.3.2.2	Dynamic or Multiple Measurements	158
6.4	Comments on Error Reduction Methods for C2D Method.....	166
6.4.1	Post Processing Data Averaging.....	166
6.4.1.1	Static Measurements	167
6.4.1.2	Dynamic Measurements.....	168
6.4.2	C2D Method Adaptations	173
6.4.2.1	Number of Beam Sections	174
6.4.2.2	Alternate Curvature Estimate Implementations.....	174
6.4.2.3	Multiple Implementation Comparison.....	174
6.5	Conclusions.....	175
Chapter 7.	SHM DURING HANAPEPE RIVER BRIDGE LOAD TESTING.....	177
7.1	Background.....	177

7.2	Bridge SHM Instrumentation.....	177
7.2.1	Vertical Deflection.....	180
7.2.2	Horizontal Deflection.....	184
7.2.3	Crack Mouth Opening Displacement.....	184
7.2.4	Rotation at Lihue Pier Support	190
7.3	Data Acquisition and Processing	192
7.3.1	Optical Survey	192
7.3.2	Temperature Effects.....	193
7.4	Load Test Program.....	196
7.4.1	Truck Loads	196
7.4.2	Static Loading.....	198
7.4.3	Dynamic Loading.....	200
7.5	Load Test Results.....	200
7.5.1	Vertical Deflections	200
7.5.1.1	Load Series 1.....	200
7.5.1.2	Load Series 2 and 3.....	202

7.5.1.3	Load Series 4 and 5.....	203
7.5.1.4	Load Series 6.....	204
7.5.2	Horizontal Deflection.....	206
7.5.3	Rotation at Lihue Piers.....	207
7.5.4	Crack Mouth Opening Displacements.....	209
7.5.4.1	General.....	209
7.5.5	Dynamic Response.....	212
7.6	Conclusions about Bridge and SHM System.....	215
Chapter 8.	OTHER PLANNED SHM IMPLEMENTATIONS.....	217
8.1	North Halawa Valley Viaduct (NHVV).....	217
8.1.1	Background.....	217
8.1.2	Results: LVDT-Taut-Wire Baseline System.....	218
8.1.3	Results: Strain Gauge Based C2D Methodology.....	220
8.2	Kealakaha Stream Bridge Seismic Instrumentation.....	221
8.2.1	Background.....	221
8.2.2	LVDT-Taut-Wire Baseline System.....	222

8.2.3	C2D Methodology	223
8.3	Salt Lake Boulevard – Halawa Stream Bridge: Shear Retrofit.....	225
8.3.1	Background.....	225
8.3.2	Planned Instrumentation	225
Chapter 9.	SUMMARY AND CONCLUSIONS	227
APPENDIX	231
REFERENCES	261

LIST OF TABLES

Table 2.1. Strain Gauge Behavior Sensitivities.	38
Table 3.1. Summary of LVDT Core-Induced Baseline Displacement.	69
Table 3.2. Estimated Error at LVDTs Due to Friction with LVDT Core.	72
Table 5.1. Matlab™ Based C2D Method Evaluation Scenarios.	105
Table 5.2. Curvature Observations Used in C2D Program.	105
Table 6.1. Curvature Input for Three Span Continuous Beam.	128
Table 6.2. Statistical Characteristics of Strain Error Based on Average Strain Value. ...	144
Table 6.3. Positive Error Combinations Calculated by Superposition.	153
Table 6.4. Alternating Direction Error Combinations Calculated by Superposition.	153
Table 6.5. Small Scale Three Span Beam Signal Error Characteristics Summary.	161
Table 7.1. Crack Gauge Details.	190
Table 7.2. Truck Load Series.	199

LIST OF FIGURES

Figure 2.2.1. LVDT Output [source: Trietily 1986, pg 69].	11
Figure 2.2.2. Effect of Sensitivity Correction Factor (SCF).	16
Figure 2.2.3. LVDT Sensitivity Correction Factor vs. Cable Length.	16
Figure 2.3.1. Voltage Divider Circuit.	20
Figure 2.3.2. Sample Calculation to Find Voltage Resolution ($5\mu\text{m}$ measurement).	21
Figure 2.3.3. Wheatstone Bridge Circuit.	23
Figure 2.3.4. Long Lead Quarter Bridge Configuration.	25
Figure 2.3.5. Thermal Output from an Electrical Resistance Strain Gauge [source: Vishay 2005, pg 6].	27
Figure 2.3.6. Fabry-Perot Fiber Optic Strain Gauge [source: Fiso 2006].	29
Figure 2.3.7. Fabry-Perot Etalon [source: Drexel 2006].	30
Figure 2.3.8. Bragg Grating Gauge Methodology [source: Chiareli 1999].	31
Figure 2.3.9. Reflected Spectrum Changes due to Residual Strains [source: Wnuk 2005, pg 5].	34
Figure 2.3.10. Typical Structural Diurnal Response.	41

Figure 2.3.11. Strain Gauge Output Change Due to α Mismatch Effects [source: Vishay 2005, pg 9].	44
Figure 3.1.1. Weighted Stretched Wire System [source: Stanton et al. 2003, pg 348]. ...	56
Figure 3.2.1. LVDT-Taut-Wire Installed on Pre-stressed Concrete Beam.....	59
Figure 3.2.2. Live End Pulleys Installed on Prestressed Concrete Beam.	60
Figure 3.2.3. T-Beam Deflected Shapes.	61
Figure 3.2.4. T-Beam capacity Curve.....	61
Figure 3.2.5. NHVV Deflection Observed with LVDT-Taut-Wire Baseline System.	64
Figure 3.2.6. Deflection Along the NHVV Span Varying with Time.	65
Figure 3.2.7. Abutment Span Elevation of Girder G-3: LVDT-Taut-Wire Baseline System.....	66
Figure 3.2.8. Bridge Cross-Section: LVDT-Taut-Wire Baseline Adjacent to Girder G-3.	67
Figure 3.2.9. Taut-Wire Baseline Dead (Left) and Live (Right) End Supports.....	67
Figure 3.3.1. Geometry of Deflection and Loads Applied to the Taut-Wire Catenary. ..	71
Figure 4.2.1. Crack Gauge Wheatstone Bridge Wiring Diagram.	81

Figure 4.2.2. Crack Gauge Design and Loading Diagram.....	82
Figure 4.2.3. Crack Gauge Installations.....	83
Figure 4.3.1. Deflection Gauge For Monitoring Pin Connection Rotation.	89
Figure 4.3.2. Installed Gauges Monitoring Rotation of Pinned Connection at Pier.	90
Figure 5.4.1. Three-Span Continuous Beam Modeled.	103
Figure 5.4.2. Three-Span Continuous Beam Finite Element Model (4 Elements).	103
Figure 5.4.3. Scenario 1MoCS: Curvature Estimation.	106
Figure 5.4.4. Scenario 1MoCS: Deflection Comparison.	107
Figure 5.4.5. Scenario 1MoAS: Curvature Estimation.	108
Figure 5.4.6. Scenario 1MoAS: Deflection Comparison.	109
Figure 5.4.7. Scenario 1QPoSC: Curvature Estimation.....	110
Figure 5.4.8. Scenario 1QPoCS: Deflection Comparison.....	111
Figure 5.4.9. Scenario 1DLoM2: Curvature Estimation.....	112
Figure 5.4.10. Scenario 1DLoM2: Deflection Comparison.....	113
Figure 5.4.11. Scenario 1DLoNb: Curvature Estimation.	114
Figure 5.4.12. Scenario 1DLoNb: Deflection Comparison.	115

Figure 5.4.13. Static Loading Strains Obtained by Fabry-Perot Strain Gauges.	117
Figure 5.4.14. C2D Static Results—Four Levels of Load.	118
Figure 5.4.15. C2D Method Observations, Dynamic Response of Small Scale Beam.	120
Figure 5.4.16. C2D Calculated Deflection Based on the Theoretical Strains, Mode 1.	121
Figure 6.2.1. Scenario 1MoCS: C2D Curvature Comparison.	129
Figure 6.2.2. Scenario 1MoCS: C2D Deflection Comparison.	130
Figure 6.2.3. Scenario 1MoAS: C2D Curvature Comparison.	131
Figure 6.2.4. Scenario 1MoAS: C2D Deflection Comparison.	132
Figure 6.2.5. Scenario 1QPoCS: C2D Curvature Comparison.	134
Figure 6.2.6. Scenario 1QPoCS: C2D Deflection Comparison.	135
Figure 6.2.7. Scenario 1DLoM2: C2D Curvature Comparison.	137
Figure 6.2.8. Scenario 1DLoM2: C2D Deflection Comparison.	138
Figure 6.2.9. Scenario 1DLoNb: C2D Curvature Comparison.	139
Figure 6.2.10. Scenario 1DLoNb: C2D Deflection Comparison.	140
Figure 6.2.11. Strain Gauge Data Acquired for 18.69 seconds at 16 Hz (300 Data Points).	143

Figure 6.3.1. Second Degree Polynomial Curvature Approximation: Error at One Gauge.	146
Figure 6.3.2. Third Degree Polynomial Rotation Approximation: Error at One Gauge.	147
Figure 6.3.3. Fourth Degree Polynomial Curvature Approximation: Error at One Gauge.	147
Figure 6.3.4. Curvature Error Based on One Measurement Location.	149
Figure 6.3.5. Rotation Error Based on One Measurement Location.	150
Figure 6.3.6. Displacement Error Based on One Measurement Location.	151
Figure 6.3.7. Deflection Based on Multiple Positive Curvature Error Locations.....	154
Figure 6.3.8. Deflection Based on Multiple Alternating (+/-) Curvature Error Locations.	156
Figure 6.3.9. All Possible Positive Error Combination Displacement Functions.....	157
Figure 6.3.10. Expected Error Deflection Envelopes for the Small Scale Beam.	162
Figure 6.3.11. LVDT Deflected Shape Observations.	164
Figure 6.3.12. C2D Based Deflected Shape Observations.	164
Figure 6.3.13. LVDT & C2D Maximum Measured Displacements.....	165

Figure 6.3.14. C2D Error Envelope Comparison with LVDT and Support Measurements.	165
Figure 6.3.15. Comparison of Error Envelopes for Deflection at Location of an LVDT.	166
Figure 6.4.1. Before (Left) and After (Right) Averaging C2D Static Displacements. ..	168
Figure 6.4.2. Rectangular Averaging Windows Effects on Deflection.	170
Figure 6.4.3. Triangular Averaging Windows Effects on Deflection.....	172
Figure 6.4.4. Comparison of Rectangular Averaging Windows for the Entire Beam. ..	173
Figure 7.2.1. Data Acquisition System.....	179
Figure 7.2.2. Elevation of Girder G-3 Showing LVDT-Taut-Wire Baseline Systems..	180
Figure 7.2.3. LVDT-Taut-Wire Baseline System in Lihue Span.	181
Figure 7.2.4. LVDT-Taut-Wire Baseline System in Center Span.	181
Figure 7.2.5. Bridge Cross-Section Showing Baseline System Location.....	182
Figure 7.2.6. Taut-Wire Baseline Dead (Left) and Live (Right) End Supports.....	183
Figure 7.2.7. LVDT-Taut-Wire Baseline LVDT Support Details.	183
Figure 7.2.8. Horizontal LVDT Measuring Deflection at Lihue Rocker Bearing.	184

Figure 7.2.9. Crack Gauge on Downstream Elevation of Center Span.	185
Figure 7.2.10. Crack Gauges on Downstream Elevation of Lihue Span.	186
Figure 7.2.11. Crack Gauges on Upstream Elevation of Center Span.....	186
Figure 7.2.12. Crack Gauges on Upstream Elevation of Lihue Span.....	187
Figure 7.2.13. Crack Gauge 9 Adjacent to Visual Crack Monitor 3.	188
Figure 7.2.14. Typical Crack Gauge (10) on Mounting Tabs.....	189
Figure 7.2.15. Rotation Monitoring Gauge (1) on Waimea Side of Lihue Pier Bearing.	191
Figure 7.2.16. Rotation Monitoring Gauge (2) on Lihue Side of Lihue Pier Bearing...	191
Figure 7.3.1. Optical Survey Points.	192
Figure 7.3.2. Thermal Compensation of Hanapepe River Bridge.	194
Figure 7.3.3. Thermocouple Locations on H3 North Halawa Valley Viaduct [Robertson & Ingham 1999].	195
Figure 7.3.4. H3 North Halawa Valley Viaduct Daily Temperature Variation [Robertson & Ingham 1999].	195
Figure 7.4.1. Trucks Loads and Dimensions.	197

Figure 7.4.2. Truck Load During Load Series 6, Location 3 (LS6-L3).....	199
Figure 7.5.1. Load Series 1 Deflected Shape of Lihue Half of Bridge.....	202
Figure 7.5.2. Load Series 2 and 3 Deflected Shape of Lihue Half of Bridge.....	203
Figure 7.5.3. Load Series 4 and 5 Deflected Shape of Lihue Half of Bridge.....	204
Figure 7.5.4. Load Series 6 Deflected Shape of Lihue Half of Bridge (R is Repeated Loading).....	206
Figure 7.5.5. Comparison of Horizontal Deflection to Vertical Deflections.....	207
Figure 7.5.6. Displacement Measurements Used to Determine Pier Rotation.....	208
Figure 7.5.7. Rotation of Lihue Pier.....	209
Figure 7.5.8. Crack Gauge measurements per Load Series.....	210
Figure 7.5.9. Crack Gauge Measurements per Load Series (Magnified).....	211
Figure 7.5.10. Dynamic Crack Opening Plots.....	211
Figure 7.5.11. Lihue Bound Dynamic Deflection at 25 mph.....	213
Figure 7.5.12. Waimea Bound Dynamic Deflection at 25 mph.....	213
Figure 7.5.13. Lihue Bound Dynamic Deflection Breaking From 25 mph.....	214
Figure 7.5.14. Waimea Bound Dynamic Deflection Breaking From 25 mph.....	215

Figure 8.1.1. Thermal Deflection Observed by an LVDT-Taut-Wire Baseline System.	219
Figure 8.1.2. Traffic Loading Observed by an LVDT-Taut-Wire Baseline System.	220
Figure 8.1.3. Strain Measurements from 1 m Long Gauges During Truck Loading.....	221

LIST OF FIGURE IN APPENDIX

Figure A8.2.17. Crack Gauges 1 (Left) and 2 Adjacent to Visual Crack Monitor 19 (Right), Shear Cracks.....	245
Figure A8.2.18. Crack Gauge 3 Adjacent to Visual Crack Monitor 11, Shear Crack....	246
Figure A8.2.19. Crack Gauge 4 Adjacent to Visual Crack Monitor 12, Flexural Crack.	246
Figure A8.2.20. Crack Gauge 5 Adjacent to Visual Crack Monitor 13., Flexural Crack.	247
Figure A8.2.21. Crack Gauge 6, Shear Crack.....	247
Figure A8.2.22. Crack Gauge 7, Shear Crack.....	248
Figure A8.2.23. Crack Gauge 8 Adjacent to Visual Crack Monitor 2, Shear Crack.....	248
Figure A8.2.24. Crack Gauge 9 Adjacent to Visual Crack Monitor 3, Shear Crack.....	249
Figure A8.2.25. Crack Gauge 10 Adjacent to Visual Crack Monitor 12, Flexural Crack.	249

Figure A8.4.3. Load Series 1 – Location 1 (LS1-L1).....	251
Figure A8.4.4. Load Series 1 – Location 2 (LS1-L2).....	251
Figure A8.4.5. Load Series 1 – Location 4 (LS1-L4).....	252
Figure A8.4.6. Load Series 2 – Location 1 (LS2-L1).....	252
Figure A8.4.7. Load Series 2 – Location 2 (LS2-L2).....	253
Figure A8.4.8. Load Series 2 – Location 4 (LS2-L4).....	253
Figure A8.4.9. Load Series 3 – Location 1 (LS3-L1).....	254
Figure A8.4.10. Load Series 3 – Location 2 (LS3-L2).....	254
Figure A8.4.11. Load Series 3 – Location 4 (LS3-L4).....	255
Figure A8.4.12. Load Series 4 – Location 1 (LS4-L1).....	255
Figure A8.4.13. Load Series 4 – Location 2 (LS4-L2).....	256
Figure A8.4.14. Load Series 4 – Location 4 (LS4-L4).....	256
Figure A8.4.15. Load Series 5 – Location 1 (LS5-L1).....	257
Figure A8.4.16. Load Series 5 – Location 2 (LS5-L2).....	257
Figure A8.4.17. Load Series 5 – Location 4 (LS5-L4).....	258
Figure A8.4.18. Load Series 6 – Location 1 (LS6-L1).....	258

Figure A8.4.19. Load Series 6 – Location 2 (LS6-L2).....	259
Figure A8.4.20. Load Series 6 – Location 3 (LS6-L3).....	259
Figure A8.4.21. Load Series 6 – Location 4 (LS6-L4).....	260

CHAPTER 1.INTRODUCTION TO STRUCTURAL HEALTH MONITORING

Only within the past century have scientists used electronic devices to verify the behavior of materials used to construct our society's infrastructure. As electronics technology has evolved, it has become more commonly available, and useful, to structural engineers in both the research and professional arenas. Today, it would be almost impossible to find a consultant who does not use computers as a design aide. Increasingly, monitoring the health of structures will not be solely a function of an annual physical, or visual, inspection by structural engineers. Engineers now, and in the future, will need to use technology in the field to help them verify the behavior of that which they have learned to analyze and design. As more structures are instrumented, we will learn more about their behavior and this can lead to more economical ways to build and maintain them. While an understanding of structural phenomena is a requirement of any structural engineer, electronics concepts can often be a mystery beyond that learned in a single physics class during an undergraduate program.

1.1 General Purpose

The academic field has been a source for advances in building technology. Through journals, conferences, and institutes, academia provides government and engineers the best consensus of technical knowledge on what is required to design an effective structure. Use of electronics devices in labs has provided the raw data used to better understand the nuances of material structural behavior. So much so that in the last decade, there has been a push toward a performance based design code. This design

philosophy provides the owner an option to choose the level of protection from events that may threaten their building or bridge. Currently, there is a lack of resources/references that today's engineers can readily utilize to directly provide a complementary value added service of structural health monitoring (SHM). This service can be an especially important assessment tool applied to critical infrastructure that will need to maintain operational capacity during a potentially catastrophic event. While several guidelines have recently been published with regard to SHM [Aktan et al. 2002, Bergmeister 2002, ISIS Canada 2001] there remains a need for a more detailed description of available measurement methodologies, associated mathematical processes including post processing, and detailed examples of implementation strategies. If the goal is to rollout SHM as a commonly available tool, it is critically important to provide a significant database of SHM successes and failures to ensure the growth and maturing of the SHM field.

In the report "Development of a Model Health Monitoring Guide for Major Bridges" [Aktan et al 2002, pg 7] the authors state that their report is, "designed to serve as a starting point for reaching consensus standards and specifications to help the bridge engineering community...to make informed decisions about the value of various technologies such as instrumentation, monitoring, load testing, field calibrated analytical modeling, etc." Their report is inclusive of a large scope of SHM issues including sensors, data acquisition systems, networking, measurement calibration, data management / interpretation, and some real world applications. However, there are still details that are left out: what has been tried unsuccessfully; what are some actual

installation procedures that have been tried? Generally, more should be done to communicate these techniques with the intent of describing the instrumentation process, not just the structural phenomenon observed.

The purpose of this dissertation is to reflect on the lessons learned during several testing programs at the University of Hawaii at Manoa over the past four years. Through interaction with other graduate and undergraduate students and their projects, the author realized that there is not one easy source that describes the currently available measurement techniques utilized in a modern structural engineering laboratory. Structural engineering students often do not understand how the electronic devices, that they use, work. Furthermore, this lack of understanding leads the author to believe that while the potential of computer software, in engineering simulation applications, has been and continues to be explored, the future engineers who will be required to provide the SHM services to clients in the future, are currently, woefully unprepared. Chapter 2 and 3 of this dissertation provides some technical background about the devices used during the presented research and that are commonly used in many SHM programs.

Hopefully, this document can contribute toward informing new students, engineers, and scientists in the structural engineering field that SHM should, “[provide] a common framework for the appropriate selection, integrated application, and especially for interpreting the results of any set of technologies for maximum reliability and payoff” [Aktan et al. 2002, pg 7]. The primary original contributions of this dissertation are processes by which to appropriately select / design three technologies to be used in an

overall SHM program. The contributions relate to the use of: an LVDT-Taut-Wire Baseline system to monitor vertical deflections; economical Wheatstone bridge based gauges to monitor crack mouth opening displacements, or the rotation of pinned support connection; and strain based deflection measurement within beams.

Chapter 3 describes the development and design process for an LVDT-Taut-Wire baseline to automatically record the displacement at multiple locations along a beam. This contribution allows future similar systems to be designed with minimum requirements to produce an effective result. The technique used will allow other researchers to more efficiently design / utilize existing technologies during a SHM program that monitors deflections. Chapter 4 describes the design process used to develop two different types of gauges. One gauge measures changes in crack widths and the other was used to monitor the relative rotation at a pinned support. Although the technology is not new, these devices were designed and built in an economical way that will allow a SHM project to collect more data under a limited budget. Furthermore, reporting this process is important, incorporating similar devices into a SHM program should help to relieve the pressure to get the newest and hottest technology, which may not be easily understood by the user and may not perform up to the manufacturers promised performance—typical of new developing technologies. Chapters 5 and 6 show the analysis of a technique that uses strain measurements to monitor the deflection of a beam. Others have used this process successfully to monitor structures [Vurpillot et al. 1998, Inaudi et al. 1998, Cho et al. 2000]. The new information in this dissertation is the error analysis performed in Chapter 6. The analysis sheds light on things to consider

when designing such a system. The result is a method to predetermine what the expected displacement error will be when collecting real-time strain data. This statement of error helps an investigator to interpret the results of a designed system a priori. If the performance is not satisfactory, it can then be redeveloped with a new measurement configuration to better account for how structure is expected to behave—a better installed SHM will result.

1.2 Literature Review

Mufti et al. [2005] posed the question, “Are civil engineers ‘risk averse’?” Anecdotally, architects, owners and contractors have answered their question with a resounding, “Yes!” Structural engineers often receive complaints that their plans are over designed and too conservative. The world over, structural engineers are wise to be conservative, they are held responsible to ensure that proper instructions are conveyed to the constructors of society’s infrastructure. They produce the plan of action to provide the basic human need for shelter from the environment. In the United States, the litigious nature of the social and justice system holds the engineers personally responsible for any mistakes that they make. It has often been said, “When a doctor makes a mistake, one person dies; when an engineer makes a mistake, hundreds of people die.”

In 1906, the San Francisco earthquake and resulting fire was the cause of the destruction of 28,000 structures [NOAA 1972] and an estimated 3,000 deaths [Hansen & Condon 1989]. Since then the engineers together with civil authorities have been developing and improving building codes such that structures are more likely to survive similar

earthquakes [Reasenberg 2000]. These building codes are the result of research that also guides insurance companies to evaluate their clients risks [Reasenberg 2000].

Building code development has been helping the structural engineering community to reduce its risk to liability exposure. The building codes are generally built on both principles of mechanics and statistics developed from empirical data generated through laboratory testing. Even the first codes provided a safety margin to prevent collapse during unintended overloading. The allowable stress design (ASD) method of designing structures for load was developed to provide a safety factor. Classically, engineers were able to test the strengths of the various materials used in a structure and determine a stress at which those materials would fail. To provide an adequate building, engineers would size their structural elements such that the internal stresses would not reach higher than a specified fraction of the failure stress level. The safety factor was based on experience, which implied, “it has been working for years so, it’s ok to keep doing it.” While this can work well, Load Resistance Factor Design (LRFD) also known as Limit State Design (LSD) was developed to provide a more rational approach that could provide a similar level of safety and to create more economical structures, utilizing the increased knowledge we have learned over the years of testing structural components.

ASD safety factors are susceptible to the question: what safety factor is an appropriate level? Even with the extensive testing that has been performed, in each structure there is usually a significant amount of reserve capacity above and beyond the recognized safety factors. The apparent risk to human life due to structural failure as outlined by Mufti et al

is at 0.1 deaths per million per year [Mufti et al 2005]. Building fires and air travel are 240 times more risky to life at 24 deaths per million per year [Mufti et al 2005]. How is this level of risk achieved or determined? The National Transportation Safety Board (NTSB) does a cost benefit analysis to determine safety requirements after a mechanical failure causes an airplane to crash. If society deems it acceptable to use economics as the sole determinate for setting air travels 24 deaths per million level of risk, is that level of risk not also appropriate for the structural engineering industry? If it is, does it not allow us to use SHM to explore the sources of this reserve capacity in existing structures?

Finally, in chapters 7 and 8 a few completed and planned SHM systems are discussed. Chapter 7 shows some results of a SHM system installed during the load testing of a bridge. The SHM system incorporated the LVDT-Taut-Wire Baseline System discussed in Chapter 3 and the Wheatstone bridge based devices discussed in Chapter 4. Chapter 8 discusses other structures currently being equipped with SHM systems and how they will incorporate the contributions of this dissertation.

CHAPTER 2. AVAILABLE MEASUREMENT METHODOLOGIES

Structural health monitoring projects can have many types of phenomenon that need to be observed, recorded, and analyzed. Each SHM system consists of four major components: transducers, signal conditioners, analog to digital converters (ADC), and a digital recording device—a personal computer is often used. Current commercially available technology for structural health monitoring is capable of obtaining up to 10 million signals per second and up to 24-bit digitization accuracy [NI 2006]. This high speed and high accuracy cannot yet be achieved at the same time: higher speed products will have fewer bits for the ADC; higher bit resolution will have lower acquisition speeds. Although this implied speed and / or accuracy can be obtained in some cases; it is highly dependant on the type of device, transducer, being used.

2.1 Overall Data Acquisition Systems

A National Instruments SCXI based data acquisition (DAQ) system running LabVIEW™ software was the primary source of data acquired during this research. Generally, a DAQ system could be set to simultaneously monitor each sensor at any frequency up to a limit dictated by the number of sensors used and the total number of signals per second the ADC and digital recording device are rated to handle. So, theoretically, if the system is rated to handle 1 million signals per second, and 500 transducers were installed into that system, the maximum acquisition rate per transducer is 2000 Hz. This will not always be achievable. The “rated” limit often is only achieved for a specific configuration—a smaller practical frequency limit exists. Acquiring data directly from many transducers to

a tabulated text file can be inhibited by; the speed of the signal conditioner, the D/A converter, and processor or hard drive. Each system will have different real time requirements that can limit the acquisition speed as well.

Some systems will only require data to be collected on an hourly basis and analyzed monthly; others may need high-speed calculated parameters to be reported live. The four DAQ implementations discussed in this research will highlight both the problems and possible solutions to the real time analysis issues that need to be overcome. In order to gain a better understanding, an in-depth synopsis of each device and its capabilities will be tested and discussed. These measurement devices, transducers, include the following: linear variable differential transformers (LVDT); electrical resistance, vibrating wire, and fiber optic strain gauges; Wheatstone bridge based crack gauges and rotation gauges; and others.

2.2 Linear Variable Differential Transformer (LVDT):

The LVDT is a device used to measure the relative displacement between two fixed locations. This type of device is based on the principle of induction. The device is constructed with three collinear coil windings, one primary and two secondary coils. The primary coil is electrified with an alternating current excitation voltage, typically either 1 or 3 volts at a frequency of between 2.5 kHz and 10 kHz. A metal ferromagnetic rod, the LVDT core, is allowed to translate within a cylinder housing the three coils. Depending on the core's location, two different currents are induced into the secondary coils. These different currents can then be measured.

The relationship between the signal voltage (including phase shift), the excitation voltage, and the displacement to the core is quantified as the sensitivity of the LVDT. The sensitivity can be thought of as the slope of the line that relates voltages in the device to the displacement observed by the device (see Figure 2.2.1). Typically sensitivity has units of $\text{mV/V}/0.001\text{in}$, or millivolts of signal per volt of excitation per thousandths of an inch displacement. Sensitivity can also be expressed in SI units as $\text{mV/V}/\text{mm}$. The manufacturer provides the sensitivity for each individual LVDT. The displacement is then calculated depending on the wiring configuration used.

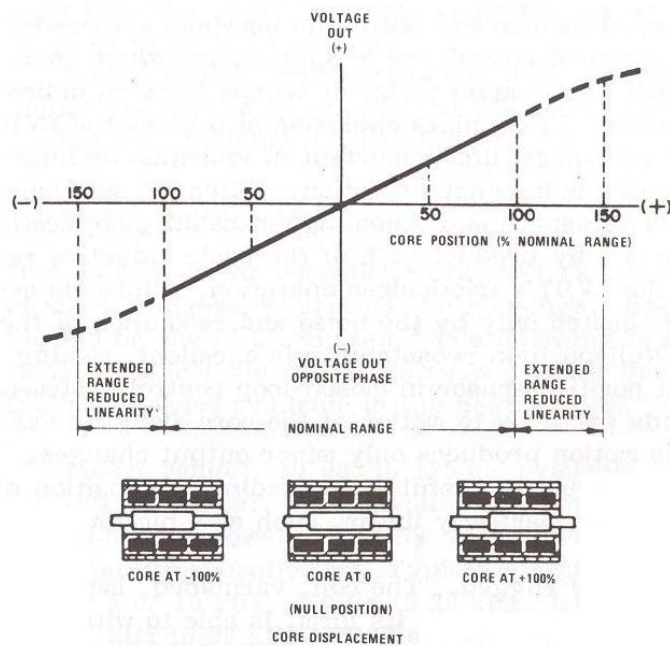


Figure 2.2.1. LVDT Output [source: Trietily 1986, pg 69].

There are two wiring configuration types: ratiometric wiring or open wiring [Techkor 2000]. The ratiometric wiring configuration is also known as either 5-wire or 6-wire configuration. The open wiring configuration is also known as the 4-wire configuration.

2.2.1 Ratiometric Wire Configuration

In the ratiometric wiring configuration, the output from each secondary coil (coil 1 and coil 2) is observed separately. The signal voltage from secondary coil 1, V_{S1} , and the signal voltage from secondary coil 2, V_{S2} , are both used to calculate the position of the core within the coil housing. The calculation is as follows:

$$D = \frac{V_{S1} - V_{S2}}{(V_{S1} + V_{S2})S} \quad (2.2.1)$$

where,

S is the LVDT sensitivity; and

D is the displacement.

2.2.2 Open Wire Configuration

In the open wiring configuration, the secondary coils are electrically connected in series—a single voltage and phase shift associated with the induced current across the secondary coils is measured (see Figure 2.2.1). The signal voltage, V_s , is directly related to the relative displacement of the core.

$$D = V_s / S \quad (2.2.2)$$

where,

S is the LVDT sensitivity; and

D is the displacement.

2.2.3 *Influence of Cable Length*

Cable length between the signal conditioner and the LVDT can affect the accuracy of the displacement reading. This occurs primarily for the open wire configuration. The impedance (total of resistance and AC related induction and capacitive effects) of longer cables causes a phase shift between the current and voltage signals. The phase shift changes the arrival time of the maximum current at the primary core of the LVDT. For a short cable the total impedance is negligible so the phase shift between the signal conditioner and the LVDT will also be negligible. However, as the cable is lengthened its impedance will increase to a point where it may cause a significant phase shift within the LVDT circuit.

Since the current induces the AC signal into the secondary coils, the phase shift continues to grow as the signal returns to the signal conditioner. Within the signal conditioner, the excitation voltage is electronically multiplied with the signal voltage and subsequently digitized without considering any phase difference [NI 2000, pg 1-6]. The arriving signal voltage and excitation voltage will be slightly out of phase. The peak excitation voltage and peak signal voltage will arrive at the voltage multiplier at different times. For the long cables (Belden 8723) and SCXI-1540 signal conditioner used in this research, the

difference causes an increase in the measured deflection. The indicated deflection of the LVDT core is larger than the actual deflection of the LVDT core. The effective sensitivity of the LVDT at the signal conditioner is reduced. To account for the cable length, several things can be done: use the ratiometric wiring method, which is subject to more ambient electrical noise; measure and electronically adjust for the phase shift during signal conditioning; or the LVDT can be calibrated with the cable that will be used in the application.

2.2.4 Sensitivity Correction Factor (SCF)

During this research, the open wiring configuration was used. The LVDTs were wired for laboratory use—short cable lengths. For structural health monitoring, the ratiometric wiring method is often less desirable due to its increase in susceptibility to noise from power lines, transformers and motors [NI 2000, pg 2-3]. The drawback is that when these LVDTs are used with long cable lengths a phase shift in the signal occurs. The signal conditioner type used during this research does not have the capability of adjusting for the phase shift. The approach used to adjust for the error caused by this phase shift was to calibrate each LVDT with the cable length used during the field application. The process requires assigning a new effective sensitivity for each LVDT on a long cable.

The intent of this process was to determine a relationship between the cable length and the change in effective sensitivity. To do this, the sensitivity correction factor, SCF, is defined as the ratio between the displacement recorded by an LVDT with a long cable length and the actual displacement of its core. The SCF is the slope of the line obtained

by plotting the displacement of an LVDT with a long cable length versus a calibrated LVDT. Figure 2.2.2 shows the data of an LVDT with a 61 m cable length before and after applying the SCF. The factory supplied sensitivity was 396 mV/V/0.001 in. Figure 2.2.2 shows a slope (SCF) of 1.082 for the factory sensitivity based data. Multiplying the slope by the factory sensitivity, and rounding to the nearest whole number, a sensitivity of 428 mV/V/0.001 in was used to acquire a new data set. A slope of 1.0009 was obtained as shown in the sensitivity correction plot in the figure. This was repeated for seven lengths of cable ranging from 49 m to 73 m at 4 m intervals—this covered the full range of cable length used during a monitoring program.

During this process, a linear relationship between the adjusted sensitivity and cable length was observed for that range. Figure 2.2.3 is a plot of a sensitivity correction factor (SCF) versus cable length, l , in meters. A trendline was plotted. The linear regression of the SCF data produces an R^2 value of 0.9867. The result of the linear regression is the following equation of the SCF in terms of cable length:

$$SCF(\lambda) = 1 + 0.0013(\lambda). \quad (2.2.3)$$

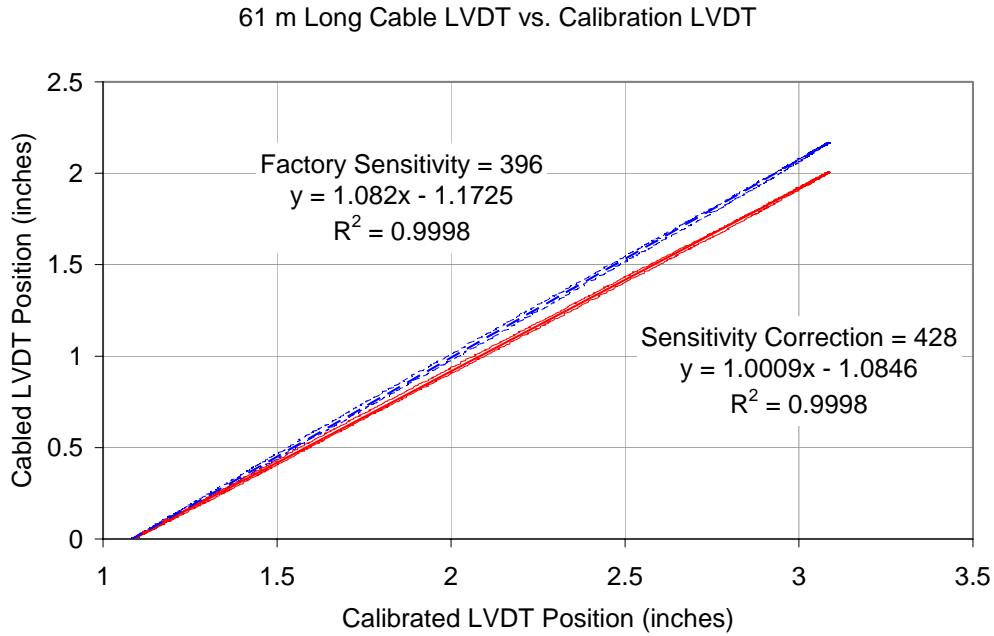


Figure 2.2.2. Effect of Sensitivity Correction Factor (SCF).

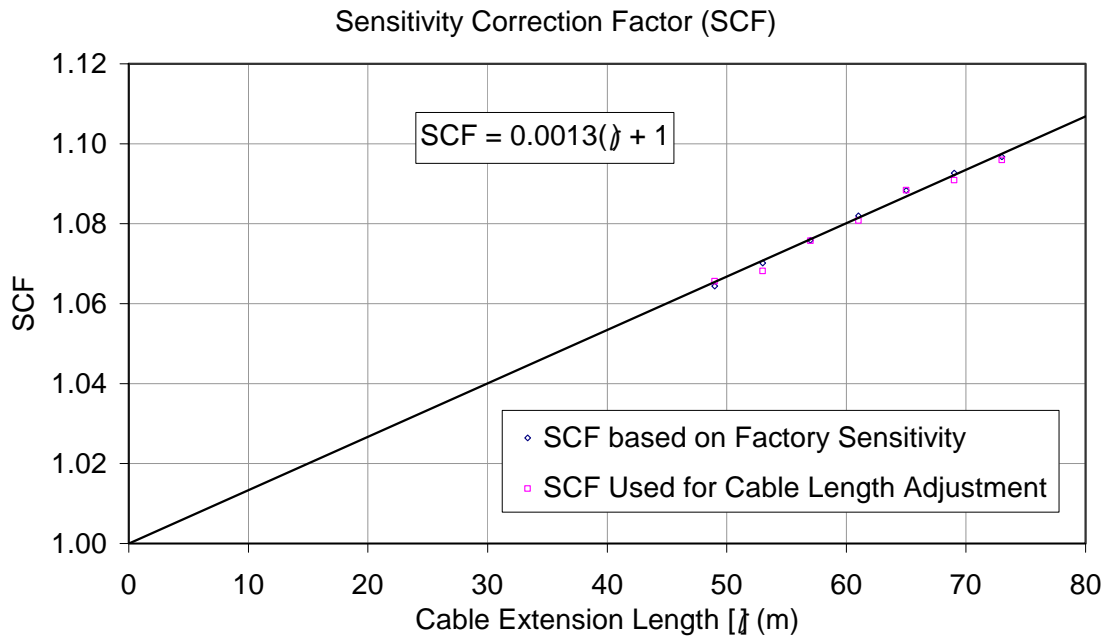


Figure 2.2.3. LVDT Sensitivity Correction Factor vs. Cable Length.

The author determined that multiplying the manufacturer's provided sensitivity by the SCF is a good adjustment to the sensitivity for the combination of cables and LVDTs used. Without the SCF adjustment, as applied to this application, the LVDT would indicate a 10% larger deflection than exists for a cable length of 75 m, as shown in Figure 2.2.3. Information such as this is not typically provided by the LVDT manufacturer or by the signal conditioner manufacturer. The documentation for the signal conditioner used during this research did state that cable lengths of greater than 100 meters could cause significant errors [NI 2000, pg 2-4]. This is just one example of a technique to determine the appropriate sensitivities for the field condition. The resulting relationship is not necessarily appropriate for any LVDT setup with long cables—the technique, however, is portable. Since every different specified cable has different impedance properties, this process should be repeated for each type of cable used.

2.2.5 Limitations for Structural Health Monitoring

The primary limitation of the LVDT is the establishment of a baseline to measure against. Typically, in the laboratory, there is a location adjacent to the structural element of interest that is not a part of the load path nor affected by the testing protocol. LVDTs can be used in bridges and buildings to measure relative movements, such as: displacements across expansion joints, thermal extension between two points along the length of a member, the diagonal racking displacement of a plywood shear wall, et cetera. To observe beam deflection, an available technique is the taut wire baseline system which is discussed in detail in Chapter 3.

2.3 Strain Gauges

A strain gauge is composed of a material with a measurable property sensitive to its own change in length. When the relationship between the measurable property and strain can be established, a material can be used as an effective strain gauge. There are many different types of strain gauges. The material of the structure studied, the full scale magnitude of expected strain, the required frequency of strain measurements, and the surrounding environmental conditions will determine what type of strain gauge is best suited for the application. As opposed to using strain gauges in a laboratory, in structural health monitoring, strain gauge thermal output must be considered a significant potential source of error. Without properly considering the thermal output of strain gauges at the beginning of a structural health monitoring program, it can be difficult to isolate mechanical behavior based on direct strain readings alone. This section will describe: three types of strain gauges; some thermal effects to consider during a SHM program; and a comparison of the discussed strain gauges.

2.3.1 *Types of Strain Gauges*

In this section, three types of strain gauges are discussed: electrical resistance strain gauges, fiber optic strain gauges, and vibrating wire strain gauges. It should be noted, strain can also be observed by devices that are designed to measure relative displacement between two discrete points. The strain is calculated as the relative displacement of the device divided by the initial distance between the discrete points. This type of strain determination will not be discussed in this section.

2.3.1.1 Electrical Resistance Strain Gauges

Electrical resistance strain gauge technology is well established and widely used. The material property of electrical resistance is sensitive to the mechanical change in length of some conductors. These conductive materials, typically metals or metal alloys, exhibit sensitivities that are linearly related to strain. The measurements can be significantly impacted by electrical connection changes in the system. Also, the sensitivity is influenced by temperature.

2.3.1.1.1 Basics of Observing Resistance Change

Directly observing the change in resistance with an ohmmeter is not generally accurate enough for currently available strain gauges. Instead we use Ohm's Law—voltage, V , equals the product of current, I , and resistance, R :

$$V = IR. \quad (2.3.1)$$

A voltage divider circuit is the simplest way to measure a change in resistance (see Figure 2.3.1). A voltage divider circuit is powered by a constant supply voltage, V_{ex} , while a signal voltage, V_s , changes with the resistance of resistors R_1 and/or R_2 . In Figure 2.3.1, V_s is measured across resistor R_2 , and V_{ex} is applied across both resistors R_1 and R_2 . By Ohm's Law and the summation of resistance: $V_{ex} = I(R_1 + R_2)$, where I is the current flowing through the resistors R_1 and R_2 .

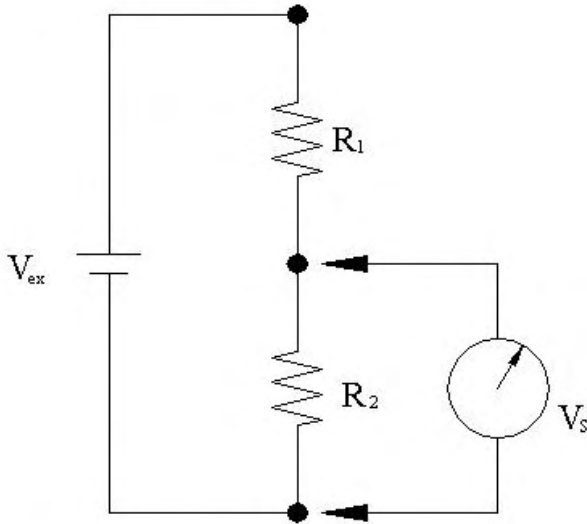


Figure 2.3.1. Voltage Divider Circuit.

Currently available strain gauges have resistances of 120, 350, and 1000 ohms. The sensitivity of each gauge is expressed as a gauge factor, GF . The gauge factor is a ratio between the relative change in resistance and strain:

$$GF = \frac{dR/R}{\epsilon} \quad (2.3.2)$$

Metallic foil strain gauges have gauge factors that are typically between 1.90 and 2.10. Consider the voltage divider circuit in Figure 2.3.1, let R_1 be a 350 ohm resistor and R_2 be a 350 ohm strain gauge with $GF = 2.00$. If $V_{ex} = 7.000$ V, the current, I , by equation (2.3.2) is 10 mA. The initial unstrained signal voltage across R_2 is $V_s = I (R_2) = 3.500$ V. As seen in the sample calculations in Figure 2.3.2, a 5 microstrain change in the strain gauge will result in a resistance change of 0.0035 ohms or a 0.035 mV change in the signal voltage.

$$dR/R = GF(\epsilon). \Rightarrow dR = GF(\epsilon) R.$$

$$\text{Let: } \epsilon = 5\mu\epsilon; R = 350 \text{ ohms}; GF = 2.0; I = V_{\text{ex}}/R_{\text{total}} = 10 \text{ mA}.$$

$$dV = I dR = I GF(\epsilon) R = 10 \text{ mA} (2.0) (0.000005 \text{ in/in}) 350 \text{ ohms}.$$

$$dV = I dR = 10 \text{ mA} (0.0035 \text{ ohms}) = 0.035 \text{ mV}.$$

Figure 2.3.2. Sample Calculation to Find Voltage Resolution ($5\mu\epsilon$ measurement).

The strain resolution will depend on the smallest increment of measurement of the voltmeter—a smaller measurable voltage leads to a better strain resolution. A better strain resolution can also be achieved by increasing the excitation voltage. This can be shown by repeating the sample calculation shown in Figure 2.3.2 with a larger excitation voltage, V_{ex} . An increased current through the strain gauge resistor will magnify the signal voltage, V_s , for a set change in strain. However, there is a practical limit to increasing the current which must be considered (see section 2.3.3.1 for more detail).

2.3.1.1.2 Wheatstone Bridge Based Strain Measurements

Temperature changes in the strain gauges and in the long cable leads between the data acquisition system and electrical resistance strain gauges can cause spurious indicated strain readings. To compensate for this occurrence, a common approach is to create an electrical compensating network [Fraden 2004, pg 326]—the Wheatstone bridge is one type.

As described in the previous section 2.3.1.1.1, a voltage divider is constructed using two resistors in series. The circuit is completed by applying an excitation voltage across the series. The voltage measured at the node between the two resistors is a fraction of the excitation voltage as determined by Ohm's law and Kirchhoff's rules. Using a strain gauge as one of the resistors causes the measured voltage to change with strain.

Similarly, a Wheatstone bridge provides a way to measure voltage to indicate strain. The bridge circuit is two voltage divider circuits in parallel—both voltage divider circuits are powered by the same excitation voltage source. The signal voltage is then measured between the two voltage divider output nodes. This circuit is the standard circuit used with electrical resistance strain gauges. It can be used to improve performance and provide application adaptability of strain gauge based measurements. The bridge circuit can increase the resolution of strain measurements and perform temperature compensation. Chapter 4 describes two applications for measuring a crack mouth opening displacement and the rotation at a pinned connection using devices built with electrical resistance strain gauges.

Shown in Figure 2.3.3, the resistors R_1 and R_3 form a voltage divider circuit; and resistors R_2 and R_4 form the other. The voltage divider outputs are at nodes b and c, respectively.

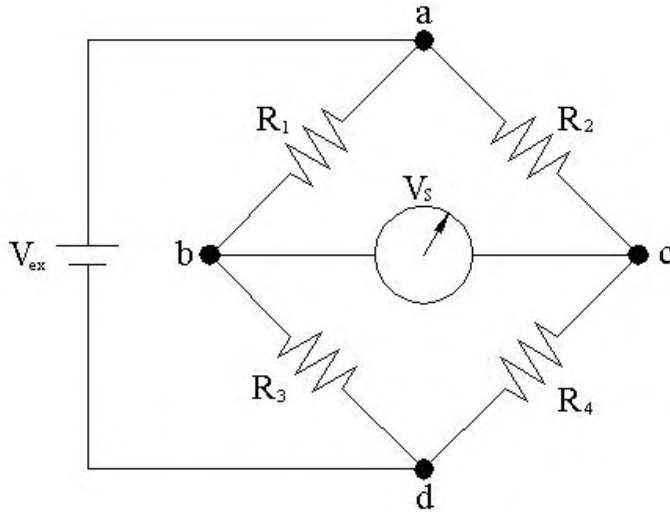


Figure 2.3.3. Wheatstone Bridge Circuit.

The Wheatstone bridge can be used to indicate strain by two methods: nulling method or direct method. The nulling method involves using a variable resistor to balance (or null) the voltage across the two voltage divider outputs: nodes b and c. The resistance required to achieve this null balance is directly related to the strain reading. The direct method simply requires measuring the voltage across the two voltage divider outputs—Figure 2.3.3 depicts this method. An output signal (V_s) of zero volts occurs at the zero strain state if each resistor and or strain gauge within the circuit has an identical resistance. In Figure 2.3.3, V_{ex} is the excitation voltage. R_1 through R_4 are the resistors within the bridge, any one, or all, of which can be a strain gauge.

There are three main configurations of the Wheatstone bridge circuit: quarter bridge, half bridge, and full bridge. These configurations refer to how many of the resistors are strain

gauges. Logically, a quarter bridge uses only one strain gauge out of four resistors, a half bridge uses two strain gauges, and a full bridge four strain gauges.

For a single strain gauge, the quarter bridge is typically used. This configuration is susceptible to the thermal output of the strain gauge. Also, this signal conditioning network is usually physically separated. The strain gauge is attached to the specimen and the other three resistors are within the data acquisition hardware. Long electrical leads will act as an antenna picking up electrical noise and changing resistance with temperature along their length. To account for these error-inducing impedances, the lead length effect is introduced to both sides of the bridge circuit—both voltage dividers. This is done by using three lead wires for the strain gauge—schematically shown in Figure 2.3.4. The signal voltage, V_s , will not change with a common equal resistance change along b-d, and c-d. A small resistance change R_L between node d and the excitation source, will not significantly change V_s either.

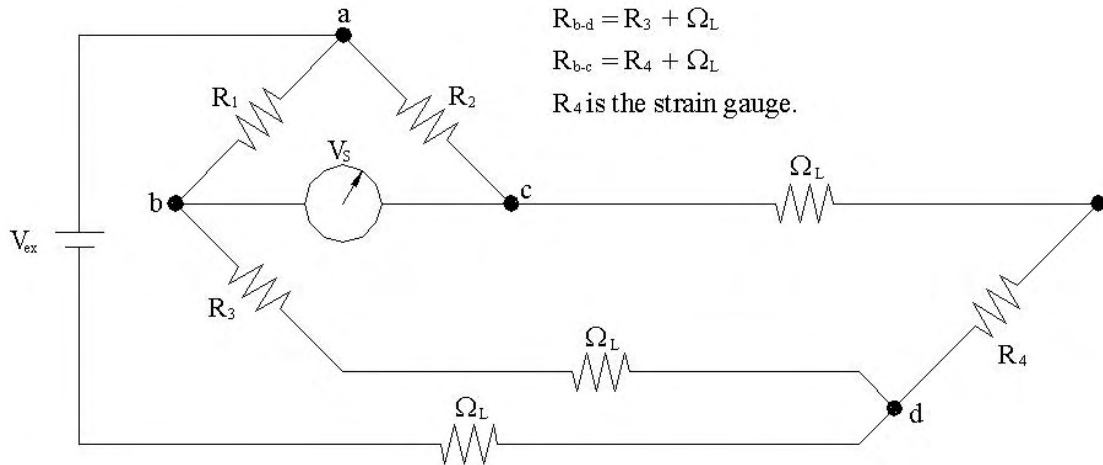


Figure 2.3.4. Long Lead Quarter Bridge Configuration.

The half bridge configuration utilizes both voltage divider circuits to perform one of the following: amplify the signal voltage; perform strain gauge thermal output compensation. For a half bridge configuration, typically, resistors R_1 and R_2 , or R_3 and R_4 , are the active strain gauges. Signal amplification is achieved by using two strain gauges which are mounted in such a way that one experiences positive strain while the other experiences negative strain. As an example, if one gauge is applied perpendicular to the other, strain applied in one direction will cause a negative strain in the other, due to Poisson's effect. This produces a greater signal voltage than one gauge alone: both voltage dividers are affected in opposing directions. The thermal output of both gauges will be identical and are already applied to both sides of the bridge—temperature compensation is automatic. If thermal output compensation is required, without signal amplification, one gauge (called a “dummy” gauge) can be mounted on similar material that is only exposed to the temperature changes and not the mechanical loading. Thermal output compensation

achieved in a half-bridge configuration can be done in such a way that adjusts for lead length. The quarter bridge configuration does not perform strain gauge thermal output compensation.

The full bridge configuration, like the half bridge, can compensate for strain gauge thermal output and can amplify the signal voltage by up to four times that of the quarter bridge. This configuration is commonly used for making load cells, extensometers, and a variety of other devices. Chapter 4 shows the use of the full bridge configuration to measure crack mouth opening displacements and rotational displacements at a bridge pinned support.

2.3.1.1.3 Thermal effects

Generally, the sensitivity as a function of temperature is non-linear. The temperature sensitivity of electrical resistance strain gauges can be compensated for in a variety of ways. There is no one best way; it all depends on the application. For structural health monitoring applications, there are two sources where temperature induced systematic error can occur: the effect of temperature change on the long cable leads between the data acquisition system and the strain gauge, and the effect of temperature change on the strain gauge itself.

The temperature change on long cable leads for a single strain gauge is easily handled. The Wheatstone bridge in a quarter bridge configuration is utilized. The specific wiring requirement to achieve this is shown in Figure 2.3.4 and discussed in section 2.3.1.1.2.

The effect of temperature change on the strain gauge itself has several mechanisms. Temperature affects the electrical resistance of conductive materials. It also affects the gauge factor (sensitivity) of the gauge. Figure 2.3.5 shows a typical relationship between temperature and the strain gauge thermal output for one type of strain gauge material. Notice that for this gauge material, bonded and tested on 2024-T4 Aluminum, there exists a range of temperature, from about 10 °C to 40 °C, where the thermal output is relatively constant. This range may be enough to assume that the strain gauge sensitivity will be constant for all measurements required for many civil and architectural structures.

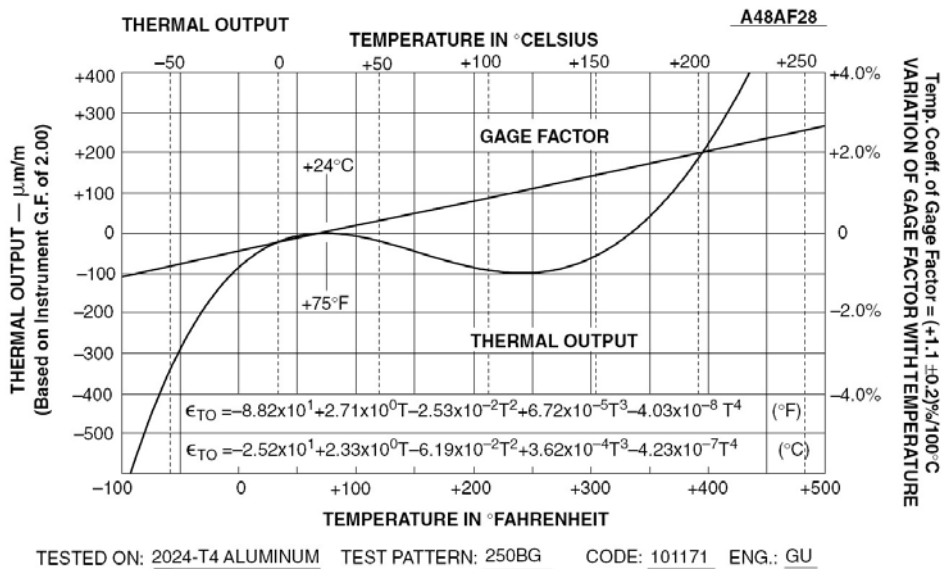


Figure 2.3.5. Thermal Output from an Electrical Resistance Strain Gauge [source: Vishay 2005, pg 6].

Notice that the gauge factor also changes with temperature; however, over the full 330 °C range of the figure it only deviates about 3.5 percent—not likely to significantly affect civil structural health monitoring measurements. The useful linear range for each strain

gauge material should be considered when selecting a gauge for a particular application. If the non-linear range is needed, temperature compensation is suggested (see section 2.3.2).

2.3.1.2 Fiber Optic Strain Gauges

Fiber optics technology is relatively new; however, it has rapidly become the standard for high speed communications equipment. This technology is capable of transmitting vastly greater amounts of data than its electronic copper wire predecessor. Fiber optic cable is composed of two layers of glass, or plastic polymer. The inner layer is called the core. The outer layer is called the cladding. Light is transmitted through the core by utilizing the phenomena of total internal reflection. This phenomenon is possible because the cladding has a lower index of refraction than the core. The cladding acts as a waveguide which helps to maintain signal intensity. Light enters the core at a polished end of a cable. As the light's angle of entry, into the core, tends toward normal, the light will tend to be reflected off the cladding back into, and propagate through, the core [Fraden 2004].

The light can be transmitted through fiber optic cables with much less energy attenuation than electricity through copper cable—subject to electrical resistance. Light also has a broader signal spectrum that can be utilized for transmitting data. The light signal is unaffected by a magnetic field-filled environment—passing vehicles, power lines, et cetera. The properties of light also allow for transmitting data in both directions on the same fiber. Fiber optic strain gauges are designed such that as the gage length of the fiber is strained, the reflective properties within the fiber core also change. This effects a

change to both the light signals reflected off, and transmitted through, the gauge. Two common approaches to making the core sensitive to strain and measuring its effects upon the reflected light are discussed here: Fabry-Perot interferometry and Bragg grating modulation.

2.3.1.2.1 Fabry-Perot Based Strain Gauges

Fabry-Perot interferometer based strain gauges relate strain to the reflection of light across a cavity between two polished partially silvered optical fibers, as seen in Figure 2.3.6. The cavity and partially reflective surfaces form a Fabry-Perot etalon, Figure 2.3.7. The purpose of this etalon is to create, and simultaneously transmit/reflect, multiple parallel rays of light. The new light signal will consist of a spectrum of light with some wavelengths in which constructive interference will occur and other wavelengths in which destructive interference will occur. The ray shown propagating across Figure 2.3.7 is that of a ray at a constructive wavelength: upon passing through the focusing lens, the rays' intensities combine on the screen. The constructive and destructive interference is dependent on the length of the Fabry-Perot cavity. By observing the change in the wavelengths where the maximum constructive interference occurs, the change in length of the Fabry-Perot cavity can be determined.

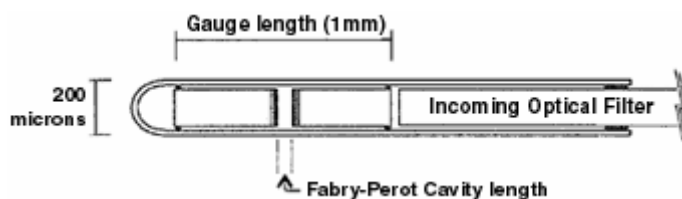


Figure 2.3.6. Fabry-Perot Fiber Optic Strain Gauge [source: Fiso 2006].

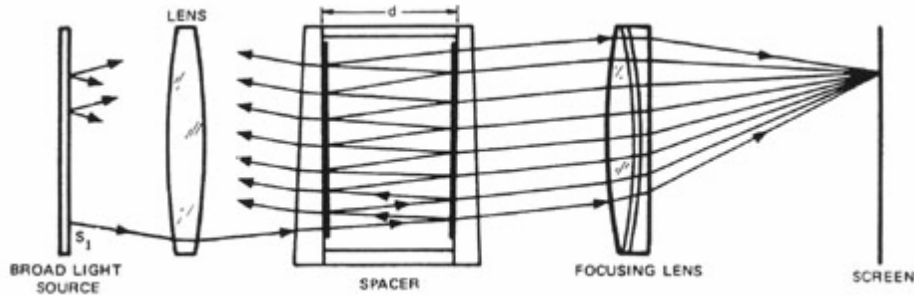


Figure 2.3.7. Fabry-Perot Etalon [source: Drexel 2006].

2.3.1.2.2 Fiber Bragg Grating Based Strain Gauges

Bragg grating modulation based strain gauges measure either the reflection or transmission of a specific wavelength of light. To make this type of gauge, the fiber optic core of a fiber is irradiated with ultraviolet light. The fiber core is photosensitive. At the location of the irradiation, periodic alterations of the core's refractive index—Bragg gratings—are created. The core alterations are burned into a single mode optical fiber at a period, Λ , selected for the gauge, where:

$$\lambda = 2 n_{\text{eff}} \Lambda. \quad (2.3.3)$$

The period of the grating, Λ , and the effective modal refractive index, n_{eff} , determine the Bragg grating wavelength, λ . As Figure 2.3.8 shows, the Bragg grating wavelength of light is reflected and does not transmit with high intensity beyond the irradiated core location. Stretching the fiber at the location of the grating changes the reflected wavelength. This change in wavelength is directly related to the strain in the fiber.

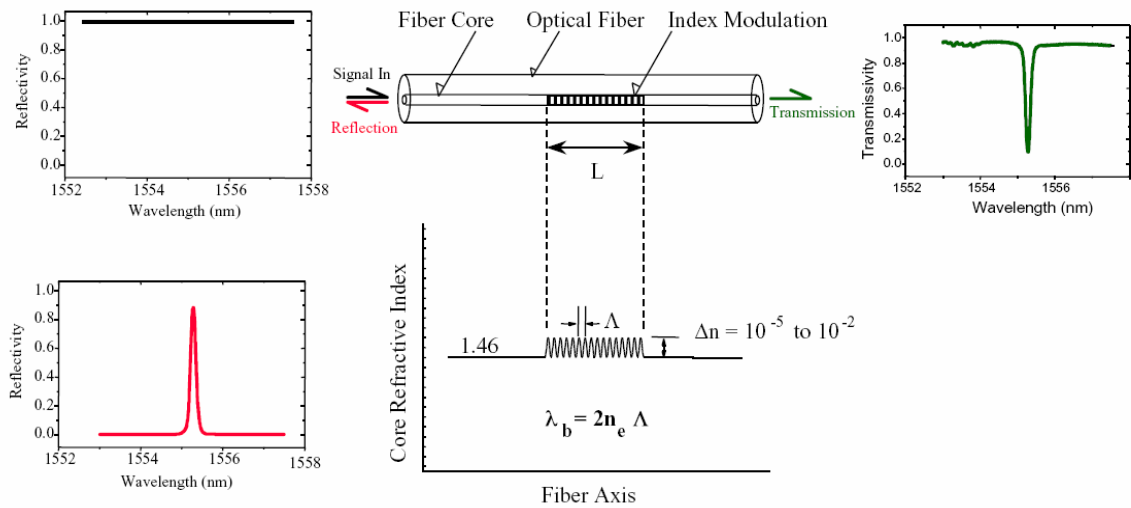


Figure 2.3.8. Bragg Grating Gauge Methodology [source: Chiareli 1999].

Any wavelength of light can be used in Bragg grating interferometry. A typical laser source used in FBG gauges generates wavelengths of light between 1510 nm and 1590 nm. The reflected light, as shown in Figure 2.3.8, does not consist of just one wavelength; instead it is a narrow bandwidth of light. Since the reflected bandwidth is small compared to the laser generated wide bandwidth, the Bragg grating approach allows a single fiber, or series of connected fibers, to have multiple gratings observed by the same signal conditioning channel. In other words, many strain gauges can be observed on one channel. As long as the expected shift(s) in wavelength for any two Bragg gratings—adjacent in the spectrum—do not collide, or overlap, no losses in effective strain readings will occur.

There is a simple relationship between gage wavelength and strain. To calculate strain, first, a “zero drift” wavelength, λ_0 , is recorded prior to loading. This wavelength is

analogous to an initial specimen length, L_i . Any observed wavelength during loading, λ , is analogous to the new length of the strained specimen, L_s . Assuming that only the grating pitch is affected by fiber extension or compression, to calculate strain, simply apply the analogous quantities to the definition of strain,

$$\varepsilon = \frac{L_s - L_i}{L_i} = \frac{\Delta L}{L_i} = \frac{\lambda - \lambda_0}{\lambda_0}. \quad (2.3.4)$$

The assumption that fiber strain only affects the grating pitch is incorrect. Fiber strain also affects the effective modal index, n_{eff} . As a structural engineer might imagine, the modal index can be affected by Poisson's ratio and transverse loading affecting a variety of optical/reflective implications within the fiber. Others have shown or observed, for the case of a homogeneous, isotropic axial straining of a Bragg grating, the relationship between strain and wavelength shift—including changes in n_{eff} —is approximated as shown in equation (2.3.3) [Meltz 1996, pg4]:

$$\frac{\lambda - \lambda_0}{\lambda_0} = \frac{\Delta \lambda}{\lambda} \approx 0.78\varepsilon. \quad (2.3.5)$$

To further illustrate this relationship; let us determine the required wavelength measuring resolution to obtain a 1 microstrain observation resolution. It is obvious that the shorter “zero drift” wavelength will experience a smaller wavelength deflection for the same value of strain—a shorter gauge length sees a smaller deflection. Since the range of available wavelengths is from 1510 nanometers to 1590 nanometers, choose the smallest

possible “zero drift” wavelength of $\lambda_0 = 1510$ nanometers and solve equation (2.3.5) for $\Delta\lambda$, where $\varepsilon = 1 \mu\varepsilon = 10^{-6}$ in/in (mm/mm):

$$\Delta\lambda \approx 0.78 * 10^{-6} (1510 \text{ nm}) = 1.178 \text{ picometers.}$$

This can also be written as a sensitivity of the gauge, $1 \mu\varepsilon / 1.178 \text{ pm}$, or $0.8490 \mu\varepsilon / \text{pm}$.

The sensitivity of a gauge at the opposite end of the spectrum is $1 \mu\varepsilon / 1.240 \text{ pm}$, or $0.8063 \mu\varepsilon / \text{pm}$.

The initial, “zero drift” wavelength should not be confused with the gauge length of the strain gauge. For this type of strain gauge, the gauge length can be flexible. If the fiber is directly, or continuously, bonded to the specimen, it is probably safe to assume the gauge length is the length over which the core alterations are manufactured. If the fiber is maintained taut between two points attached to the specimen, the gauge length is the distance between those two points—even if the gratings only occur over a shorter distance. It should be noted that if part of the FBG is strained more than another, the reflected wavelength spectrum will be broader than the initial reflected wavelength [Wnuk 2005].

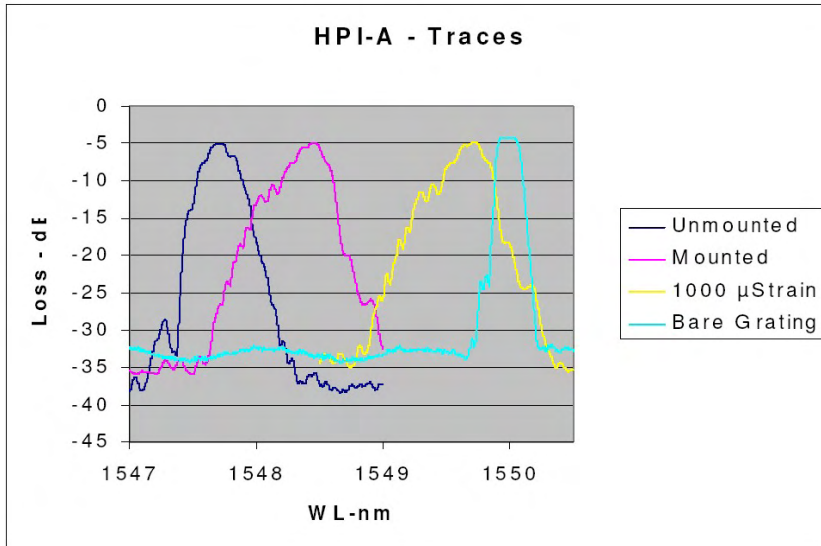


Figure 3.2: Spectral reflectivity for FBG sample HPI-A at different stages of packaging and testing.

Figure 2.3.9. Reflected Spectrum Changes due to Residual Strains [source: Wnuk 2005, pg 5].

The methodology of gauge attachment dictates actual strain observation. The curing of the epoxy may cause residual strains to occur at the Bragg grating locations. Observation of this behavior during installation is necessary such that the true "zero drift" reading is known. Care should be taken to understand the method by which the data acquisition interrogator determines the reflected wavelength. The broadening of the reflected spectrum—shown in Figure 2.3.9 by the difference in mounted and unmounted pattern—may cause different effects on the acquisition of the light signal. This could take the form of multiple “detected” wavelengths (multiple peak intensities), or a less stable detected wavelength. This effect may vary on different signal conditioning products

since this technology is still in the product development stage and has not arrived at a standard “best” method yet.

2.3.1.3 Vibrating Wire Strain Gauges

Vibrating wire strain gauge technology is widely used and well established. The vibrating wire strain gauges operate on the principle of resonance. These gauges operate by magnetically plucking a tensioned wire and measuring its free vibration response. The wire is pre-tensioned across the length of the gauge; as the gauge is stretched the tension in the wire changes and its resonant frequency changes. The resonant frequency is a function of both strain and the ambient temperature. Equation (2.3.6) expresses that function in terms of the mechanical properties of the wire. Equation (2.3.7) is the temperature-compensated strain as a function of the measured frequency and temperature.

$$f^2 = \frac{EA}{4mL^2} \varepsilon - \alpha \frac{EA}{4mL^2} \Delta T . \quad (2.3.6)$$

$$\varepsilon = \frac{4mL^2}{EA} f^2 + \alpha \Delta T . \quad (2.3.7)$$

For equations (2.3.6) and (2.3.7): f is the resonant frequency of the wire; L is its length; m is the mass per unit length; E is the elastic modulus; A is the cross-sectional area; α is the coefficient of thermal expansion; ΔT is the change in temperature from the initial temperature.

Vibrating wire strain gauges are very stable strain gauges. These gauges can be embedded or surface mounted. The thermal output, in terms of the change of resonant frequency, is easily compensated. However, because the wire needs to be plucked each time a reading is taken, the minimum recording period is approximately one second. This does not allow for observation of dynamic events.

2.3.2 Thermal Effects and Considerations for Strain Gauges

For structural health monitoring applications, there are two primary sources where temperature induced systematic error can occur: the effect of temperature change on the strain gauge material itself, and the effect of thermal expansion interactions between the gauge and attached material. Generally, the first source relates to the gauge sensitivity as a function of temperature. This is commonly non-linear over a broad range of temperatures. However, it can be represented as a linear function within a used range that is narrow. In any range of use, the thermal sensitivity/output should be identified for variable temperature environments—usually affecting structural health monitoring applications.

The second source can promulgate false strain readings when the strain gauge and test specimen material have differing coefficients of thermal expansion. Temperature affects the physical behavior of both the strain gauge and the material to which it is adhered. Any change in temperature of a material causes thermal straining of that material. Usually, the thermal strain, ϵ_t , is directly related to the temperature change, ΔT . This linear relationship is described by the coefficient of thermal expansion, α , where

$$\varepsilon_t = \alpha \Delta T. \quad (2.3.8)$$

If the mechanical loading of a structure is to be considered alone, and it is tested in a constant temperature environment, any difference in α between the strain gauge and the material being strained would not affect the indicated strain. However, identical coefficients of thermal expansion are desirable if a structure is being tested in an environment with varying temperature. Differing thermal expansion of the strain gauge and the specimen will cause an apparent strain. The stiffness of the specimen, by design, is much greater than that of the gauge. A strain gauge will be restrained by the specimen stiffness such that the gauge's thermal expansion will create an apparent strain that is only internal to the gauge material. This effect can and should be calibrated to the specimen thermal material properties. The indicated strain would be the sum of the real strain of the specimen and the apparent strain [Norton 1989]. The terms apparent strain, indicated strain and real strain are nicely defined in chapter 9.5 of "Handbook of Transducers" [Norton 1989].

For each strain gauge technology, both gauge sensitivity and apparent strain effects will be handled in different ways. As a general analytical tool, the measurable phenomenon observed by each technology can be described as a function of mechanical strain and temperature change.

$$\Delta P/P = S_\varepsilon \varepsilon + S_T T \quad (2.3.9)$$

ΔP is the change in the measurable phenomenon. P is the initial phenomenon measurement. S_ϵ is the mechanical strain sensitivity of the gauge. ϵ is the mechanical strain in the specimen. S_T is the thermal expansion sensitivity of the gauge—or the gauge restrained by the specimen—some gauges are calibrated on a particular material, say 1018 steel [Vishay 2005].

Table 2.1 shows the different parameters, as applied to equation (2.3.9) for some strain gauge technology types. The first column lists the strain gauge technology type. The second column is the measurable phenomenon. The third column lists the expression that describes the mechanical strain sensitivity. The fourth column lists the expression that describes the thermal expansion sensitivity.

Table 2.1. Strain Gauge Behavior Sensitivities.

Strain Gauge Technology	Phenomenon Measured (P)	Mechanical Strain Sensitivity Expression ($S_\epsilon \epsilon$)	Thermal Expansion Sensitivity Expression ($S_T T$)
Electrical Resistance Foil (ERSG)	$\Delta R/R$	$GF \epsilon$	$\epsilon_{to}(T)$
Fabry Perot Fiberoptic (FPSG)	ΔL_{cavity}	$L_g \epsilon$	$\beta L_g \epsilon$
Fiber Bragg Grating Fiberoptic (FBGSG)	$\Delta \lambda / \lambda_0$	$(1-P_e) \epsilon$	$Z \Delta T$
Vibrating Wire (VWSG)	f^2	$EA/(4mL^2) \epsilon$	$\alpha EA/(4mL^2) \Delta T$

As an illustration, for electrical resistance strain gauges (row one of Table 2.1) the full indicated output, equation (2.3.9), can be described by the following equation:

$$\Delta R/R = GF \varepsilon + \varepsilon_{to}(T). \quad (2.3.10)$$

R is resistance in ohms; GF is called the gauge factor, usually between 1.90 and 2.10. The GF is also a function of temperature but has a much less significant impact than the $\varepsilon_{to}(T)$ function—described further in Vishay [Vishay 2005, pg 6]. In this case, the thermal output of the strain gauge, ε_{to} , is a non-linear function of T which is provided by the manufacturer. An example function from Vishay Micro-Measurements is as follows:

$$\varepsilon_{to}(T) = -73.7 + 5.10 (T) - 9.17(10)^{-2} (T^2) + 4.48(10)^{-4} (T^3) - 5.50(10)^{-7} (T^4)$$

T has the units of °C. ε_{to} has units of microstrain.

These relationships should help an investigator to determine the best course of action to account for thermal loading of the structure and attached instrumentation.

2.3.2.1 Thermal Output Compensation Techniques

The relationships generally described by equation (2.3.9) and Table 2.1 above help the investigator to understand the potential effect of temperature and mechanical deformation on indicated strain. The strain indicated by a data acquisition device directly from the measured phenomena is not segregated into thermal and mechanical components. Signal conditioning per each respective strain gauge technology can help to do this. It is usually done through the use of a signal conditioning network [Fraden 2004, pg 195]. However,

this type of compensation is discussed in other sections. Aside from signal conditioning networks, the calculation of real strain can be handled in other ways based on the principles of the constitutive relationships described in Table 2.1. The problem addressed here is the measured strain value is inseparable from the sum of the mechanical and thermal effects. This section describes temperature compensation as a function of the thermal output of a strain gauge, specifically two techniques: (1) using a baseline of indicated strain, due to diurnal temperature effects, observed on the test specimen; and (2) using a second temperature observation applied to a formula based compensation routine.

2.3.2.1.1 Thermal Baseline Measurements Technique

The first technique involves installing the strain gauges onto the test specimen and observing the change with temperature over a period of time to establish a baseline. If a continuous structural health monitoring program is planned this is easily incorporated. As an illustration, Figure 2.3.10 shows typical data that is collected during one day of a bridge structure. As one can see, even without an in-depth analysis, for structures such as bridges, traffic loading or earthquake loading measurements are quite identifiable even with the thermal loading superimposed onto it. The mechanical loading happens much quicker than the thermal loading. The measurements just prior to the mechanical loading event can be considered the zero baselines and will provide sufficient “temperature compensated” results.

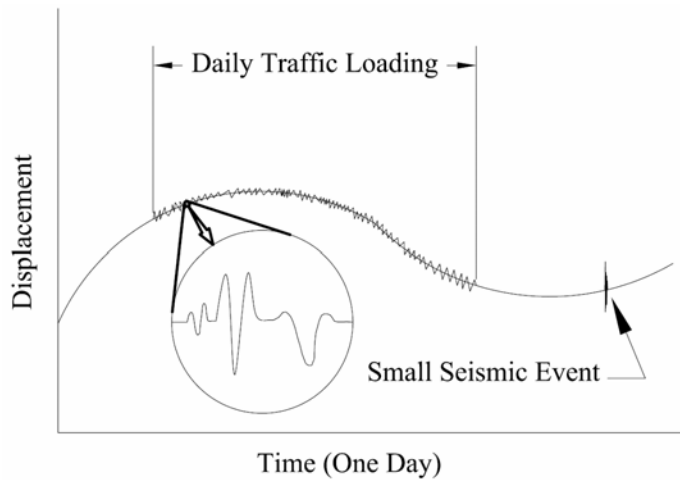


Figure 2.3.10. Typical Structural Diurnal Response.

To apply this idea to an automated SHM system, more sophistication is required but this technique can still be reasonably applied. It can be done by calibrating a thermal compensation algorithm with data from an initial short-term study at the start of a project. This algorithm can apply a compensating calculation to future data based on the initial temperature dataset. This refinement could be utilized to help isolate the mechanical strain behavior of interest to the structural engineer.

During the initial study period, thermal fluctuations representative of the expected temperature range through the course of the project should be used. This becomes more important when the type of gauge has a non-linear thermal output over the expected range—this is not common for civil or architectural structures, but should be considered as new technologies are evaluated.

More research needs to be done to see if periodic “thermal cycle” testing, during the course of an instrumentation project, can provide relevant information about systematic mechanical deterioration. A change in the temperature / indicated strain relationship has the potential to identify the change in mechanical properties such as flexural rigidity. To illustrate this point, if a reinforced concrete beam’s effective flexural rigidity was determined to be 50% of the gross section during a load test, and the thermal deflection behavior was also observed, any deviation from subsequent thermal behavior could indicate deterioration of the flexural rigidity as a result of crack growth or increased number of cracks. This has not yet been tested, but there is potential.

2.3.2.1.2 Calculated Apparent Strain Removal Technique

The second method to extract the real mechanical strain from a temperature influenced indicated strain is to measure the temperature. This can be done either directly or by use of a “dummy” gauge isolated from the mechanical loading of the test structure. Applying those measurements to the associated compensation formulas, characterized by Table 2.1, allow identification of the apparent strain. In this approach, the temperature will determine the apparent strain that needs to be removed from the indicated strain to obtain the real mechanical strain.

As an example, fiber Bragg gratings have a typical temperature sensitivity of 10 pm/°C near a wavelength of 1550 nm [Meltz 1996, pg 4]. Following the wavelength to strain conversion methodology in section 2.3.1.2.2, the strain thermal sensitivity is $1\mu\epsilon / (0.78 * 1.55\text{pm}) * 10 \text{ pm}/^\circ\text{C}$, or 8.27 $\mu\epsilon/^\circ\text{C}$. This is also known as the gauges

coefficient of thermal expansion, α_G . Concrete's α value is typically between 8 and 12 $\mu\epsilon/^\circ\text{C}$. Steel's α value is typically between 11 and 12 $\mu\epsilon/^\circ\text{C}$. Any difference in α between the gauge and the material can cause a spurious "apparent strain" to be observed [Norton 1989, pg 184].

When a strain gauge is used in a temperature-controlled environment, with a constant temperature, the "apparent strain" will be constant for all readings and is automatically removed when comparing two strain readings. However, when the temperature is variable, the "apparent strain" is not constant. This spurious strain can be removed with the use of an additional temperature compensation gauge. A temperature compensation gauge should be mounted, such that it is unaffected by the mechanical loading of the observed specimen. It should also be designed such that it correctly reflects the boundary conditions—restraint—of the other strain gauges measuring mechanical strain. For example, if a strain gauge is attached to the structure at only two points—as some gauges are designed—and is unbonded along the length of the gauge, the temperature compensation gauge should also be unbonded along its length. In this way, the α of both strain gauges is matched; a direct subtraction of the mechanically free strain gauge reading from the mechanically sensitive strain gauge reading eliminates the "apparent strain" from the signal acquired during the observation of the structure.

Figure 2.3.11 shows the output of a type of strain gauge that has a coefficient of thermal expansion of 30 $\mu\epsilon/^\circ\text{F}$ when mounted on two different materials. The plot labeled "A" results when the gauge is bonded to a steel specimen ($\alpha = 6.7 \mu\epsilon/^\circ\text{F}$). The plot labeled

“B” is what the manufacturer of the gauge describes as the estimated result if the same gauge was installed on a material with $\alpha = 35 \mu\epsilon/^\circ\text{F}$ [Vishay 2005].

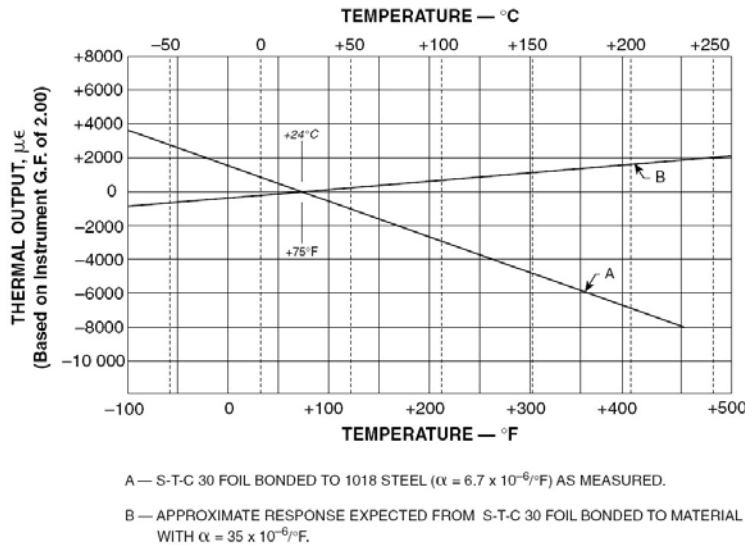


Figure 2.3.11. Strain Gauge Output Change Due to α Mismatch Effects [source: Vishay 2005, pg 9].

If the α of the gauge and the material to which it is bonded match, the indicated strain as a function of temperature would produce a flat line on the graph. The slopes of the plots in Figure 2.3.11 represent a difference in α between the material and the gauge. A negative indicated strain, mechanically analogous to compression, for an increase in temperature is the result of α being larger for the gauge than for the specimen. A negative slope in Figure 2.3.11 is consistent with this type of gauge and specimen interaction. A positive slope is consistent with the inverse behavior.

Equation (2.3.11) is a simplified thermal output formula that can be used to help compensate for the apparent strain experienced by electrical resistance strain gauges [Vishay 2005, pg 8]. It provides a way to estimate the change in thermal output of a gauge that is bonded on a material that is different from the material on which it is calibrated.

$$\varepsilon_T = \left(\frac{\beta_G}{F_G} - \alpha_G \right) \Delta T + \alpha_S \Delta T. \quad (2.3.11)$$

The process to obtain the estimate involves utilizing the difference between two iterations of this equation [Vishay 2005]. We consider both iterations for the same gauge type so the first term in the equation cancels (variables within the parenthesis are identical). What remains is an equation that states that the difference in thermal output, ε_T , due to the difference in the α values of two substrates:

$$\varepsilon_T(S_1) - \varepsilon_T(S_2) = (\alpha_{S_1} - \alpha_{S_2}) \Delta T. \quad (2.3.12)$$

This information and technique can be applied to determine the thermal output of a strain gauge on a substance with a different coefficient of thermal expansion, α ; it can be applied to determine the α of the test specimen; and to determine the effective coefficient of thermal expansion, α_{eff} , of other strain gauges for narrow ranges of temperature—such as with civil SHM. By using this technique with additional strain gauges that are only affected by temperature changes of the substrate material, the real mechanical strain can be retrieved from the indicated strain.

2.3.3 Structural Health Monitoring Strain Gauge Comparison

Each type of strain gauge has advantages and disadvantages depending on the phenomena of interest in an investigation. Civil engineering structural materials have varying mechanical properties that affect which strain gauge type should be used.

Concrete, steel, wood, aluminum, fiber reinforced plastic, and other materials will each have similar but distinct issues that need to be addressed. Some questions that need to be considered when observing the behavior of concrete or reinforced concrete structures include: Will cracking behavior occur? What gauge length is appropriate to measure the phenomena? Will the assumption that the concrete is homogenous be appropriate? Will aggregate shape, size and location potentially affect the results? Will the strain be monitored on a short-term or a long-term time scale? What type of surface preparation is required for adhesion of the gauge? Will temperature be stable or variable? This section will not attempt to answer all these questions, instead, it will help the investigator to make their own decision based on some of the identified advantages and disadvantages of each discussed strain gauge type.

2.3.3.1 Electrical Resistance Strain Gauges

As shown by the sample calculation in Figure 2.3.2, a typical strain change, of interest to engineers, causes a very small change in resistance and in turn measured voltage. This has several significant consequences. First, as mentioned earlier, an ohmmeter does not provide an adequate resolution for direct measurement of strain. Second, in terms of portability of a structural health monitoring system, the strain gauge leads cannot be

disconnected from the system without loss of the initial reading. This is limiting such that once the strain gauges are installed, they must be left installed to acquire long-term measurements—no disconnecting and reconnecting the data acquisition system. Third, special care must be taken to protect the electrical leads from corrosion and other similar physical damage that may alter the resistance within the measurement circuit.

Additionally, the user should be aware that both resistors and electrical resistance strain gauges cannot tolerate an infinite range of current. Indeed, the maximum applied current, or guidance on how to determine such [Vishay 2005], is usually reported by the manufacturer of the strain gauge. Also, the smallest measurable voltage is usually reported by the manufacturer of the signal conditioner. Lastly, although the signal from an ERSG is analog, digitization for storage can limit either the resolution or dynamic range of the signal. Any one of these may limit the usefulness of the data acquisition system for the electrical resistance strain gauges.

2.3.3.2 Fiber Optic Strain Gauges

Fiber optic strain gauge technology is still in the development phase. The two technologies discussed in this chapter—Fabry-Perot and Bragg grating—have both been developed to the point where they can be used in structural health monitoring projects. However, there are not many producers of quality gauges that have withstood the test of time. Product development on both the gauge design side and the signal conditioning side continues.

Fabry-Perot gauges and Bragg grating gauges are competing for which provides the best product. An earlier advantage of Fabry-Perot gauges having a better resolution of strain must be weighed against the Bragg grating's ease of multiple sensors on a single fiber/signal conditioning channel.

Some of the primary advantages for using fiber optic strain gauges include: a stable reading that can be disconnected and reconnected without loss of the initial measurement; the ability to acquire high frequency data—up to 250 Hz; newer models are advertised to 1000 Hz; and resistance to electromagnetic radiation from power lines, larger vehicles, and broadcast stations.

At this time, it is this author's opinion that Bragg gratings are more easily and cheaply incorporated into a structural health monitoring program. However, current research continues in its search to perfect designs of both these technologies [Ferreira et al. 2000, Henriksson et al. 1996, Zhu et al. 2003, Lopez-Higuera 2005, etc.] as well as to develop other methodologies to observe strain. A new gauge being developed / tested is a highbred extrinsic Fabry-Perot interferometric/in-fiber Bragg grating gauge; the gauge simultaneously measures strain and temperature [Rao et al. 2002]. Another fiber optic gauge technology that is under development is the distributed Brillouin sensor. This gauge is designed to measure strain at many locations along the length of a single fiber. This technology has good potential for the structural health monitoring application, and currently it is being tested for detecting pipeline buckling [Ravet et al. 2005].

Since these fiber optic based technologies are relatively new, there are only a few vendors that provide the signal conditioning devices to read the various sensors. There has not been much standardization relating specifically toward structural health monitoring. There remain some hurdles toward integrating these sensors into a system including other non-fiber based transducers. Issues like signal timing and data storage still need to be worked through and depend on each signal conditioning vendor.

2.3.3.3 Vibrating Wire Strain Gauges

Vibrating wire strain gauges are well established. These gauges are a robust temperature compensated strain device. They have long term stability that is independent of the connection to the data acquisition system. The main drawback with respect to structural health monitoring is that the readings take one second to make. Another issue; a square wave signal must be transmitted to the device to cause an electromagnet to pluck the wire; this requires the use of a specialized signal conditioner. Sometimes it can be difficult to incorporate these signal conditioners into a larger SHM system which includes other types of devices.

CHAPTER 3. LVDT-TAUT-WIRE BASELINE DEFLECTION SYSTEM DESIGN

In this chapter, the design and use of linear variable displacement transformers (LVDTs) supported by a taut-wire catenary to measure the vertical deflection of a beam are discussed. The system provides a good baseline for LVDTs to measure the deflection of beams both in the laboratory and in the field. It is especially useful when there is no stable datum to measure against. The system is insignificantly affected by axial deformations of the beam. The author also proposes a possible way to monitor the axial deformations with the system as well.

This chapter goes on to describe the design procedure for the LVDT-taut-wire baseline system used for projects discussed in this report. LVDTs are used to measure relative displacement. In the laboratory, it is easy to establish a datum that is unaffected by any movements of a loaded beam. The datum can be an unloaded beam parallel to the test specimen; or the floor of the lab itself. However, it is not a trivial task to measure the deflection of a beam outside a laboratory, e.g. a long bridge that spans over water.

The need to develop this system came about from experience with monitoring the long term deflection of the North Halawa Valley Viaduct [Robertson & Ingham 1999, Robertson & Yoshimura 2004, Robertson et al. 2005]. The researchers realized that an automated system will save vast time, effort, and money on future similar projects.

3.1 Literature Review

Measuring the deflection of a beam relative to a taut-wire baseline is not new. However, using a taut wire to support the core of an LVDT has not been done often. Indeed, this

approach has not been widely used for long spans or with many LVDTs on the same baseline.

There have been several published projects that have used, or proposed, a taut wire as a datum from which to measure beam displacement [Aktan et al. 2003, Land et al. 2003, Basu & Knickerbocker 2005, Myers & Yang 2005, Bohnhoff et al. 1997, Hernandez et al. 2005, Robertson & Ingham 1999, Robertson & Yoshimura 2004, Robertson et al. 2005]. The State of Virginia Department of Transportation has established a list of standard test methods used during construction. The Virginia Test Method-20, Prestressed Concrete Beam Load Test, describes the use of a piano wire, a mirror, and a scale to manually observe beam deflection [Virginia DOT 2006]. The method does not prescribe how to load the piano wire. Instead, it requires that the wire be “stretched tight to remove as much sag as possible” [Virginia DOT 2006]. This procedure does not warn to take special care where the piano wire supports are installed. The thermal elongation or shortening of a taut wire will increase or relieve the tension in the taut wire—thereby changing the profile of the baseline. This non-specific procedure is likely sufficient for the type of loading prescribed in the method—short term and unlikely to be significantly impacted by diurnal thermal and other changes.

Myers and Yang [2005] used a taut wire system to measure the development of camber in prestressed concrete beams. To apply a consistent tension to their taut wire baseline, they attached a wire to a weight that hung over an anchor bolt installed at one end of the beam. The wire was fixed to another anchor bolt at the opposite end of the beam. A constant

tension will provide a constant catenary profile. In a short beam, with short term loading, and a sufficiently heavy tensioning weight, the assumption of zero friction between the anchor bolt “pulley” and the piano wire is probably not a bad assumption. However, in a long bridge, susceptible to larger axial deformations, the friction could impair the tensile load consistency needed in the wire to maintain the wire’s profile. Ultimately, Myers and Yang chose to use a different method to monitor the beam deflections once the beams were installed in the structure [Myers & Yang 2005].

Basu and Knickerbocker were performing research on a bridge that had been previously instrumented with a manually observed taut wire monitoring system. They noted several systematic problems with the existing system that used a fabric string as the catenary: wind caused movement of the string; the baseline profile changed as dirt loaded the string over time; and the system was hard to access where it was installed [Basu & Knickerbocker 2005]. That system applied the tensile load with a pulley and tensioning weight. A pulley should reduce the friction to a tolerable level with respect to the problems noted with the Myers and Yang system. Basu and Knickerbocker proposed to replace the string with a piano wire as a better option. In the final implementation of the bridge project, they decided to use a laser electronic distance meter (EDM), a theodolite, and triangulation to determine the bending displacement [Basu & Knickerbocker 2005].

The new Benicia-Martinez Bridge, across the Carquinez Strait on Interstate 680 in California was being instrumented during construction [Aktan et al. 2003]. One option, mentioned by Aktan et al., for the bridge’s vertical deflection monitoring system

consisted of a taut piano wire tensioned by a mass hanging across a pulley. The deflection would be monitored manually with a digital caliper at specified locations along the span [Aktan et al. 2003, Land et al. 2003]. The system is designed for use on the main long span of the bridge. The authors state that the system requires a tensile load in the wire that is 80% of its breaking strength [Aktan et al. 2003, Land et al. 2003]. Presumably, this requirement is for maintaining the catenary profile based on the size, self weight and span length of the wire. The reason for choosing that level of load was not discussed in either reference. However, mentioning the level of load does suggest that it is an important consideration that needs to be considered when designing such a system. The authors of those articles also mention an alternate method using a liquid leveling system that is automatically recorded.

A similar taut wire system was installed in the North Halawa Valley Viaduct during a ten year monitoring program [Robertson et al. 2005]. The system was installed in four spans along the viaduct. The taut wire was arbitrarily loaded to about 80% of its breaking strength—similar to that planned by Aktan et al. and Land et al. The system was able to effectively capture both short-term and long-term deflection. The deflected shape measured by the system within two adjacent instrumented spans during a controlled load test was consistent with tiltmeter and optical survey measurements, as well as a SAP2000™ model's predictions [Robertson et al. 2005]. Long-term deflection measurements on all four instrumented spans compared well with an SFRAME™ model calibrated for the local concrete creep and shrinkage properties at the end of an eight year period [Robertson et al. 2005]. Indeed, the measured deflection with the taut wire system

provides good results. One major drawback of this system is that the readings are not done automatically. For this reason, work began to incorporate LVDTs into the system [Robertson et al. 2005].

Others have used a taut wire system as a baseline to measure beam deflection in the lab [Bohnhoff et al. 1997, Hernandez et al. 2005]. Both the Bohnhoff et al. and Hernandez et al. taut wire systems used a single LVDT to automatically record the displacement of a short beam in laboratory experiments. The systems did not utilize a pulley type loading apparatus. Bohnhoff et al. tensioned the piano wire with a spring. Hernandez et al. described the wire as “tightly strung” along the beam. Both systems attached the wire over the beam supports at the neutral surface—likely to minimize any change in wire tension—recognizing that the shortening or lengthening of the non-neutral fibers of the beams during bending would cause a change in the wires catenary profile.

Stanton et al. [2003] proposed a similar base-line system they called the Weighted Stretched Wire System, or WSWS. Figure 3.1.1 portrays their concept. As described in their article, the system is designed by maximizing the tensioning weight and sizing the trolley weight such that wire vibration is minimized and the force applied by the displacement transducer to the catenary does not poorly impact accuracy of the measurement [Stanton et al. 2003]. The displacement transducer allows for continuous monitoring of the structure.

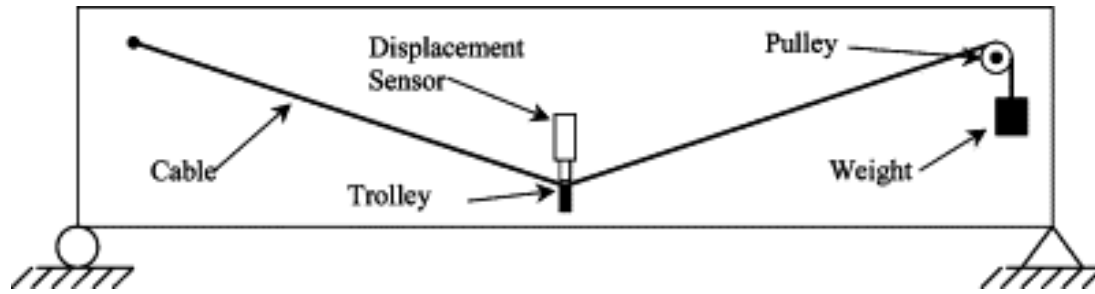


Figure 3.1.1. Weighted Stretched Wire System [source: Stanton et al. 2003, pg 348].

As with all catenary systems, the displacement is highly impacted by static equilibrium. During analysis, the wire is a tension-only member—bending is ignored. The low geometric stiffness of the system is the greatest source of displacement. By providing a large tensioning weight, the system becomes geometrically much stiffer. A stiffer system has a higher resonant frequency. Stanton et al. suggested using a weighted trolley at the location of the displacement sensor to help tune the dynamic properties of the WSWS setup—the system can be tuned to perform to a range of measurement specifications. Stanton et al. have performed a comprehensive parameter analysis of their WSWS system [Stanton et al. 2003]. However, the system and analysis is limited to the use of only one displacement transducer.

During recent and ongoing research projects at the University of Hawaii, a system has been developed to take the next step. Chapters 7 and 8 describe the implementation of several LVDT-taut-wire systems for measuring vertical deflection of bridges and beams. These chapters show the use of multiple LVDTs on a single taut-wire baseline. The next section describes the general approach toward designing such a system.

3.2 University of Hawaii System Design Process

This section describes the design procedure for the LVDT-taut-wire baseline system used for projects discussed in chapters 7 and 8. LVDTs are used to measure relative displacement. Each end of an LVDT must be attached to a point of reference. In the laboratory, it is easy to establish a datum that is unaffected by any movements within the test setup. However, it is not a trivial task to measure the deflection of a long span beam with accuracy, especially if exposed to wind, or if it spans over water. During the North Halawa Valley Viaduct monitoring program [Robertson et al. 2005] access to the instrumented sections of the viaduct, located deep within Halawa Valley, was time consuming, tedious, and physically demanding. Accessing the bridge required clearing a trail and hiking through the rainforest. Manual reading of the deflection by the taut-wire baseline system was at least a half day process. The investigators realized that using LVDTs to automatically collect the data would result in significant savings.

The purpose of the LVDT-taut-wire baseline system is to monitor long term and non-seismic short term vertical deflections, such as those induced by traffic. To capture seismic or other high frequency movement, another system should be used. An investigator should not count on this system to provide a stable baseline during a seismic event. However, this system has the potential to recover in-span residual displacements after a seismic event.

In a bridge structure, there are significant axial deflections due to diurnal and seasonal temperature changes. The taut-wire system provides a baseline for measurement that is

insignificantly affected by these axial displacements. The taut wire acts as a catenary with a pinned support at one end (dead end) and a tensioning weight and pulley at the other end (live end). The weight at the live end provides a constant tension in the taut wire to maintain a deflected shape along the length of the beam.

An appropriate tensioning weight and taut wire size can be selected to support the cores of several LVDTs. Free core LVDTs should be used as opposed to spring loaded LVDTs. The constant weight of the free core helps to eliminate baseline movement due to a variable load applied by a spring. The smaller free core self weight applied to the catenary reduces the required tensioning weight and taut wire size. The required stiffness of the installed taut wire will only need to be large enough to overcome the small static friction between the core and LVDT coil housing—this small friction should only cause a catenary displacement within the desired measurement tolerance. The coil housing of the LVDT is suspended from the deflecting structure. There have been many lessons learned during the development of this system. The following three sections describe the development process including problems encountered and their practical solutions.

3.2.1 In Laboratory Prestressed Concrete T-Beam Testing

The first application of the LVDT-taut-wire baseline system occurred during the research program “Test of Prestressed Concrete T-Beams Retrofitted for Shear and Flexure using Carbon Fiber Reinforced Polymers” [Agapay & Robertson 2004, Aki & Robertson 2005]. A taut wire was installed on one of the beams during a destructive test. Figure 3.2.1 shows the system as installed. Seven LVDTs were installed. The cores of the

LVDTs each weigh 0.12 lbs (0.54 N) were supported on a #12 piano wire with a diameter of 0.029 inch (0.74 mm). The beam span was 25.67 feet (7.83 m).



Figure 3.2.1. LVDT-Taut-Wire Installed on Pre-stressed Concrete Beam.

The first problem encountered was the low clearance of the beam above the strong floor. The flexibility of the system allowed for two pulleys to be used to hang the 40 lb (178 N) tensioning weight. This live end configuration is shown in Figure 3.2.2. Red lines highlight the taut wire's path around the 6 in (152 mm) diameter pulleys.



Figure 3.2.2. Live End Pulleys Installed on Prestressed Concrete Beam.

Plots of the deflected shape are shown for different loading levels in Figure 3.2.3. Figure 3.2.4 shows a comparison of three displacement measurements at mid-span. Two were obtained by LVDTs mounted to the floor and within the test frame. The other is the mid-span measurement of the LVDT-taut-wire setup.

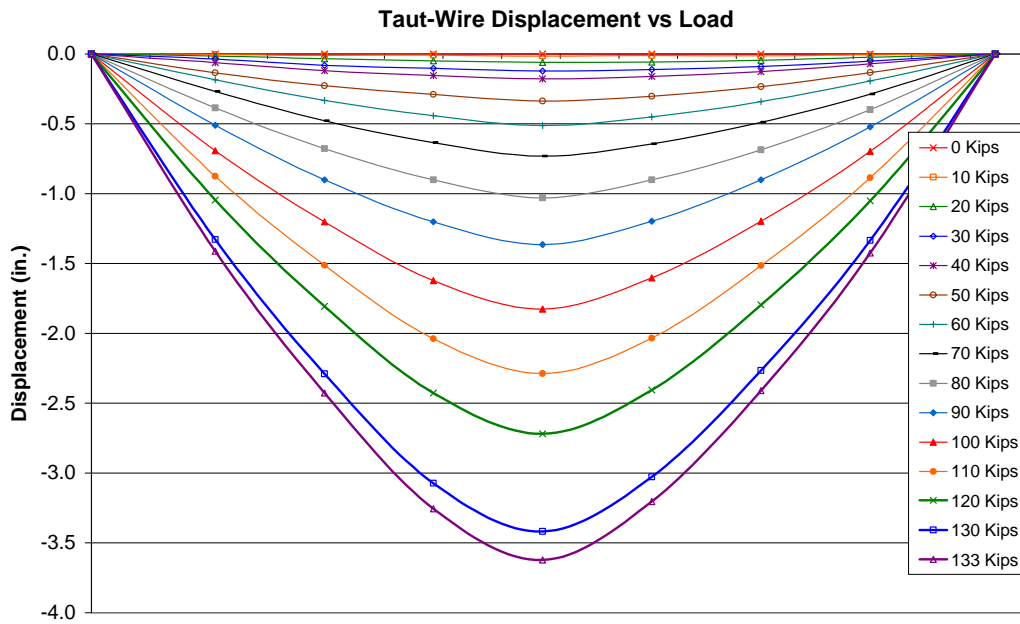


Figure 3.2.3. T-Beam Deflected Shapes.

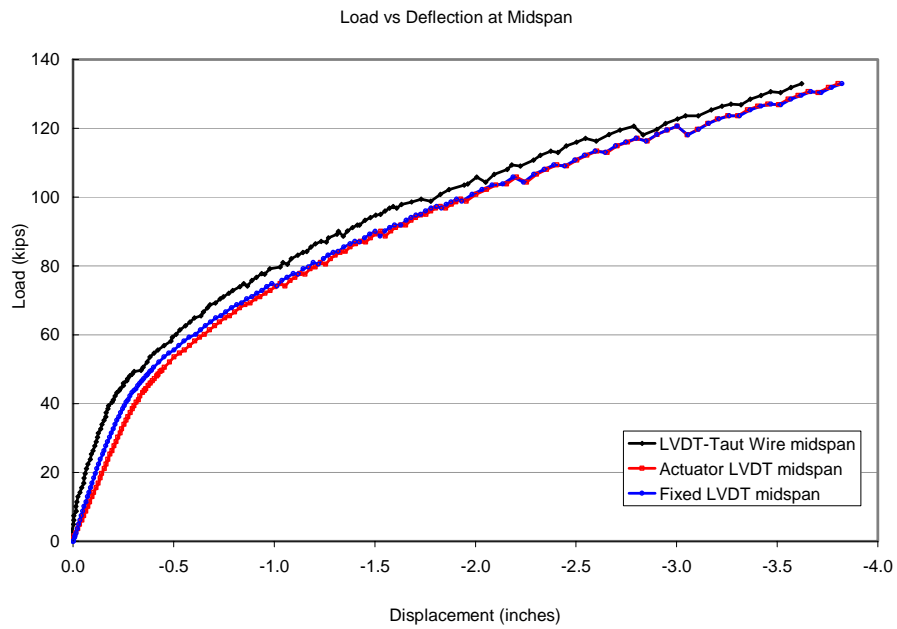


Figure 3.2.4. T-Beam capacity Curve.

While there is a difference in the deflections in Figure 3.2.4, this is likely attributed to systematic inequalities—each LVDT is measuring at a different location within the cross-section of the beam. In particular, the taut wire supported LVDT is actually measuring the slab deflection away from the web of the beam. Upward curling of the unsupported flange or rotation of the beam in the frame could be causing the observed displacement discrepancies. It is the author's opinion that it is not due to any under performance of either system to capture the displacements. When comparing the cracking behavior displacement jumps at the higher loads, the relative displacements at those levels are essentially equivalent.

3.2.2 North Halawa Valley Viaduct (H3 Freeway) Field Installation

This test application was the first attempt at using the LVDT-Taut-Wire system on a long span. Chapter 8 describes the overall instrumentation used on the viaduct as well as the goals of the instrumentation program as it relates to SHM. During the instrumentation program, four manually observed taut-wire baseline systems were installed on four different spans along the viaduct—which was of prestressed segmental box construction. During the course of the program, the need for an automated system became apparent. After testing the LVDT-Taut-Wire system in the laboratory environment, a single span of the NHVV was instrumented. There were several attempts to get the system to work. At the end of the system development, the investigators concluded that the system was viable for measuring deflections of long span beams with reasonable success.

The manual taut-wire system installed used #8 gauge piano wire—diameter 0.020” (0.51 mm). The beam span is 360 ft (110 m) from center to center of support. The taut-wire baseline span was approximately 340 ft (104 m). The live end pulley used was 3 inches (76 mm) in diameter supporting an 80 lbs (356 N) tensioning weight. This system was installed within 6 inches (152 mm) of the bottom of the top slab.

Incorporating the LVDTs into the system required several changes. The baseline was lowered to 24 inches below the top slab to accommodate the length of the LVDT coil housing and cores. Pulleys installed were 6 inches (152 mm) in diameter to ensure less influence from friction and wire flexing. After securing the coil housing to the slab soffit, the cores were attached by eye loops onto the LVDT. The cores of the LVDTs each weigh 0.12 lbs (0.54 N). During the installation, as the LVDT cores were placed onto the taut wire significant deflection on the order of several inches occurred at each location. Data was collected from the system for a short time period—the investigators were in the box girder when truck traffic crossed the bridge. Typical traffic loading should cause deflections of up to a quarter inch (6 mm). The data showed that the displacements observed were much smaller than expected. Also, there were residual displacements measured. It was clear that the friction between the core and the coil housing was greater than the restoring force of the very flexible taut wire baseline. This was visually confirmed by plucking the baseline at the location of one of the LVDTs; the core oscillated a few times then ceased moving before it could damp out as one would expect.

To improve the performance the taut wire baseline needed to be stiffened. To that end, a #20 gauge piano wire—diameter 0.045” (1.14 mm)—replaced the #8 gauge piano wire to allow for additional required tensioning load. The tensioning load was increased to 255 lbs (1135 N). The same LVDT cores were used, each weighing 0.12 lbs (0.54 N). As the LVDT cores were placed onto the taut wire, little if any deflection was noticed due to the much stiffer baseline. Data was again collected from the system for a short time during typical truck traffic crossing the bridge. The data showed that the displacements observed were as expected (see Figure 3.2.5). This deflection was caused by two trucks of unknown but significant weight. The deflection observed is consistent with the uplift of the span as the trucks are on the adjacent spans. The magnitude of the downward deflection is similar to that of the HS-20 truck loading performed during load tests at the beginning of the monitoring program.

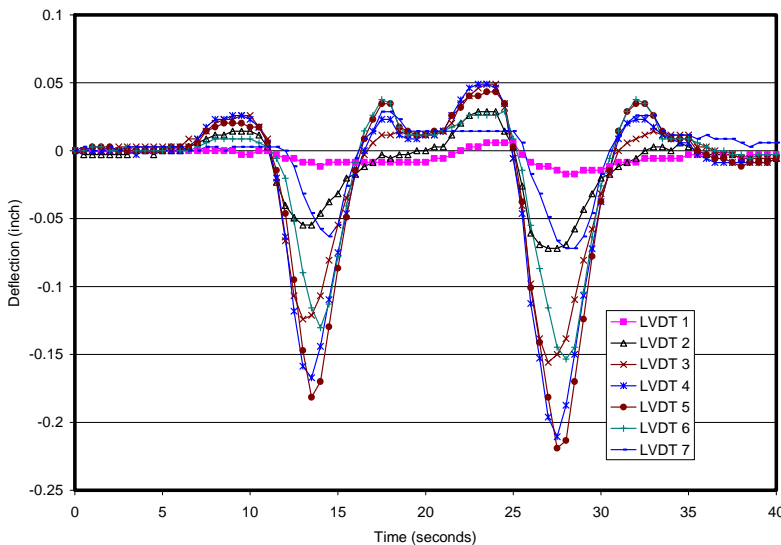


Figure 3.2.5. NHVV Deflection Observed with LVDT-Taut-Wire Baseline System.

From this data it is apparent that the first truck was nominally smaller than the second. Figure 3.2.6 shows a time history plot of the instrumented span showing the progression of two trucks crossing. The plot first shows uplifting when the truck is on the adjacent span; followed by downward deflection when the truck is on the instrumented span; followed by an additional uplifting event when the truck is on the next adjacent span.

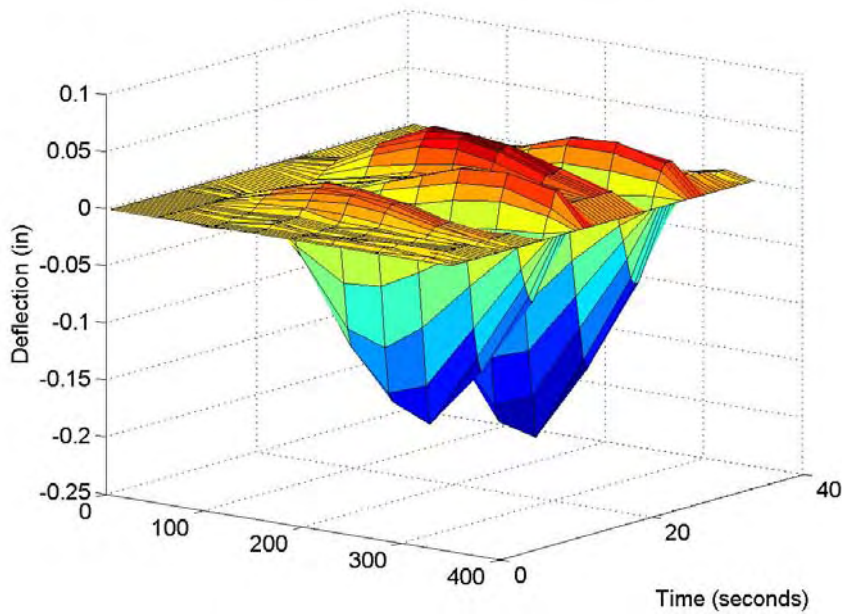


Figure 3.2.6. Deflection Along the NHVV Span Varying with Time.

3.2.3 Hanapepe River Bridge Load Test Field Installation

The Hanapepe River Bridge Load Testing program is completely described in Chapter 8. This section will only describe the application of the LVDT-Taut-Wire baseline system during the project. This was the first full instrumentation program to utilize the LVDT-taut wire baseline system to acquire and analyze data from a remote location.

Figure 3.2.7 shows the placement in elevation of one of the two taut wire-LVDT baselines implemented during the load testing of the Hanapepe River Bridge. The two baselines were installed on adjacent spans to capture the deflected shape of a single girder. Figure 3.2.8 shows a section of the bridge with the placement of the baseline adjacent to girder G-3. The baselines were placed next to the beams to minimize wind induced vibration of the system. That placement also allowed for the continuous use of the Hanapepe River for recreational users. Figure 3.2.9 shows the installed dead and live end supports of the taut wire baseline used.

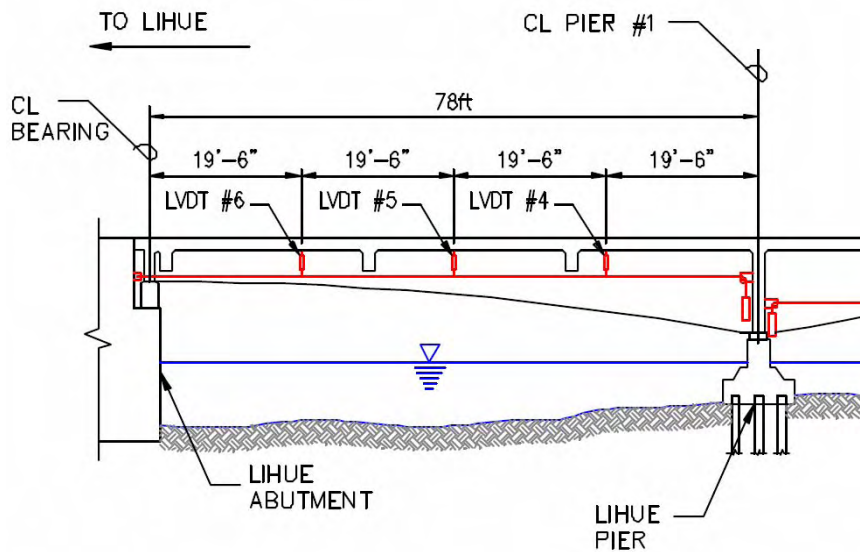


Figure 3.2.7. Abutment Span Elevation of Girder G-3: LVDT-Taut-Wire Baseline System.

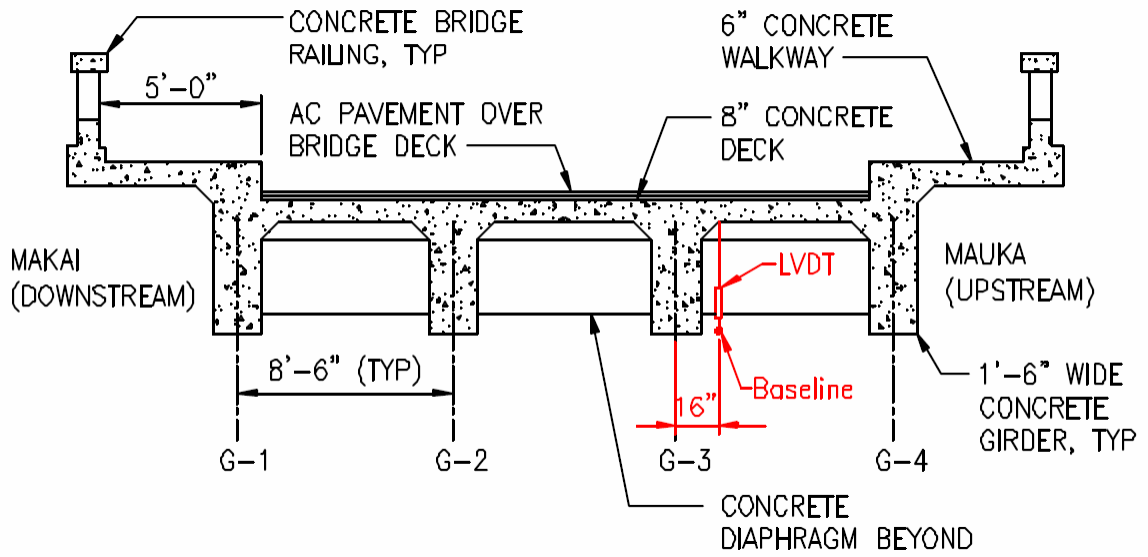


Figure 3.2.8. Bridge Cross-Section: LVDT-Taut-Wire Baseline Adjacent to Girder G-3.

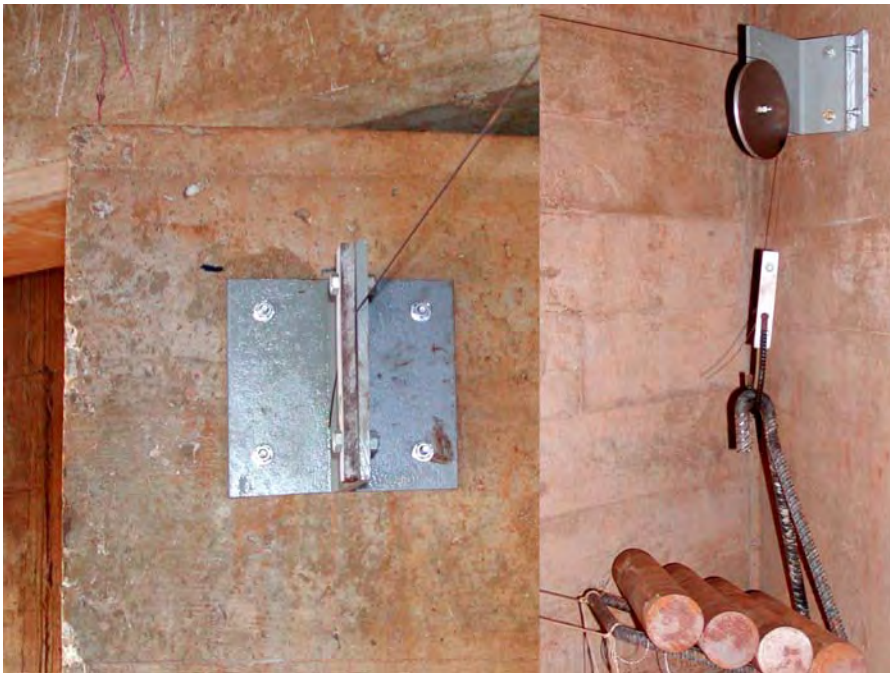


Figure 3.2.9. Taut-Wire Baseline Dead (Left) and Live (Right) End Supports.

3.3 System Sizing Considerations

When designing a LVDT-taut-wire baseline system, there are several things to consider. The purpose for using the system is to measure displacement. LVDTs have a wide range of total measurable displacement capabilities and corresponding displacement resolutions. In most cases, the LVDT resolution will not be achieved when mounted onto a taut-wire baseline. The cause is from two general sources: environmentally-induced movement of the baseline; systematic error induced by the interaction between all the parts of the system. One of the environmental error sources includes excitation of the baseline by the wind. The primary source of systematic error is loading of the taut wire baseline. When the baseline is subjected to a transverse load, the profile will change. The change is induced to satisfy static equilibrium. The designed strategy discussed here is a rule of thumb process determined from the experience of the three implementations tried in section 3.2. The suggested quantitative design process requires incorporating the span of the taut wire baseline, an estimate of the maximum static friction force applied to the baseline by the free core LVDT, and a conservative desired resolution of measurement. These three factors will determine the minimum tensioning load to achieve the desired resolution. After finding the required tensioning load, the wire size can be determined.

3.3.1 Implemented System Comparisons

The quantitative design process was determined by observing successful and unsuccessful implementations of several LVDT-taut wire baseline systems. A total of 27

LVDTs were installed on five different taut wire baselines. When the following analysis started, it was understood that the largest source of deflection error would occur at the mid-span of the baseline system—where the weight of the core will cause the largest displacement. Table 3.1 shows the results of the determination of the displacement of the baseline system due to the weight of an LVDT core. The displacement was calculated by satisfying static equilibrium. The calculations were performed for an LVDT at mid-span of the five different baseline cases (column 1) used during the course of this research. Columns 2 through 5 are the self weight of the LVDT core, W_{core} ; length of the baseline, L ; position of the LVDT on the baseline, x ; and Tensioning load in the taut wire, T , respectively. These were used to calculate the deflection, d , under the LVDT due to the core’s weight—listed in column 6. Column 7 and 8 are a ratio of the span of the baseline to the deflection and a ratio of the tensile load to the deflection. These ratios were used to identify which parameter best correlates with the good or bad performance of the evaluated systems. Column 9 describes if the system performed adequately and column 10 states the assumed cause of poor performance.

Table 3.1. Summary of LVDT Core-Induced Baseline Displacement.

Case [1]	W_{core} (lb) [2]	L (ft) [3]	x (ft) [4]	T (lb) [5]	d (ft) [6]	L/d [7]	T/d (lb/ft) [8]	ok? [9]	if n why? [10]
Lab Beam Test-4	0.12	25	12.5	40	0.0188	1333	2133	y	
NHVV-80-Midspan	0.12	345	172.5	80	0.1294	2667	618	n	core friction
NHVV-240-Midspan	0.12	345	172.5	240	0.0431	8000	5565	y	
Hanapepe-1-Midspan	0.12	114	57	200	0.0171	6667	11696	y	
Hanapepe-2-5	0.12	78	39	200	0.0117	6667	17094	y	

The system that performed the poorest was the second case at the North Halawa Valley Viaduct (NHVV-80) with an 80 pound tensioning load. In Table 3.1, the T/d ratio (column 8) corresponds best with the performance of the system (column 9). During the initial installation and data acquisition, it was noticed that the LVDT core caused a fairly large displacement of the baseline system. While the investigators were still in the field, it was observed that an LVDT was only recording about a 0.05 inch displacement at mid-span when a large truck was traversing the span. An approximate visual observation of a parallel manually read taut-wire baseline indicated that the true displacement was closer to 0.25 inch. This is consistent with the deflection caused by a single AASHTO HS-20 truck load. Upon closer inspection, it was observed that the core was restricted by friction (see section 3.2.2). Knowing the geometry of the system, the tension load, and the approximate error caused by friction, an estimate of the friction force, P_f , was determined. The typical deflected shape including the self weight is controlled by statics. The deflected shape is shown in Figure 3.3.1 below. The moment caused by the core at mid-span, $M_c = P_f L/4$, is determined; the displacement of the baseline at mid-span is calculated by equation (3.3.1). The deflection at any point along the length of the baseline is equal to the load-induced moment at that point divided by the tensioning force:

$$d(x) = M(x) / T . \quad (3.3.1)$$

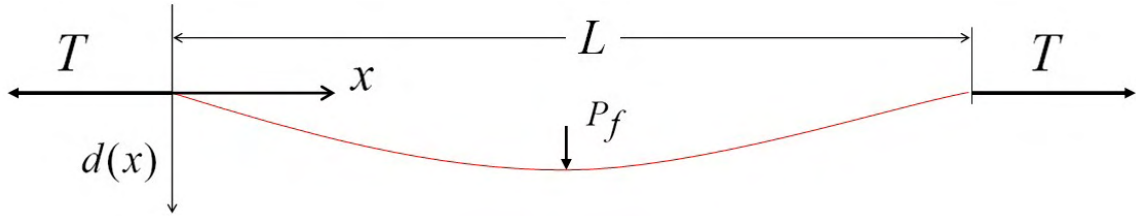


Figure 3.3.1. Geometry of Deflection and Loads Applied to the Taut-Wire Catenary.

Substituting Mc for $M(x)$ and solving for the friction force, P_f :

$$P_f = \frac{4Td}{L}. \quad (3.3.2)$$

Applying a displacement error of 0.20 inch to the NHVV-80 LVDT-Taut-Wire system, the maximum friction force estimate is:

$$P_f = \frac{4(80\text{lb})(0.20\text{in})}{345\text{ft}(12\text{in}/\text{ft})} = 0.015\text{lb}.$$

Using this friction force, Table 3.2 was generated to estimate the baseline deflection caused by the LVDT core at each location installed for all five baselines tested. The lab beam test LVDTs were used as described in section 3.2.1; the NHVV-80 and NHVV-240 LVDTs were used as described in section 3.2.2; the Hanapepe-1 and Hanapepe-2 LVDTs were used as described in section 3.2.3 and chapter 7.

Table 3.2. Estimated Error at LVDTs Due to Friction with LVDT Core.

Case [1]	x (ft) [2]	L (ft) [3]	Pf (lb) [4]	Mf (lb-ft) [5]	T (lb) [6]	d (ft) [7]	d (in) [8]
Lab Beam Test-1	3.52	23.82	0.015	0.045	40	0.0011	0.0135
Lab Beam Test-2	6.33	23.82	0.015	0.070	40	0.0017	0.0209
Lab Beam Test-3	9.20	23.82	0.015	0.085	40	0.0021	0.0254
Lab Beam Test-4	12.07	23.82	0.015	0.089	40	0.0022	0.0268
Lab Beam Test-5	14.93	23.82	0.015	0.084	40	0.0021	0.0251
Lab Beam Test-6	17.80	23.82	0.015	0.067	40	0.0017	0.0202
Lab Beam Test-7	20.66	23.82	0.015	0.041	40	0.0010	0.0123
NHVV-80-1	48	345	0.015	0.620	80	0.0077	0.0930
NHVV-80-2	96	345	0.015	1.039	80	0.0130	0.1559
NHVV-80-3	145	345	0.015	1.261	80	0.0158	0.1891
NHVV-80-4	182	345	0.015	1.290	80	0.0161	0.1935
NHVV-80-5	220	345	0.015	1.196	80	0.0149	0.1793
NHVV-80-6	268	345	0.015	0.897	80	0.0112	0.1346
NHVV-80-7	316	345	0.015	0.398	80	0.0050	0.0598
NHVV-240-1	48	345	0.015	0.620	240	0.0026	0.0310
NHVV-240-2	96	345	0.015	1.039	240	0.0043	0.0520
NHVV-240-3	145	345	0.015	1.261	240	0.0053	0.0630
NHVV-240-4	182	345	0.015	1.290	240	0.0054	0.0645
NHVV-240-5	220	345	0.015	1.196	240	0.0050	0.0598
NHVV-240-6	268	345	0.015	0.897	240	0.0037	0.0449
NHVV-240-7	316	345	0.015	0.398	240	0.0017	0.0199
Hanapepe-1-1	61	114	0.015	0.425	205	0.0021	0.0249
Hanapepe-1-2	34	114	0.015	0.358	205	0.0017	0.0209
Hanapepe-1-3	30	114	0.015	0.332	205	0.0016	0.0194
Hanapepe-2-4	58.5	78	0.015	0.219	205	0.0011	0.0128
Hanapepe-2-5	39	78	0.015	0.293	205	0.0014	0.0171
Hanapepe-2-6	19.5	78	0.015	0.219	205	0.0011	0.0128

Column 7 and 8 in Table 3.2 express the error induced by the maximum expected static friction as a displacement. The NHVV LVDTs significantly improve their performance by increasing the tensioning load, T, from 80 lbs to 240 lbs. The lab beam test and the Hanapepe LVDTs have an error small enough to capture the magnitude of deflection behavior of interest for their respective SHM applications. As a note, the LVDTs installed have a reliable resolution of about 0.001 inch when used in a non-taut wire baseline system. Also, the error induced by wind driven vibrations during the Hanapepe

testing kept the LVDT cores in motion and likely was the greatest source of error for any single data point.

3.3.2 Suggested Design Process

SHM practitioners should be aware that this outlined design process considers only one of many possible sources of error that could be induced in a particular system. This process quantifies the experience of the investigators who use this only as a rule of thumb calculation. Further research into identifying and quantifying all the error sources and interaction of multiple errors is planned.

The overall process involves the following steps: determine the maximum expected static friction force, or force applied to the taut wire baseline; determine the moment induced by friction of a single LVDT at mid-span of the taut-wire baseline; calculate the minimum required tensioning load that will provide a conservative resolution of displacement; select the taut wire size, pulley, and placement.

There is no one way to determine the maximum expected friction force of the system. It can be done by performing a theoretical calculation. It could be done by systematically following the process used in section 3.3.1—place the LVDTs on the taut-wire baseline and measure the deflection error with an accurate parallel system. The friction could also be determined with a classical friction measurement laboratory test setup.

The moment of the loads applied to the baseline system can easily be determined by statics. Use the estimated friction force to determine the maximum moment at the

location of the LVDT. The worst case for any system will occur when an LVDT is located at the mid-span of the baseline. The maximum moment of a point load at mid-span on a catenary is: $M = P_f L/4$. P_f is the friction force; L is the length of the baseline.

Substituting $P_f L/4$ into equation (3.3.1) and solving for the tensile load, T :

$$T = \frac{P_f L}{4d_{res}} . \quad (3.3.3)$$

The displacement, d_{res} , should be a conservative resolution desired of the LVDT-Taut-Wire baseline system. A conservative resolution is some displacement smaller than the minimum needed resolution. It should be noted that the system is not truly loaded by just one friction force. Each LVDT applies a friction force. The friction force will not be a maximum at every reading. Not all the LVDTs will have the same friction force acting on the baseline at the same time. The tensile load calculated by equation (3.3.3) should be considered a minimum load. If a larger load is practical, it will provide a better resolution.

Several considerations should be considered while choosing a wire size. Obviously, the tensile strength of the wire is important and easily considered with mechanics of materials and equation (3.3.4).

$$\sigma_a = T / A_{wire} . \quad (3.3.4)$$

where,

σ_a is the axial stress caused by the tension in the wire,

T is the tension in the wire, and

A_{wire} is the cross-sectional area of the wire.

While considering the wire size, the pulley should be appropriately sized such that its radius does not yield the wire as it is bent by the tensioning load. The stress at the extreme fiber induced by bending the wire around the pulley can be calculated by equation (3.3.5). The sum of equations (3.3.4) and (3.3.5) should be less than the yield stress of the wire material.

$$\sigma_b = Er / R. \quad (3.3.5)$$

where,

σ_b is the longitudinal stress at the extreme fiber of the wire caused by bending,

E is the wire materials elastic modulus,

r is the radius of the wire, and

R is the radius of the pulley plus the radius of the wire.

The baseline profile should be checked: the profile calculation should include both the maximum sag due to wire self-weight and the additional displacement due to weight of the LVDT cores. Although elastic deformation obviously occurs, this is taken up by the

pulley during the addition of the tensioning weight. A sufficiently accurate baseline profile can be calculated by satisfying statics along the length of the beam.

Other considerations such as pulley friction, dynamic interaction with the attached structure, and other concerns are not yet considered for this system. A similar system called a weighted-stretched-wire system (WSWS) [Stanton et al. 2003] was modeled including the above considerations; this was noted in the literature review section of this chapter (section 3.1).

CHAPTER 4. WHEATSTONE BRIDGE DEVICE DESIGN

4.1 Background

During the course of a structural health monitoring program it is common for observations of one phenomenon to cause the investigators to focus on a new phenomenon. In some cases, the increase in scope might not be matched with an increase in budget. New devices may be needed. Most of the time, buying a device is the best option because the time involved in the development is more costly than the device—sometimes this is just not an option. When this happens, there are often solutions that allow the researcher to “go back to the basics” of instrumentation design and measurement. This can mean using the cheaper transducers such as strain gauges to measure other phenomenon such as pressure, or load, or crack opening movement, or torsion, et cetera. This chapter describes two devices that the author designed and built to allow more data to be collected for a project with a limited budget. Both devices use four strain gauges in a Wheatstone bridge to measure deflection. While the principles used to build the devices are not new, it is useful information to help other researchers and engineers to improvise solutions when needed. The first device described is a crack gauge that is used to monitor the crack mouth opening displacement on concrete structures. The second device described measures deflection at a very fine resolution—two were used to measure the relative rotation of a pinned connection between the top of a pier and a bridge superstructure.

4.2 Crack Gauge Device

Concrete structures crack. Cracking in a reinforced concrete structure forces the reinforcing steel to maintain the load carrying capacity of the structure in tension. Due to environmental concerns, specifically reinforcing corrosion, the ACI Committee 224 report provides a guide for the maximum tolerable flexural crack width in various environmental conditions [Nawy 2000]. Engineers currently use visual crack comparators—clear plastic cards with multiple lines of various widths—to determine the crack width in existing structures. They use visual crack “monitors” to observe the crack opening overtime via the initial alignment of crosshairs. These devices cannot provide information on whether a crack is active while under load, or if the crack is merely a result of initial restrained shrinkage—of no analytical capacity reducing consequence. A crack mouth opening displacement (CMOD) observable during a load test provides a quantitative indicator of a detrimental condition.

There exist commercially available electronic crack meters that can easily be integrated into a data acquisition system. In the laboratory, they can be very useful in determining the material properties of fiber reinforced composite materials, for testing of cracked concrete structural elements, for observing crack opening behavior related to fracture mechanics, et cetera. Each of these devices must be installed after the initiation of the crack and is not generally robust enough or cost effective for longer term field installation.

During the course of this research, the need for monitoring the movement of multiple cracks on an existing bridge became an issue. During the Hanapepe River Bridge load test program a new crack gauge device was designed and evaluated as an alternative to the commercially available devices. The investigators chose to build them, instead of buying them, to reduce the cost of the instrumentation installation. The cost of strain gauges is very small compared to that of the commercially available crack gauges. Harris and Piersol [2002] describes various ways to use strain gauges to measure displacement. In particular, they describe using a C-shaped spring to monitor the displacement of its two legs [Harris & Piersol 2002, pg 17.8]. The design and construction of one such device is shown here. By building these devices ten times as many crack locations can be monitored for the same cost. Also, they can be designed per application to achieve a better resolution on the same data acquisition system.

4.2.1 Design Basis

The crack gauges described in this section were built with the intent to provide an economical, reliable, and robust device to withstand a field installation. The concept is based on using bending strain to amplify the relative movement between two locations. Using a bending based gauge provides a higher resolution than an axial based gauge. Four strain gauges are used to monitor the flexural strain within the device. The crack gauge was designed and built based on a full Wheatstone bridge configuration of electrical resistance strain gauges (see Chapter 2.3.1.1.2).

4.2.2 *Physical Specifications*

The devices were built using Vishay Micro-Measurements CEA-06-125UN-350 foil strain gauges. Two gauges were mounted side by side on one face of the device such that when the distance between the legs of the gauge increases they are in tension. At the same time, the other two gauges are in compression and in a similar configuration on the opposite face. Again, the gauges are oriented so that they theoretically experience the same level of flexural straining—opposite signs for opposing faces on the device. The gauges were connected in a full Wheatstone bridge configuration using 30 gauge wire. The wiring diagram indicating strain direction ($+\epsilon$ or $-\epsilon$) of each gauge is shown in Figure 4.2.1. The configuration used maximizes the signal voltage based on a given change in strain—four times the output signal of a single strain gauge in a quarter Wheatstone bridge configuration. The full bridge and placement configuration of the gauges automatically compensates for the thermal output of all the strain gauges—including coefficient of thermal expansion mismatch. Any thermal effect occurs on all four legs of the circuit negating any change at the signal voltage (see Chapter 2.3.1.1.2). Axial straining does not contribute toward the signal voltage either.

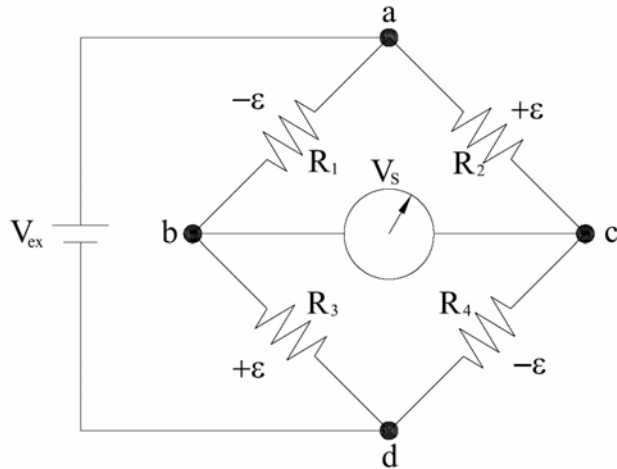


Figure 4.2.1. Crack Gauge Wheatstone Bridge Wiring Diagram.

The gauge was constructed from aluminum stock 1/16 in x 3/4 in x 6 in. The 1/16 in x 3/4 in ends were sharpened to a point at a 63.4° angle (2:1 slope) to allow any rotation to be unrestricted during the extension and relaxation of the gauge. The thin aluminum plate was then bent around a machined steel stock template that measured 1 in x 1 in x 3 in. The resulting C shape, shown in Figure 4.2.2, measures 3.125 inches tall by 1.125 inches wide with 0.5625 inch sharpened flanges. The sharpened flanges are spaced 2.0 inches apart when unstrained. The structure of the “clip gauge” [Harris & Piersol 2002, pg 17.8] is idealized by symmetry in Figure 4.2.2 as well. The crack mouth opening displacement (CMOD) is proportional to the load, P , applied as shown in the figure. This loading, and the shape of the crack gauge, results in a constant moment region ($M = Pe$). This constant moment region benefits the bending strain measurement; the strain reading will not be very sensitive to where the gauges are located along the length of that portion of the gauge. It is still best to locate the center of the strain gauges at the middle of the

constant moment region—this helps to reduce the effects of a small amount of unintentional twisting.

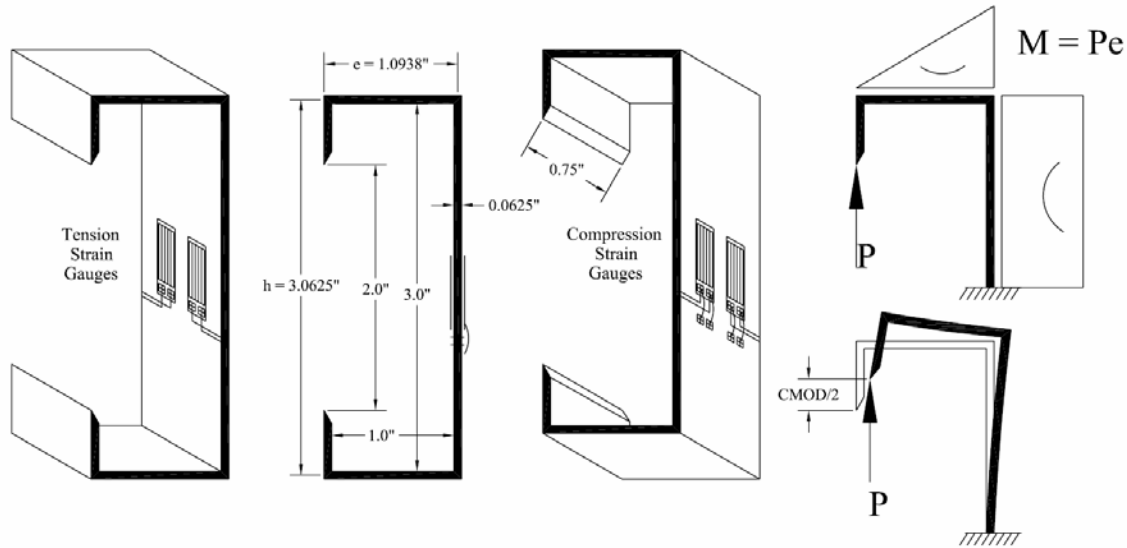


Figure 4.2.2. Crack Gauge Design and Loading Diagram.

The most important considerations to obtain good, consistent, readings are three fold: align the sensitive axis of the strain gauge with the axis of the aluminum plate; provide an even loading (at P) to prevent twisting; and provide effective strain relief at the cable connection such that the cable will not pull on the gauge as loading occurs. Proper strain gauge alignment will be achieved with good strain gauge installation technique. Figure 4.2.3 shows the strain relief that was provided during an installation at the Hanapepe River Bridge (see Chapter 7). The strain relief was simply a large washer clamping against the concrete surface. Notice the slack of the cabling between the crack gauge and the strain relief is minimal but not tight.

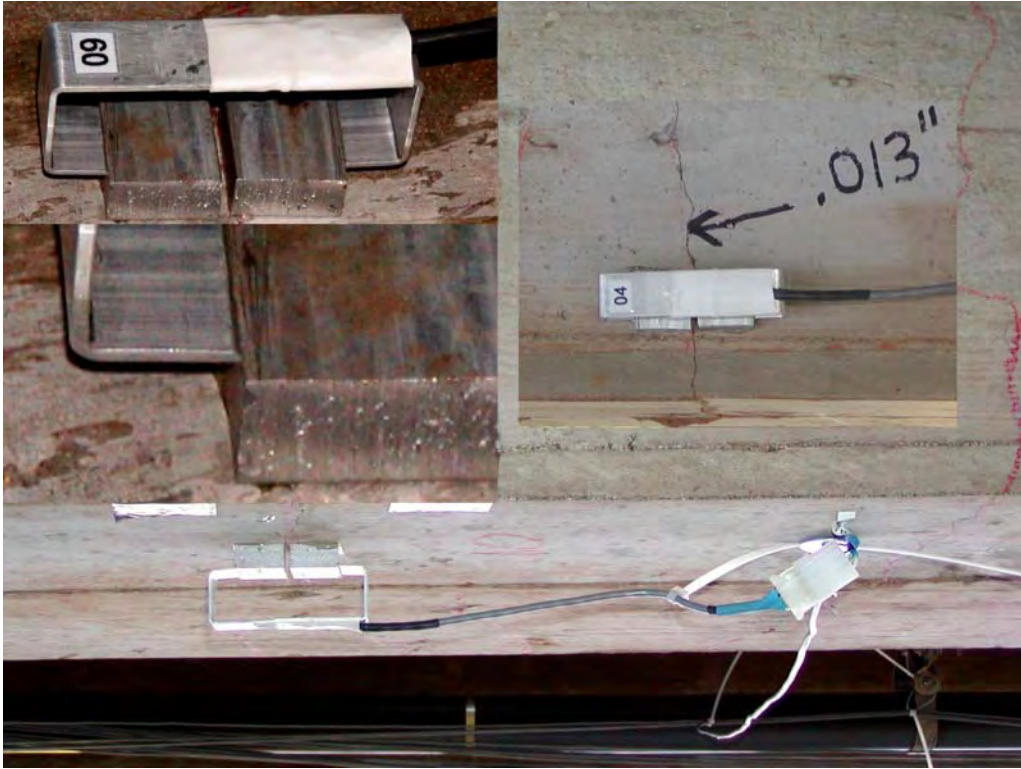


Figure 4.2.3. Crack Gauge Installations.

Finally, the crack gauge is attached to the concrete surface by epoxying two 1 in x 1 in x 0.5 in aluminum blocks as seen in Figure 4.2.3. They are accurately spaced by using a 1/8 inch thick gauge spacer while the quick setting epoxy is curing. This spacer performs two functions. First, it ensures a consistent pretension for each gauge to support its own weight, as well as, allows for crack closure to be measured. Second, it allows for the tips of the crack gauge to sit flush and firm within the 90° triangular groove milled into the two aluminum blocks (see Figure 4.2.3). The 90° groove is used to lock the gauge into a stable position. It also allows for the rotation of the 63.4° beveled edge during the

extension and contraction of the crack mouth. Using a sharp edge minimizes any friction or rotational restraint that would induce a moment into the tips of the crack gauge.

4.2.3 Estimating Crack Mouth Opening Displacement (CMOD) Resolution

The vertical deflection due to bending caused by the load, P , of the idealized system in Figure 4.2.2 is easily calculated by the moment-area method. The maximum moment can be expressed as a function of strain within the deflection solution equation. The maximum moment occurs at the fixed support in the idealized model; in the real crack gauge structure the strain gauges are attached at this location. The deflection of the idealized model is equal to one-half the total CMOD observed with the crack gauge. To estimate the CMOD resolution of the gauge; first, the structural strain response of the gauge must be understood; then, the resolution of the strain gauge technology must be used as the strain input for the deflection calculation.

To establish the relationship between deflection and strain, first, the deflection due to an unknown load, P , should be determined. The load, P , is shown in Figure 4.2.2. Only the bending strain will be observed by the Wheatstone bridge used in the device. Therefore, only the vertical deflection resulting from the load P will be considered. It is assumed this displacement is of a much larger magnitude than any axial straining. The moment diagrams are shown in Figure 4.2.2. The maximum moment is equal to the load, P , multiplied by the eccentricity, e , of that load to the idealized fixed support. The area under the moment diagrams—normalized by the flexural rigidity, EI —is calculated below:

$$\psi_1 = \frac{Pe}{EI} \left(\frac{e}{2} \right) \quad (4.2.1)$$

$$\psi_2 = \frac{Pe}{EI} \left(\frac{h}{2} \right) \quad (4.2.2)$$

In equation (4.2.1) and equation (4.2.2): ψ_1 is the change in the angle of rotation across the horizontal flange of the gauge; ψ_2 is the change in the angle of rotation across the vertical leg at the fixed support of the idealized structure; e is shown in Figure 4.2.2 as the eccentricity of the load P to the fixed support; h is the distance, shown in Figure 4.2.2, between the centroids of the two horizontal flanges of the crack gauge.

The vertical deflection of the idealized structure, equal to one-half the CMOD observed by the crack gauge, is given as:

$$\frac{CMOD}{2} = \psi_1 \left(\frac{2e}{3} \right) + \psi_2(e). \quad (4.2.3)$$

Substituting equations (4.2.1) and (4.2.2) into equation (4.2.3) gives:

$$\frac{CMOD}{2} = \frac{Pe^2}{2EI} \left(\frac{2e}{3} \right) + \frac{Peh}{2EI} (e),$$

Simplifies to:

$$\frac{CMOD}{2} = \frac{Pe^2}{EI} \left(\frac{e}{3} + \frac{h}{2} \right), \text{ or,}$$

$$CMOD = \frac{Pe^2}{EI} \left(\frac{2e}{3} + h \right). \quad (4.2.4)$$

From mechanics of materials, the flexural formula, $\sigma_x = -\frac{My}{I}$, can be combined with Hooke's law, $\sigma_x = E\varepsilon_x$, to relate the bending moment to the strain. Substituting the magnitude of the moment at the location of the strain gauges, Pe ; and one-half the aluminum plate thickness, $t/2$, for $-y$; the following results:

$$Pe = \frac{2EI}{t} \varepsilon_x. \quad (4.2.5)$$

Finally, substituting equation (4.2.5) into equation (4.2.4), the crack mouth opening displacement as a function of strain due to bending at the location of the strain gauges is:

$$CMOD = e \left(\frac{2e}{3} + h \right) \frac{2}{t} \varepsilon_x, \text{ or,}$$

$$CMOD = \left(\frac{4e^2}{3} + \frac{2he}{t} \right) \varepsilon_x. \quad (4.2.6)$$

From equation (4.2.6), it can be seen that the crack gauge sensitivity—in parenthesis—is solely dependant on the geometry of the gauge. If a greater sensitivity is required, increasing the eccentricity, e , will produce the greatest effect: increasing the gauge height, h , or decreasing the gauge plate thickness, t , will also increase the crack gauge sensitivity. Finally, for the crack gauge shown in Figure 4.2.2, the crack gauge

sensitivity, can be calculated using $e = 1.09375''$, $h = 3.0625''$, and $t = 0.0625''$. The resulting gauge sensitivity is 109 inches. A reasonable strain resolution of the full Wheatstone bridge is 2 microstrain; the smallest observable CMOD for that resolution of strain is $109 \text{ in} (0.000002) = 0.000218$ inches. During the calibration of the gauges built during this research program, the CMOD measurement resolution obtained was 0.00022 inches.

4.3 Rotation Monitoring by Deflection Device

In the structural health monitoring field, it is advantageous to run two, or more, systems in a side by side comparison. For example, it is common to measure deflections by an optical survey at the same time as recording the deflections with a SHM data acquisition system. One data set can validate or backup the other. A side by side comparison can also be performed between two transducer based systems—an established system can help to validate a newer technique. The rotation monitoring device described in this section was used to augment, or fill in the gaps, between two LVDT-Taut-Wire baseline systems that monitored the deflected shape of the Hanapepe River Bridge. The instrumentation is fully described in chapter 7.

4.3.1 *Design Basis*

The displacement gauges described in this section were built with the intent to provide a cheap, reliable, and robust device to withstand a field installation. The concept is based on using bending strain to amplify the relative movement between two locations. Using a bending based gauge provides a higher resolution than an axial based gauge. Four strain

gauges are used to monitor the flexural strain within the device. The displacement gauge was designed and built based on a full Wheatstone bridge configuration of electrical resistance strain gauges (see Chapter 2.3.1.1.2).

4.3.2 Physical Specifications

The strain gauges used and their configuration are the same as those used for the crack gauges described in section 4.2. The configuration provides an accurate measurement of displacement based on strain magnification induced by bending. The wiring provides temperature compensation.

The gauge was constructed from aluminum stock 1/16 in x 3/4 in x 12 in. A 3/8 in diameter hole is drilled into each end of the plate. The center of the holes are located 3/4 of an inch from the end of the plate. The thin aluminum plate was then bent around a machined steel stock template that measured 1 in x 1 in x 3 in to form a C shape. The two ends are then bent back parallel to the 3 inch portion of the bent plate. The resulting shape, shown in Figure 4.3.1, measures 10 inches tall by 1.0625 inches wide 3.5 inch long flanges.

The gauge is designed to measure the relative movement between the 3.5 in flanges—measuring the change in distance between the two 3/8 in diameter holes at each end. To do this effectively, care must be taken to ensure the deflected shape of the device is symmetrical and consistent. The 1.5” long steel clamps on each side and each end of the device are used to establish consistent boundary conditions for each installation. The

holes are used to allow a single 3/8 diameter bolt to provide a clamping force to the 1/2 inch thick steel plates.

Similar to the structure of the crack gauge, in section 4.2, the displacement is proportional to the load applied to extend or contract the device. The loading and the shape of the gauge creates a constant moment region at the location of the strain gauges. This constant moment region benefits the bending strain measurement; the strain reading will not be very sensitive to where the gauges are located along the length of that portion of the gauge. It is still best to locate the center of the strain gauges at the middle of the constant moment region—this helps to reduce the effects of a small amount of unintentional twisting.

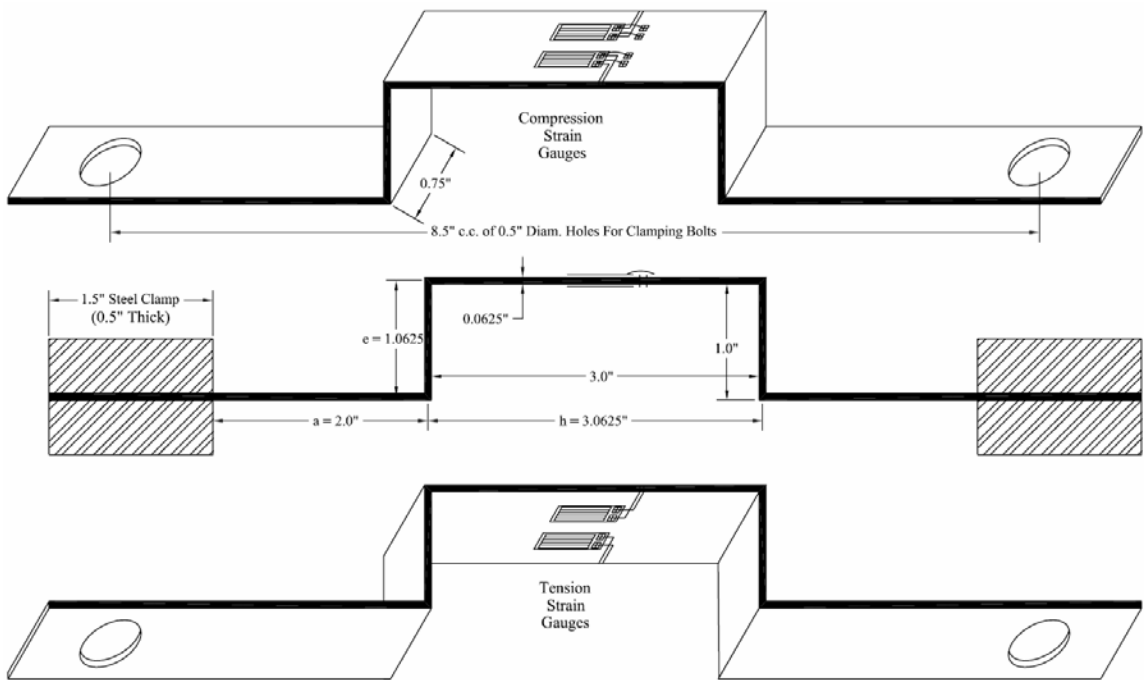


Figure 4.3.1. Deflection Gauge For Monitoring Pin Connection Rotation.

The most important considerations to obtain good, consistent, readings are three fold: align the sensitive axis of the strain gauge with the axis of the aluminum plate; provide an even loading to prevent twisting; and provide effective strain relief at the cable connection such that the cable will not pull on the gauge as loading occurs. Proper strain gauge alignment will be achieved with good strain gauge installation technique. Figure 4.3.2 shows the strain relief that was provided during an installation at the Hanapepe River Bridge (see Chapter 7). The strain relief was simply a large washer clamping against the concrete surface. Notice the slack of the cabling between the crack gauge and the strain relief is minimal but not tight.



Figure 4.3.2. Installed Gauges Monitoring Rotation of Pinned Connection at Pier.

Finally, the gauge is attached to the concrete surface by use of heavy steel brackets. The brackets must provide boundary conditions consistent with those used to calibrate the device. The bracket must also be appropriate to the geometry of the structure to which it is attached. Figure 4.3.2 shows how two gauges were installed to monitor the rotation of the pinned connection shown in the image on the right. As shown in the figure heavy

steel angles and steel plates were used. These attachment brackets need to be stiff enough that the load induced in the gauge by its deformation does not significantly deform the brackets as well—that measurement will be lost.

4.3.3 Estimating Displacement Resolution

The structural system of the installed gauge is indeterminate to the 3rd degree when idealized as a two dimensional bent beam. To estimate the displacement resolution, the relationship between the axial displacement and bending strain at the strain gauge locations can be analyzed using mechanics of materials principles. The strain measurement resolution can then be applied to the equation and the displacement resolution is determined. This process was demonstrated in section 4.2.3 for the crack gauge device. During the course of development, it was decided that since the two devices were geometrically quite similar, with a similar mode of loading, a detailed calculation of the estimated resolution was not necessary. In the end, the resolution of the device was similar to that of the crack gauge.

CHAPTER 5. STRAIN GAUGE BASED DEFLECTED SHAPE CALCULATION

Directly observing the relative movement between a structure and a stationary object during loading seems trivial. However, this cannot always be done easily. Chapter 3 addresses some, but not all, of the difficulties by using a catenary device to establish a baseline from which to directly measure displacement. In some cases an indirect measurement is more practical. In structural health monitoring, most transducers indirectly monitor one phenomenon by observing another. The device's physical, electrical, or optical properties are designed such that an easily observable quantity is amplified with a change of the phenomenon of interest. With this in mind, it should be possible to use our experience and observations of material behavior to indirectly measure the displacement of structures. Specifically, we can utilize our knowledge of constitutive, kinematic and equilibrium relationships. This chapter discusses one method to calculate the displacement of a beam from discrete observations of longitudinal strain.

5.1 Literature Review

Vurpillot et al. propose a mathematical model to determine the vertical displacements of beams from internal horizontal deformations—strains [Vurpillot et al 1998]. They verified their model both in the laboratory, on a timber beam, and in the field, on the Lutrive Highway Bridge in Switzerland [Vurpillot et al 1998]. They applied a static uniformly distributed load onto one span of a two span timber beam. The results agreed well with traditional displacement measurements in the laboratory. They monitored the Lutrive Highway Bridge, in Switzerland, to verify diurnal temperature deflections of a

single cantilever span. The diurnal temperature induced deflections—calculated by their method—agreed well with an installed hydrostatic deflection monitoring system in the bridge. The rotation at the end of the cantilever was measured and applied as a boundary condition to their mathematical model. The temperature loading in this case is very similar to a uniformly distributed load. The Vurpillot et al. model will work well for these types of loading conditions. Indeed, by design, their mathematical model is based on a discretization of the beam into sections; each of which has a constant inertia and a uniformly distributed load. The application of a concentrated force or a bending moment must occur at the nodes between the beam sections [Vurpillot et al. 1998]. The mathematical model assumes a deflected shape that is C_1 continuous; fourth order polynomial—the Bernoulli solution to a uniformly loaded beam [Vurpillot et al. 1998]. The curvature function, for this situation, is a second degree polynomial fit to the strain based curvature measurements. To determine the curvature function for each section, they suggest three curvature measurements—preferably at locations with high values of curvature. They mention that for a triangular distributed load only one additional curvature measurement is needed. They state that the precision of displacement measurements can be calculated with a sensitivity study—they conclude with 10 microstrain precision for the strain gauges, a deflection measurement can be obtained with less than 8% error [Vurpillot et al. 1998, pg 524-526]. Without other instrumentation systems, the rigid body displacements cannot be obtained—this method is for measuring internal relative displacements.

Cho et al. [2000] also utilize a methodology similar to Vurpilot et al. They apply it to a simply supported beam with midpoint loading. They obtain strain readings from both electrical resistance and fiber optic strain gauges to compare their performance. They convert strain readings to curvature based on the section properties of the beam. They assume a linear curvature function for each half of the beam based on the known loading condition. They obtain a best fit of the curvature data with linear regression. They cycle the load up to 86% of yielding of the steel beam. The results match well between the dial gauges, electrical resistance strain gauges, fiber optic strain gauges, and the analytical predictions. They observe a maximum relative error of 8% at one location (of seven) during one of the smallest levels of loading. Generally, they observe the largest relative error at the smallest load levels. They attribute this to “unstable settlement of supports” [Cho et al. 2000, pg 345]. They conclude that this method can be used for measuring bridge deflections [Cho et al. 2000, pg 346].

Fung and Robertson [2003] applied this method to several beams in a laboratory. They tested it on a simply supported tube steel beam subjected to four-point loading; a small scale three-span continuous beam subjected to point loads, support movements, and free vibration after plucking between beam sections. They also tested the method for several levels of load on a concrete beam before and after cracking occurred. Each of these beams was tested using electrical resistance strain gauges. The dynamic measurements were able to identify the general mode shape and resonant frequency of deflection, but were not able to identify the magnitude—this was attributed to the type of electric

resistance strain gauges used, not the calculation methodology. For all beams they fitted a second degree polynomial to the curvature data to obtain the curvature function.

Aki and Robertson [2005] applied this system to a small scale three-span continuous tube steel beam. Fabry-Perot fiber optic strain gauges were evaluated in a side-by-side comparison with electrical resistance strain gauges on the small scale beam. The magnitude of the dynamic displacement observed by the fiber optic strain gauges was similar to the magnitude observed by LVDTs. However, the two interior supports which were not defined by applied boundary conditions of the mathematical model showed displacements when there were none. Some of the deflected shapes with large displacements at these supports were not consistent with the expected mode shape of vibration. The deflections were “normalized” by shifting the curves such that normalization forced the displacement at those supports to be zero. The resulting deflected shapes matched very well with the displacements observed by LVDTs. Using the small scale steel beam, they also attempted to use the method to observe torsional displacements—placing four strain gauges at each cross-section. They noted torsional displacements that were not consistent with the applied loading. For all beams they fit a second degree polynomial to the curvature data to obtain the curvature function.

5.2 General Methodology

As described in section 5.1, Vurpillot et al. [1998] published the methodology for converting strain measurements to a deflected shape of a beam. Essentially, strain is converted to curvature; either based on section properties, or from multiple strain gauges

through the depth of the beam. The method ultimately describes a process that estimates the curvature function then uses that generated function to calculate the beam displacement function. To simplify, the methodology will be called the C2D method from here on. In this chapter, only the C^1 continuous fourth-order polynomial assumption for deflected shape will be considered.

5.3 Curvature to Displacement (C2D) Derivation

From calculus, we know that the curvature of a plane curve is the change in slope per unit of arc length [Salas 1995, pg 888]. In terms of the standard Cartesian coordinate system, curvature, κ , is:

$$\kappa = \frac{y''}{[1+(y')^2]^{2/3}}. \quad (5.2.1)$$

where;

y is a function of x , $y(x)$;

y' is the first derivative of $y(x)$ with respect to x ;

y'' is the second derivative of $y(x)$ with respect to x .

Generally, in structural engineering, only small deflections are considered. This simplifies the curvature function to the expression:

$$\kappa = y''. \quad (5.2.2)$$

Therefore, the first derivative of the displacement function, y' , provides the functions slope (angle of rotation); and the second derivative is considered the curvature function.

Let the curvature function be a second degree polynomial:

$$\kappa(x) = ax^2 + bx + c. \quad (5.2.3)$$

The coefficients a , b , and c are unknowns. To obtain them, three equations are needed—three curvature observations at three locations ($i = 1, 2, 3$) along the length of the beam section. The curvature observations are determined from strain measurements along the beam. If the gauge length of the strain measurement is very short, we can assume that strain occurs at the center of the gauge. Using the x ordinate at the center of the gauge in equation (5.2.3) is probably appropriate in this case. Evaluate equation (5.2.3) at each “ i ” location to create and solve a system of three equations for a , b , and c .

If, however, the gauge length of the strain measurement is long (ex., 1 meter) then the assumption that the average strain occurs at the center of the strain gauge may not be appropriate. The true location of the indicated strain cannot be determined; arbitrarily choosing the x ordinate will generate biased error of unknown magnitude and direction. Instead, the Mean Value Theorem can be used in combination with equation (5.2.3) to produce a new equation to rationally choose the coefficients a , b , and c . The new equation becomes the mean curvature equation:

$$\kappa_m = \frac{\int_{x^l}^{x^r} (ax^2 + bx + c)dx}{x^r - x^l}. \quad (5.2.4)$$

where;

κ_m is the mean curvature on the interval from x^l to x^r .

x^l is left most (starting) ordinate of the strain gauge (x increasing to the right);

x^r is right most (ending) ordinate of the strain gauge (x increasing to the right).

Integrating equation (5.2.4) produces:

$$\kappa_m(x^l - x^r) = \frac{a}{3}(x^{l3} - x^{r3}) + \frac{b}{2}(x^{l2} - x^{r2}) + c(x^l - x^r). \quad (5.2.5)$$

Evaluate equation (5.2.5) at each “ i ” location to create and solve a system of three equations for a , b , and c .

The process of determining a , b , and c is repeated for all of the beam sections in the model. Again, for this derivation of the C2D method, a beam section will have a constant flexural rigidity and a uniformly distributed load. Point loads, support reactions, and applied moments should only be applied at ends of a beam section, or intersection of two beam sections.

Integration of the curvature function—equation (5.2.3)—results in the C^0 continuous third degree polynomial angle of rotation equation:

$$\theta(x)_j = \int \kappa(x) dx = \frac{a_j}{3} x^3 + \frac{b_j}{2} x^2 + c_j x + \alpha_j. \quad (5.2.6)$$

where;

$\theta(x)_j$ is angle of rotation as a function of location along beam section;

j is the index for the beam section;

α_j is the constant of integration, for beam section j , that is defined by the boundary conditions with the adjacent beam sections to ensure angle of rotation continuity (due to C^1 continuity of the deflection curve).

Completing the double integration of the curvature function—equation (5.2.3)—results in the C^1 continuous fourth degree polynomial beam section deflection equation:

$$v(x)_j = \int (\theta(x)_j) dx = \iint \kappa(x) dx = \frac{a_j}{12} x^4 + \frac{b_j}{6} x^3 + \frac{c_j}{2} x^2 + \alpha_j x + \beta_j. \quad (5.2.7)$$

where;

$v(x)_j$ is the beam section deflection function;

β_j is the constant of integration, for beam section j , that is defined by the boundary conditions with the adjacent beam sections to ensure displacement continuity.

It is up to the user of the C2D method to decide on the appropriate global boundary conditions. Only two global boundary conditions need to be assigned to proscribe the rigid body orientation of the beam. Any additional boundary conditions can be checked by verifying the displaced shape obtained by the process.

The process for assembly of the entire beam deflection function is up to the user; however, the following two requirements will ensure the C^1 continuity along the entire length of the beam. The first ensures continuity of displacements; the second ensures continuity of the angle of rotation:

$$v(l_j)_j = v(0)_{j+1}. \quad (5.2.8)$$

$$\theta(l_j)_j = \theta(0)_{j+1}. \quad (5.2.9)$$

If the loading condition is not consistent with the description of the defined beam sections, the C^1 continuous fourth degree polynomial—generated by the double integration of the curvature functions—may not accurately describe the deflected shape of the beam. The curvature function, generated by the aforementioned process, should be consistent with the M/EI diagram of the beam. Any difference will result in erroneous calculated deflections.

5.4 C2D Method Matlab™ Implementation:

The method used by Vurpillot et al [1998] was incorporated into a Matlab™ program which uses the locations, lengths, and measurements of strain gauges within each beam

segment; combines them with boundary condition assumptions; and calculates the deflected shape of the beam. The method assumes that a C^1 continuous fourth degree polynomial accurately represents the deflected shape. The Matlab™ program assumes zero deflection at the two end supports, the deflections at the two interior supports are not forced by boundary conditions. Only two boundary conditions are required to obtain the solution so the interior support displacements are calculated. Using the cantilever deflection of the beam, the program determines the initial angle of rotation at the left support. The program takes into account the length of the strain gauge; in other words, the Mean Value Theorem based “integral” form of the curvature function approximation is used as shown in equations (5.2.4) and (5.2.5). The program files are in the Appendix, section A5.4.

5.4.1 RISA-2D Strain Input

The Matlab™ program is used to perform the calculations and generate some of the figures in this section. The strain data used in this section are the theoretical strains of the system shown in Figure 5.4.1. The structural system is a three span continuous beam identical to that tested by others [Fung & Robertson 2003, Aki & Robertson 2005]. The strain data was generated from the stresses indicated by a beam finite element (FE) model using the RISA-2D™ software by RISA Technologies, Inc. The idealized FE model is shown in Figure 5.4.2.

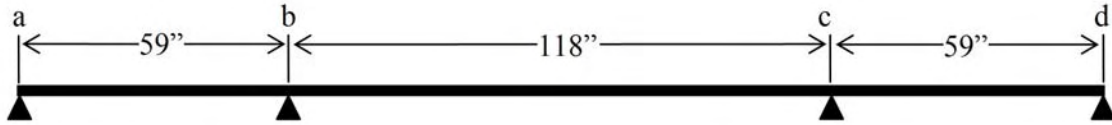


Figure 5.4.1. Three-Span Continuous Beam Modeled.

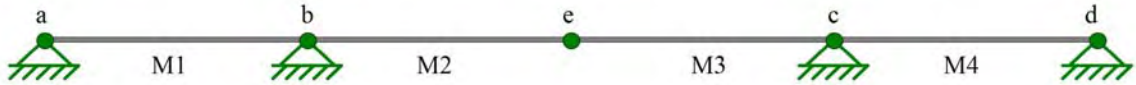


Figure 5.4.2. Three-Span Continuous Beam Finite Element Model (4 Elements).

The extreme bending stresses were extracted from the model at three cross-sections in each beam element. Each beam element is divided into three equal beam sections. The stress data locations were selected as the midpoint of each beam section. A total of 12 locations were used. The strain was then calculated by dividing the stress by the elastic modulus of the material: $E_{\text{steel}} = 29 \times 10^6$ psi. The two strain values at each cross section were then converted to curvature.

The magnitude of the smallest value of calculated curvature was less than 10^{-6} inch^{-1} . This is well beyond the accuracy of any currently available strain gauge or device that could be used on this small scale beam test bed. However, all calculated digits were used as input to the C2D Matlab program (resolution of curvature = 10^{-10} inch^{-1}). This was done to ensure the best possible chance for the C2D algorithm to perform well during the evaluation of the method. Discussions on strain gauge accuracy and noise as it pertains to the accuracy of the C2D methodology are covered in Chapter 6. The following

sections show the performance of the C2D method for several static loading scenarios—as implemented with the Matlab program in Appendix A5.4.

5.4.2 Evaluated Loading Scenarios

The different scenarios are listed in Table 5.1 below. In the RISA-2D program, each point load scenario (1 through 3 in Table 5.1) involved a single 5 lb point load. The results for member forces, member stresses and member deflections were extracted. They were then scaled by the superposition principle such that the scaled results reflect the behavior of the same beam with a 1 lb point load. Similarly, for the distributed load scenarios (4 and 5 in Table 5.1), a 1 lb/in load was applied to the structure. The results were then divided by a factor of 59 to modify them such that a total load of 1 lb was acting on the beam—the distributed loads in both scenarios are 59 inches long. This was done because RISA-2D only reports deflections to the nearest 0.001 inch. The scale model being tested (Figure 5.4.1 and Figure 5.4.2) and the loads applied (Table 5.1) are much smaller than the typical members and loads used in this software package—some of the deflections along the length of the beam are less than 0.001 inches.

Table 5.1. Matlab™ Based C2D Method Evaluation Scenarios.

Scenario	Location of Loading	Load Type	Load (lb) or (lb/in)	Placement On FE Model
1) 1MoCS	Middle of Center Span	Point Load	1	At node e
2) 1MoAS	Middle of Abutment Span	Point Load	1	Middle of element M1
3) 1QPoCS	Quarter Point of Center Span	Point Load	1	Middle of element M2
4) 1DL0M2	Left Half of Center Span	Uniform Load	1/59	Length of element M2
5) 1DL0Nb	Centered over Left Interior Support	Uniform Load	1/59	Half of elements M1 & M2

A summary of the curvatures calculated from the RISA-2D data along the length of the beam is shown in Table 5.2. The total length of the beam is 236 inches. In this C2D calculation the gauge length for each strain / curvature reading is accounted for; the gauge length used was 0.5 inch. This is to compare to strain gauge readings obtained by on the real structure as discussed in Chapter 6—their gauge lengths are about 0.5 inches. The actual gauge length varies: the electrical resistance gauges were 1 inch long; the fiber optic gauges were 0.2 inches long.

Table 5.2. Curvature Observations Used in C2D Program.

Scenario	Curvature Reading (10^{-6} /inch)											
	Beam Axis X-ordinate for Strain Reading (inches)											
	9.8333	29.5000	49.1667	68.8333	88.5000	108.1667	127.8333	147.5000	167.1667	186.8333	206.5000	226.1667
1) 1MoCS	-0.9327	-2.7982	-4.6637	-3.1091	1.8655	6.8401	6.8399	1.8654	-3.1091	-4.6636	-2.7982	-0.9327
2) 1MoAS	2.1375	6.4125	0.7384	-1.8655	-1.3991	-0.9327	-0.4664	0.0000	0.4664	0.5830	0.3498	0.1166
3) 1QSoCS	-0.9327	-2.7982	-4.6636	-1.6323	6.2959	4.2750	2.2541	0.2332	-1.7877	-2.3318	-1.3991	-0.4664
4) 1DL0M2	-0.7773	-2.3318	-3.8864	-1.1918	3.2645	4.4045	2.6427	0.4664	-1.7100	-2.3318	-1.3991	-0.4664
5) 1DL0Nb	0.2089	0.6267	-0.6137	-0.5409	0.8453	0.5732	0.3012	0.0291	-0.2429	-0.3158	-0.1895	-0.0632

5.4.3 Matlab Implementation Scenario 1MoCS

This scenario represents a single unit load applied to the middle of the center span of the structure represented in Figure 5.4.1. The curvature used in the C2D calculation is reported in Table 5.2 above.

The first step to estimate the curvature function from the discrete curvature measurements results in Figure 5.4.3. The figure shows three plots. The solid line represents the theoretical M/EI , or curvature, diagram based on the known loading. The dashed line with the square data points represents the estimated curvature function. The large solid circle plot represents the curvature data used as input for the C2D calculation.

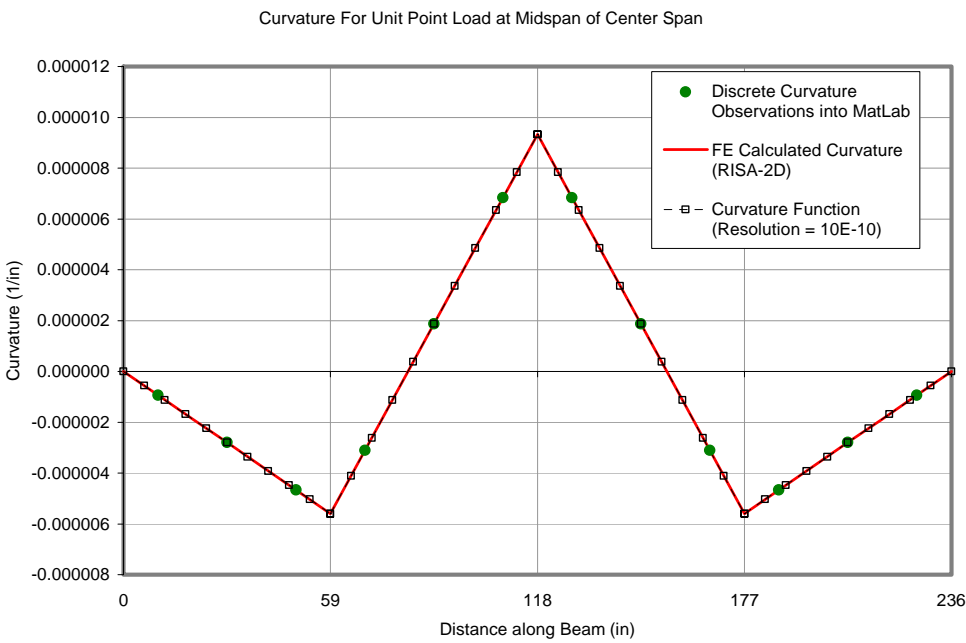


Figure 5.4.3. Scenario 1MoCS: Curvature Estimation.

After integrating twice and applying the boundary conditions (zero deflection at nodes “a” and “d”). Figure 5.4.4 results. The dashed line with the circular data points represents the deflection calculated by RISA 2-D. The solid line with square data points represents the deflection calculated by the C2D method.

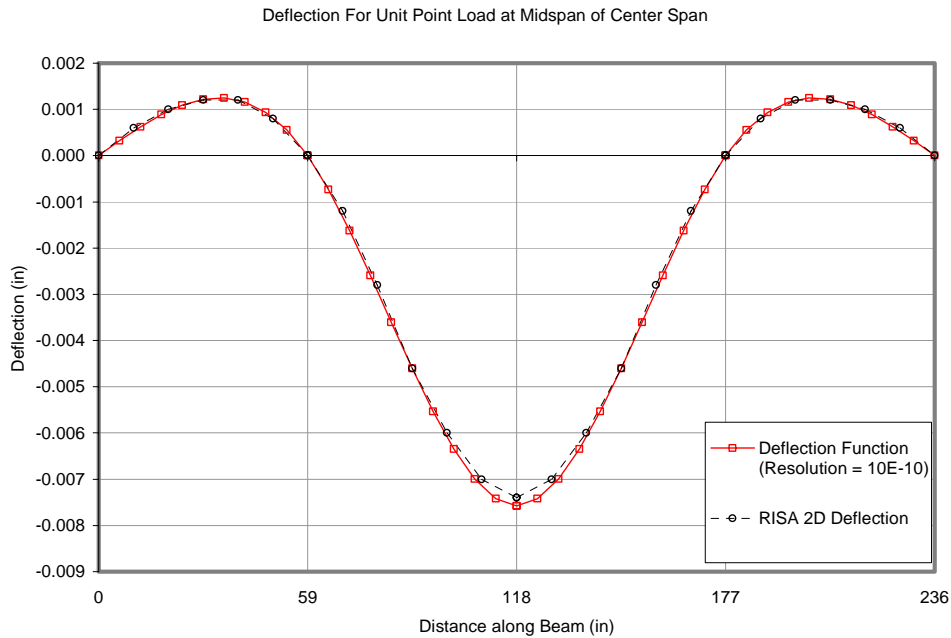


Figure 5.4.4. Scenario 1MoCS: Deflection Comparison.

Both the curvature and deflection are well represented for this load condition.

5.4.4 Matlab Implementation Scenario 1MoAS

This scenario represents a single unit load applied to the middle of the abutment span of the structure represented in Figure 5.4.1. The curvature used in the C2D calculation is reported in Table 5.2 above.

The first step to estimate the curvature function from the discrete curvature measurements results in Figure 5.4.5. The figure shows three plots. The solid line represents the theoretical M/EI , or curvature, diagram based on the known loading. The dashed line with the square data points represents the estimated curvature function. The large solid circle plot represents the curvature data used as input for the C2D calculation.

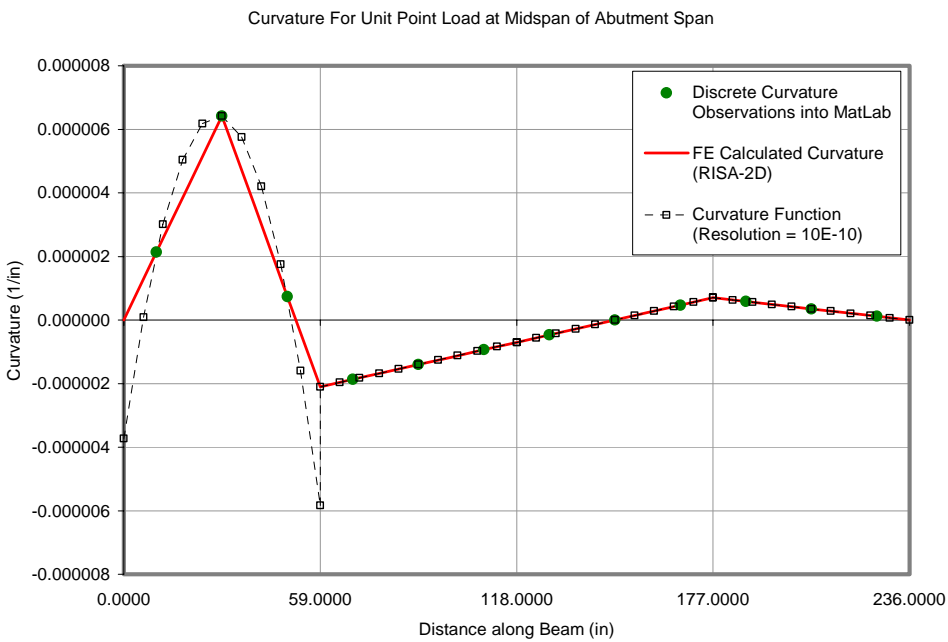


Figure 5.4.5. Scenario 1MoAS: Curvature Estimation.

After integrating twice and applying the boundary conditions (zero deflection at nodes “a” and “d”). Figure 5.4.6 results. The dashed line with the circular data points represents the deflection calculated by RISA 2-D. The solid line with square data points represents the deflection calculated by the C2D method.

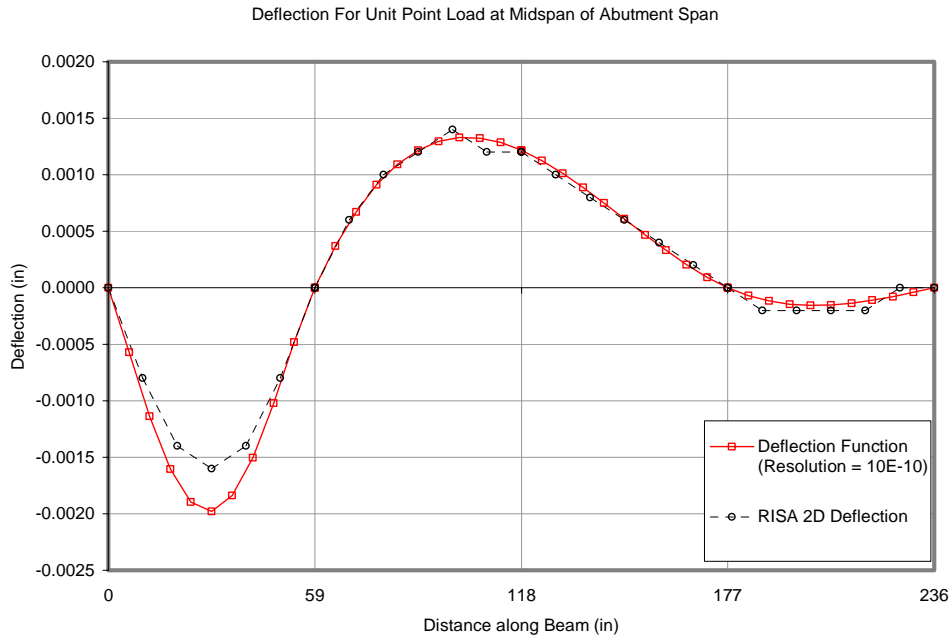


Figure 5.4.6. Scenario 1MoAS: Deflection Comparison.

For this load condition, the C2D calculated functions significantly deviate from both the theoretical curvature and deflection within the left abutment span where the point load is applied within the beam section. However, the curvature and displacement functions of the three other beam sections are well represented.

5.4.5 Matlab Implementation Scenario 1QPoCS

This scenario represents a single unit load applied to the left quarter point of the center span of the structure represented in Figure 5.4.1. The curvature used in the C2D calculation is reported in Table 5.2 above.

The first step to estimate the curvature function from the discrete curvature measurements results in Figure 5.4.7. The figure shows three plots. The solid line represents the

theoretical M/EI , or curvature, diagram based on the known loading. The dashed line with the square data points represents the estimated curvature function. The large solid circle plot represents the curvature data used as input for the C2D calculation.

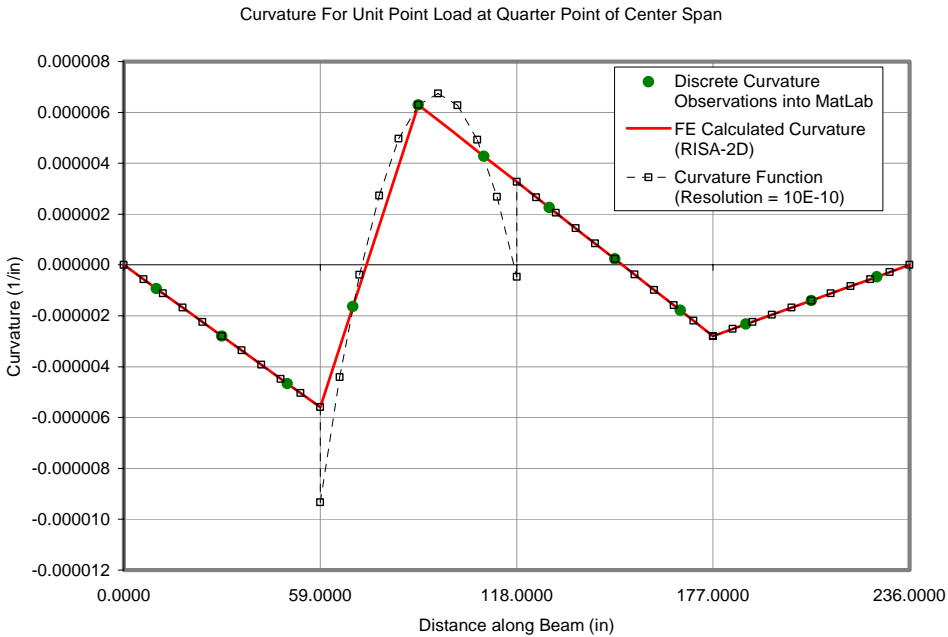


Figure 5.4.7. Scenario 1QPoS: Curvature Estimation.

After integrating twice and applying the boundary conditions (zero deflection at nodes “a” and “d”). Figure 5.4.8 results. The dashed line with the circular data points represents the deflection calculated by RISA 2-D. The solid line with square data points represents the deflection calculated by the C2D method.

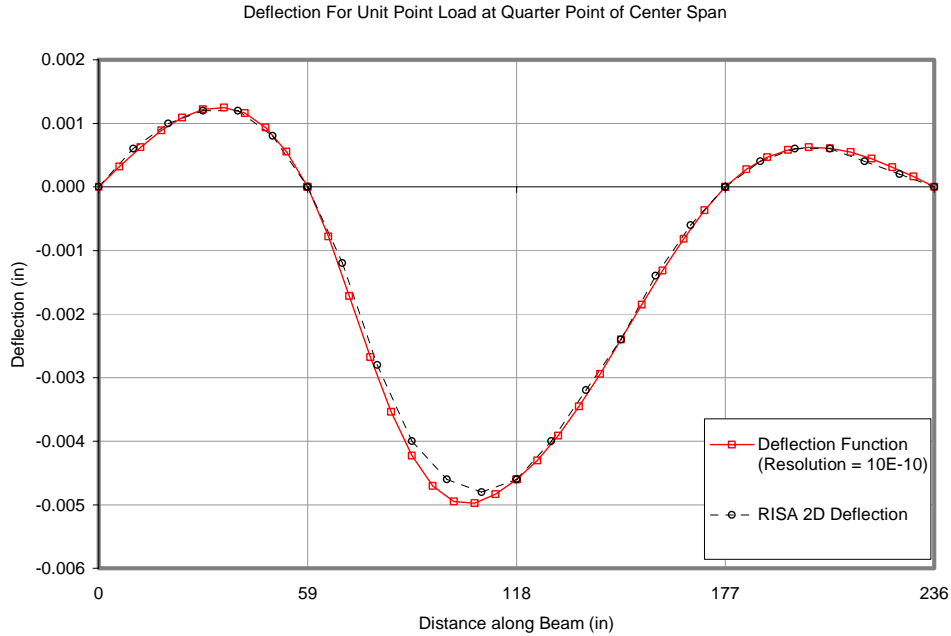


Figure 5.4.8. Scenario 1QPoCS: Deflection Comparison.

For this load condition, the C2D calculated curvature function deviates from the theoretical curvature within the left half of the center span where the point load is applied within that beam section. However, the curvature function within the three other beam sections are well represented. The deflection curve deviates slightly within the left half of the center span where the point load is applied. However, the overall displacement curve is well represented by the C2D results.

5.4.6 Matlab Implementation Scenario 1DLoM2

This scenario represents a uniformly distributed load totaling one pound applied to the left half of the center span of the structure represented in Figure 5.4.1. The curvature used in the C2D calculation is reported in Table 5.2 above.

The first step of estimating the curvature function from the discrete curvature measurements results in Figure 5.4.9. The figure shows three plots. The solid line represents the theoretical M/EI , or curvature, diagram based on the known loading. The dashed line with the square data points represents the estimated curvature function. The large solid circle plot represents the curvature data used as input for the C2D calculation.

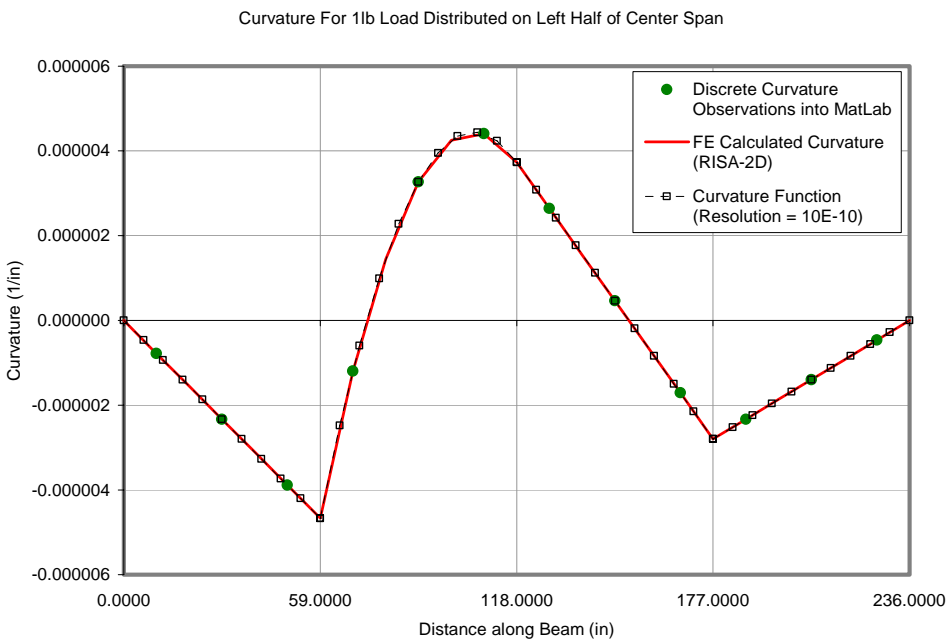


Figure 5.4.9. Scenario 1DLoM2: Curvature Estimation.

After integrating twice and applying the boundary conditions (zero deflection at nodes “a” and “d”). Figure 5.4.10 results. The dashed line with the circular data points represents the deflection calculated by RISA 2-D. The solid line with square data points represents the deflection calculated by the C2D method.

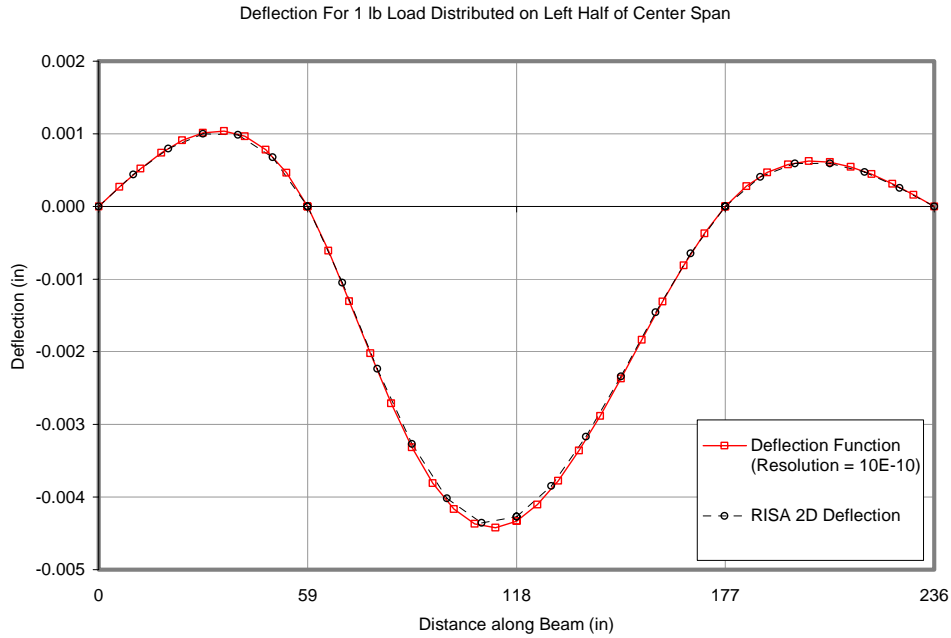


Figure 5.4.10. Scenario 1DLoM2: Deflection Comparison.

Both the curvature and deflection are well represented for this load condition.

5.4.7 Matlab Implementation Scenario 1DLoNb

This scenario represents a uniformly distributed load totaling one pound applied along the right half of member M1 and left half of member M2 of the structure represented in Figure 5.4.1. The curvature used in the C2D calculation is reported in Table 5.2 above.

The first step of estimating the curvature function from the discrete curvature measurements results in Figure 5.4.11. The figure shows three plots. The solid line represents the theoretical M/EI , or curvature, diagram based on the known loading. The dashed line with the square data points represents the estimated curvature function. The large solid circle plot represents the curvature data used as input for the C2D calculation.

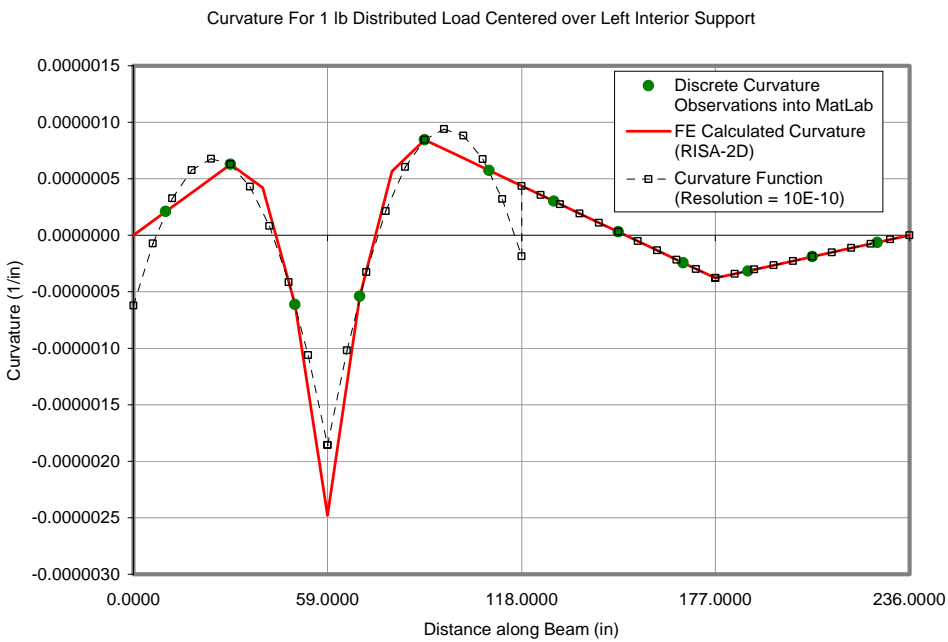


Figure 5.4.11. Scenario 1DLoNb: Curvature Estimation.

After integrating twice and applying the boundary conditions (zero deflection at nodes “a” and “d”). Figure 5.4.12 results. The dashed line with the circular data points represents the deflection calculated by RISA 2-D. The solid line with square data points represents the deflection calculated by the C2D method.

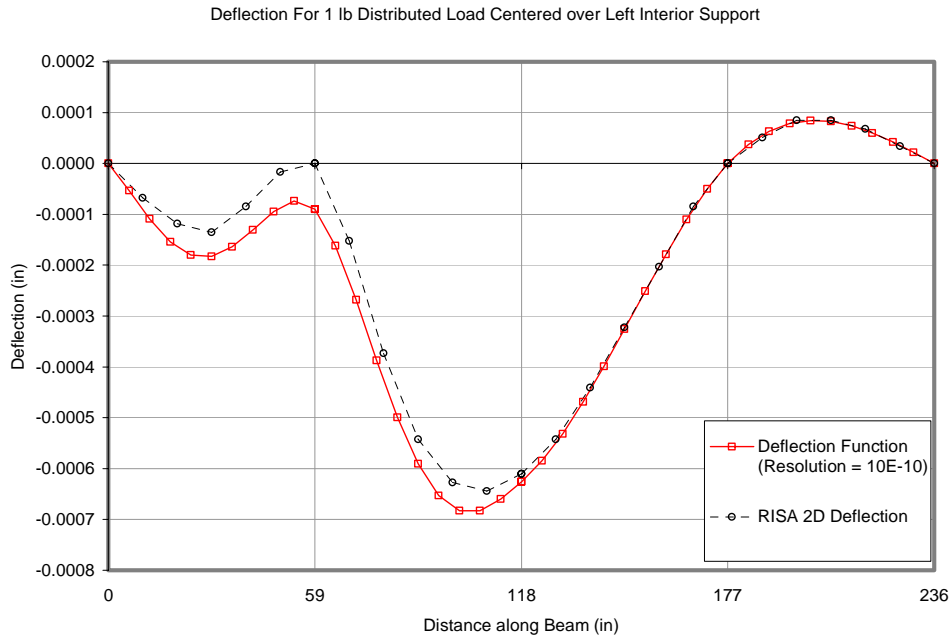


Figure 5.4.12. Scenario 1DLoNb: Deflection Comparison.

For this load condition, the C2D calculated functions deviate from both the theoretical curvature and deflection on the left half of the beam. These deviations occur on the two beam sections where the distributed load is applied within the beam section. The most significant deviation occurs at the calculated deflection of the interior support. The curvature and displacement functions of the two other beam sections—on the right half of the beam—are well represented.

5.4.8 Small Scale Implimentation

A small scale three span continuous beam was constructed and instrumented. The idealized computer model used in section 5.4 intends to represent this small scale structure. Both the scale model and computer model were subjected to a regime of loads

along each of the spans. The scale model was instrumented with weld-on electrical resistance strain gauges, Fabry-Perot fiber optic strain gauges, and LVDTs. A static loading case and a dynamic loading case are presented here.

5.4.8.1 Static Test

The beam supports are pinned at the left end and roller support at each of the other supports. The data was acquired at 100 readings per second. Six Fabry-Perot fiber optic strain gauges were used. The strain gauges are located at the top fiber of the tube steel beam within two of the four beam sections defined by the C2D method—half of the beam is instrumented while it was symmetrically loaded. The observed strains were mirrored about the center of the beam to perform the C2D method calculations. The neutral axis was assumed to be at mid-depth of the beam.

The data was acquired while the beam was loaded to four levels of load and held at each level for several seconds. The loads were applied at the middle of the center span similar to theoretical scenario 1MoCS in section 5.4.3. The four point loads were 2 lb, 4 lb, 6 lb, and 9.5 lb in magnitude. The recorded strains are shown in Figure 5.4.13.

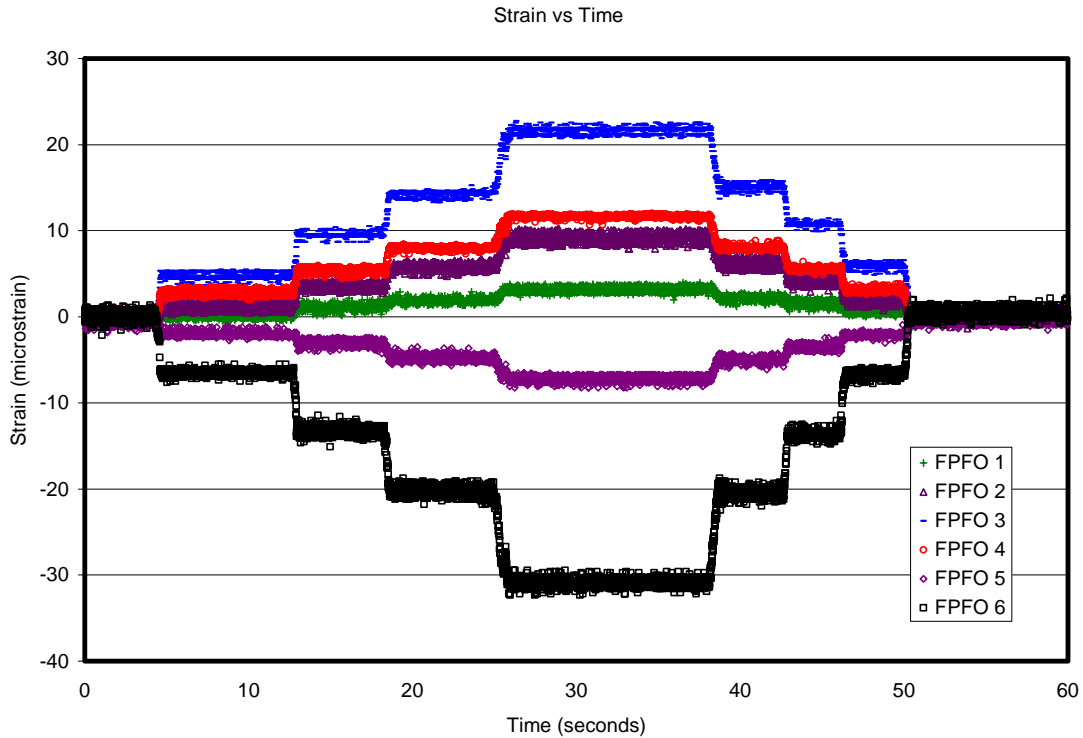


Figure 5.4.13. Static Loading Strains Obtained by Fabry-Perot Strain Gauges.

The C2D calculation was performed for 250 data points (2.5 seconds of time) at each load step shown in Figure 5.4.13. Figure 5.4.14 shows two sets of the results. Each set includes the curvature (top), angle of rotation (middle), and deflection (bottom) results plotted at all four levels of load. The set on the left shows the solutions for all 250 discrete data points obtained at each of the four load steps. The set on the right shows the solution for the average of all 250 data points chosen for each static load case. It is obvious that for this setup, there is a significant dispersion of results even for the static case. This is the result of the resolution of the strain reading shown in Figure 5.4.13. An

analysis of how to estimate this spread before installing instrumentation is covered in Chapter 6.

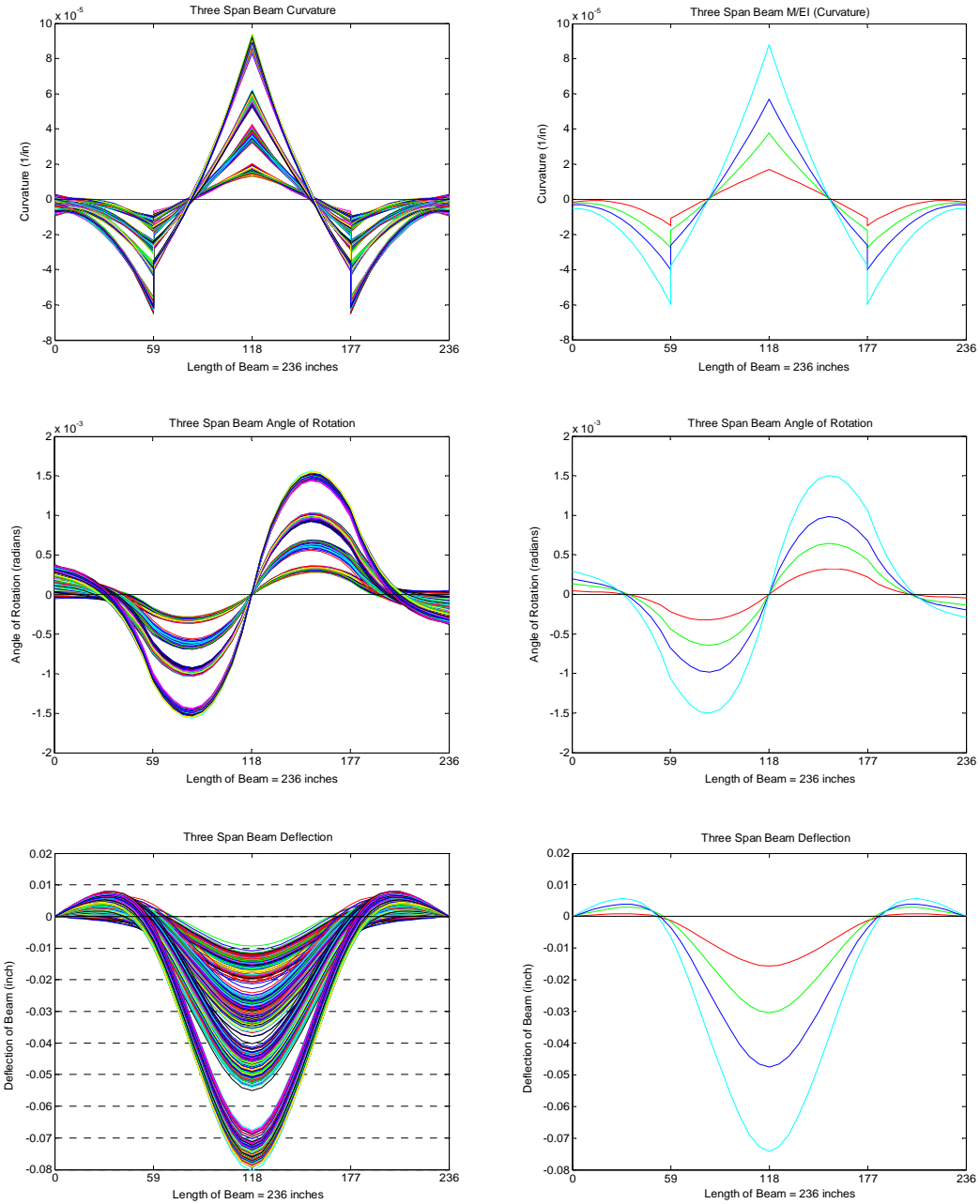


Figure 5.4.14. C2D Static Results—Four Levels of Load.

5.4.8.2 Dynamic Tests

The small scale three-span beam was dynamically loaded by plucking the midpoint of the center span. The beam was instrumented with 12 Fabry–Perot strain gauges located on one half of the beam. They were arranged such that six curvature observations could be made. Since the loading and boundary conditions are assumed to be symmetrical, the acquired data was mirrored across the entire length of the system—all four beam sections. The data was acquired at 200 readings per second. A single cycle (15 time steps) of the free vibration was extracted to calculate the displaced shape of the beam by the C2D method. The six obtained curvatures are shown in the top plot of Figure 5.4.15.

The C2D methodology was then applied to determine the curvature, angle of rotation, and deflection functions of the beam. The results are shown in the lower three graphs of Figure 5.4.15: curvature, angle of rotation, and deflection from left to right respectively.

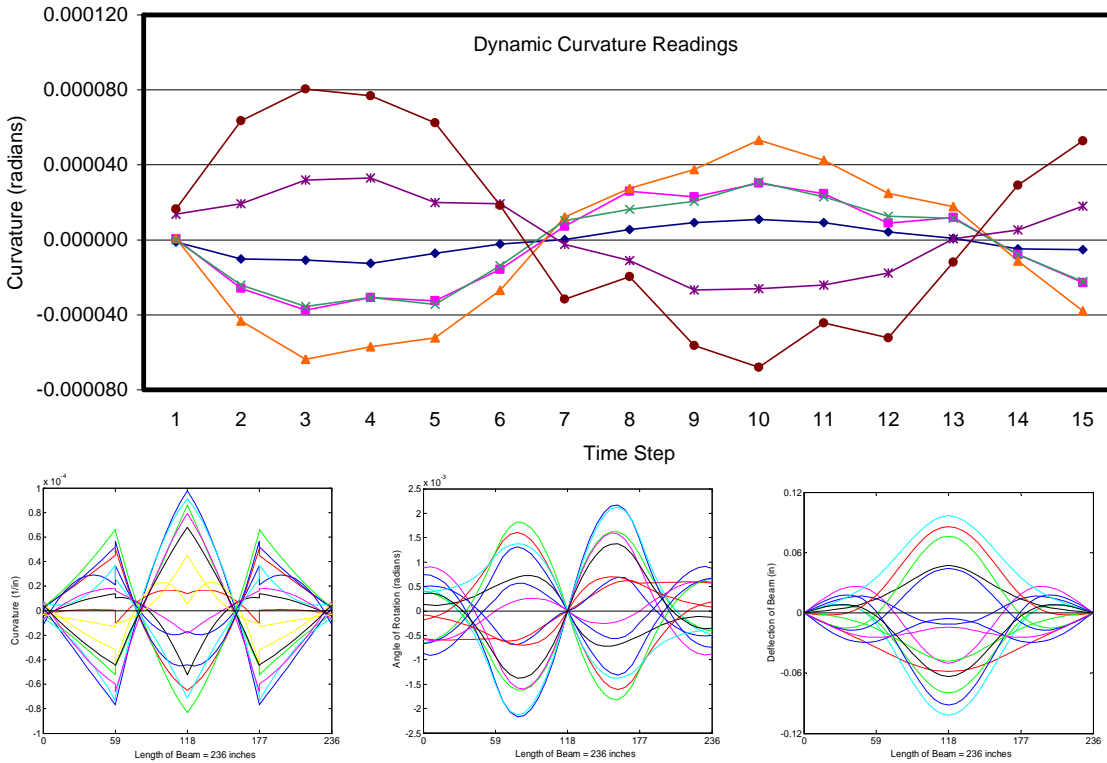


Figure 5.4.15. C2D Method Observations, Dynamic Response of Small Scale Beam.

The results for the curvature are fairly consistent with the point loading applied to induce the free vibration. However, some curvature plots that appear to have similar errors observed in the theoretical static loading conditions; scenarios 1MoAS, 1QSoCS, and 1DLoNb described in section 5.4.2. Others [Aki & Robertson 2005] have shown that the mode 1 dynamic deformed shape is obtained when excited by similar plucking. They needed to perform some data “normalization” to force the deflection at the two interior supports to zero [Aki & Robertson 2005]. Figure 5.4.16 shows the theoretical response for mode 1 vibration that is scaled through a similar cycle of free vibration. Theoretically calculated strains were linearly scaled to create 15 different states of strain to represent a

complete half cycle of a single oscillation of the beam. This result might be obtainable if there were sufficient data points within the dynamic cycle that could be averaged to avoid the signal noise problem identified during the static test of section 5.4.8.1.

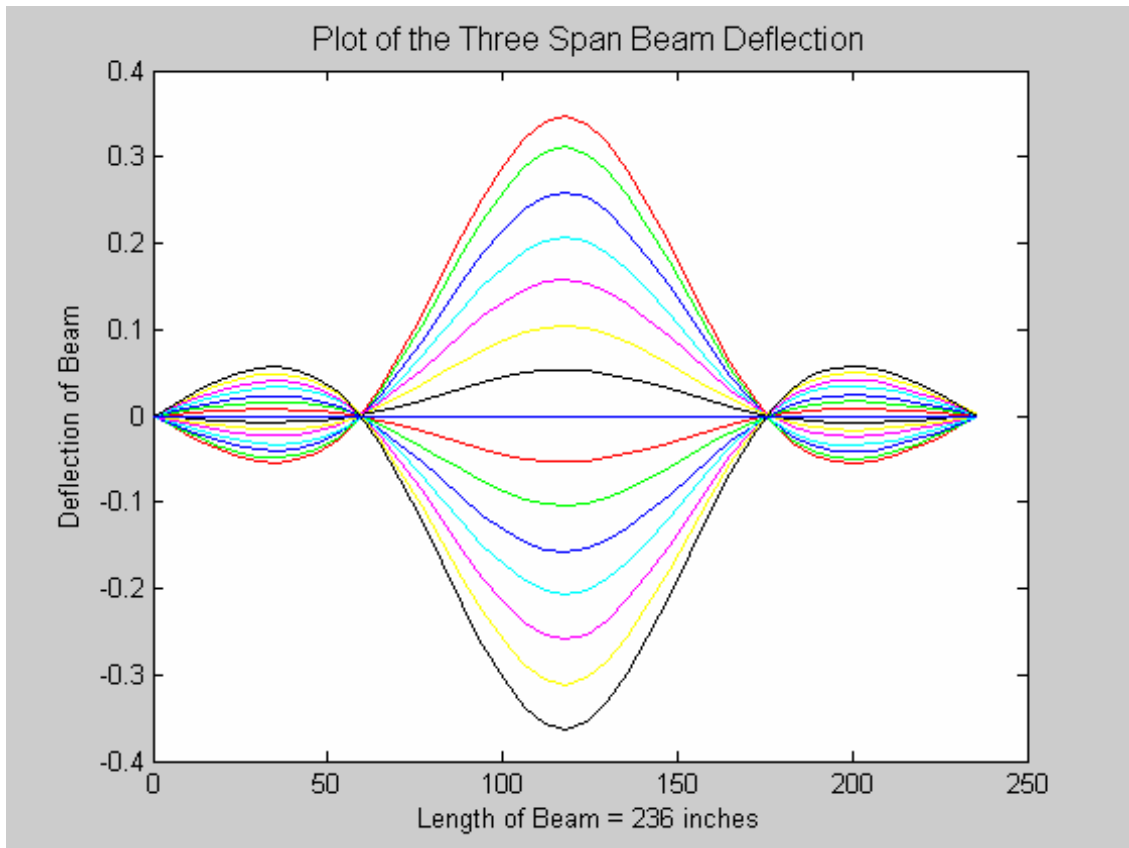


Figure 5.4.16. C2D Calculated Deflection Based on the Theoretical Strains, Mode 1.

5.5 Conclusions

Generally, in most cases, the C2D method has worked well to reproduce the curvature, angle of rotation, and displacement functions of the continuous beam tested. The best performance occurs with the theoretically generated data. If the curvature function is correctly identified by the curve fitting process, the deflected shape errors are small. The

use of data acquired from a real structure does not perform as well. The uncertainty of the acquired curvature is likely the cause.

5.5.1 Comments on Curvature Estimation

The presented C2D method uses a second degree polynomial to estimate the curvature function within each beam section. This estimate works well when the beam section is loaded such that it satisfies the exact solution of the loading condition. However, when the beam section is loaded by a point load within the beam section span, or partially loaded with a distributed load, the second degree polynomial cannot replicate the real curvature function. In the cases observed, this inability of the second degree polynomial to replicate the curvature is limited to the beam sections where the non-conforming loads occur—the curvature is well represented by the second degree polynomial at adjacent beam sections. This is the advantage of a C^1 continuous deflection solution—a discontinuity of curvature is allowed at the node between beam sections. The C^1 continuity only forces the displacement and angle of rotation function to be continuous.

5.5.2 Comments on Deflected Shape

The C2D method as implemented by the Matlab™ program assumes zero deflection at the two end supports. The deflections at the two interior supports were not forced by boundary conditions: they were calculated. The data used to generate the deflected shapes can correctly identify the two interior support locations at the two internal zero deflection nodes. However, in the theoretical loading scenario with a distributed load partially loading two beam sections over the left interior support (1DLoNb), the C2D

result shows a non-zero displacement at that support. The general deflected shape was still identified, but as with the other error-generating scenarios, this support error was significantly larger than the support errors with different loading conditions. The errors generated by loads that do not conform with the exact solutions best represented by a second degree polynomial curvature function—or a fourth degree polynomial deflection function—will require an alternate curvature function and requisite alternate number of curvature measurement locations to obtain an exact solution.

5.5.3 Comments on Real Data Implementation

The real data acquired shows promise; however, there exists significant error beyond the limitations identified by the theoretical loading scenarios. One example, in the small scale implementation the C2D result shows non-zero displacement at the interior supports. In other cases, the deflected shape is inconsistent with what is expected. The static cases appear to perform better than the dynamic cases. This is likely due to the fact that the static cases used averaged curvature as the input while the dynamic case used raw data for a particular time step. Since the theoretical scenarios and its generated data work quite well, these errors must be associated with measurement error. How the systematic measurement error affects the C2D results will be discussed in Chapter 6.

CHAPTER 6. ANALYSIS OF STRAIN GAGE BASED DEFLECTED SHAPE CALCULATIONS

6.1 Background

In chapter 5, we saw that by mechanics of materials, the slope of the normal strain distribution through the depth of a beam at any section can be considered the curvature at that section—assuming small deflections. Determining curvature from strain can provide reasonable deflection estimates in some cases. The curvature to displacement (C2D) Method (described in Chapter 5) utilizes fitting a function to observed curvatures and applying appropriate boundary conditions to calculate an approximate deflected shape by double integration.

In this type of deflection calculation, there are several practical issues to consider: where to place the strain gauges that provide the curvature information; how many strain gauges to use; and which strain measurement device to use.

Engineers will often want to observe events that are not approaching “design magnitude” events. Typically to understand the system, an engineer and owner would much prefer to test their structure in the elastic region subjected to service loads. The owner could also wish to monitor “typical” events which may only cause a very small change in strain within the structure. This could be a systematic problem that is difficult to overcome. Some researchers have observed that smaller strain or load levels produce greater relative error in the calculated deflection [Cho et al. 2000]. Others have noted that a minimum precision in measuring strain is needed to reduce potential error [Vurpillot et al. 1998].

Some gauges are appropriate for some types of deflection measurements while others may not be appropriate—an example would be performance observations of epoxy bonded fiber optic strain gauges versus weldable electrical resistance strain gauges for dynamic deflection measurements on a steel beam as noted by Aki and Robertson [2005].

This chapter discusses how real measurements—subject to systematic noise, limited resolution, and digitization—can affect the C2D calculation results.

6.2 Error Sources in Real Data used in C2D Method

Measuring data using electronics have allowed us to increase the capacity to acquire more information than ever before. However, there still exists a limit to the resolution of these measurements. Two phenomena that can affect resolution of data acquired electronically are the digitization process and the signal noise characteristics of the transducer.

The digitization process translates a signal from a transducer/signal conditioner into a binary number to be stored in the computer system. Since there is finite memory available for storage, even an analog signal is truncated, or rounded off, at a resolution consistent with the capabilities of the analog to digital converter (ADC) of the data acquisition system. For example, if the ADC is a 12 bit device there is only enough available processor capacity to store 2^{12} (4096) distinct signal quantities. This means that if the full range of the transducer is calibrated to measure +/- 5000 microstrain, the smallest recordable difference in strain will be $2(5000)/4096 = 2.44$ microstrain. This

resolution for the case of the C2D method may not be accurate enough to provide acceptable results.

The signal noise characteristics of the transducer usually will provide the dominant source of error in the C2D method algorithm. In most cases, transducers can be calibrated into a data acquisition system such that the signal noise surpasses the digitization round-off as the primary source of error. As described in previous chapters, measurement devices are always subject to environmental phenomena that introduce error into the signal observed by the data acquisition system. This noise limits the resolution of the device. The C2D method can be greatly affected by these erroneous observations.

6.2.1 Measurement Round Off

Measurement round off due to either signal digitization or post processing rounding of data can greatly affect the output of the C2D method. In Chapter 5 five different loading scenarios were used to observe how the C2D method performed as a tool to obtain the deflected shape of a three-span continuous beam. The beam analyzed in that chapter had a cross-sectional depth of 1 inch. The resolution of curvature used as input to the C2D method algorithm was 10^{-10} inch⁻¹. To achieve this resolution with real measurements it would need to be instrumented with strain gauges that could observe changes of 0.0002 microstrain with stable readings at the top and bottom extreme fibers of the beam. This type of system does not currently exist and / or would be too expensive to implement. This effect of this resolution is that between four and five significant figures are used as

input data. A realistic goal for the measurement resolution of curvature to observe for the beam setup used would be 1 microstrain. Rounding the data used in chapter 5 provides a method to observe the effects of measurement round off in the C2D methodology. In this section, all five cases observed in chapter 5 are repeated including the effects of rounding to a resolution of 10^{-6} inch⁻¹. Rounding to this level of resolution has the effect of limiting the input data to one significant figure. The curvatures used as input for this analysis are listed in Table 6.1.

Table 6.1. Curvature Input for Three Span Continuous Beam.

Scenario	Rounded Curvature Reading (10^{-6} inch ⁻¹)											
	Beam Axis X-ordinate for Strain Reading (inches)											
	9.8333	29.5000	49.1667	68.8333	88.5000	108.1667	127.8333	147.5000	167.1667	186.8333	206.5000	226.1667
1) 1MoCS	-1	-3	-5	-3	2	7	7	2	-3	-5	-3	-1
2) 1MoAS	2	6	1	-2	-1	-1	0	0	0	1	0	0
3) 1QPoCS	-1	-3	-5	-2	6	4	2	0	-2	-2	-1	0
4) 1DL0M2	-1	-2	-4	-1	3	4	3	0	-2	-2	-1	0
5) 1DL0Nb	0	1	-1	-1	1	1	0	0	0	0	0	0

6.2.1.1 Matlab Implementation Scenario 1MoCS

This scenario represents a single unit load applied to the middle of the center span of the structure represented in Figure 5.4.1. The curvature used in the C2D calculation is reported in Table 6.1 above.

The first step of estimating the curvature function from the discrete curvature measurements results in Figure 6.2.1. The figure shows four plots. The solid line represents the theoretical M/EI , or curvature, diagram based on the known loading. The dashed line with the square data points represents the estimated curvature function at the 10^{-10} inch⁻¹ resolution. The large solid circle plot represents the curvature data used as

input for the C2D calculation before rounding. The heavy dashed line represents the estimated curvature function obtained by the second-degree polynomial after rounding the input curvature to the nearest 10^{-6} inch⁻¹ resolution.

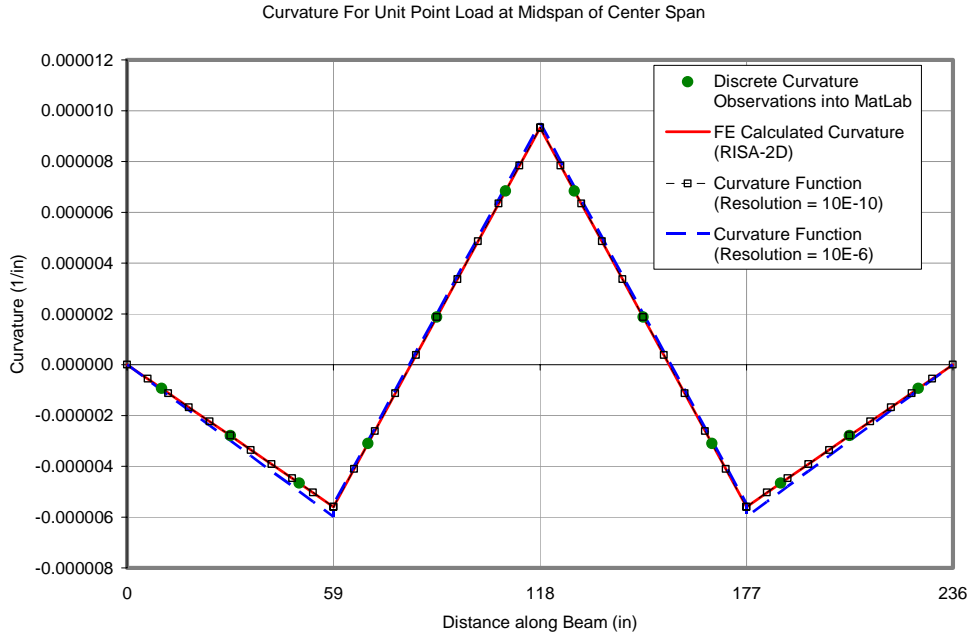


Figure 6.2.1. Scenario 1MoCS: C2D Curvature Comparison.

After integrating twice and applying the boundary conditions (zero deflection at nodes “a” and “d”). Figure 6.2.2 results. The dashed line with the circular data points represents the deflection calculated by RISA 2-D. The solid line with square data points represents the deflection calculated by the C2D method before round off. The solid line with triangular data points represents the deflection by the C2D method after round off.

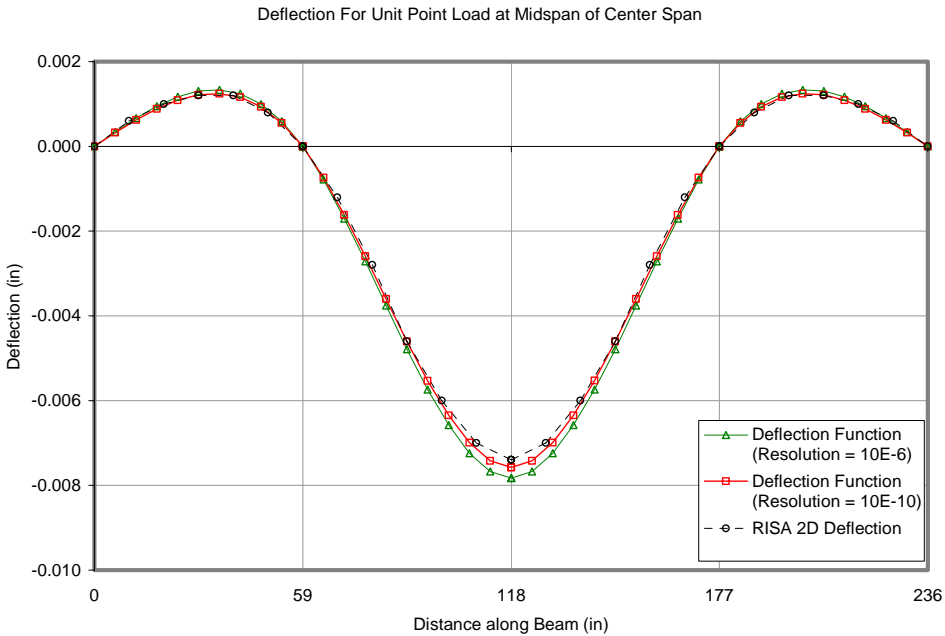


Figure 6.2.2. Scenario 1MoCS: C2D Deflection Comparison.

Both the curvature and deflection are well represented for this load condition. However, for the round off curvature function there is a slight discrepancy in the two short spans of the beam. This error results in a slightly large deflection near the middle of the center span.

6.2.1.2 Matlab Implementation Scenario 1MoAS

This scenario represents a single unit load applied to the middle of the abutment span of the structure represented in Figure 5.4.1. The curvature used in the C2D calculation is reported in Table 6.1 above.

The first step of estimating the curvature function from the discrete curvature measurements results in Figure 6.2.3. The figure shows four plots. The solid line

represents the theoretical M/EI , or curvature, diagram based on the known loading. The dashed line with the square data points represents the estimated curvature function at the $10^{-10} \text{ inch}^{-1}$ resolution. The large solid circle plot represents the curvature data used as input for the C2D calculation before rounding. The heavy dashed line represents the estimated curvature function obtained by the second-degree polynomial after rounding the input curvature to the nearest $10^{-6} \text{ inch}^{-1}$ resolution.

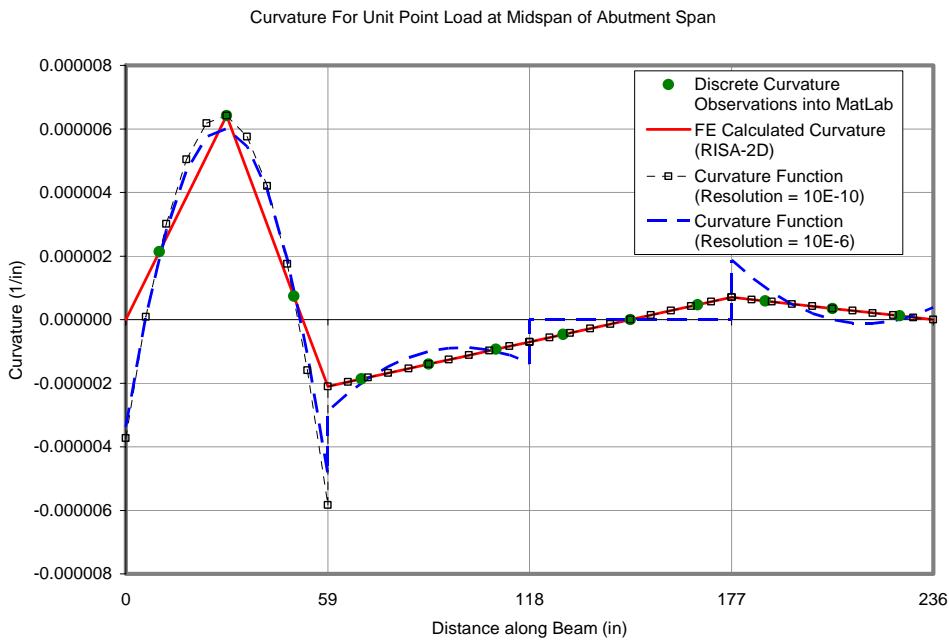


Figure 6.2.3. Scenario 1MoAS: C2D Curvature Comparison.

After integrating twice and applying the boundary conditions (zero deflection at nodes “a” and “d”). Figure 6.2.4 results. The dashed line with the circular data points represents the deflection calculated by RISA 2-D. The solid line with square data points

represents the deflection calculated by the C2D method before round off. The solid line with triangular data points represents the deflection by the C2D method after round off.

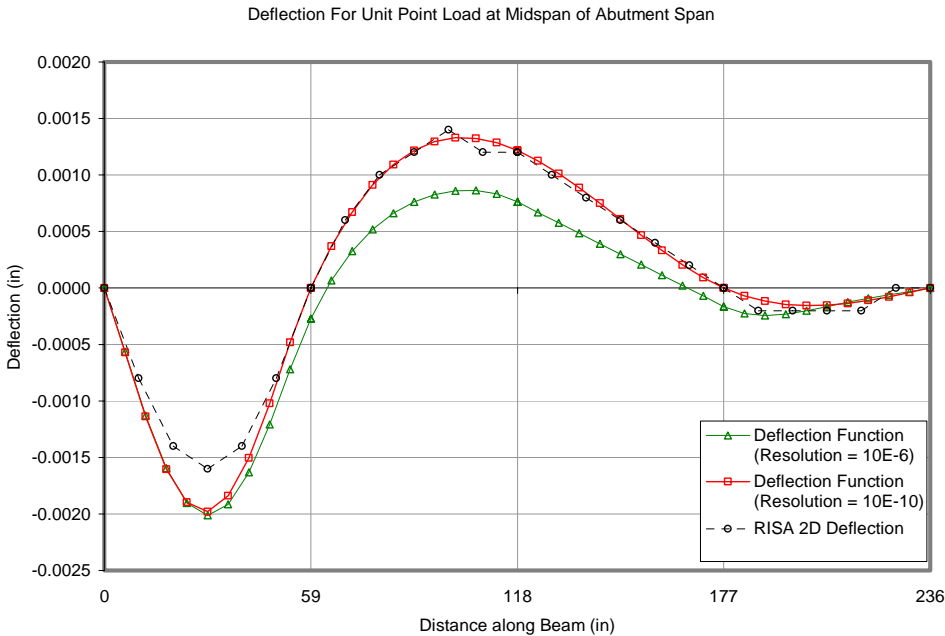


Figure 6.2.4. Scenario 1MoAS: C2D Deflection Comparison.

Prior to rounding, the C2D calculated functions significantly deviate from both the theoretical curvature and deflection within the left abutment span where the point load is applied within the beam section. Before rounding, the curvature and displacement functions of the three other beam sections are well represented. However, after rounding the curvature function misrepresents the theoretical curvature at all four beam sections. Also, after rounding, the deflection calculated by the C2D method significantly deviates from the theoretical deflection curve at the two beam sections within the central span.

6.2.1.3 Matlab Implementation Scenario 1QPoCS

This scenario represents a single unit load applied to the left quarter point of the center span of the structure represented in Figure 5.4.1. The curvature used in the C2D calculation is reported in Table 6.1 above.

The first step of estimating the curvature function from the discrete curvature measurements results in Figure 6.2.5. The figure shows four plots. The solid line represents the theoretical M/EI , or curvature, diagram based on the known loading. The dashed line with the square data points represents the estimated curvature function at the 10^{-10} inch⁻¹ resolution. The large solid circle plot represents the curvature data used as input for the C2D calculation before rounding. The heavy dashed line represents the estimated curvature function obtained by the second-degree polynomial after rounding the input curvature to the nearest 10^{-6} inch⁻¹ resolution.

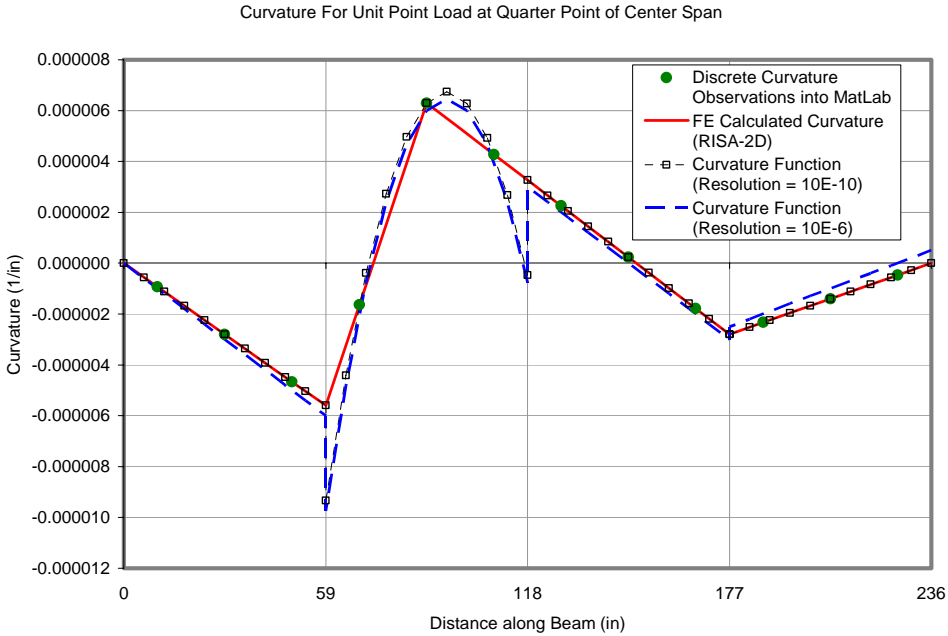


Figure 6.2.5. Scenario 1QPoCS: C2D Curvature Comparison.

After integrating twice and applying the boundary conditions (zero deflection at nodes “a” and “d”). Figure 6.2.6 results. The dashed line with the circular data points represents the deflection calculated by RISA 2-D. The solid line with square data points represents the deflection calculated by the C2D method before round off. The solid line with triangular data points represents the deflection by the C2D method after round off.

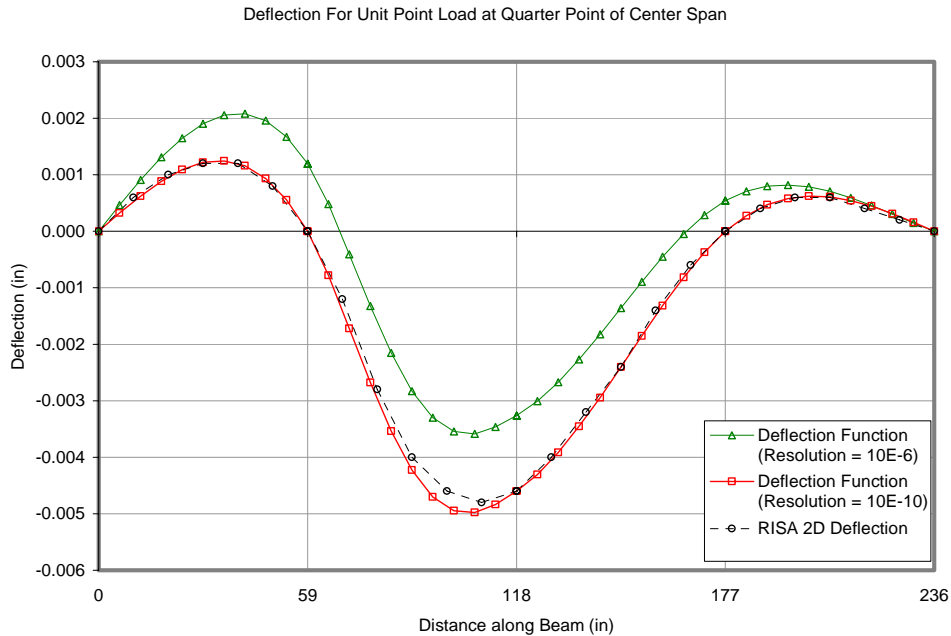


Figure 6.2.6. Scenario 1QPoCS: C2D Deflection Comparison.

Prior to rounding, the C2D calculated curvature function deviates from the theoretical curvature within the left half of the center span where the point load is applied within the beam section. Also, the curvature function within the three other beam sections are well represented. The deflection curve deviates slightly within the left half of the center span where the point load is applied. Despite these discrepancies, the overall displacement curve is well represented by the C2D results. However, after rounding, the C2D calculated curvature function deviates from the theoretical curvature at all beam sections. This deviation is small but results in significant deviation of the deflected shape along the entire length of the beam.

6.2.1.4 Matlab Implementation Scenario 1DLoM2

This scenario represents a uniformly distributed load totaling one pound applied to the left half of the center span of the structure represented in Figure 5.4.1. The curvature used in the C2D calculation is reported in Table 6.1 above.

The first step of estimating the curvature function from the discrete curvature measurements results in Figure 6.2.7. The figure shows four plots. The solid line represents the theoretical M/EI , or curvature, diagram based on the known loading. The dashed line with the square data points represents the estimated curvature function at the 10^{-10} inch⁻¹ resolution. The large solid circle plot represents the curvature data used as input for the C2D calculation before rounding. The heavy dashed line represents the estimated curvature function obtained by the second-degree polynomial after rounding the input curvature to the nearest 10^{-6} inch⁻¹ resolution.

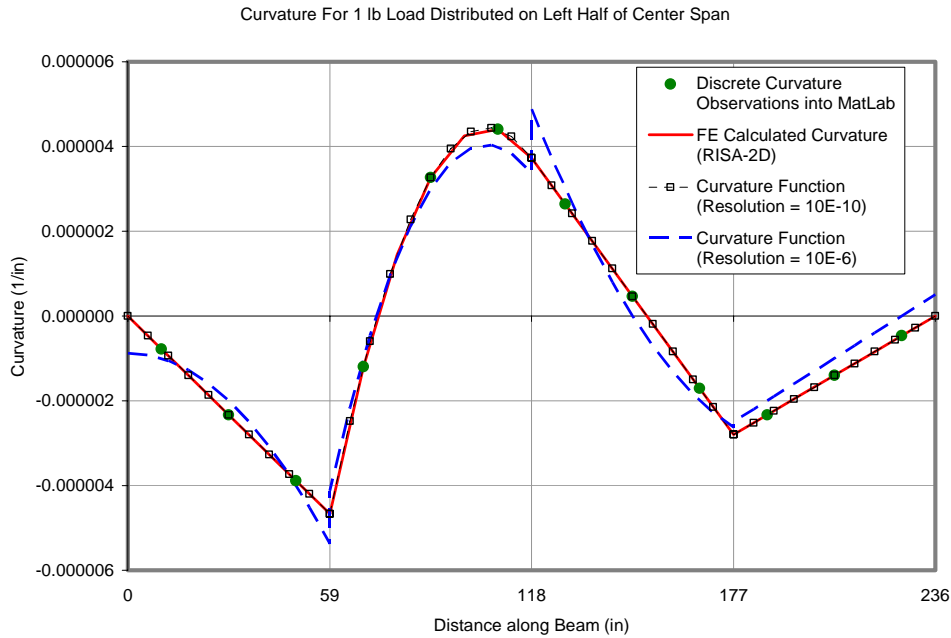


Figure 6.2.7. Scenario 1DLoM2: C2D Curvature Comparison.

After integrating twice and applying the boundary conditions (zero deflection at nodes “a” and “d”). Figure 6.2.8 results. The dashed line with the circular data points represents the deflection calculated by RISA 2-D. The solid line with square data points represents the deflection calculated by the C2D method before round off. The solid line with triangular data points represents the deflection by the C2D method after round off.

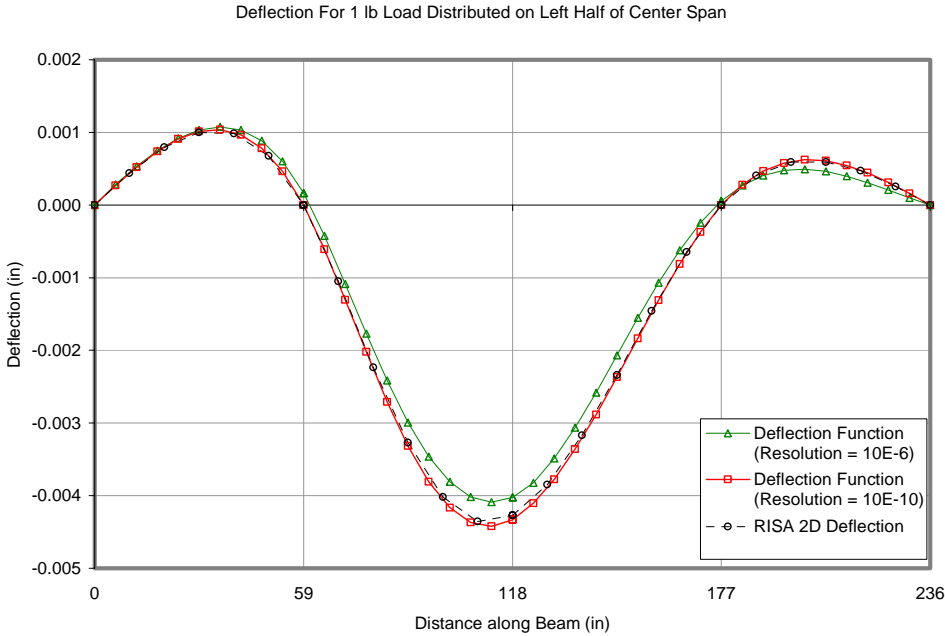


Figure 6.2.8. Scenario 1DLoM2: C2D Deflection Comparison.

Prior to rounding, both the curvature and deflection are well represented for this load condition. However, after rounding, the curvature function noticeably deviates from the theoretical diagram. This deviation results in a small deviation from the theoretical deflection function.

6.2.1.5 Matlab Implementation Scenario 1DLoNb

This scenario represents a uniformly distributed load totaling one pound applied along the right half of member M1 and left half of member M2 of the structure represented in Figure 5.4.1. The curvature used in the C2D calculation is reported in Table 6.1 above.

The first step of estimating the curvature function from the discrete curvature measurements results in Figure 6.2.9. The figure shows four plots. The solid line

represents the theoretical M/EI , or curvature, diagram based on the known loading. The dashed line with the square data points represents the estimated curvature function at the 10^{-10} inch⁻¹ resolution. The large solid circle plot represents the curvature data used as input for the C2D calculation before rounding. The heavy dashed line represents the estimated curvature function obtained by the second-degree polynomial after rounding the input curvature to the nearest 10^{-6} inch⁻¹ resolution.

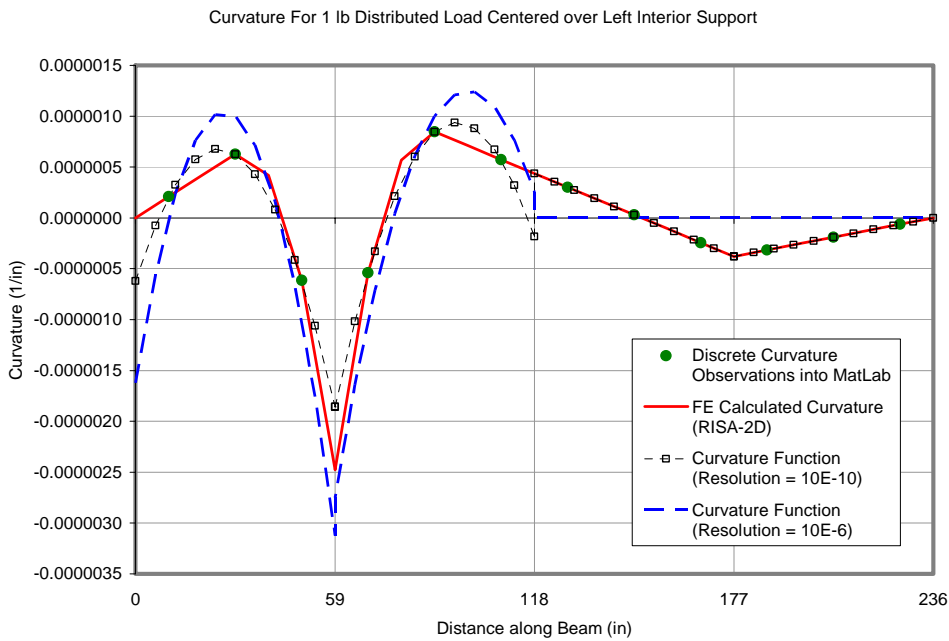


Figure 6.2.9. Scenario 1DLoNb: C2D Curvature Comparison.

After integrating twice and applying the boundary conditions (zero deflection at nodes “a” and “d”). Figure 6.2.10 results. The dashed line with the circular data points represents the deflection calculated by RISA 2-D. The solid line with square data points

represents the deflection calculated by the C2D method before round off. The solid line with triangular data points represents the deflection by the C2D method after round off.

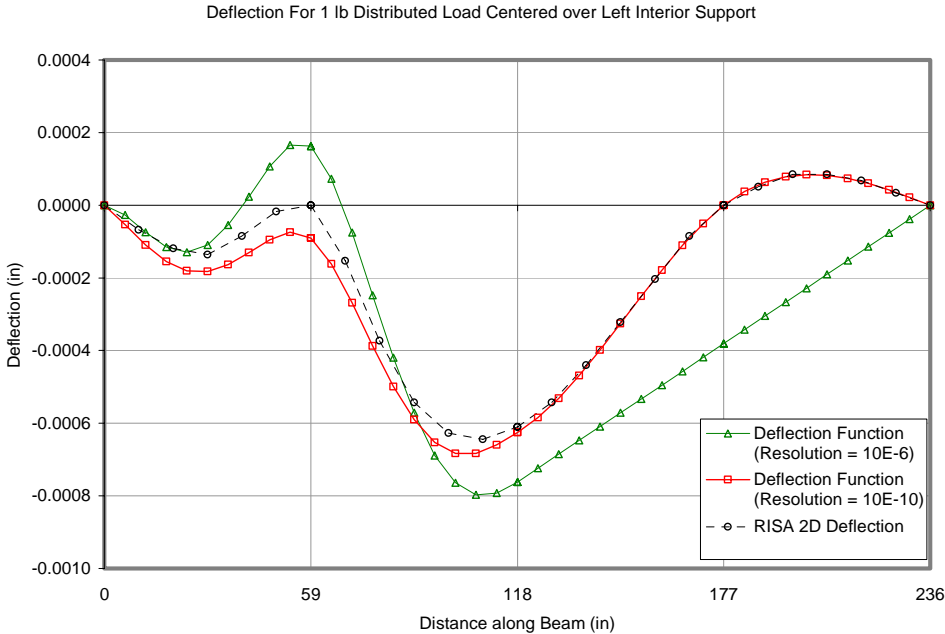


Figure 6.2.10. Scenario 1DL0Nb: C2D Deflection Comparison.

Prior to rounding, the C2D calculated functions deviate from both the theoretical curvature and deflection on the left half of the beam. These deviations occur on the two beam sections where the distributed load is applied within the beam section. The most significant deviation occurs at the calculated deflection of the interior support. The curvature and displacement functions of the two other beam sections—on the right half of the beam—are well represented. There is significant deviation from both the theoretical curvature and deflection functions after averaging occurs. The largest deviation occurs at a location that is far from the applied load.

6.2.2 *Signal Noise Characteristics*

The purpose of this section is to show that signal noise characterization is important to determining the type and placement of strain gauges used to observe curvature in the C2D methodology. Signal noise characterization can also provide a tool to simulate the effect of real noise on theoretical data sets. To determine the sensitivity of a mathematical model to noise within a signal, both the signal and noise must first be classified. Signals can be classified by morphological, phenomenological, energy, and spectral criteria [Zepernick & Finger 2005, pg 7]. This section will show one such example based on Fabry-Perot strain gauge data observed on the three-span continuous beam described earlier in this chapter and defined in chapter 5.

Morphological classification describes the form of the signal as continuous or discrete. The classification considers that both the time and the signal could be either continuous or discrete. There are four possible combinations of these morphologic signal characteristics. Each combination dictates how to handle the analysis and representation of the signal. It is obvious that the data collected to monitor structures are a discrete time based signal. Even during seismic events—when an analogue signal would be preferable—an acceleration time history would be sampled at a frequency on the order of 200 Hz. It is less intuitive, however, that the signal value is also a discrete form of data. The phenomenon is usually measured by an analogue device, but its signal becomes digital by two potential limiting factors: the minimum detectable change within the signal conditioner (often the smallest voltage change) and the digitization limits of the analogue to digital converter (ADC) used to allow a computer to store the data points. To better

understand these limiting factors, consider measuring a rod with a ruler marked to every 1 cm. Let the actual length of the rod be 3.25 cm; this represents an analogue signal. By standard scientific practice, the closest detectable values that are observable, per an error of measure of 0.5 cm, would be either 3 cm or 3.5 cm. This is analogous to digital round off error due to the detection limits of the signal conditioner. Now, if the required format of recording the rod length only allows for eight possible values for a range from 0 cm to 10 cm the recorded length would be either 2.9 cm or 4.3 cm. This is analogous to an ADC imposed rounding error. Strain based data has a morphological classification of discrete-time and discrete-value signal. Typically, these signals will also be aperiodic. Section 6.2.1 adequately demonstrates the possible effects of this classification on the C2D methodology.

Phenomenological classification describes whether the data is deterministic or random. Deterministic signals can be described by mathematical expressions. Examples would be the Dirac impulse, sine waves, et cetera. A random signal could be described by probabilities, probability distributions, probability densities, averages, et cetera. The data for strain measurements are deterministic with random characteristics. A signal of this type of data is also known as a pseudo random signal. Rather than performing a full criteria check that this data meets the pseudo random signal criteria, it was assumed based on the general definition of pseudo random signals that strain gauge data met all the criteria described by Zepernick & Finger [2005].

6.2.3 Sample of Real Strain Data

This section describes the acquired data used to help simulate real induced error into a theoretical response of a mathematical model of a three-span continuous beam. This data is representative of the noise that is introduced into the signal distinct from the deterministic signal. The signals shown in Figure 6.2.11 were acquired with 12 Fabry-Perot fiber optic strain gauges. The strain gauges and signal conditioners were manufactured by RocTest Inc. Their specified resolution was 1 microstrain—their apparent strain resolution is quantified by standard statistical measures and shown in Table 6.2.

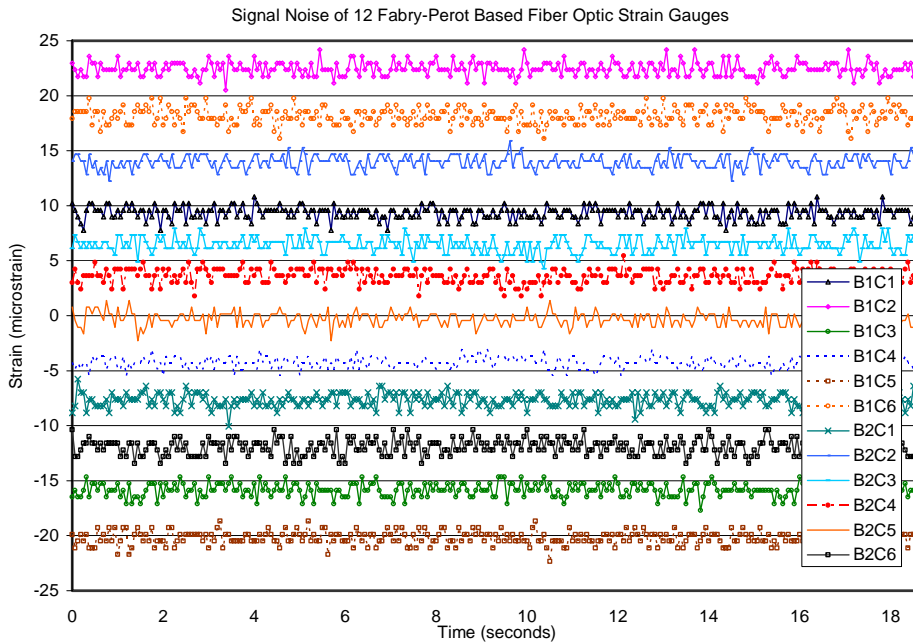


Figure 6.2.11. Strain Gauge Data Acquired for 18.69 seconds at 16 Hz (300 Data Points).

Table 6.2. Statistical Characteristics of Strain Error Based on Average Strain Value.

Statistical Description	Strain Resolution (microstrain): Signal Noise Error per Statistical Description											
	Beam Axis X-ordinate for Strain Reading (inches)											
	9.83	29.50	49.17	68.83	88.50	108.17	127.83	147.50	167.17	186.83	206.50	226.17
1) Standard Deviation	0.5829	0.6231	0.6306	0.5343	0.6163	0.7657	0.6294	0.6109	0.6910	0.6823	0.6354	0.7190
2) 2 x Std. Deviation	1.1659	1.2462	1.2612	1.0686	1.2326	1.5314	1.2588	1.2218	1.3820	1.3646	1.2707	1.4380
3) 4 x Std. Deviation	2.3318	2.4925	2.5223	2.1373	2.4651	3.0628	2.5175	2.4436	2.7640	2.7293	2.5414	2.8760
4) Average Deviation	0.4839	0.4837	0.4745	0.3985	0.5184	0.6337	0.4973	0.4889	0.5769	0.5317	0.5094	0.6048
5) 2nd & 3rd Quartile	0.6103	1.2207	1.2207	0.7629	0.6104	0.6103	1.2207	1.2207	0.6104	1.2207	0.7629	0.6104
6) 95% Confidence Interval	1.8311	2.4414	2.4414	2.1515	1.8311	3.0518	2.4414	1.8311	3.0518	2.4414	2.4414	3.0518
7) Total Range	3.0518	3.6621	3.6621	2.4414	3.6621	3.6621	4.2725	3.6621	3.6621	3.6621	3.6621	3.0518

6.3 Analysis of Error Propagation in C2D Method

In this section the propagation of error is analyzed. Primarily, signal noise will be discussed; the propagation of round off error has been demonstrated in section 6.2.1. In most cases, round off error will occur when a static loading condition is observed and many readings are averaged. If the result of the averaging is not carried to enough digits, round off error might cause problems. In dynamic loading, or continuous data sets, signal noise will generally be larger than the round off error. During the following analysis, different assumed magnitudes of error are applied to theoretical data to observe the effect how the C2D methodology results are affected. In some cases, real data with its natural error will be compared to the theoretically generated error modified data.

First, observations of the effects of error at an individual sensor are shown. The error affects the beam section where the error occurs as well as the entire length of the beam. Second, observations of the effects of error at multiple sensors are shown. Errors at different sensors may combine to increase the overall error, or errors at multiple sensors may counteract each other in some places and increase the error in others.

6.3.1 Error at Individual Sensors

In section 6.2.3 we saw some examples of real strain data. The standard deviation of the noise fluctuation for each gauge type ranged from 0.7 microstrain to 3 microstrain. If this is a random error occurrence, the maximum expected error magnitude could be +/-1 microstrain to +/-5 microstrain. A two microstrain error corresponds to a 10^{-6} inch⁻¹ curvature error. The effect of a 10^{-6} inch⁻¹ error at an individual curvature location has been applied to a single beam section. A 10^{-6} inch⁻¹ error has also been applied to one sensor along the full length of the three-span small scale beam as well. These maximum likely strain errors can be scaled to account for any expected signal error of a strain gauge technology.

6.3.1.1 Single Beam Section

The typical beam section of the system in Figure 5.4.1 has three curvature measurements. Assume that a 10^{-6} inch⁻¹ error of curvature occurs at one of the three locations. In that beam section, there are three possible sets of curvature, rotation and deflection curves generated by the C2D method. Figure 6.3.1 shows the three curvature functions that are produced by a second degree polynomial. Note that the x-axis represents zero error along the length of the beam section. The rotation and deflection functions are based on zero rotation and zero deflection at the left support—cantilever beam. The functions are shown in Figure 6.3.2 and Figure 6.3.3, respectively. Again, with no error, both the rotation and deflection curves would be zero along the entire length of the beam section. The plots represent the error that propagates from a single erroneous curvature

measurement at one location. From these results, it is shown that the maximum rotation error of the beam section is 2.21×10^{-5} radians. The maximum deflection error of the beam section is 1.09×10^{-3} inches. The graphs show that the most error is generated by the case when the signal error occurs next to the end of the beam with the fixed boundary conditions. This shows two things: the further from the prescribed boundary conditions, the larger the error; the greater the signal error near the prescribed boundary conditions, the larger the error along the beam section.

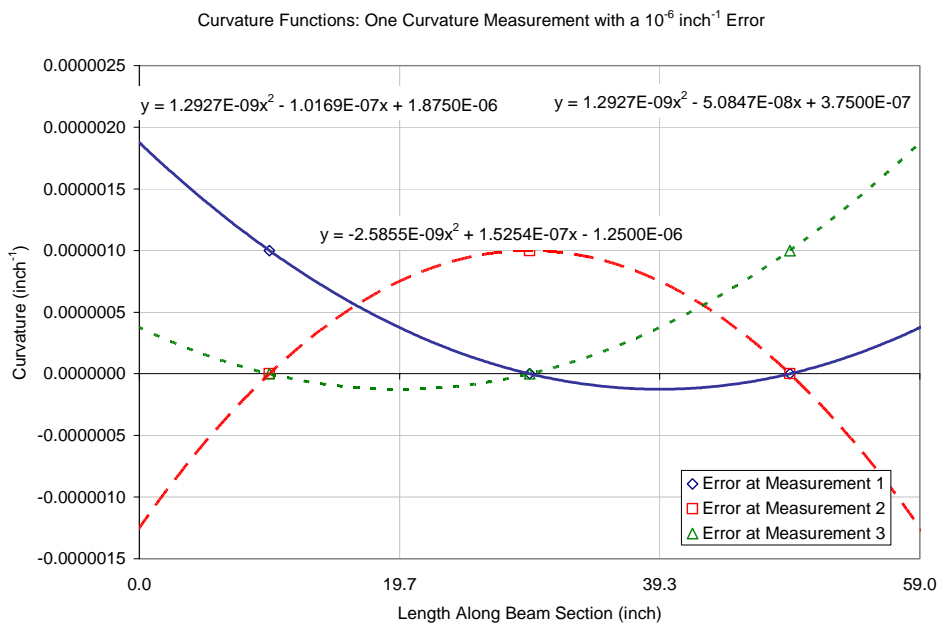


Figure 6.3.1. Second Degree Polynomial Curvature Approximation: Error at One Gauge.

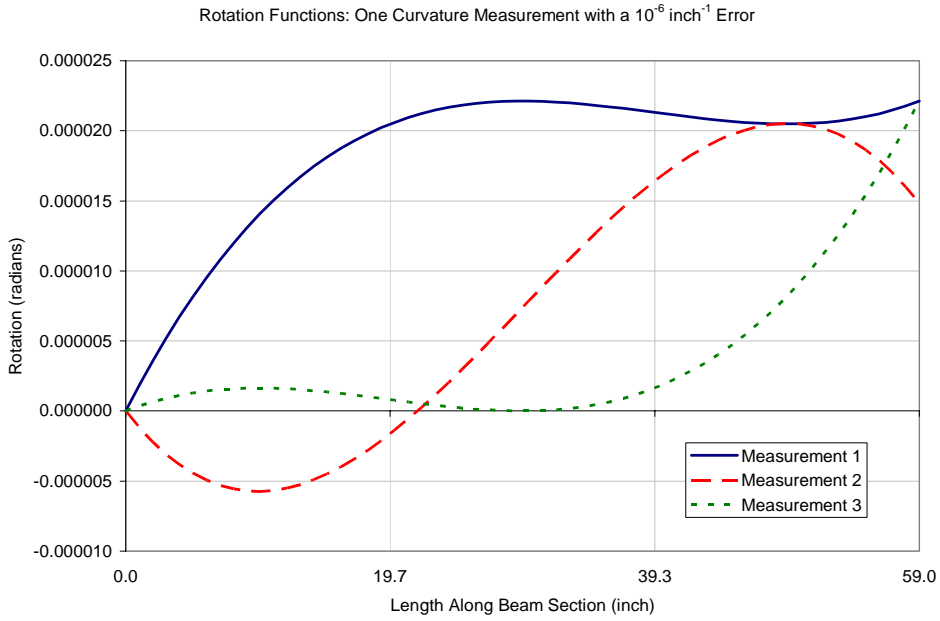


Figure 6.3.2. Third Degree Polynomial Rotation Approximation: Error at One Gauge.

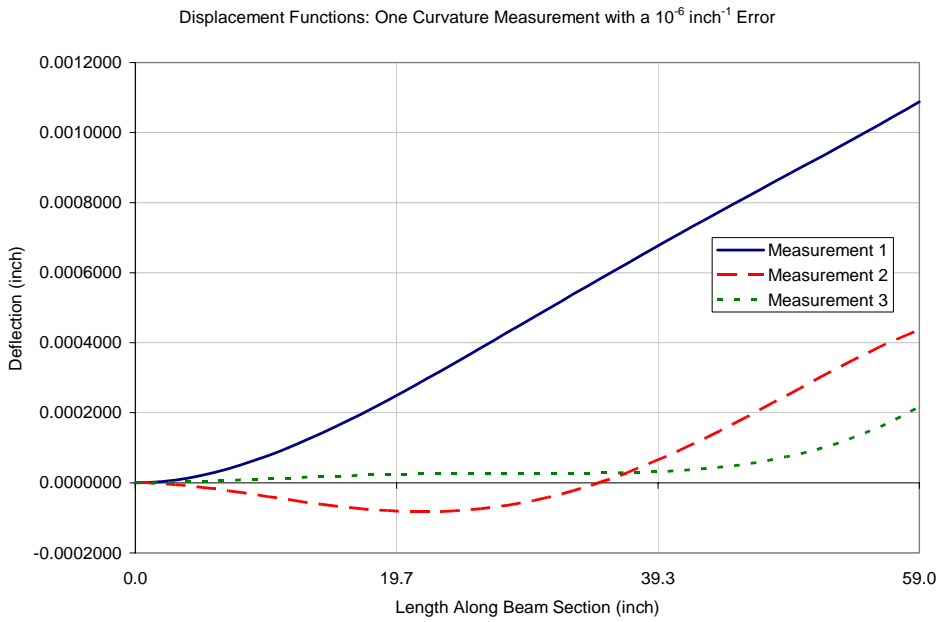


Figure 6.3.3. Fourth Degree Polynomial Curvature Approximation: Error at One Gauge.

6.3.1.2 Entire Beam

The previous section shows how the error at a single curvature measurement can propagate through a single beam section. Generally, as the location along the axis of the beam section is further from the prescribed boundary conditions, the larger the error. In the previous case, the error exists at an end of the beam section. Since the formulation of the C2D method ensures C^1 continuity of the deflection curve, the error at the end of one beam section becomes the boundary condition of the next beam section. This is demonstrated in this section. The structural system analyzed in the three-span continuous beam is shown in Chapter 5.

The C2D idealized beam uses four beam sections with three curvature measurement locations. This system is analyzed in a similar manor as the previous section, however, the global boundary conditions prescribe that the deflection at the ends of the beam are zero. Assuming a 10^{-6} inch⁻¹ error of curvature occurring at one of the 12 locations generates the 12 possible plots in the curvature, rotation and deflection functions in Figure 6.3.4, Figure 6.3.5, and Figure 6.3.6 respectively.

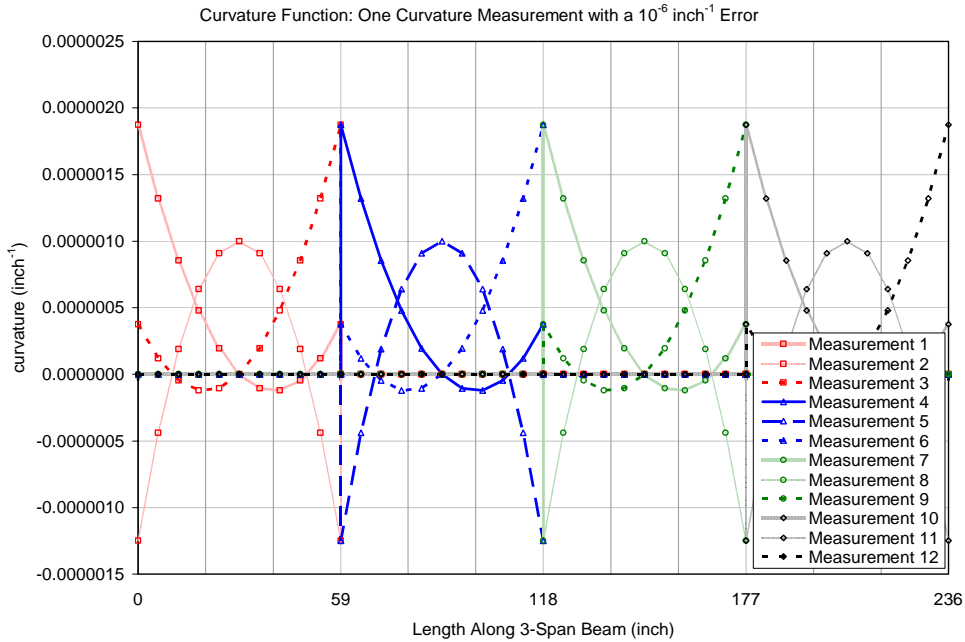


Figure 6.3.4. Curvature Error Based on One Measurement Location.

Notice that the same curvature functions are generated within each beam section as shown in Figure 6.3.4. At all other beam sections, with no error, the curvature function is zero. For the rotation and displacement functions, the second beam section between 59 and 118 inches along the length of the beam will be discussed for clarity.

In Figure 6.3.5, the rotation varies only within the beam section where the error occurs. Zero error presents as a constant angle of rotation—horizontal line. Notice that the angle of rotation is more negative on the left end of the beam than on the right end of the beam. This is consistent with a downward deflection as shown in Figure 6.3.6.

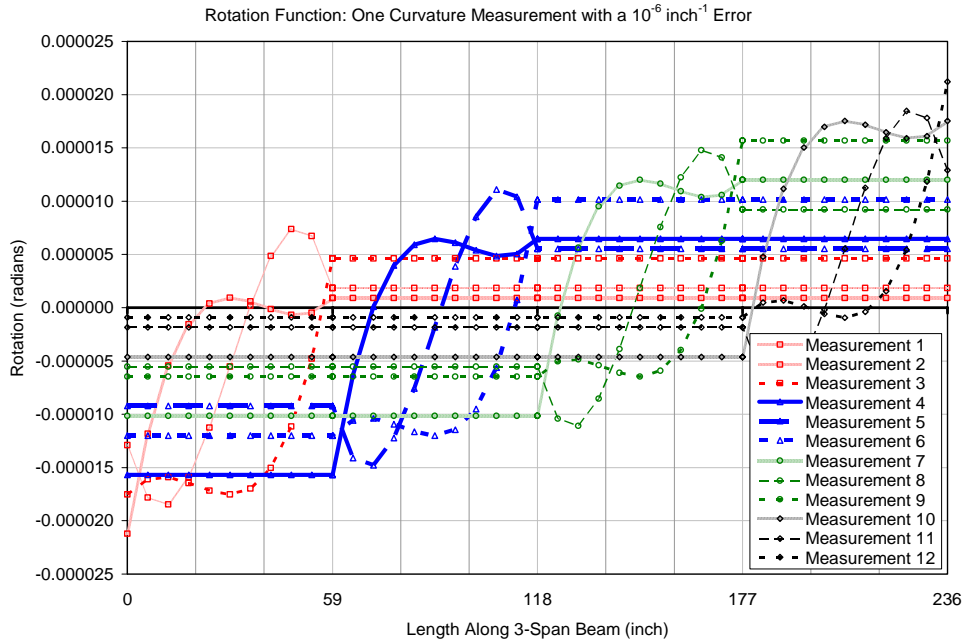


Figure 6.3.5. Rotation Error Based on One Measurement Location.

Figure 6.3.6 represents the 12 displaced shapes that are superimposed onto the real displaced shape when a $10^{-6} \text{ inch}^{-1}$ curvature error occurs at one measurement location. These can also be thought of as the 12 shape functions that combine to form the displaced shape of the three-span continuous beam. They are analogous to the sine and cosine combinations in a Fourier series to produce another function.

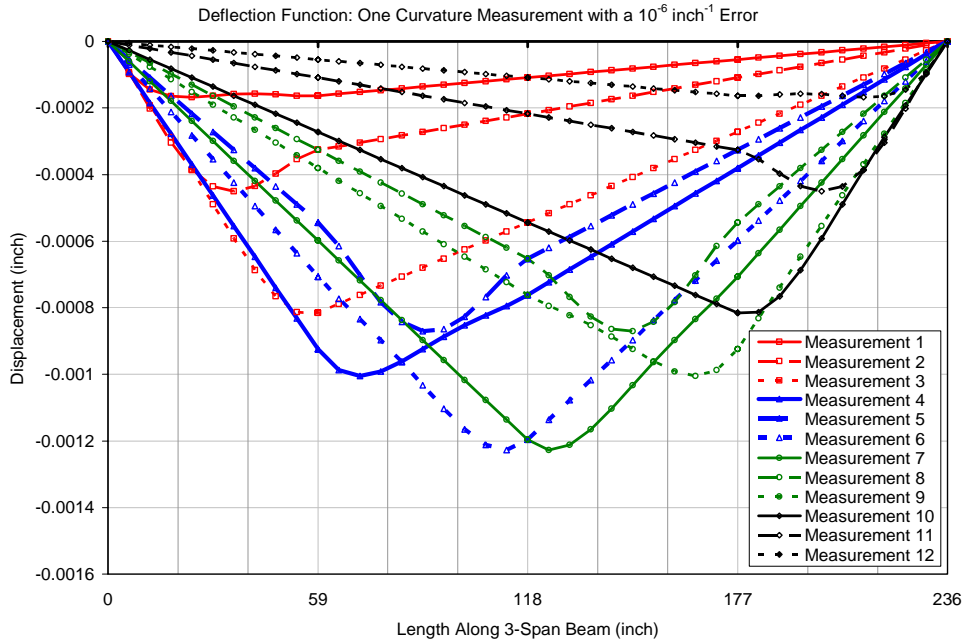


Figure 6.3.6. Displacement Error Based on One Measurement Location.

The displacement functions in Figure 6.3.6 can be combined by superposition to show the magnitude of error due to any combination of errors at any combination of measurement locations for a C2D modeled beam. The figure shows that the largest error occurs away from the specified boundary conditions. In this example, the two boundary conditions that control are zero displacement at zero and 236 inches along the length of the beam.

6.3.2 Error at Multiple Sensors

In section 6.3.1, error in the estimated curvature, angle of rotation, and displaced shapes due to a single erroneous measurement were considered. Unfortunately, every measurement of curvature used for the C2D method will introduce its own magnitude and direction of error into the system. Each error will affect the entire length of the modeled

beam. The last section has provided us with a tool to estimate the maximum expected error within the C2D beam model. In this section, the use of this tool will be demonstrated using superposition of the results, obtained in section 6.3.1, as applied to several measurement locations. The outcome will be compared to real data from the small scale model as tested in the Materials Testing Laboratory at the University of Hawaii. The C2D method will produce results which show the entire deflected shape of the beam as well as for single locations measured by devices such as LVDTs.

6.3.2.1 Deflected Shape of the Entire Beam

In the entire length of a beam, multiple errors will occur. The errors will occur simultaneously. To analyze the effect of these multiple errors, in a general sense, it can be assumed that the errors will be of unit magnitude (10^{-6} inch⁻¹). The errors can be incorporated into the C2D method to see what effect it has on the deflected shape. To get an idea of how the resulting displaced shapes combine when the error occurs at multiple locations, several cases were manually combined by superposition. In section, 6.3.1, unit errors were applied at individual locations, the error in one direction or the other caused the same magnitude of error displacement. However, during a real data acquisition process, signal noise will generate positive and negative measurement errors. Table 6.3 shows eight different combinations of unit error applied as a positive unit curvature at various locations. The combinations were chosen to represent a large range of possible error combinations. Table 6.4 shows eight different combinations of unit error applied in either the positive or negative curvature direction. The combinations chosen in Table 6.4 represent the variability in positive and negative error from one

measurement location to the next. At the top of the table, the error alternates direction at each adjacent measurement location, and at the bottom of the table, half the beam has a positive unit error and half has a negative unit error.

Table 6.3. Positive Error Combinations Calculated by Superposition.

Positive Error Combination	Curvature Measurement Error (10^{-6} inch $^{-1}$)											
	[Location Number] and X-ordinate (inches)											
	[1] 9.8333	[2] 29.5000	[3] 49.1667	[4] 68.8333	[5] 88.5000	[6] 108.1667	[7] 127.8333	[8] 147.5000	[9] 167.1667	[10] 186.8333	[11] 206.5000	[12] 226.1667
At Locations 1 and 7	1	0	0	0	0	0	1	0	0	0	0	0
At Locations 3 and 9	0	0	1	0	0	0	0	0	1	0	0	0
At Locations 1, 2, and 3	1	1	1	0	0	0	0	0	0	0	0	0
At Locations 4, 5, and 6	0	0	0	1	1	1	0	0	0	0	0	0
At Locations 1 through 6	1	1	1	1	1	1	0	0	0	0	0	0
All Locations but 6	1	1	1	1	1	0	1	1	1	1	1	1
All Locations but 12	1	1	1	1	1	1	1	1	1	1	1	0
All Locations	1	1	1	1	1	1	1	1	1	1	1	1

Table 6.4. Alternating Direction Error Combinations Calculated by Superposition.

Positive/Negative Error Combination	Curvature Measurement Error (10^{-6} inch $^{-1}$)											
	[Location Number] and X-ordinate (inches)											
	[1] 9.8333	[2] 29.5000	[3] 49.1667	[4] 68.8333	[5] 88.5000	[6] 108.1667	[7] 127.8333	[8] 147.5000	[9] 167.1667	[10] 186.8333	[11] 206.5000	[12] 226.1667
Positive at All, but Negative at Location 6	1	1	1	1	1	-1	1	1	1	1	1	1
Positive at All, but Negative at Location 9	1	1	1	1	1	1	1	1	-1	1	1	1
Positive From 1 to 6; Negative From 7 to 12	1	1	1	1	1	1	-1	-1	-1	-1	-1	-1
Square Wave Error (Positive at 1)	1	-1	1	-1	1	-1	1	-1	1	-1	1	-1
Square Wave Error (Negative at 1)	-1	1	-1	1	-1	1	-1	1	-1	1	-1	1
2x Square Wave Error (Positive at 1 and 2)	1	1	-1	-1	1	1	-1	-1	1	1	-1	-1
2x Square Wave Error (Negative at 1 and 2)	-1	-1	1	1	-1	-1	1	1	-1	-1	1	1
Positive At All Locations	1	1	1	1	1	1	1	1	1	1	1	1

Figure 6.3.7 shows eight iterations of error that act in the positive curvature direction as they affect the deflection function along the three-span small scale beam. The deflections are calculated by superposition from the results shown in Figure 6.3.6—these results are re-plotted in light gray in Figure 6.3.7 for comparison. The first two combinations are errors that occur at locations 1 and 7 and at locations 3 and 9. These combinations show that when at least one of the errors occurs near the specified boundary conditions, the

error will not be significantly magnified. The third and fourth combinations show the effect of three errors occurring at adjacent measurement locations. When the errors occur further from a specified boundary condition, the error is greater. The fifth combination is a sum of the third and fourth combination. This combination shows a clear representation of the superposition principle in action—it is clearly seen that the fifth is the sum of three and four. The sixth and seventh combinations show the deflected shape with unit errors at all the measurement locations except for one. When comparing these two deflected shapes with the eighth combination, again, it is obvious that the error occurring at the furthest position away from a specified boundary condition makes the biggest difference in the overall error within the deflected shape.

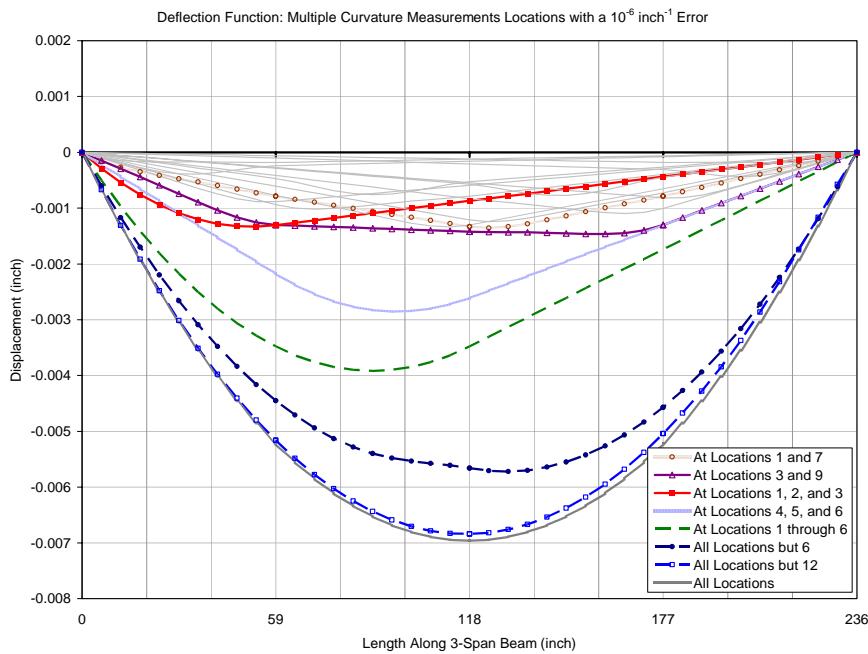


Figure 6.3.7. Deflection Based on Multiple Positive Curvature Error Locations.

Figure 6.3.8 is similar to Figure 6.3.7. It shows another seven iterations of possible deflection results due to both positive and negative unit curvature error. The maximum deflection consistent with all measurement locations having a positive error is also plotted—for comparison. Again, these deflection functions represent possible error along the three-span small scale beam. The deflections are calculated by superposition from the results shown in Figure 6.3.6—these results are re-plotted in light gray in Figure 6.3.8. The combinations of error plotted in Figure 6.3.8 are listed in Table 6.4. The first two combinations consist of errors that all act in one direction (positive curvature) except for one which occurs in the opposite direction (negative curvature) at locations 6 and 9. These combinations show that when an error direction reversal occurs away from the boundary conditions the error at that location is significantly reduced. The shape associated with the unit curvature error is clearly seen, in both cases, removed from the maximum deflection error curve. The next five combinations show the effect of alternating error reversals. The third combination has the largest positive and negative error magnitudes. The fourth and fifth combinations show that a unit curvature error that alternates between adjacent measurement locations keeps the error low. If the errors occur in the same direction at two or more adjacent gauges, the deflected shape is more significantly impacted as seen in combinations six and seven.

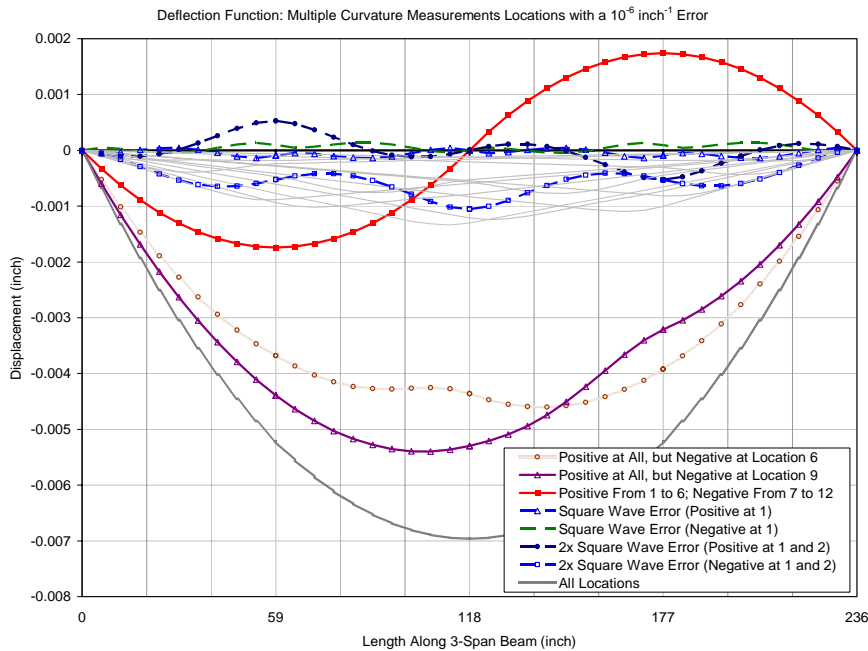


Figure 6.3.8. Deflection Based on Multiple Alternating (+/-) Curvature Error Locations.

All of these combinations do not refute that when errors occur further from a specified boundary condition, the overall error is larger. The superimposed combinations which do have error direction reversal benefit by reducing the overall error. A larger overall error will occur with more errors occurring at adjacent measurement locations and in the same direction. In all the cases described in Table 6.4 and shown in Figure 6.3.8 the deflection for combinations of error do not exceed the case where all the error is in the same direction at all the measurement locations.

The maximum deflection error for the three-span structure considered is 0.007 inches. To ensure this is the absolute maximum theoretical case for the unit level of curvature error for a single direction, the C2D Matlab program was used to run all 2^{12} (= 4096)

binary combinations for the selected beam. The result of the Matlab C2D run is shown in Figure 6.3.9. Indeed the maximum error determined by the C2D calculation is the same as that determined by the superposition of the previous individual error data. Considering error direction reversals, a trinary number of combinations equal to 3^{12} (= 531,441) would include all possible combinations. The C2D method was initiated; however, the required computation capacity was not available to complete the analysis. A supercomputer platform; alternate programming software; or more efficient coding, is probably better suited to perform this analysis.

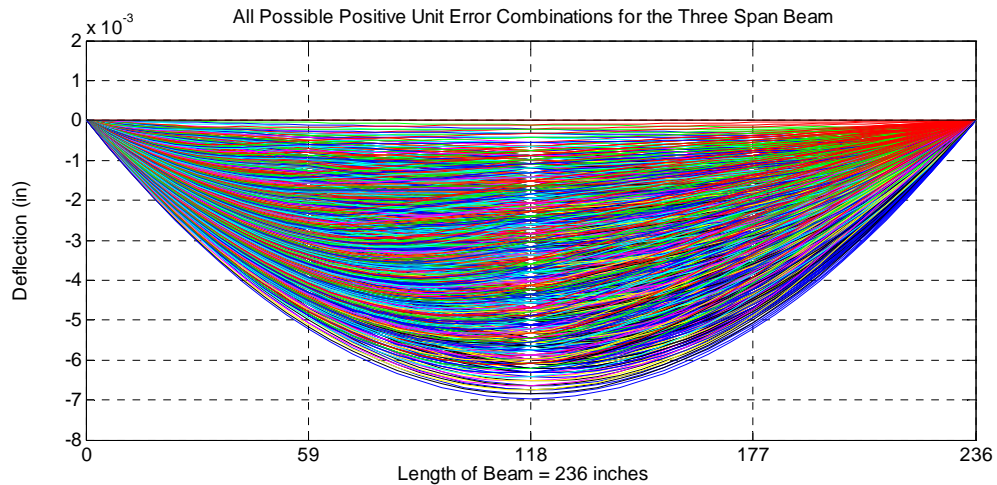


Figure 6.3.9. All Possible Positive Error Combination Displacement Functions.

In any event, the results of the binary analysis for single direction (Figure 6.3.9) give the maximum error envelope based on superposition. This result is based on a unit magnitude of error (10^{-6} inch⁻¹ of curvature) at a single measurement location. This error envelope can be used to estimate the expected displacement error of the C2D method. After determining the expected maximum error of the curvature measurements due to

noise, and or digitization round off, a confidence envelope could be shown on the deflection diagram as well. It is more difficult to compensate for error during real-time dynamic or continuous measurements, so a confidence interval is useful; this will be demonstrated in section 6.3.2.2.

6.3.2.2 Dynamic or Multiple Measurements

The simplest way to reduce random signal error is to acquire that signal at a static condition of the tested structure and average many readings. However, in many cases, a dynamic or continuous signal is the desired data product. Often signal conditioning equipment is the only practical device that can be used; the errors recorded after signal conditioning will remain a characteristic of the data collected. When we choose transducers such as an LVDT to measure displacement, we specify a resolution such that we can measure the movement we expect to see with reasonable accuracy. The deflected shape envelope developed in section 6.3.2.1 can be used to help calculate the expected resolution or noise associated with a specific configuration of curvature measurements and the C2D method. This section shows an example of this as applied to the same three-span continuous small scale beam that is described in chapter 5.

The overall process involves first determining the expected signal error and its characteristics as described in section 6.2.3. The analysis should result in a reasonable quantity of expected signal error. It could be expressed as the standard deviation of error; or as the maximum expected error; or the 95th percentile confidence error, or any variety of statistical quantities. The only qualification is that the signal error should describe an

error relative to the mean of the measured phenomenon over a long period of time at a stable loading condition. Some possible statistical descriptors, and their quantities, are shown in Table 6.5. The table is generated from data shown in Figure 6.2.11. The table shows the statistical properties of the 12 Fabry-Perot fiber optic strain gauges used on the three-span scale model.

The second step is to convert the signal error of the device into its corresponding error in the curvature measurement. This error is highly dependant on the method of obtaining the curvature; the constitutive and kinematic relationships will supply the equations that relate the measured quantity to curvature. If multiple devices are used to measure a single curvature state, their error will propagate through the equations used. If an averaging or line fitting technique is employed to obtain curvature from many measurements, then that process should be used to obtain the overall error of the curvature measurement. In this section, the example calculation is based on a single strain reading to obtain the beam curvature.

An alternate technique is to combine the first and second step. Acquire static data over time from all the devices used and calculate the curvature directly. The calculated curvature can then be characterized as a signal to obtain its error. Whichever technique is used, the curvature signal error obtained is used in the next step: it can also be called the curvature resolution.

The magnitudes of the curvature signal error is simply a scalar multiple of the unit curvature error (10^{-6} inch⁻¹) used to analyze the C2D method in previous sections. Those

sections showed that the principle of superposition can be applied to the displaced shapes generated by a single curvature reading. Using this, two techniques can be applied to generate the final expected error envelope for a system. The first technique uses the maximum expected error of all curvature measurements and the maximum unit deflection error function—sum of all unit deflections as individual curvature readings—per the structural system. The second technique involves using each measurement locations expected curvature error with its corresponding unit error deflected shape. The summation of each locations resulting deflection error contribution is the final expected error envelope for the system.

The first technique is appropriate in the case that each curvature measurement location has the same characteristic signal error. By multiplying the maximum unit deflection error function by the ratio of the curvature signal error (resolution) to unit curvature error, the maximum expected deflection error envelope is obtained. For the three-span small scale model, used as an example in this section, the maximum unit deflection error function is shown in Figure 6.3.9. Its maximum value is 0.007 inches; which occurs at the middle of the structure. Table 6.5 lists the curvature resolution for each measurement location. Each row is calculated based on the listed statistical property. The values in the table are based on the same 300 strain data points shown in Figure 6.2.11 and used to make Table 6.2. The unit of curvature in Table 6.5 is the same as the unit curvature error (10^{-6} inch⁻¹) used to generate the maximum unit deflection error function. Using the largest value of curvature resolution calculated by the maximum range statistical description (row 7 of Table 6.5), the maximum expected deflection error at the middle of

the continuous beam is $8.4436 \times (0.007 \text{ inches}) = 0.0591 \text{ inches}$. The maximum unit curvature error function is plotted as the heavy grey line in Figure 6.3.10.

The second technique applies each measurement's individual error deflection contribution to establish the total expected deflection error function. By multiplying the unit deflection error function, per measurement location, by the ratio of the curvature resolution to unit curvature error, at that location, the result is the expected deflection error envelope contribution of that curvature measurement. Summing all the resulting functions from each measurement location throughout the beam, the total expected deflection error function of the structural system is established. For the example structure, the curvature resolution is listed in Table 6.5; the unit deflection error functions are shown in Figure 6.3.6. The total deflection error function that results from using the maximum range curvature resolution descriptor (row 7 of Table 6.5) is shown in Figure 6.3.10. The unit deflection error functions for each curvature measurement are plotted in light gray. The total deflection error function has a smaller magnitude of error than the maximum expected error function as shown in the figure.

Table 6.5. Small Scale Three Span Beam Signal Error Characteristics Summary.

Statistical Description	Curvature Resolution ($10^{-6} \text{ inch}^{-1}$): Signal Noise Error per Statistical Description											
	Beam Axis X-ordinate for Curvature Reading (inches)											
	9.83	29.50	49.17	68.83	88.50	108.17	127.83	147.50	167.17	186.83	206.50	226.17
1) Standard Deviation	1.1521	1.2315	1.2462	1.0560	1.2179	1.5132	1.2438	1.2073	1.3656	1.3485	1.2556	1.4209
2) 2 x Std. Deviation	2.3041	2.4629	2.4924	2.1119	2.4359	3.0265	2.4877	2.4147	2.7312	2.6969	2.5113	2.8419
3) 4 x Std. Deviation	4.6082	4.9258	4.9848	4.2239	4.8718	6.0529	4.9753	4.8293	5.4625	5.3938	5.0226	5.6837
4) Average Deviation	0.9563	0.9558	0.9377	0.7875	1.0245	1.2523	0.9828	0.9663	1.1400	1.0508	1.0068	1.1952
5) 2nd & 3rd Quartile	1.2062	2.4125	2.4125	1.5078	1.2062	1.2062	2.4125	2.4125	1.2062	2.4125	1.5078	1.2062
6) 95% Confidence Interval	3.6187	4.8249	4.8249	4.2519	3.6187	6.0311	4.8249	3.6187	6.0311	4.8249	4.8249	6.0311
7) Maximum Range	6.0311	7.2374	7.2374	4.8249	7.2374	7.2374	8.4436	7.2374	7.2374	7.2374	7.2374	6.0311

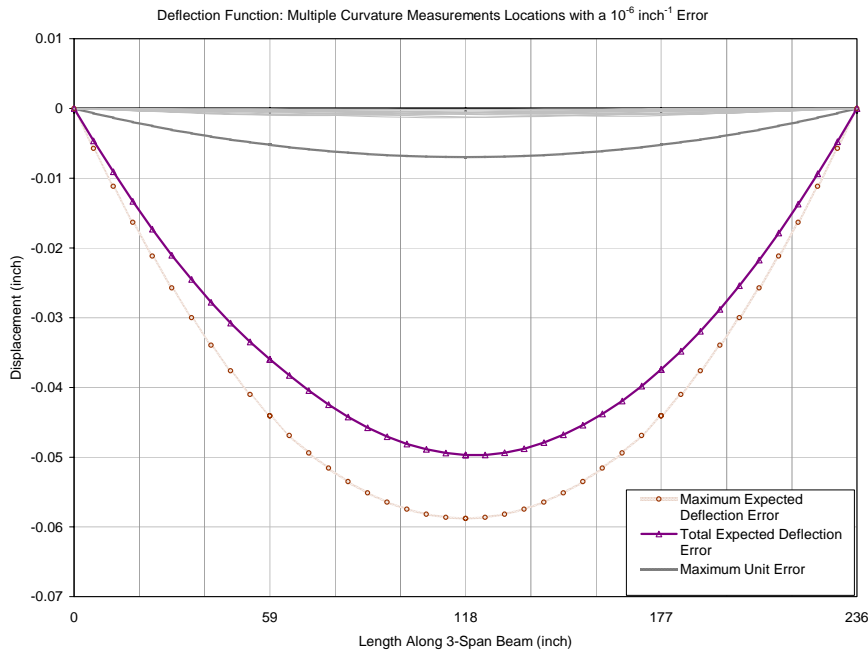


Figure 6.3.10. Expected Error Deflection Envelopes for the Small Scale Beam.

To verify that this is a reasonable method, the small scale three-span beam was also instrumented with LVDTs and fiber optic strain gauges. The deflected shapes generated by the LVDTs for one half cycle of oscillation are shown in Figure 6.3.11. The deflected shapes generated by the C2D method from the strain gauge data over the same period of time are shown in Figure 6.3.12. Figure 6.3.13 shows a comparison between the positive and negative maximum values of the two measurement techniques. In the figure, a third displaced shape is plotted for the C2D method result that generated the largest support displacement error. The internal supports are located at the 59 inch and 177 inch ordinate of the beam. In Figure 6.3.13, there are obvious differences in the deflected shape measure by the two systems; especially considering the relatively large support displacement discrepancies. Figure 6.3.14 shows these same plots bracketed by thin lines

that represent the total expected deflection error due to the signal noise characteristics of the fiber optic strain gauges used. While the error envelopes look too large to be useful, they do show that the LVDT displaced shapes fall within the estimated maximum error. The zero displacement at the interior supports also falls within the range of error for that C2D result as well. Figure 6.3.15 shows a time history of the deflection at the midpoint of the middle span of the structure. In the figure, the total expected deflection error is rarely reached. In the figure, the LVDT deflection is considered the true deflection so the error deflection limits are offset from that reference point. This figure shows that different statistical descriptors of the signal error will reasonably represent a majority of the data collected over a period of time. It is up to the user to choose an acceptable confidence interval. This process can be repeated on any C2D instrumentation scheme to help identify the resulting resolution of deflection.

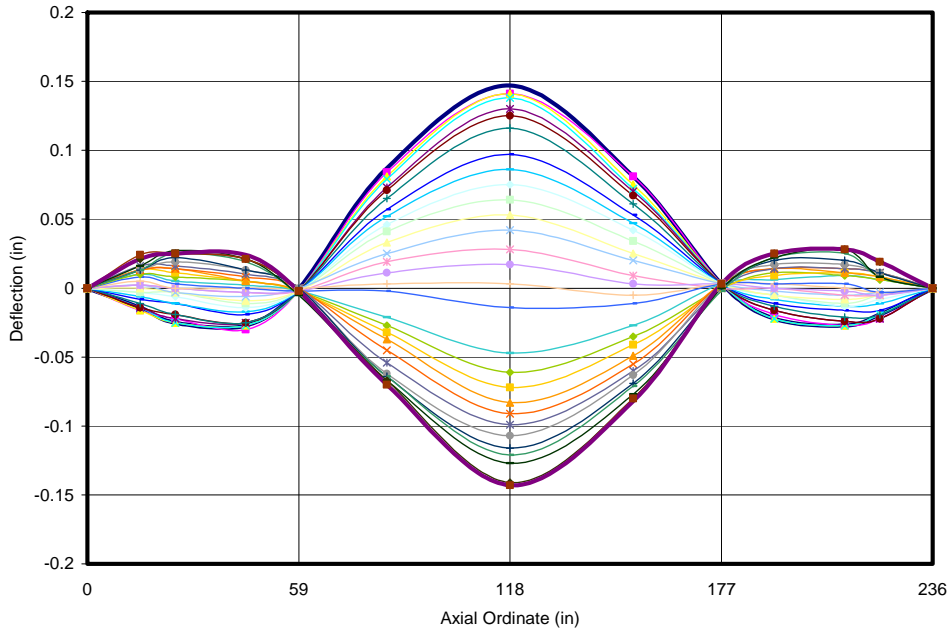


Figure 6.3.11. LVDT Deflected Shape Observations.

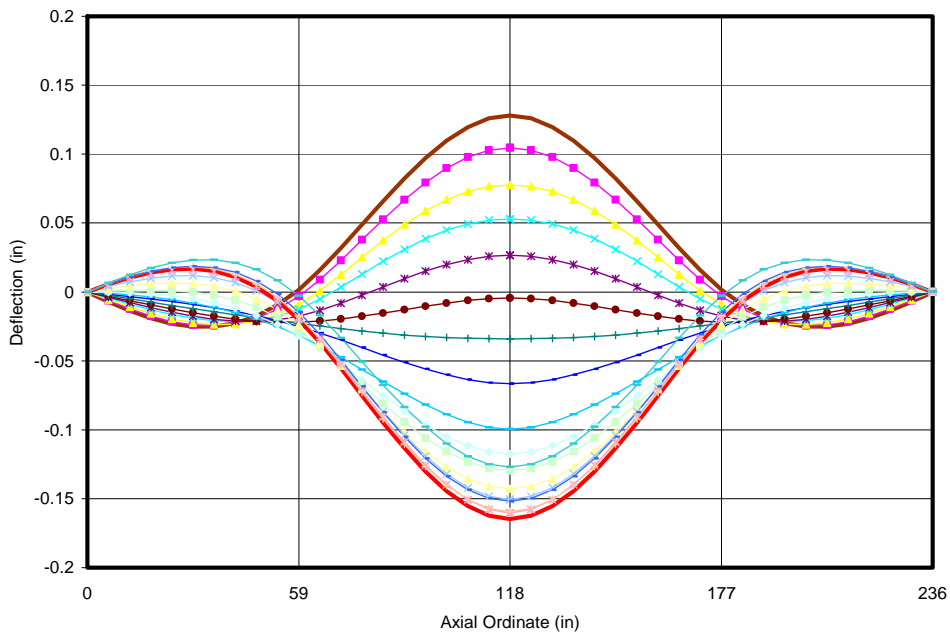


Figure 6.3.12. C2D Based Deflected Shape Observations.

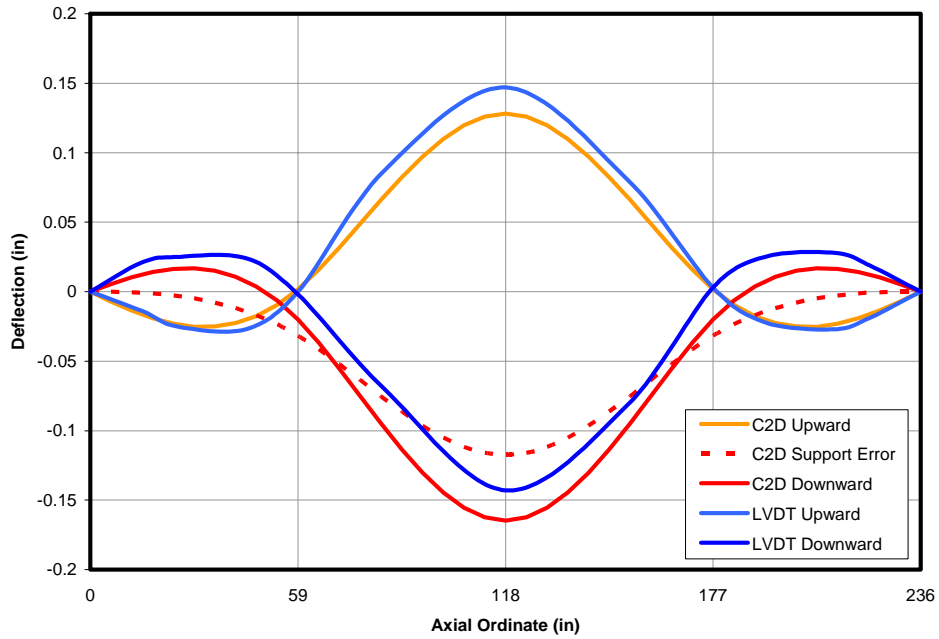


Figure 6.3.13. LVDT & C2D Maximum Measured Displacements.

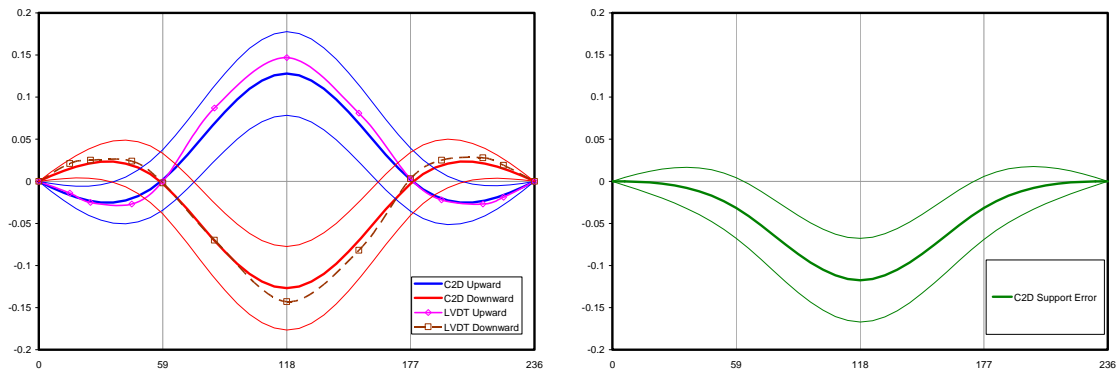


Figure 6.3.14. C2D Error Envelope Comparison with LVDT and Support Measurements.

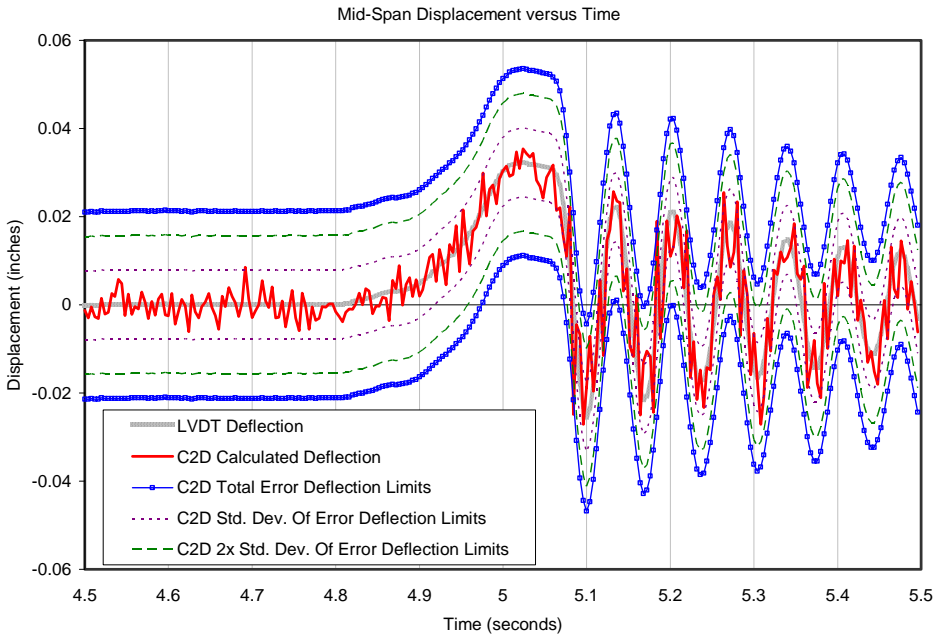


Figure 6.3.15. Comparison of Error Envelopes for Deflection at Location of an LVDT.

6.4 Comments on Error Reduction Methods for C2D Method

The errors noted in the previous sections can be mitigated to some extent by various methods. This section will highlight some possible ways to reduce the error that exists for the C2D method of determining beam deflection. Some methods discussed here include: post processing data averaging and adaptations to the C2D method discretization.

6.4.1 Post Processing Data Averaging

There are a lot of signal analysis techniques that can be utilized during a post processing regime. In structural testing, most of the useful data has been analyzed with post processing. A large hurdle to overcome in real-time structural health monitoring is to

perform all the calculations that convert the raw signal data into useful, structurally significant, quantities for real-time decision making. At this time, for the typical application, the C2D methodology is itself not likely usable for a true real-time structural health monitoring application; it is more appropriately used with a post-processing routine. Data averaging can easily be incorporated to improve the observations by the C2D method. A few data averaging techniques are applied for static measurements and for dynamic measurements in this section. The impact on the acquired data is discussed by use of selected examples.

6.4.1.1 Static Measurements

Data averaging can help to improve the analysis of a beam's deflection when there is a difference between the assumed boundary conditions and the real boundary conditions of the structure. In the case of the three-span small scale beam defined in chapter 5, the actual boundary conditions of the real structure effect the assumptions used to measure curvature as a result of axial loading that may or may not be considered in the idealized structure.

By averaging two or more strain readings at a particular curvature measurement location, the axial strain can be indicated. This may not directly eliminate error in the deflected shape; however, it may help to provide a clue as to other effects that may be causing strange results for the deflected shape. If only a single strain gauge were used to acquire data for the C2D method input, the axial strain will cause significant errors.

In another case, directly averaging curvature measurements, over time, eliminates noise from the individually obtained deflection results. For example, data was collected from the three-span small scale beam setup at a frequency of 100 Hz for 2.5 seconds at four different static loading conditions. Figure 6.4.1 shows the deflection calculated by the C2D method. The plot on the left is of the raw data—250 deflection curves for each load condition. The plot on the right results from averaging all 250 raw data points for each load condition. The averaged data clearly show the difference between the four load conditions; there is no guarantee that a single raw data point would reproduce such a clear representation.

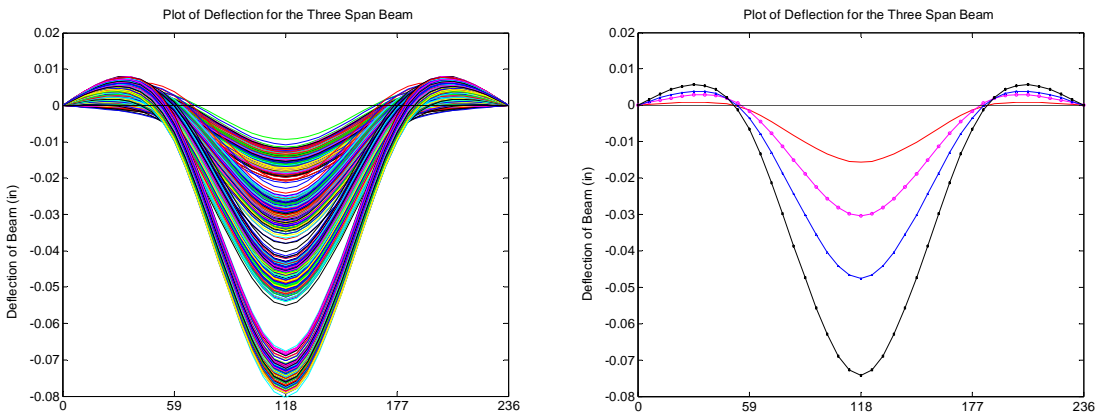


Figure 6.4.1. Before (Left) and After (Right) Averaging C2D Static Displacements.

6.4.1.2 Dynamic Measurements

During dynamic measurements, the luxury of averaging many data sets is not always possible. Depending on the structural system and measurement capabilities of the data

acquisition system, an optimum number of data points averaged can be determined. Sometimes, the averaging solution may include using a weighted averaging technique.

The simplest averaging technique for dynamic data is the use of a rectangular averaging window. The rectangular averaging window is defined such that an equal weight is applied to each of the data points used to calculate the final value. The averaging windows length is specified in terms of number of data points. Two triangular weighting functions are also tested.

6.4.1.2.1 Determined At a Single Location with an LVDT

An example of using the rectangular averaging windows with the C2D method is shown here for the deflection calculated at the location of a single LVDT measurement at the mid-span of a beam. To see the effect of different lengths of the averaging window, the deflection versus time was plotted for three cases. Four deflection data sets are compared in Figure 6.4.2: LVDT measurements; C2D calculated deflection based on raw data; C2D calculated deflection based on a rectangular window with four data points averaged; C2D calculated deflection based on a rectangular window with eight data points averaged.

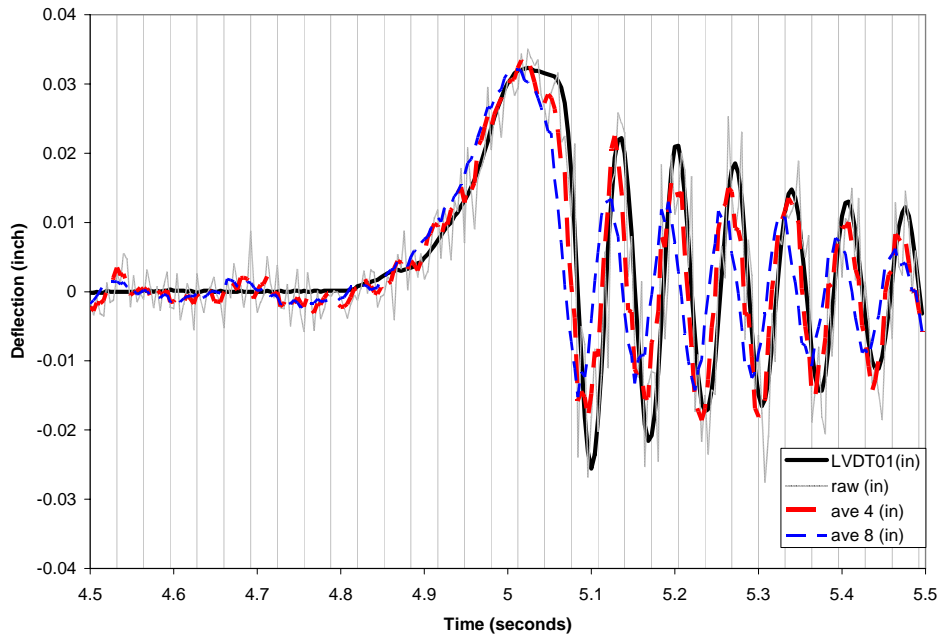


Figure 6.4.2. Rectangular Averaging Windows Effects on Deflection.

The LVDT plot provides a clean displacement signal; it will provide a consistent modal frequency and damping ratio calculation. Notice that the raw data does follow the LVDT deflection; however, it has a larger amount of noise and probably will not produce a consistent modal frequency or damping ratio. The C2D plot that is generated by an averaging window with a length of four data points follows the LVDT data more tightly than the noisy raw signal. It can be seen that the modal frequency and damping ratio can probably be extracted more consistently than from the raw data plot as well. The C2D plot that is generated by an averaging window with a length of eight data points is a smoother signal; however, the displacement peaks during the free vibration are clipped. The modal frequency can probably still be calculated, however, the clipping of the displacements will likely not produce the correct damping ratio.

To try to mitigate the clipping effect observed in the eight point rectangular averaging window case, triangular averaging windows were tried using the same four and eight data point lengths. For the four data point case, the weights applied from oldest to newest data point were 0.1, 0.2, 0.3, and 0.4. For the eight data point case, the weights applied from oldest to newest data point were $1/36$, $2/36$, $3/36$, $4/36$, $5/36$, $6/36$, $7/36$, and $8/36$. Figure 6.4.3, shows an improvement in the peak magnitude when using the eight point triangular averaging windows. There was no significant difference for the four point data averaging whether rectangular or triangular windows were used. The improvement for the eight point case might help to identify the damping ratio, however, in the figure this is likely only the case for the positive displacements during the free vibration. There is likely a best window length and weighting function to preserve as many structural properties as possible.

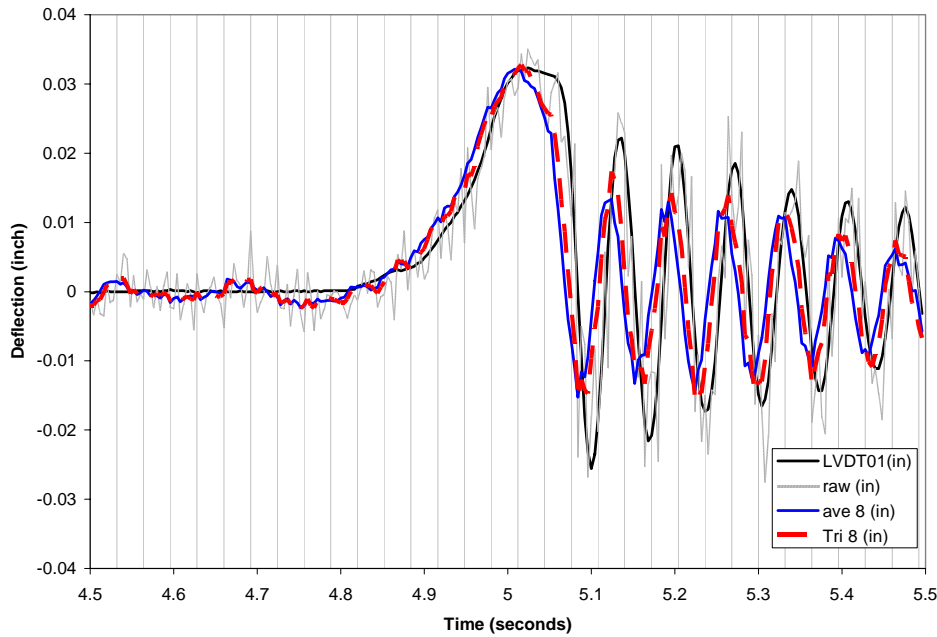


Figure 6.4.3. Triangular Averaging Windows Effects on Deflection.

6.4.1.2.2 Along Full Length of Beam

The raw data and two rectangular averaging windows generated the displacement versus time plots in Figure 6.4.4. The graphs on the left show the time domain results comparing raw data, four data points averaged, eight data points averaged—in order from top to bottom. The deformed shape becomes clearer as the number of averaged points increase. The mode shape is well defined within the free vibration as seen in the two alternate views of the eight point rectangular window result—right side of the figure. The averaging is effective as an easy low pass filter.

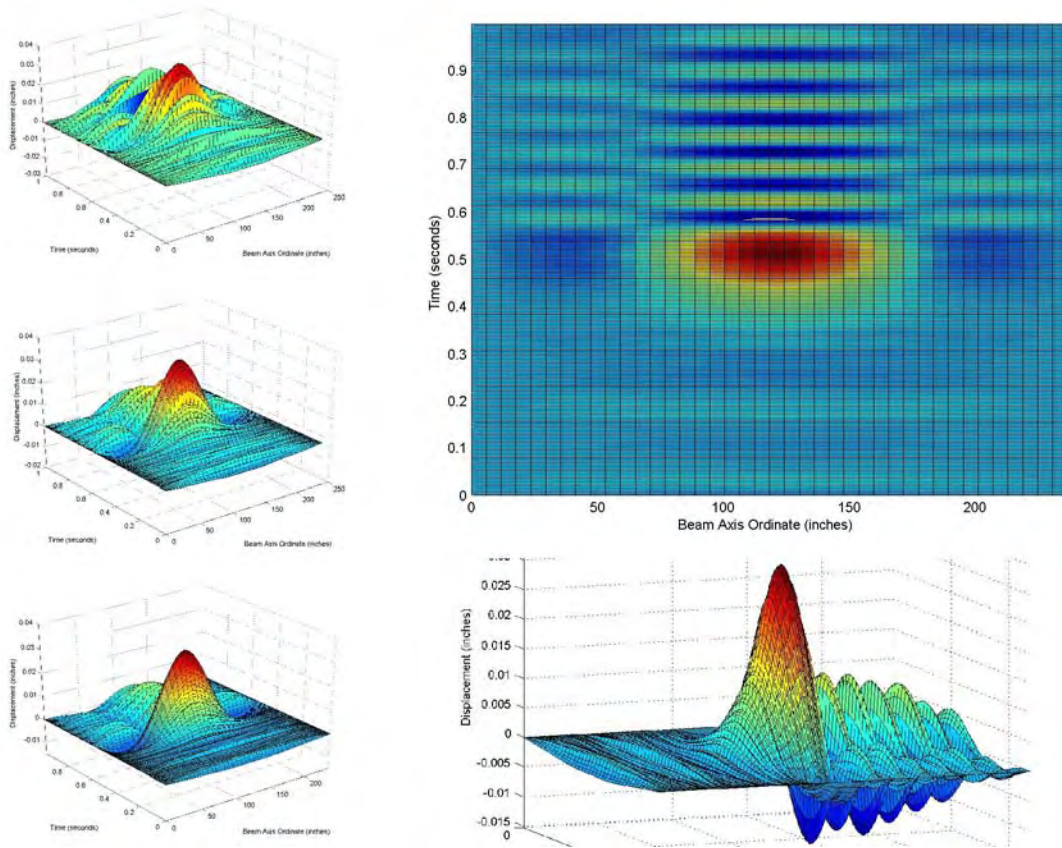


Figure 6.4.4. Comparison of Rectangular Averaging Windows for the Entire Beam.

6.4.2 C2D Method Adaptations

The following subsections highlight other techniques that can be applied as well. These adaptations have not yet been tried by the author, however, the error-inducing behavior observed during the sensitivity analysis preceding this section suggest that they may provide improvements to the system.

6.4.2.1 Number of Beam Sections

By changing the number of beam sections, there are more data points that are acquired that will help to match the curvature function. The problem associated with point loads applied within beam sections will be reduced in two ways. First, there will be more locations where the point load may occur such that it satisfies the exact solution—application at the ends of beam sections. Second, even if the point load falls within a beam section, the mismatched curvature diagram is only affected within that beam section. As the error propagates through the double integration, the error is applied to a shorter length of beam. The overall error will be reduced.

6.4.2.2 Alternate Curvature Estimate Implementations

The method shown in chapter 5 fits a second degree polynomial to three curvature readings. This implementation provides the exact solution for a beam element loaded with either a uniformly distributed load along the entire length of the beam element or discrete loads applied at the end of each beam element. When this is the case, and the error is small, the system works very well. Utilizing other functions that represent different loading conditions for beam elements will likely produce beneficial results.

6.4.2.3 Multiple Implementation Comparison

Another way to help identify loading conditions, and the proper displaced shapes, is to run several parallel alternate solutions and compare the results. For example, for the real data cases tested earlier in this chapter, it was common that the curvature diagram was not continuous. This is obviously possible since the solution described is a C^1 continuous

solution for displacement; however, in many cases, especially within the long span of a bridge structure, moments might not be applied between beam sections. The curvature diagram, or M/EI diagram, is C^0 continuous in this case. So it may be useful to compare a solution that requires inter-sectional curvature continuity—this can be done with a third degree polynomial curvature function assumption applied incrementally across all the beam sections.

6.5 Conclusions

The purpose of this chapter was to analyze how errors in indicated strain, or curvature measurements, affect the results of the C2D methodology for calculating the deflection of beams. Understanding the implications of the discussed topic toward a particular structural health monitoring program should help to better plan an instrumentation strategy. Modifications to the strategy can include transducer placement, transducer type, curvature estimate formulation, and data smoothing techniques. Currently we see, the signal noise and significant digits of measurement ultimately control the accuracy of the C2D methodology. As curvature measurements become more accurate and more stable, the method will perform better.

Greater accuracy in curvature measurement will help to minimize error in two ways. First, if accuracy of curvature is carried to enough significant digits for all measurements, the deviation of the estimated curvature function along the length will be reduced. This in turn will minimize the cumulative error induced through the integrated angle of rotation and subsequent displacement functions.

Second, loads within a beam element which do not conform to the exact solution that is best represented by a second degree polynomial curvature function will only generate significant error in the deflected shape within that element. All other elements that exist within that structure will provide a reasonably accurate deflected shape assuming sufficient accuracy of strain / curvature measurements.

Some possible strategies to reducing error through other alternate strategies are suggested for further study in section 6.4.2. Some of which include changing the number of beam sections, using a different function to estimate curvature in the beam section, and providing an algorithm that compares the results of several implementation strategies.

CHAPTER 7. SHM DURING HANAPEPE RIVER BRIDGE LOAD TESTING

7.1 Background

The Hanapepe Bridge is located in Hanapepe, Hawaii on the west side of the island of Kauai. The bridge runs east-west across the Hanapepe River as part of Highway 50 (Kaunuaulii Highway) between Waimea and Lihue. According to a previous inspection report performed by a consulting firm in 2001, the bridge is structurally deficient. While it may be rehabilitated, there is some question as to whether it should be replaced. To address concerns regarding this bridge, a load test was requested of Nagamine Okawa Engineers Inc. The instrumentation described here was designed to measure several indicators of structural health; static load-deflection behavior, dynamic traffic load deflection behavior, and loaded shear and flexural crack opening behavior. The instrumentation used include: LVDT-taut-wire baseline systems, LVDTs, crack gauges, and pin-support rotation monitoring devices. The intent of the structural health monitoring system is to provide additional information, beyond visual inspection, for engineers to validate/calibrate a computer model of the bridge to properly determine the present capacity of the bridge. Ultimately, the data is used to obtain a field calibrated analytical model that will be used to justify a recommendation on the status of the bridge—answering the question, “Is the bridge structurally deficient?”

7.2 Bridge SHM Instrumentation

The instrumentation was installed on one girder of the bridge—Girder G-3. This girder was selected because it was deemed to be the most deteriorated girder (of four) on the

bridge—by visual inspection. To save on cost most of the gauges were installed on the Lihue half of the bridge—the symmetry of the statically determinate structure helped in the decision as well. A selection of the largest existing cracks, which existed throughout the entire length of the beam, were instrumented with gauges.

All LVDTs, crack gauges and rotation sensors were monitored by a National Instruments data acquisition system running LabVIEW™ software. The data acquisition system was set to monitor each sensor at a frequency of 25 hertz during each static and dynamic loading condition. For the static load conditions, 25 successive readings were averaged for each sensor to minimize potential effects of gauge sensitivity to wind and other effects. Sensor calibration was adjusted for the electronic lead length required to connect each sensor to the data acquisition system (see sections 2.2.3 and 2.2.4 for process and calibration details). The data acquisition system was housed in a minivan located near the Lihue abutment (Figure 7.2.1). Near real-time deflection and crack gauge plots were prepared after each load condition to ensure no unexpected response had occurred.



Figure 7.2.1. Data Acquisition System.

A total of 19 electronic gauges were used to acquire data. Two LVDT-taut-wire baseline systems equipped with a total of six LVDTs were used to measure vertical deflection of the Lihue abutment span and the center span. An optical survey of the roadway surface was performed before all testing, during the heaviest loading patterns, and after static testing for comparison with the LVDT-taut-wire baseline systems. One LVDT was used to measure the horizontal displacement in the longitudinal direction at the Lihue abutment. Ten crack gauges were used to monitor crack mouth opening displacements on selected cracks during the load test. Two Wheatstone bridge based deflection gauges were used to monitor the rotation at the Lihue pier. These were used to verify/augment the two LVDT-taut-wire baseline systems—to ensure continuity of deflection measurements across the Lihue Pier.

The automated data acquisition system was powered by a Honda EU1000i generator—this generator is equipped with a low noise regulated true sine wave inverter and designed for use with sensitive computer equipment. A true sine wave backup power supply was also used to ensure no power loss to the data acquisition system in case the generator needed to be refueled.

7.2.1 Vertical Deflection

Vertical deflections of the Lihue abutment span and the center span were monitored by two LVDT-taut-wire baseline deflection monitoring systems. Chapter 3 has a full discussion on the design of such a system. The baseline system consists of a high-strength piano wire spanning the full length of the span to be monitored, and tensioned by means of a tensioning weight hanging over a pulley at the live end of the baseline system. Figure 7.2.2 shows a schematic of this system in both the center span and the Lihue abutment span. Figure 7.2.3, Figure 7.2.4, and Figure 7.2.5 show more details of the systems in each span.

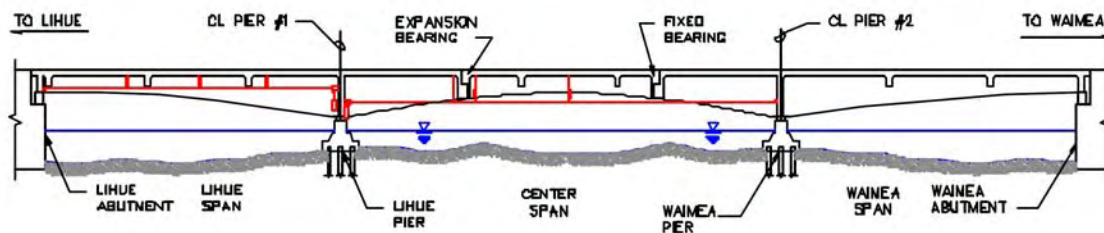


Figure 7.2.2. Elevation of Girder G-3 Showing LVDT-Taut-Wire Baseline Systems.

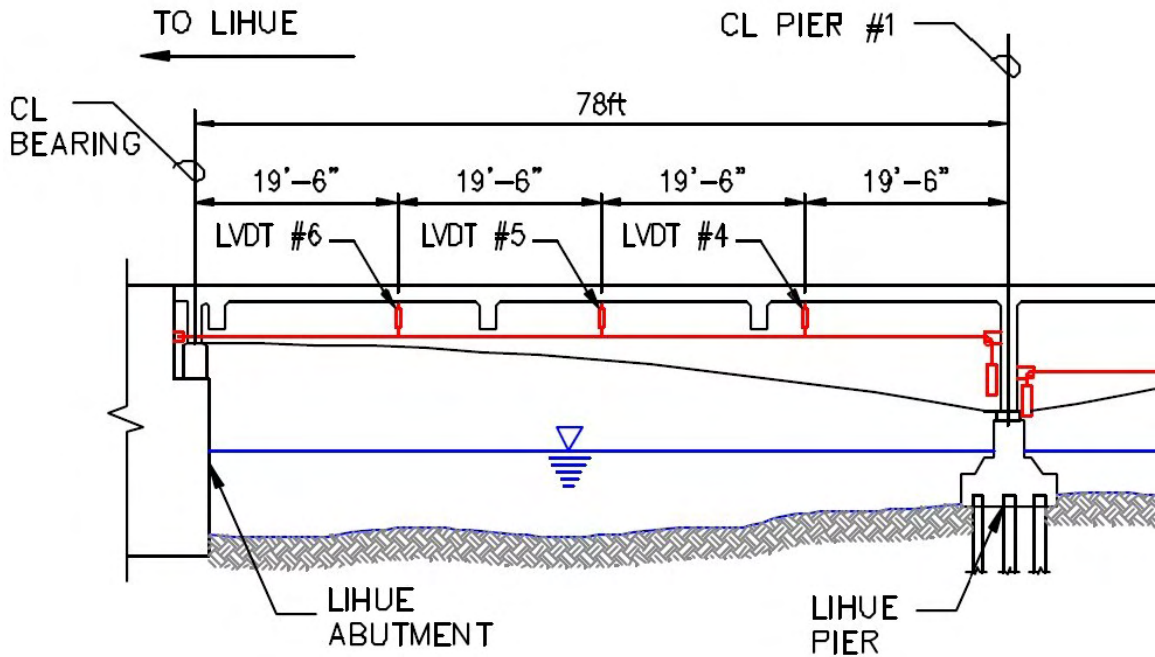


Figure 7.2.3. LVDT-Taut-Wire Baseline System in Lihue Span.

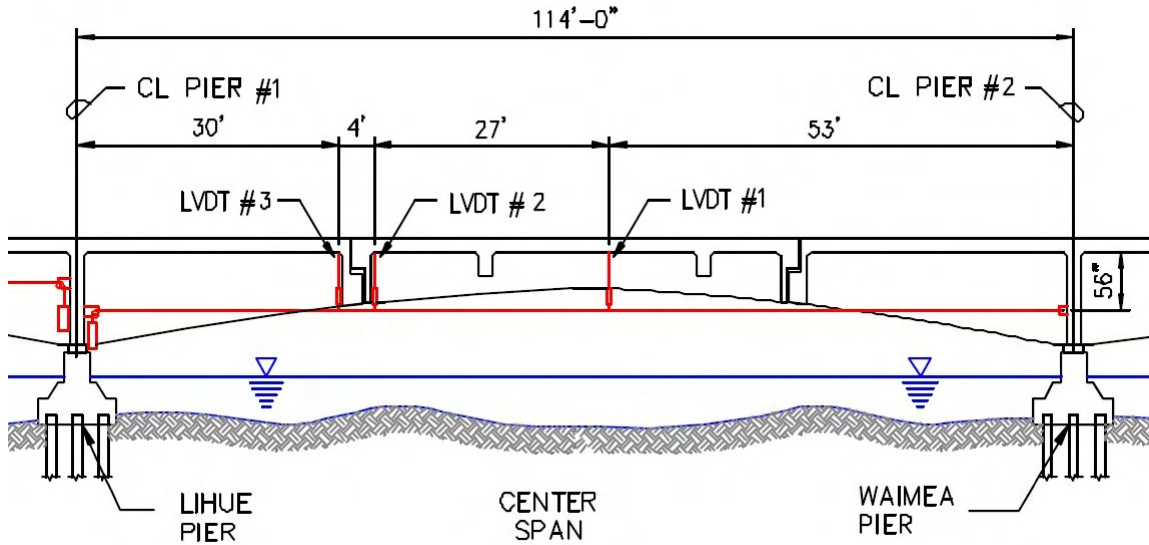


Figure 7.2.4. LVDT-Taut-Wire Baseline System in Center Span.

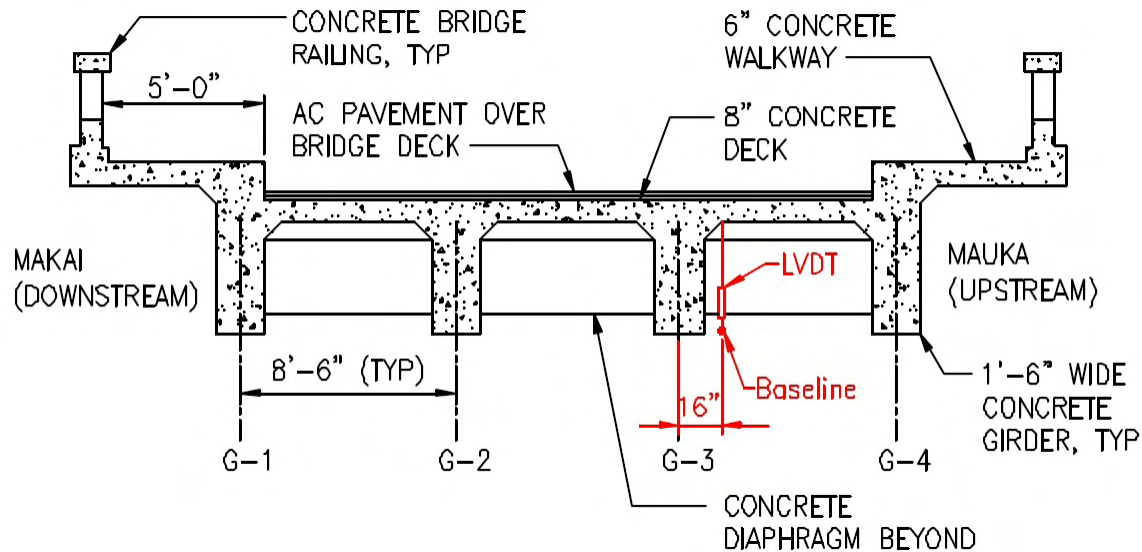


Figure 7.2.5. Bridge Cross-Section Showing Baseline System Location.

For this application, a #20 piano wire with a nominal diameter of 0.045 inch (1.14 mm) and break strength of 450 ksi (3.10 GPa) was used. The dead end of the wire was attached to one end of the span by means of a steel bracket (Figure 7.2.6). The other end of the wire passed over a six inch (152 mm) diameter pulley and supported a 205 lb (912 N) load (Figure 7.2.6) to maintain a stable catenary with sufficient stiffness for the taut-wire spans. The center span is 114 feet (35.7 m); the abutment spans are 78 feet (23.8 m). Six LVDTs were located at various points along each instrumented span to monitor the movement of the bridge deck relative to the baseline (Figure 7.2.3 and Figure 7.2.4 above). The LVDT coil housings are suspended from an all thread rod and anchor bolt in the soffit of the deck slab, while the LVDT cores are attached to the piano wire as shown in Figure 7.2.7. Any movement of the bridge deck, adjacent to girder G-3, relative to the reference baseline is measured by the LVDTs.

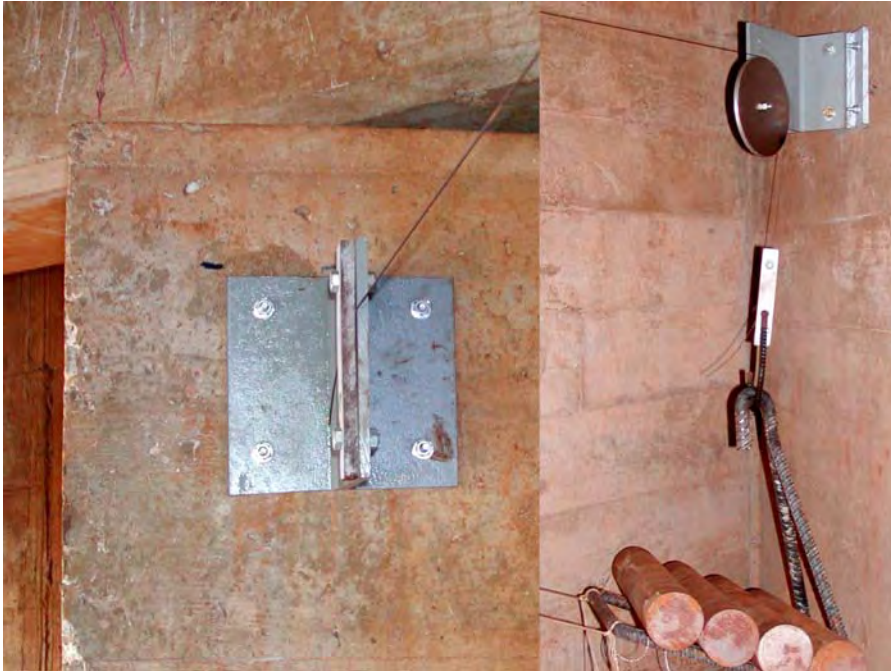


Figure 7.2.6. Taut-Wire Baseline Dead (Left) and Live (Right) End Supports.

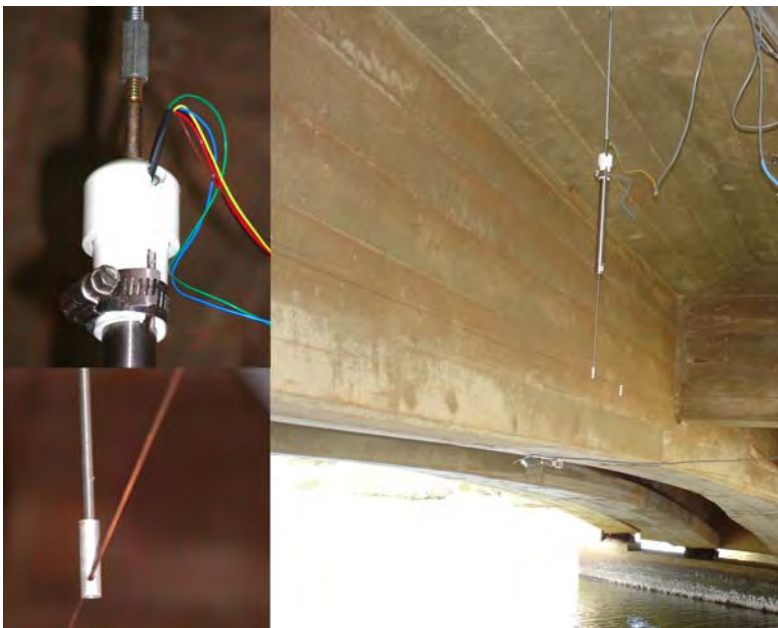


Figure 7.2.7. LVDT-Taut-Wire Baseline LVDT Support Details.

7.2.2 *Horizontal Deflection*

A single LVDT was installed to monitor horizontal movement between the end of bridge girder G-3 and the Lihue abutment (Figure 7.2.8). The vertical face of the web appeared to be rubbing against the shear block. This LVDT was installed to verify the rocker bearings were not seized and able were able to perform as designed despite the apparent contact between the shear block and the girder.



Figure 7.2.8. Horizontal LVDT Measuring Deflection at Lihue Rocker Bearing.

7.2.3 *Crack Mouth Opening Displacement*

Electronic crack gauges were installed at 10 locations to measure changes in the width of existing shear and flexural cracks in girder G-3. These gauge locations are shown in

Figure 7.2.9 through Figure 7.2.12. A number of these gauges were located close to previously installed long-term optical crack monitor stations, see Figure 7.2.13.

Crack gauges 1, 2, 6, and 7 are located on shear cracks in the cantilever girders supporting either end of the drop-in section of the center span. Crack gauge 3 is located on a shear crack in the drop-in section. Crack gauges 4 and 5 are located over flexural cracks at midspan of the center span drop-in section. Crack gauges 8 and 9 are on shear cracks in the Lihue abutment span. Crack gauge 10 is on the soffit of girder G-3 over a flexural crack in the Lihue span.

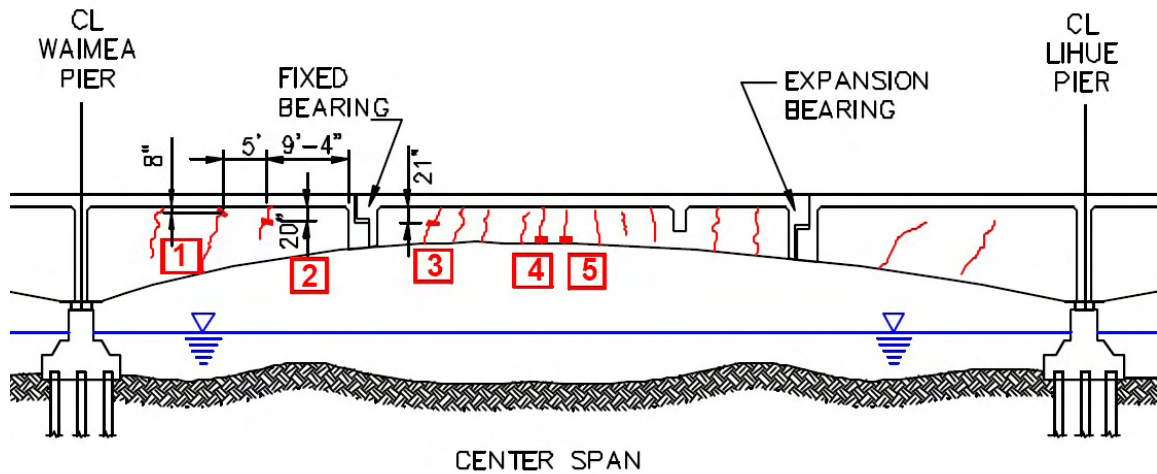


Figure 7.2.9. Crack Gauge on Downstream Elevation of Center Span.

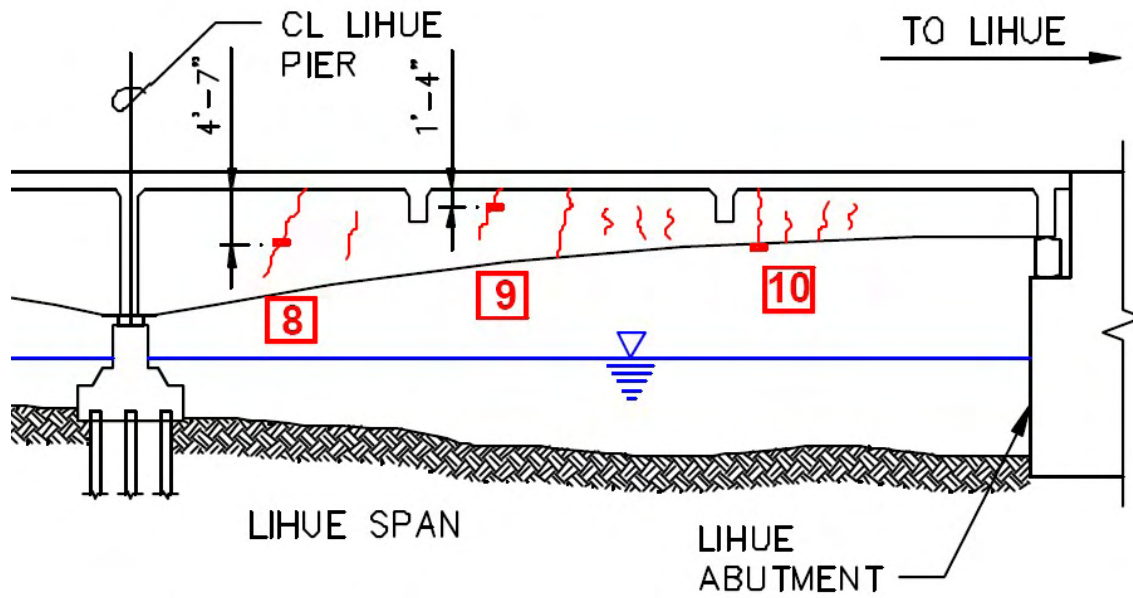


Figure 7.2.10. Crack Gauges on Downstream Elevation of Lihue Span.

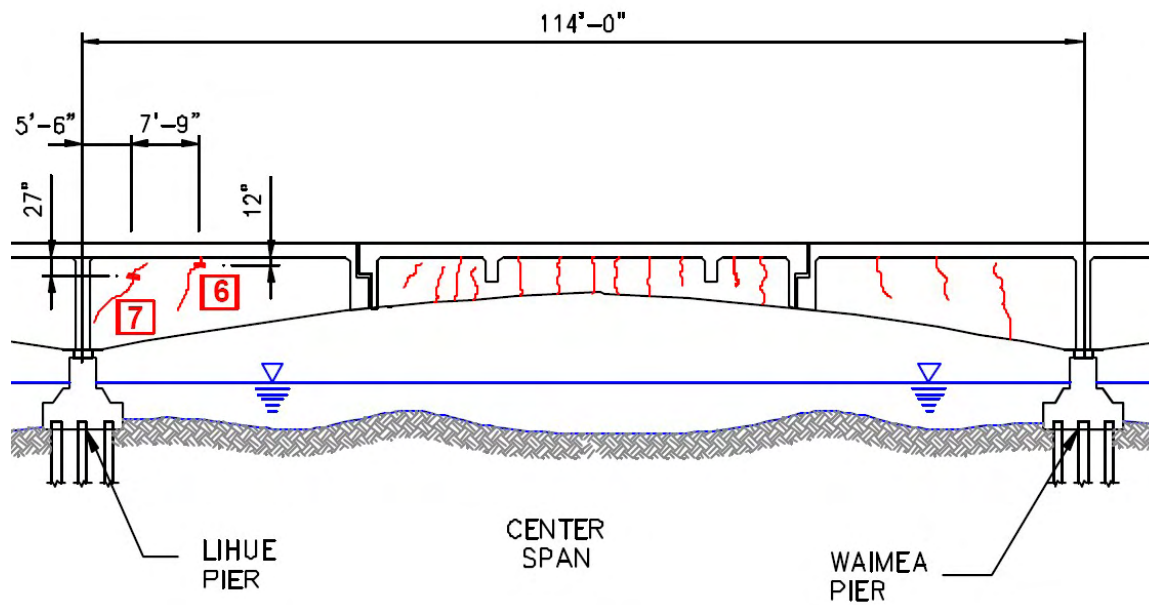


Figure 7.2.11. Crack Gauges on Upstream Elevation of Center Span.

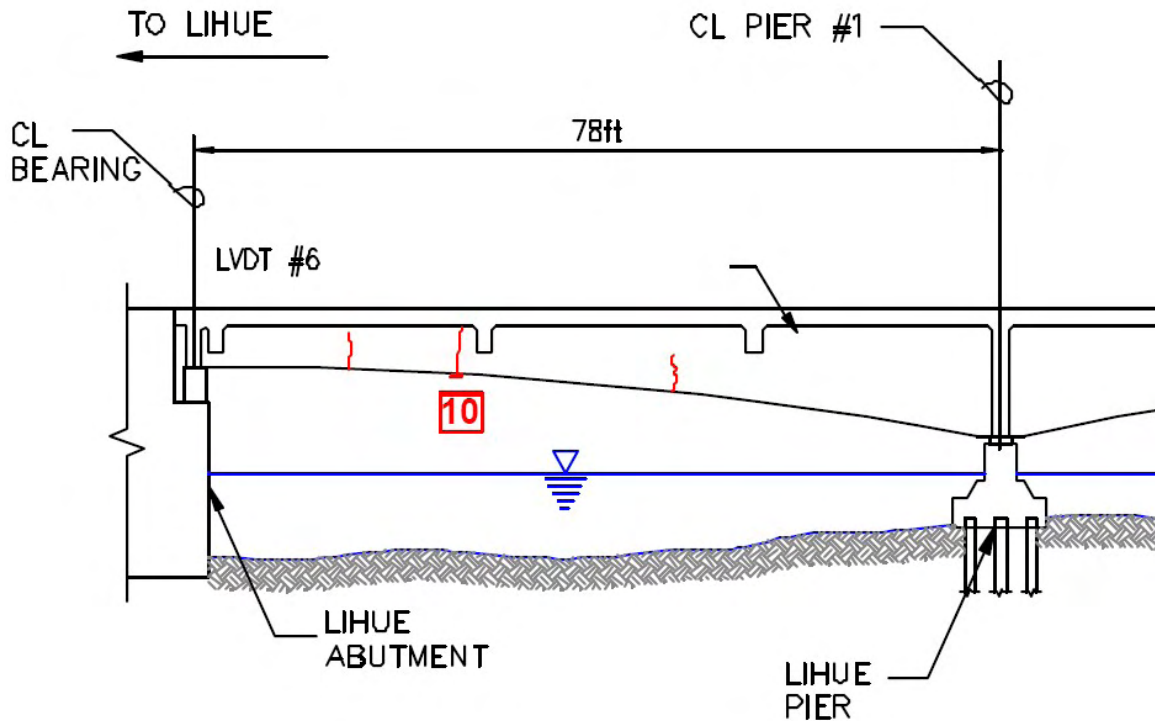


Figure 7.2.12. Crack Gauges on Upstream Elevation of Lihue Span.

Figure 7.2.13 and Figure 7.2.14 show the typical installation of the electronic crack gauges. The crack gauges were fabricated specifically for this project. Each gauge consisted of a C-shaped aluminum plate instrumented with electrical resistance strain gauges and calibrated to accurately measure changes in the gauge opening (See Chapter 4 for design details). Mounting tabs were epoxied to either side of the crack to be monitored, and the crack gauge installed as shown in Figure 7.2.14. Notice the strain relief screw and washer used to eliminate the influence of cable movement. The aluminum tabs were spaced at 0.125 inches (3.18 mm) by using a machined spacer bar—this also insured that they were installed parallel. The gauges clip onto the tabs such that

they will measure the crack closing as well as opening—they maintain their contact with the aluminum tabs for any crack mouth opening displacement. The grooves milled into the outside ends of the tabs are cut to align and hold secure the sharpened edge of the clip gauge—ensuring a true pin support at the gauge to aluminum tab interface.

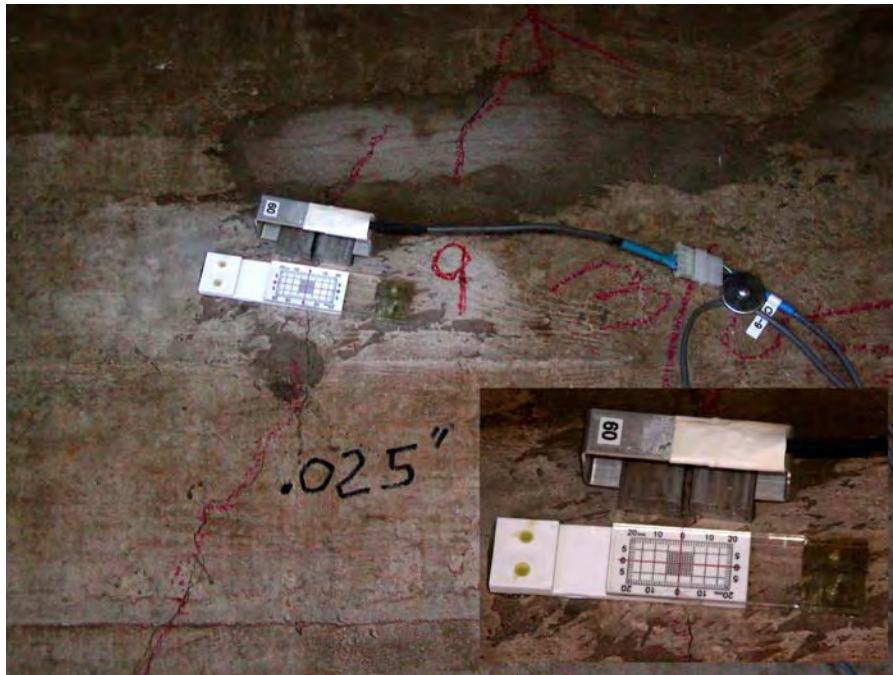


Figure 7.2.13. Crack Gauge 9 Adjacent to Visual Crack Monitor 3.

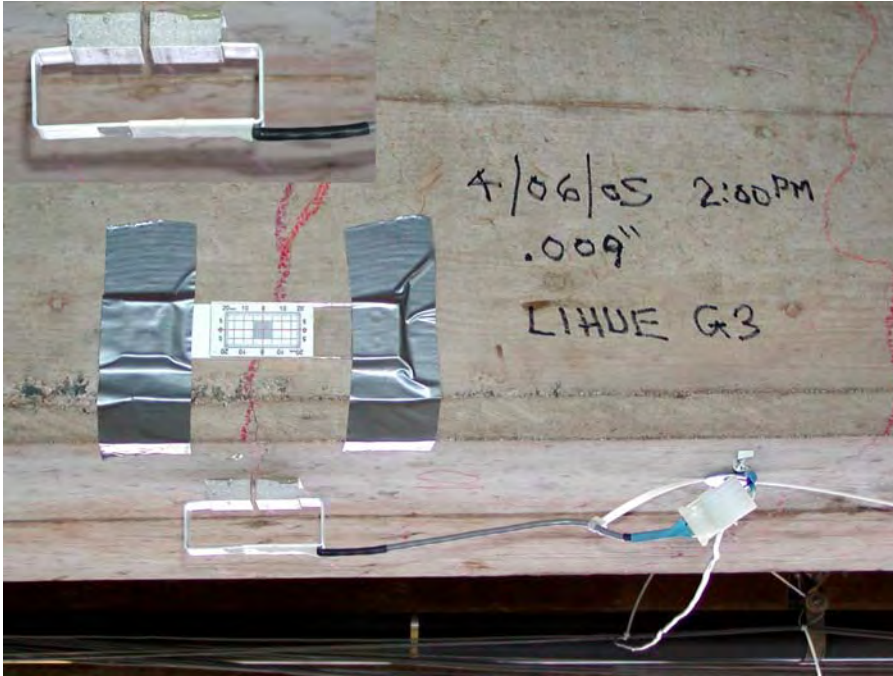


Figure 7.2.14. Typical Crack Gauge (10) on Mounting Tabs.

Table 7.1 gives details related to each crack gauge, including location, crack type, adjacent crack monitor number, and original estimated crack width (based on prior visual inspection). Reference Figure A7.2.17 through Figure A7.2.25 in the Appendix—photos of all the installed crack gauges.

Table 7.1. Crack Gauge Details.

Gauge No.	Location	Crack Type	Crack monitor	Crack Width	Figure
1	Waimea Pier cantilever	Shear	19	0.025"	Figure A7.2.17
2	Waimea Pier cantilever	Shear	-	-	Figure A7.2.17
3	Center span drop-in	Shear	11	0.025"	Figure A7.2.18
4	Center span drop-in	Flexure	12	0.013"	Figure A7.2.19
5	Center span drop-in	Flexure	13	0.016"	Figure A7.2.20
6	Lihue Pier cantilever	Shear	-	-	Figure A7.2.21
7	Lihue Pier cantilever	Shear	-	-	Figure A7.2.22
8	Lihue Abutment span	Shear	2	0.025"	Figure A7.2.23
9	Lihue Abutment span	Shear	3	0.025"	Figure A7.2.24
10	Lihue Abutment span	Flexure	4	0.009"	Figure A7.2.25

7.2.4 Rotation at Lihue Pier Support

Two custom-designed high-resolution displacement sensors were fabricated to monitor the rotation of girder G-3 over the Lihue pier. See chapter 4 for design details. The sensors were attached to steel brackets on either side of the bearing as shown in Figure 7.2.15 and Figure 7.2.16. The measured rotation was used to confirm the slope of the deflected shape as measured by the baseline systems on either side of the Lihue pier.



Figure 7.2.15. Rotation Monitoring Gauge (1) on Waimea Side of Lihue Pier Bearing.



Figure 7.2.16. Rotation Monitoring Gauge (2) on Lihue Side of Lihue Pier Bearing.

7.3 Data Acquisition and Processing

7.3.1 Optical Survey

In order to verify the two LVDT-Taut-Wire baseline deflection systems, optical surveys of the bridge roadway were performed during each of the heaviest loading conditions. The heaviest load series was anticipated to have deflections of an order that could be measured by optical survey. The smallest recordable increment of displacement for the theodolite and rod used is 0.06 inches (1.52 mm). The survey points are shown in Figure 7.3.1. Survey points G1 through G6 are located over girder G-3, at the same locations as LVDTs 1 to 6 on the baseline systems. Survey points C1 through C6 are located on the centerline of the roadway corresponding to G1 through G6, but adjusting for the 45° bridge skew. Survey points GS and CS are located over the Lihue Pier to measure any settlement of the pier during the load test.

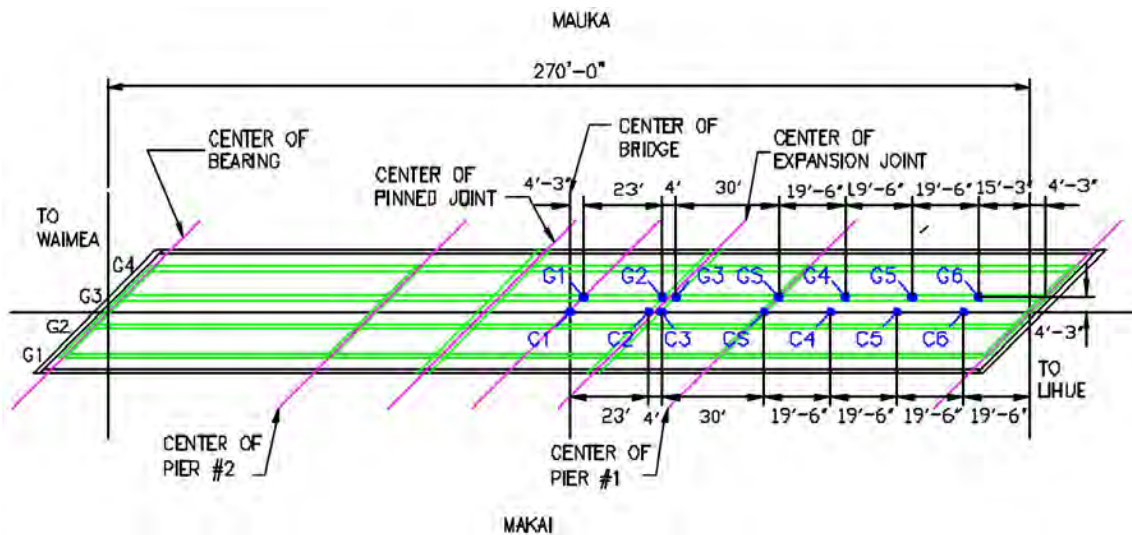


Figure 7.3.1. Optical Survey Points.

7.3.2 *Temperature Effects*

The load test started at about 12:00 AM and ended at 3:30 AM. During this time, the bridge roadway was cooling down, affecting the deflected shape of the bridge. The final deflected shape after removal of the truck loads differed from the initial deflected shape as shown in Figure 7.3.2. Although no thermal measurements or thermal analysis was performed on the bridge, the likely thermal effects can be inferred from the H3 North Halawa Valley Viaduct records. Numerous thermocouples were embedded in the NHVV during construction, and monitored for 10 years (Figure 7.3.3 and Figure 7.3.4). A typical daily temperature variation at the top of the roadway (sensor 14) and lower in the cross-section (sensor 21) shows that the thermal changes are limited to the top surface of the superstructure.

During the 12:00 AM to 3:30 AM time period, the thermal variation at all sensors in the NHVV was approximately linear (Figure 7.3.3). Linear interpolation was therefore used to adjust the Hanapepe Bridge load test results based on the difference between the original deflected shape and the final deflected shape.

Figure 7.3.2 shows the thermal adjustment based on initial and final zero deflection measurements. The initial deflection measurements are all set to zero before any truck load was applied to the bridge. These readings were taken at 12:00 AM. The final readings taken after all truck load tests had been performed, shows that the bridge deflection has changed during the load test due to cooling of the roadway surface, as previously observed on the H3 NHVV. As the top surface cools, the bridge forms a

concave up shape as shown by the final zero readings taken at 3:30 AM. Adjusting the final readings for the temperature effects produces a compensated final zero deflection that agrees exactly with the initial zero readings. This same adjustment was then made to all load test deflection measurements based on a linear time interpolation between initial and final zero readings. Flexural crack gauge readings showed crack closing behavior during this time period as well—the readings were also corrected for this behavior as well.

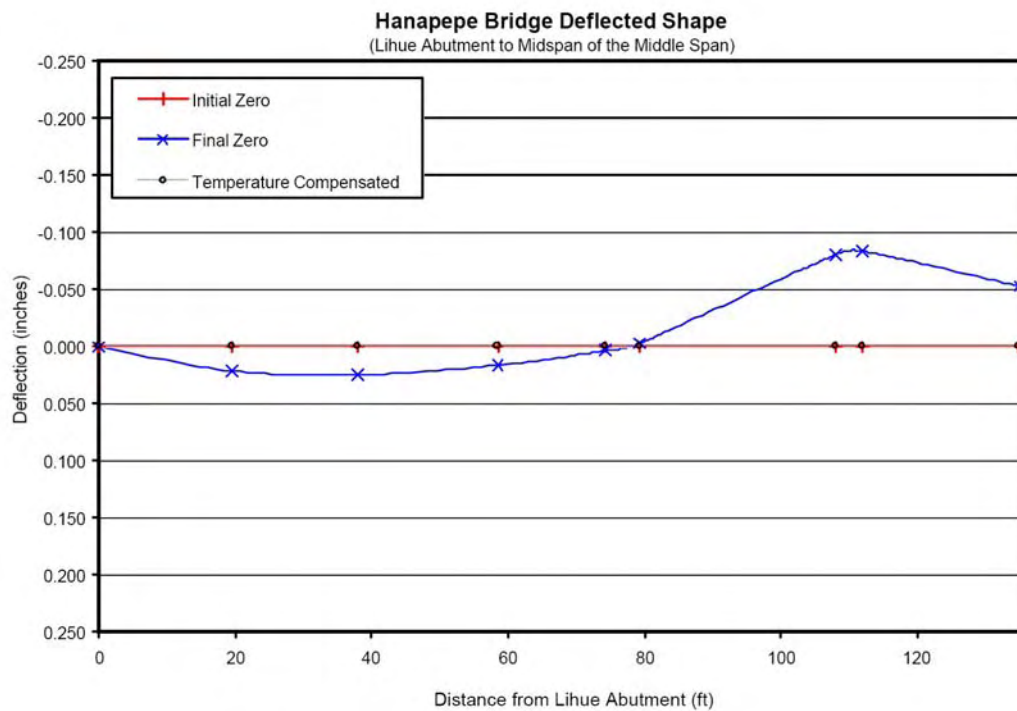


Figure 7.3.2. Thermal Compensation of Hanapepe River Bridge.

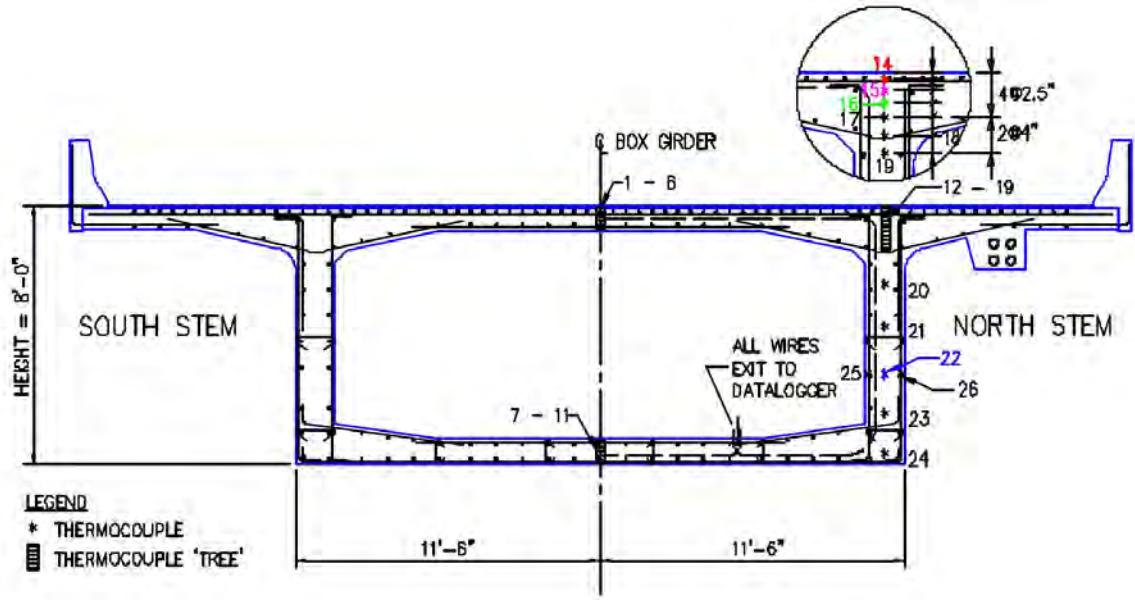


Figure 7.3.3. Thermocouple Locations on H3 North Halawa Valley Viaduct [Robertson & Ingham 1999].

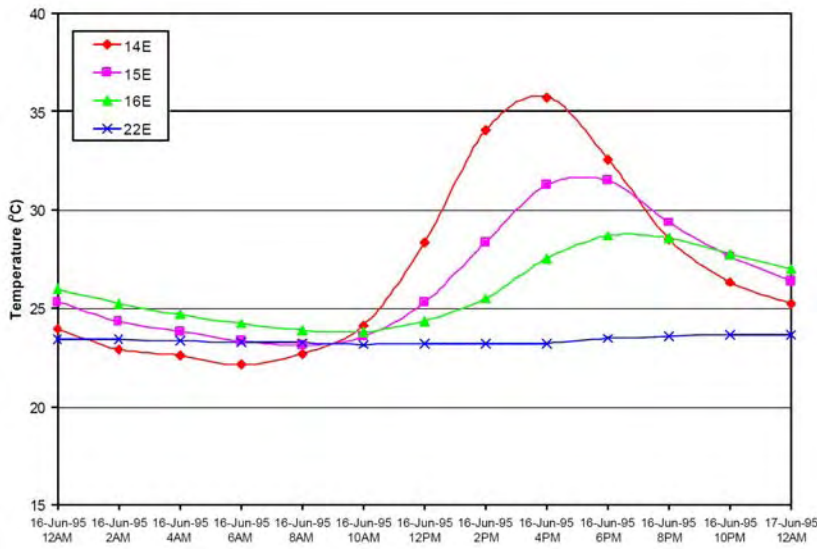


Figure 7.3.4. H3 North Halawa Valley Viaduct Daily Temperature Variation [Robertson & Ingham 1999].

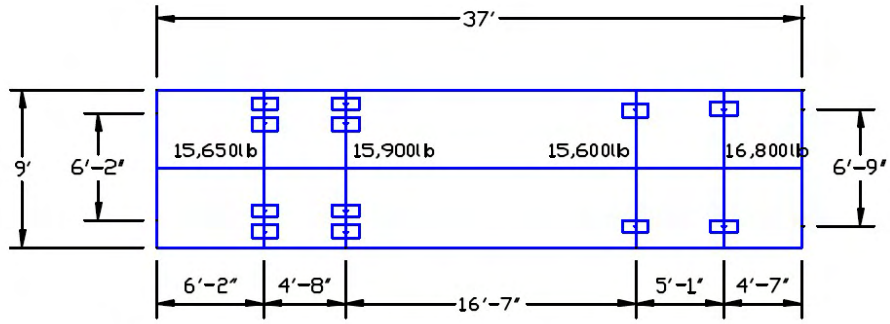
7.4 Load Test Program

The purpose of the load test was to determine the load ratings of the bridge and evaluate its short term performance in terms of service loads. This test program is not a proof load test. The load rating is instead evaluated through observing the elastic behavior of the bridge to assist in calibrating a computer model.

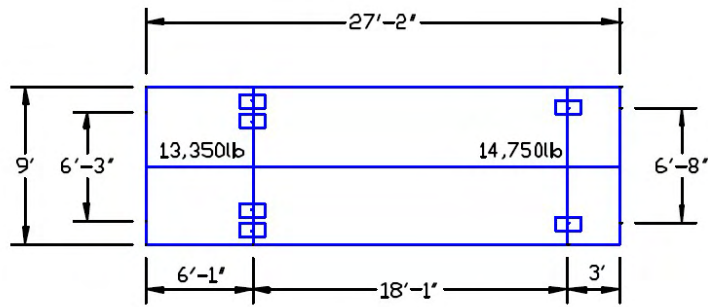
The load used includes different configurations of three trucks of varying weight as described in section 7.4.1. The bridge is on the main thoroughfare connecting Lihue and Waimea—the only route for heavy truck traffic. During the nighttime testing, all light vehicle traffic was diverted; any heavy traffic was allowed to pass.

7.4.1 *Truck Loads*

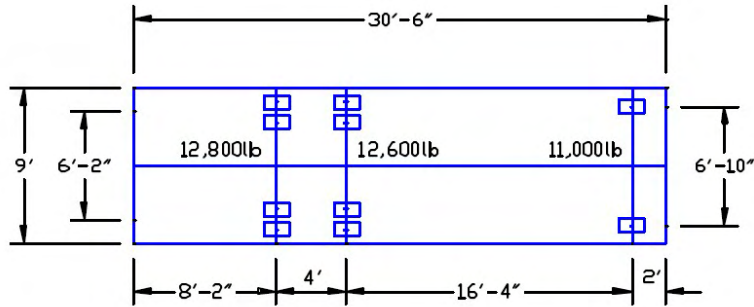
All truck axle loads were measured using a calibrated load scale prior to testing. Each of the three truck's dimensions and axle loads are shown in Figure 7.4.1. Truck 1 is the HDOT's "reach-all" truck (2003 Aspen Ariels Model UB60). Truck 2 is an HDOT boom truck while Truck 3 is a rented boom-truck.



TRUCK 1 - 63,950 lb



TRUCK 2 - 28,100 lb



TRUCK 3 - 36,400 lb

Figure 7.4.1. Trucks Loads and Dimensions.

7.4.2 *Static Loading*

The static load test involved 6 load series as described in Table 7.2. For each load series, a selected truck pattern was applied at pre-determined locations on the bridge. Four pre-determined loading locations were designated as L1 through L4. L1 was at the critical loading location on the Lihue abutment span, located 30 feet from the Lihue abutment support bearing. L2 was at the pinned joint in the center span. L3 was such that the rear wheels of truck 1 were centered over the pinned joint. L4 was at the midspan on the center span. All load series used loading locations L1, L2 and L4. Loading location L3 was only used for the heaviest load series, LS6.

The results for a particular truck loading condition are referred to using both the load series and load location. For example, during load series LS6, when the truck load was centered over midspan of the center span (load location 4), the test is referred to as LS6-L4. Figure 7.4.2 shows the truck loads in place for LS6-L3 during the load test. Graphical representations of all truck load conditions are given in the Appendix—Figure A7.4.3 through Figure A7.4.21. After completing all static loading cases, the trucks were removed from the bridge to record the final unloaded condition.

Table 7.2. Truck Load Series.

Load Series	Truck pattern	Load Locations	Graphic
LS1	Trucks 2 & 3 side by side	L1, L2 and L4	Figures A7.4.3, 4, 5
LS2	Trucks 1 & 2 side by side with 1 in the upstream lane	L1, L2 and L4	Figures A7.4.6, 7, 8
LS3	Trucks 1 & 2 side by side with 1 in the downstream lane	L1, L2 and L4	Figures A7.4.9, 10, 11
LS4	Truck 1 in the upstream lane	L1, L2 and L4	Figures A7.4.12, 13, 14
LS5	Truck 1 in the downstream lane	L1, L2 and L4	Figures A7.4.15, 16, 17
LS6	Truck 1 in downstream lane and trucks 2 & 3 in upstream lane	L1, L2, L3 and L4	Figures A7.4.18, 19, 20, 21



Figure 7.4.2. Truck Load During Load Series 6, Location 3 (LS6-L3).

7.4.3 *Dynamic Loading*

A series of four dynamic tests was then performed using only Truck 1. The first two tests involved driving Truck 1 across the bridge along the centerline of the roadway at 25 mph in each direction. The first pass was traveling towards Lihue (D1) while the second was traveling towards Waimea (D2). The third and fourth dynamic tests were the same as D1 and D2 except that the truck brakes were applied as the truck front wheels passed over the Lihue Pier. Dynamic test D3 was the braking test with the truck traveling towards Lihue, while D4 was the braking test with the truck traveling towards Waimea. These dynamic tests were performed to study the impact effect of a truck traveling at speed, and to monitor any horizontal movement of the bridge during heavy braking.

7.5 Load Test Results

The data acquired during 19 static load cases and 4 dynamic load cases helps us to understand the current performance of the Hanapepe River Bridge. Please note that all static load cases were adjusted for the structural deflection due to thermal cooling during the test period.

7.5.1 *Vertical Deflections*

7.5.1.1 Load Series 1

Figure 7.5.1 shows the deflected shapes recorded by the LVDT-Taut-Wire baseline systems during the three load conditions (L1, L2 and L4) of Load Series 1. Recall that Load Series 1 consisted of Trucks 2 and 3 side-by-side on the bridge roadway (Table

7.2). Note that these deflected shapes have all been adjusted for thermal effects as described in Section 7.3.2.

Under LS1-L1, when the truck load is at the critical section on the abutment span, the abutment span deflects downwards, as expected, while the hinge in the center span deflects upwards. The drop-in section of the center span is unloaded, and therefore remains a straight line segment between the two pinned end conditions. The pinned condition at the hinge is clearly evident from the kink in the deflected shape.

Under LS1-L2, when the truck load is located over the hinge in the center span, the hinge deflects downwards, while the abutment span deflects upwards, as would be expected. The drop-in section at the middle of the center span remains unloaded, and is therefore still a straight line between the pinned ends.

Finally, under LS1-L4, when the truck load is located at mid-span of the center span, the hinge deflection remains approximately the same as for LS1-L2, while the abutment span deflection decreases slightly. The drop-in section at the middle of the center span now shows a deflected shape similar to a simply supported beam, as would be expected.

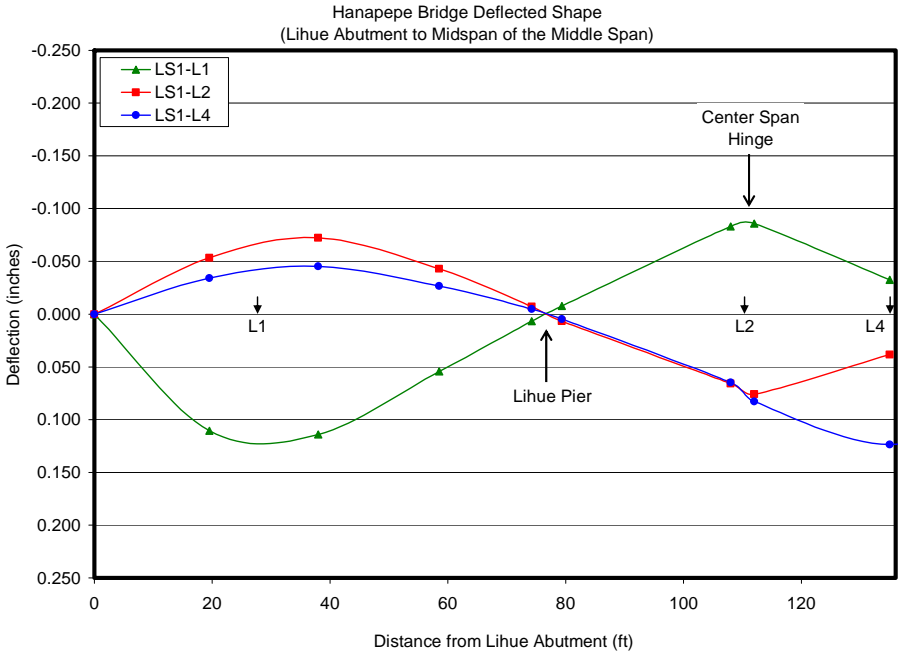


Figure 7.5.1. Load Series 1 Deflected Shape of Lihue Half of Bridge.

7.5.1.2 Load Series 2 and 3

Figure 7.5.2 shows the deflected shapes recorded by the baseline systems during each load condition (L1, L2 and L4) of Load Series 2 and 3. Load Series 2 consisted of Trucks 1 and 2 side-by-side on the bridge roadway with Truck 1 (the larger load) in the upstream lane (Table 7.2). In Load Series 3, the trucks are reversed so the heavier truck is in the downstream lane. All deflected shapes are similar to those observed for Load Series 1, but the measured deflections are slightly larger since the combined truck load is greater for Load Series 2 and 3.

The LVDT-Taut-Wire baseline system records slightly larger deflections under Load Series 2 than for Load Series 3 because the larger truck load (Truck 1) is more directly over Girder G-3 and the baseline system for Load Series 2.

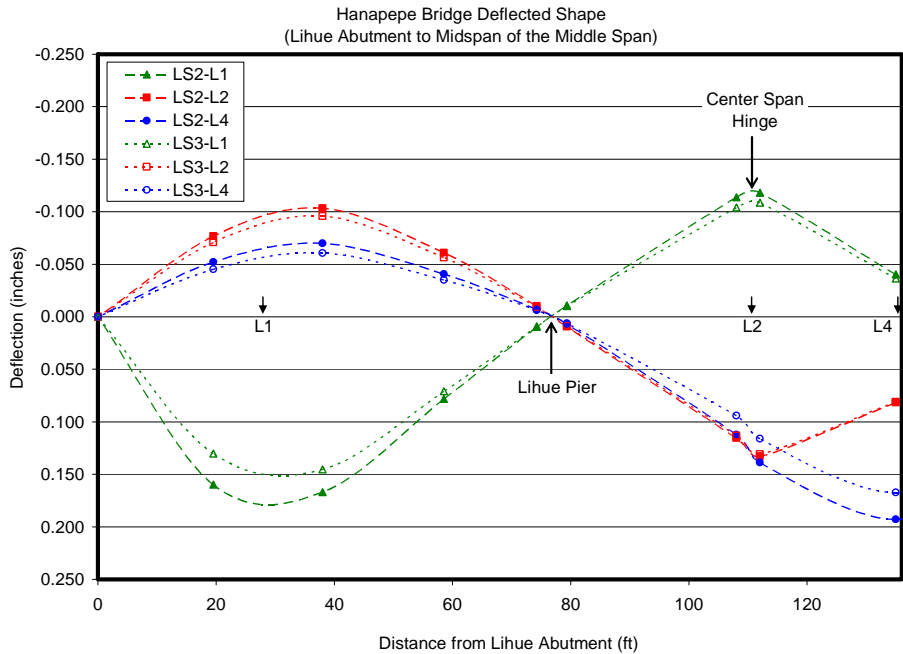


Figure 7.5.2. Load Series 2 and 3 Deflected Shape of Lihue Half of Bridge.

7.5.1.3 Load Series 4 and 5

Figure 7.5.3 shows the deflected shapes recorded by the LVDT-Taut-Wire baseline systems during each load condition (L1, L2 and L4) of Load Series 4 and 5. Load Series 4 consisted of Truck 1 (the largest truck load) in the upstream lane (Table 7.2). In Load Series 5, Truck 1 is in the downstream lane. All deflected shapes are similar to those observed for Load Series 1. The total weight of Truck 1 is slightly less than the combined weight of Trucks 2 and 3 used in Load Series 1. However, when Truck 1 is located over

girder G-3 and the baseline system, the deflections measured by the baseline system increase, as would be expected.

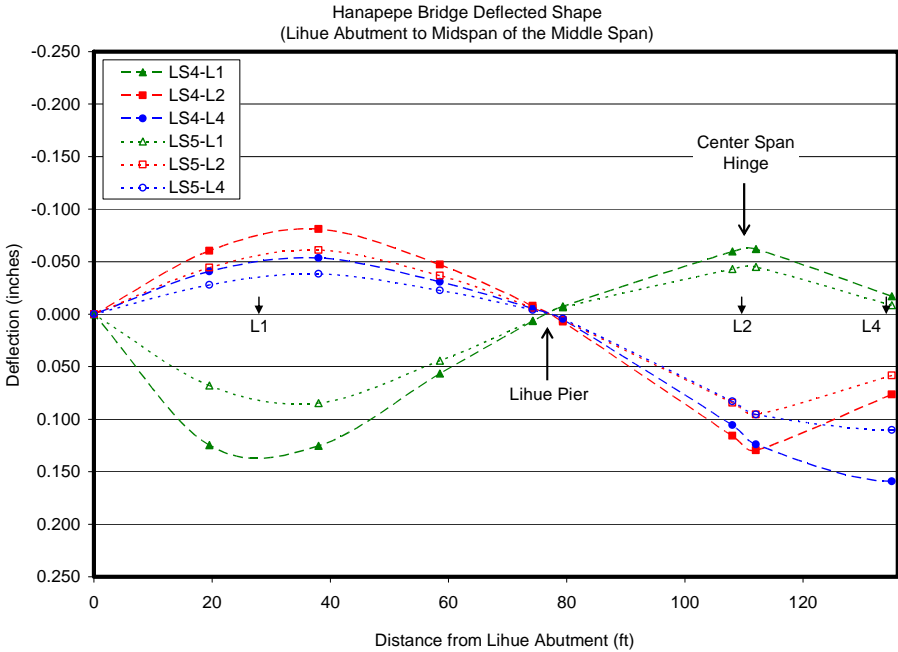


Figure 7.5.3. Load Series 4 and 5 Deflected Shape of Lihue Half of Bridge.

7.5.1.4 Load Series 6

Figure 7.5.4 shows the deflected shapes recorded by the LVDT-Taut-Wire baseline systems during each load condition (L1, L2, L3 and L4) of Load Series 6. Load Series 6 consisted of Truck 1 (the largest truck load) in the downstream lane and Trucks 2 and 3 immediately behind each other in the upstream lane (Table 7.2). Load condition LS6-L4 is shown in Figure A7.4.21 in the Appendix.

Load Series 6 was repeated twice so as to verify repeatability of the load application and measuring systems. The deflected shapes recorded by the baseline system compare very well for the two load applications as shown by the close agreement in Figure 7.5.4.

As expected, the deflections measured under Load Series 6 were the largest of all load tests because it consisted of the greatest truck loading. The largest downward deflection in the Lihue Abutment span of 0.19 inches (4.83 mm) was recorded during load condition L1. This load condition also produced the largest upward deflection at the pinned joint in the center span of 0.136 inches (3.45 mm). The largest downward deflection at the pinned joint in the center span was 0.19 inches (4.83 mm) when the trucks were located with their rear wheels over the joint, and front wheels on the center drop-in portion (Load condition L3). This was expected to be the worst condition for deflection at the joint, as confirmed by the deflected shapes recorded by the baseline system. The maximum upward deflection of the Lihue Abutment span (0.12 inches or 3.05 mm) also occurred under load condition L3, though load condition L2 with the truck load centered over the pinned joint produced very similar abutment span deflections.

The maximum midspan deflection in the center span (0.224 inches or 5.69 mm) occurred when the truck load was centered at midspan (Load condition L4) as expected. Because the truck load was now supported by both the Lihue and Waimea cantilevers, the upward deflections in the Abutment span reduced, as did the deflections at the pinned joint. The additional deflection at midspan is the result of downward deflection of the simply-supported drop-in section as seen in Figure 7.5.4.

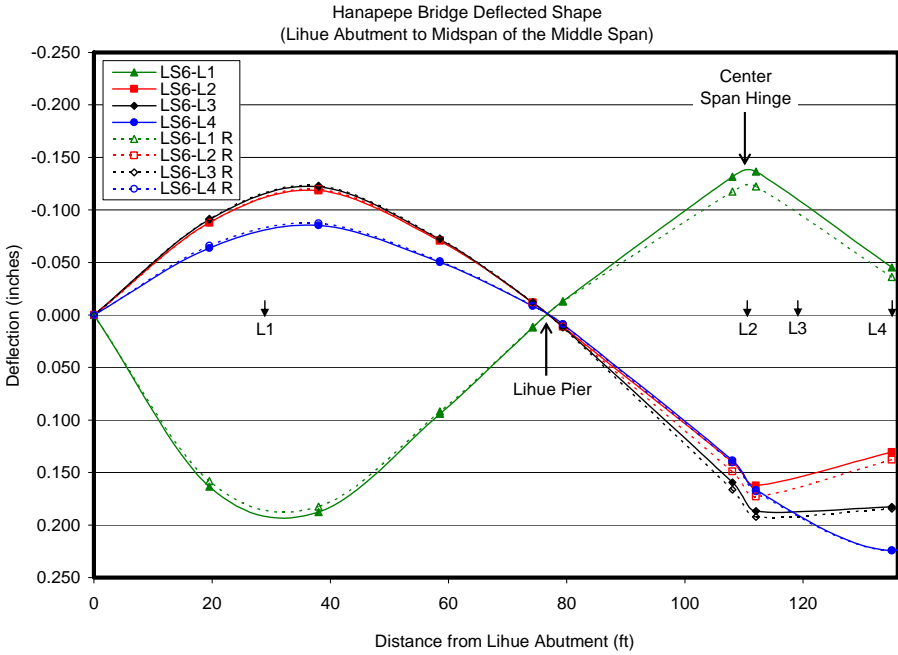


Figure 7.5.4. Load Series 6 Deflected Shape of Lihue Half of Bridge (R is Repeated Loading).

7.5.2 Horizontal Deflection

LVDT 7 was located at the Lihue abutment to monitor horizontal movement of girder G-3 relative to the abutment, as described in Section 7.2.2. Figure 7.5.5 shows the horizontal deflection recorded by LVDT 7, along with the vertical deflections at midspan of the center span and Lihue abutment span as recorded by LVDTs 1 and 5 respectively. The maximum horizontal deflection recorded by LVDT 7 is 0.04 inch (1.02 mm), and occurs simultaneously with maximum vertical deflection in the Lihue abutment span. The horizontal deflection reverses when the load is located in the center span. It was concluded that the horizontal movement observed during the static load tests was a result

of the location of LVDT 7 at mid-depth of girder G-3, above the rocker bearing support (Figure 7.2.8).

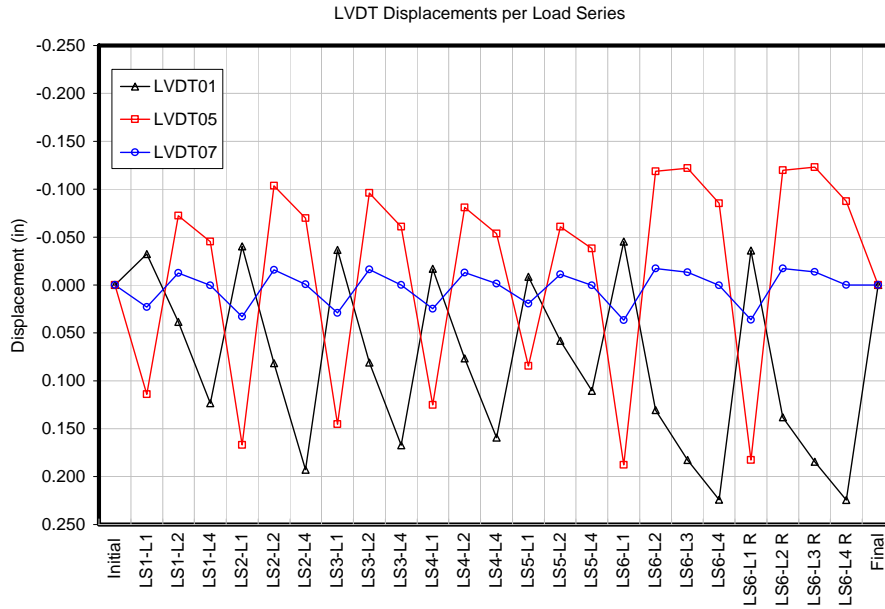


Figure 7.5.5. Comparison of Horizontal Deflection to Vertical Deflections.

7.5.3 Rotation at Lihue Piers

The girder slope at the Pier is shown by the two rotation gage records plotted along with the baseline deflected shapes in Figure 7.5.1 to Figure 7.5.4. In all deflection plots, the rotation measured at the Lihue Pier compared well with the LVDT-Taut-Wire baseline system. These measurements confirm the reliability of the baseline measurements, and provide confirmation that the two separate baseline systems in the abutment and center spans can be combined to provide a single deflected shape for the instrumented half of the bridge. Figure 7.5.6 shows the recorded displacements of the two rotation gauges at

each loading condition. The displacement is in millimeters which is the calibrated unit of the gauge. The calculated relative rotation between the top of the Lihue Pier and the abutment of girder G-3 is shown in Figure 7.5.7 for each static load condition. These rotations are consistent with the expected rotation direction.

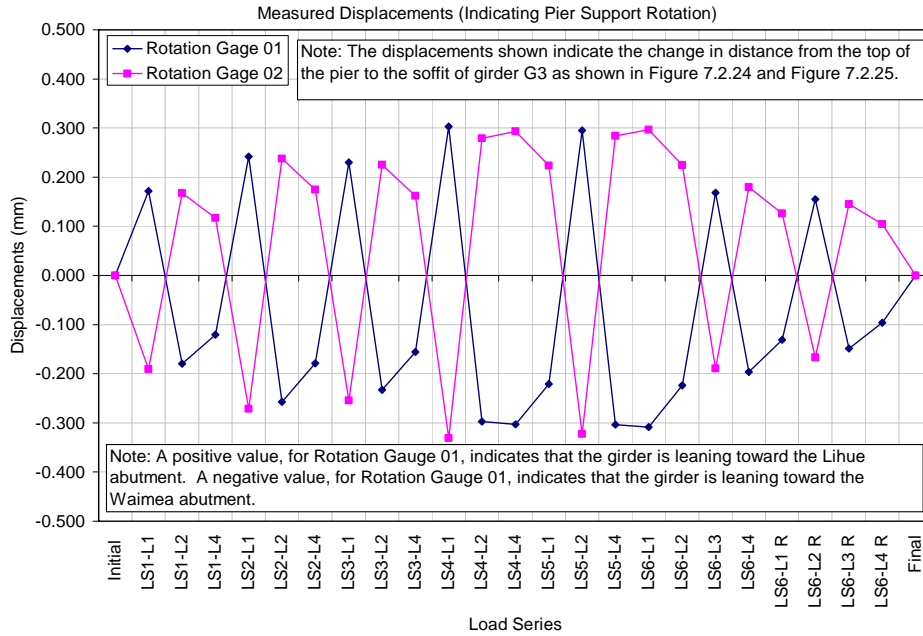


Figure 7.5.6. Displacement Measurements Used to Determine Pier Rotation.

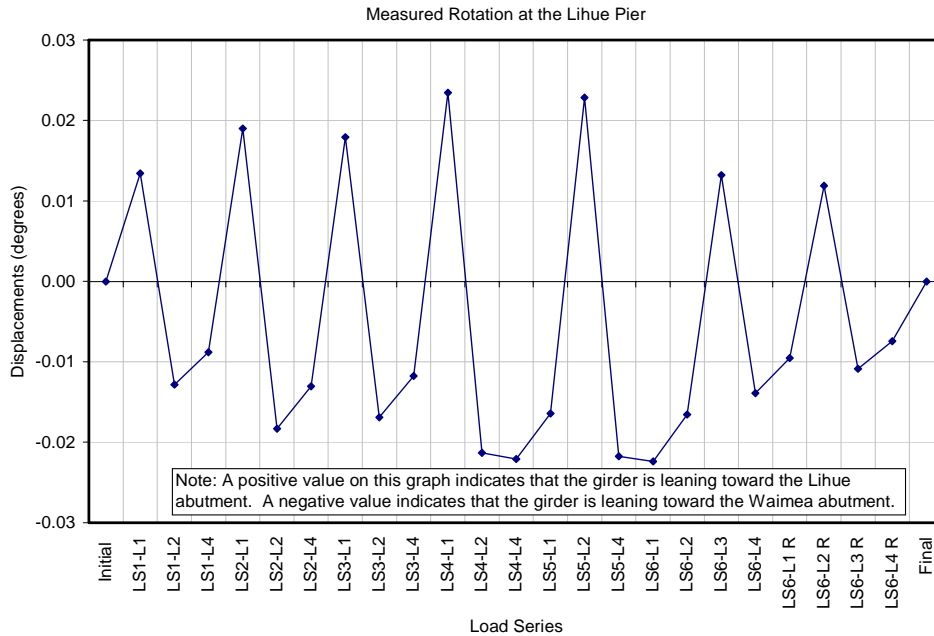


Figure 7.5.7. Rotation of Lihue Pier.

7.5.4 Crack Mouth Opening Displacements

The crack mouth opening displacements were monitored during static and dynamic truck loading conditions. The maximum extension of the existing cracks was found to be very small and of no structural concern. The results are shown per span per load series in the Figure 7.5.8 through Figure 7.5.10 below.

7.5.4.1 General

Girder G-3 has a number of flexural and shear cracks in all spans. Crack gages were installed at 10 locations on selected cracks as described in Section 7.2.3. The largest existing crack on girder G-3 was 0.025” (0.64 mm) wide, based on prior visual inspections. Figure 7.5.8 shows the changes in crack width as recorded by all 10

electronic crack gages under each loading condition. Drawn on a scale of +/-0.02 inch (+/-0.51 mm), it is clear that the changes in crack size are very small. Figure 7.5.9 shows a magnified plot of the crack gage records.

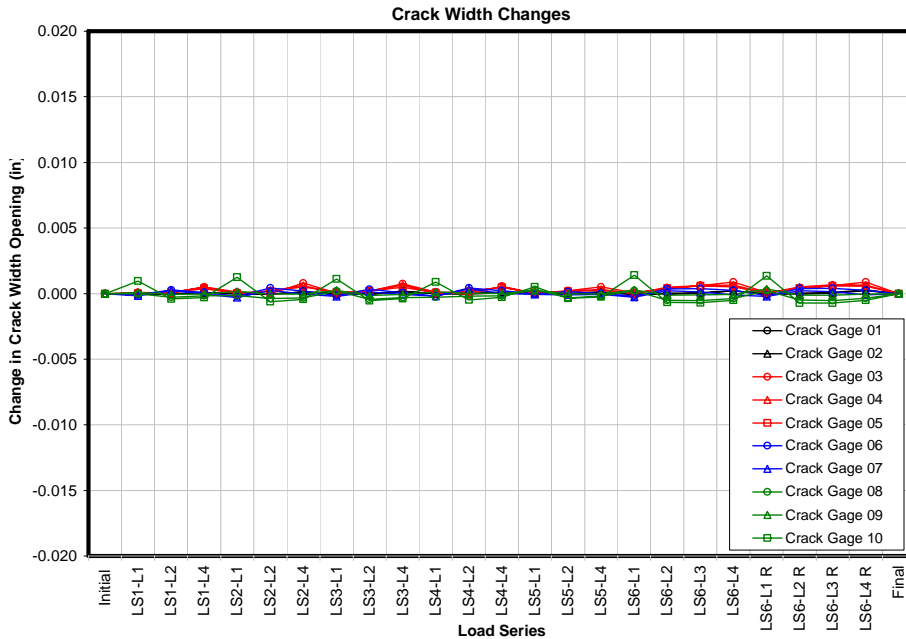


Figure 7.5.8. Crack Gauge measurements per Load Series.

The largest crack opening recorded by any of the electronic crack gauges during all of the loading conditions was 0.0014” (1.4 thousandths of an inch or 0.036 mm). This is an extremely small change in crack width, which occurred at crack gauge 10, located over a flexural crack in the soffit of the Lihue Abutment span. The existing crack size of 0.009” (0.229 mm) therefore increased to 0.0104” (0.264 mm) under maximum loading on this span (LS6-L1), before returning to its original size after removal of the truck load. All other crack gauges recorded width changes less than one thousandth of an inch.

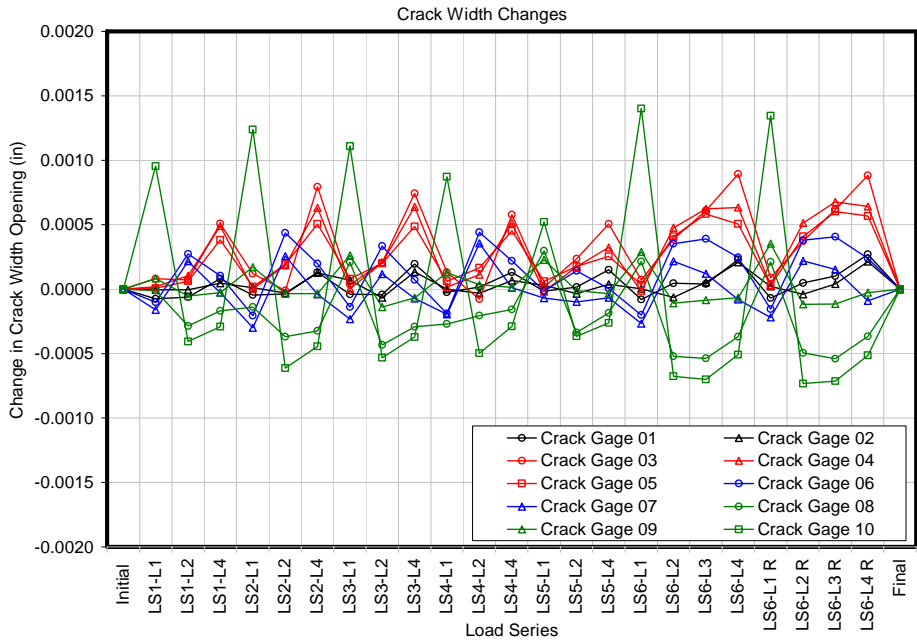


Figure 7.5.9. Crack Gauge Measurements per Load Series (Magnified).

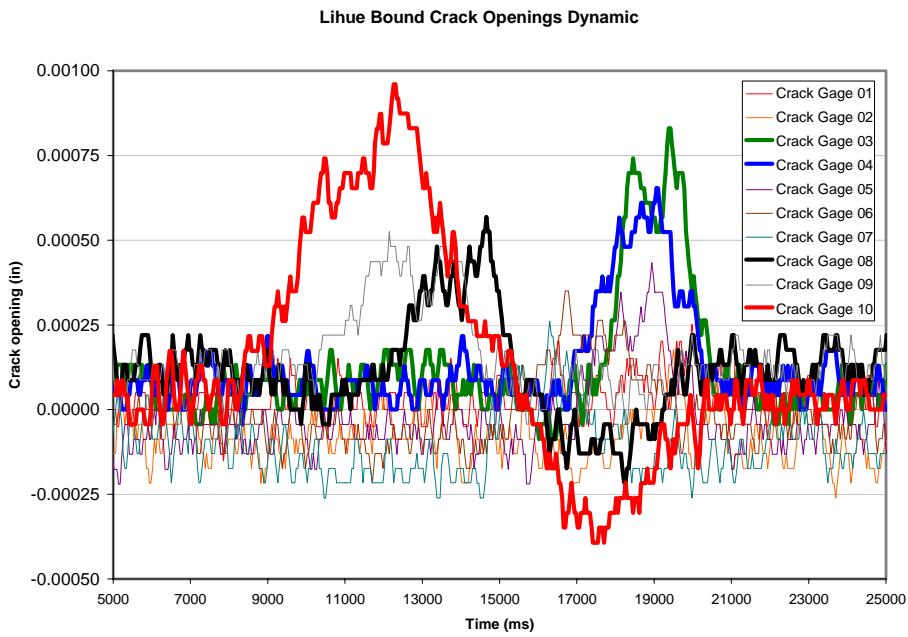


Figure 7.5.10. Dynamic Crack Opening Plots.

Figure 7.5.10 shows the effect on crack mouth opening behavior due to Truck 1 traveling Lihue bound at 25 mph (40 km/h). This indicates both the resolution and small magnitude of the observed behavior. The largest magnitude is that of crack gauge 10 which is installed at the soffit in the shallowest portion of the girder across a flexural crack.

7.5.5 Dynamic Response

In order to determine the effect of dynamic loading on the bridge, Truck 1 was driven over the bridge in both directions at 25 mph. Figure 7.5.11 and Figure 7.5.12 show vertical deflections recorded by the LVDT-Taut-Wire baseline systems, and the horizontal deflection recorded by LVDT 7, while Truck 1 was driven over the bridge at 25 mph towards Lihue and towards Waimea, respectively. The maximum vertical deflections measured during these dynamic tests were 0.014" downward at midspan of the center span, and 0.0075" upward at midspan of the Lihue abutment span. These deflections are similar to those observed during static load tests utilizing the same Truck 1 in either the upstream or downstream traffic lane (Figure 7.5.3). It was also noted that LVDT 7 recorded similar horizontal deflections as observed during the static load tests (Figure 7.5.5).

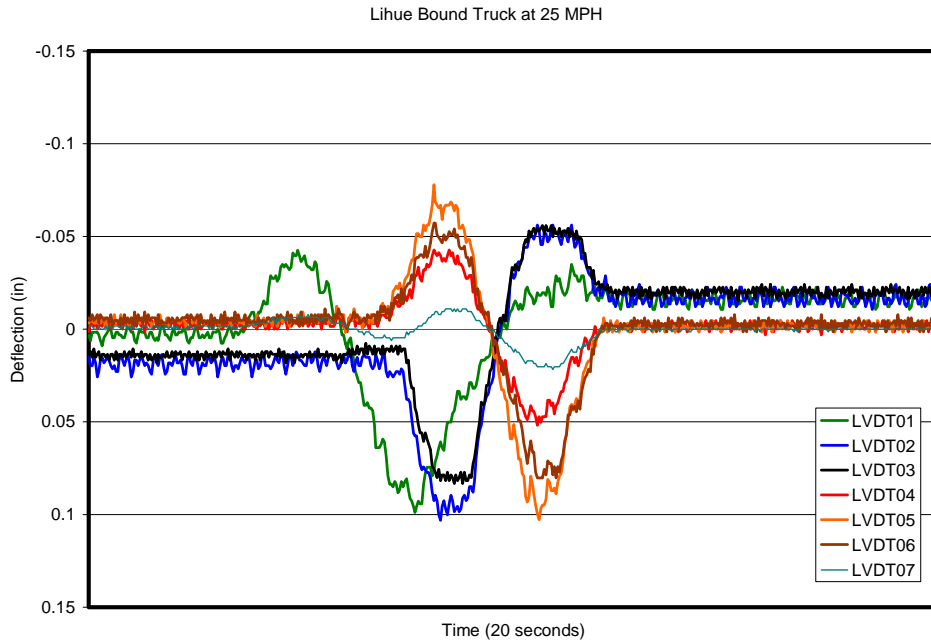


Figure 7.5.11. Lihue Bound Dynamic Deflection at 25 mph.

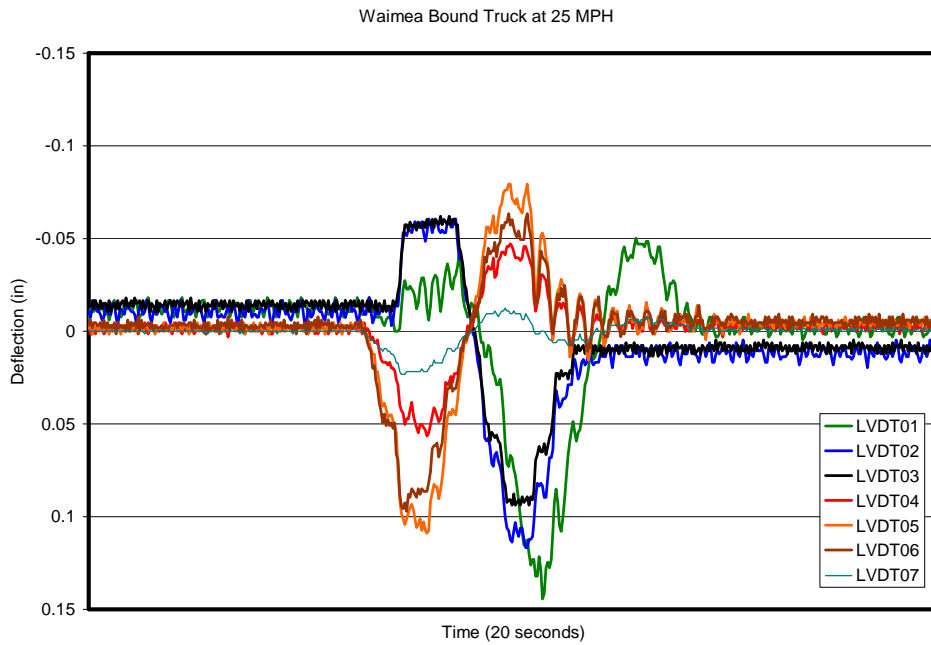


Figure 7.5.12. Waimea Bound Dynamic Deflection at 25 mph.

In order to determine whether the bridge was experiencing significant horizontal movement longitudinal to the roadway, two dynamic tests were performed with Truck 1 breaking from 25 mph to zero while crossing the Lihue Pier. Figure 7.5.13 shows all LVDT records during breaking of Truck 1 while Lihue bound. Figure 7.5.14 shows all LVDT records during breaking of Truck 1 while Waimea bound. The horizontal deflection recorded by LVDT 7 during both of these breaking tests show no indication of additional deflection caused by the horizontal load. The sustained deflection occurred while the truck was stationary after breaking, and prior to driving off the bridge. Apart from the period while the truck was stationary, the vertical deflections recorded during the breaking tests matched those recorded during the corresponding drive-through tests.

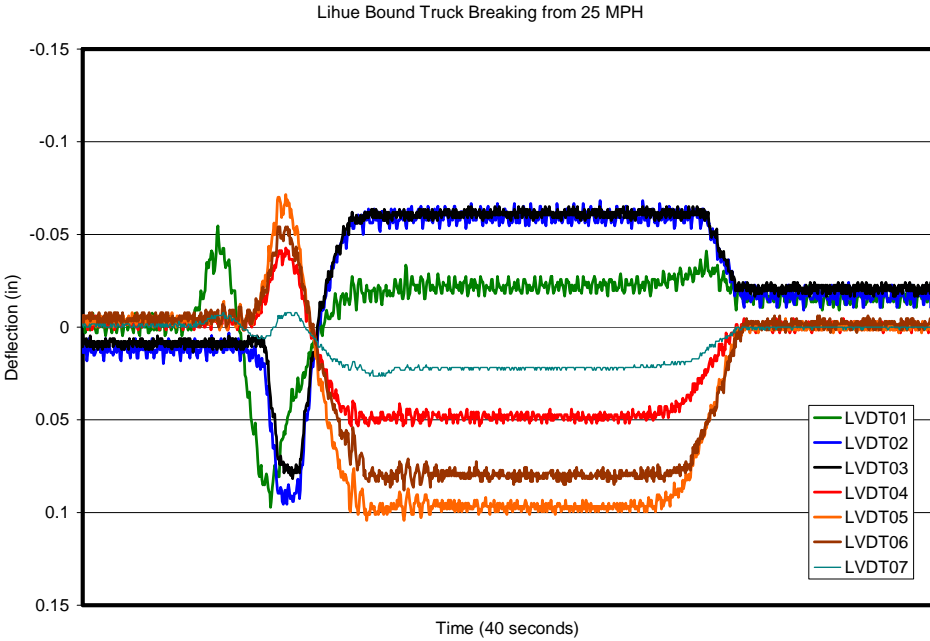


Figure 7.5.13. Lihue Bound Dynamic Deflection Breaking From 25 mph.

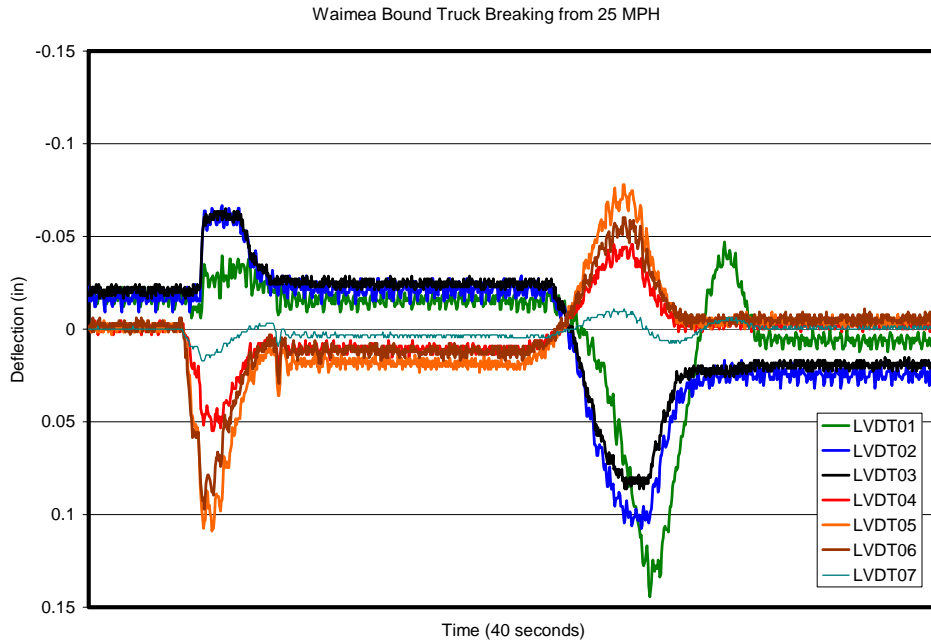


Figure 7.5.14. Waimea Bound Dynamic Deflection Breaking From 25 mph.

7.6 Conclusions about Bridge and SHM System

A diagnostic load test was performed on the bridge on July 19, 2005 to better understand its strength and serviceability characteristics. A 3-dimensional computer model was used as an analytical tool to help predict the bridge's response to various loading conditions. The model's predictions were compared with field measurements. Based on the load test results, the computer model was calibrated by adjusting the material property values. The final calibrated computer model matched the bridge's observed behavior very closely, allowing for a more accurate load rating of the bridge.

The LVDT-Taut-Wire system has been used successfully for both short and long-term static deflections using a manual reading system [Robertson et al. 2005, Chapter 3]. For

the Hanapepe Bridge application, the manual readings were replaced by automated LVDTs because of limited access below the bridge, and to reduce the time required to take readings. This automated system also allowed for dynamic tests to be performed with a moving truck load. The Wheatstone Bridge based pin-rotation monitoring gauges designed for this bridge performed well during this application as well. These gauges provided the continuity of measurements across the Lihue Pier support; they confirmed the overall displaced shape of the structure at all loading cases including the dynamic cases. The Wheatstone bridge based crack gauges designed for this bridge performed well during this application. The crack gauges showed that the instrumented crack are active, however, they are well bridged by non-yielding reinforcing.

CHAPTER 8. OTHER PLANNED SHM IMPLEMENTATIONS

8.1 North Halawa Valley Viaduct (NHVV)

8.1.1 Background

The NHVV is a segmental cast-in-place post-tensioned concrete box-girder bridge. Previously, the viaduct was instrumented for long-term monitoring of creep and shrinkage behavior for this type of construction [Robertson & Ingham 1999]. The project produced more knowledge about the unique constitutive properties of the local concrete and allows for better design and performance analysis of future structures of this type. The data obtained was used to calibrate computer models of the long term behavior of the viaduct.

Instrumentation used during that structural monitoring project include: LVDTs, vibrating wire strain gauges, electrical resistance strain gauges, demec strain gauges, thermocouples, tiltmeters, extensometers, and load cells.

Using the NHVV as a test bed allows us to properly configure future SHM systems to observe short and long-term deflection behavior and the effects of dynamic traffic loading. During the course of the research described in this dissertation, the viaduct structure was used as a test bed for components of a SHM system planned for installation during the Kealakaha Stream Bridge Seismic Instrumentation Program. Specifically, the LVDT-Taut-Wire baseline system was installed along one of the spans of the viaduct. The observations obtained during the process are described in chapter 3. The most recent

iteration of the system provides reasonable vertical deflection results for long span applications—some of the observations are shown below. Also, 12 one meter long strain gauges were installed on one span of the viaduct to test the C2D method deflection calculation. Some of the initial results and systematic implications for the method are described here as well. The intent of both of these systems is to monitor a structural response phenomenon to help determine the structural health of the structure. Another SHM process that will be tested on the NHVV is real-time website publication of the test bed application data.

8.1.2 Results: LVDT-Taut-Wire Baseline System

The following plots were acquired during a single day from the LVDT-Taut-Wire baseline system. There are seven LVDTs attached to a single taut-wire baseline that spans 345 ft (105m). The total pier to pier length of the monitored span is 360 ft (110m).

The data captured both truck loading and temperature-induced loading. The prior instrumentation program determined that for this span the thermal-induced deflection displaces downward as the top surface heats up and it displaces upward as it cools. This is due to the boundary conditions of the adjacent spans. The LVDT-Taut-Wire system captured this behavior as shown in Figure 8.1.1. Traffic-induced deflections were also captured with the LVDT-Taut-Wire baseline system as shown in Figure 8.1.2. The figure shows the result of two large trucks traveling down the viaduct in succession. From the data, we can determine that the trucks were traveling at about 50 mph (80 km/h) and the first truck was heavier than the second truck. Furthermore, the previous study showed

that a single HS-20 truck produces about a 0.25” deflection at midspan. If the system is accurately providing the proper deflection, the trucks are likely close to the HS-20 size. However, at this stage in development, it is prudent to calibrate an LVDT-Taut-Wire baseline system with a load test to accurately evaluate the deflection results and subsequently determine truck loads. A load test was not performed for this structure in the course of the LVDT-Taut-Wire system development. However, the system was observed in a side by side comparison with an optical survey as discussed in chapter 7.

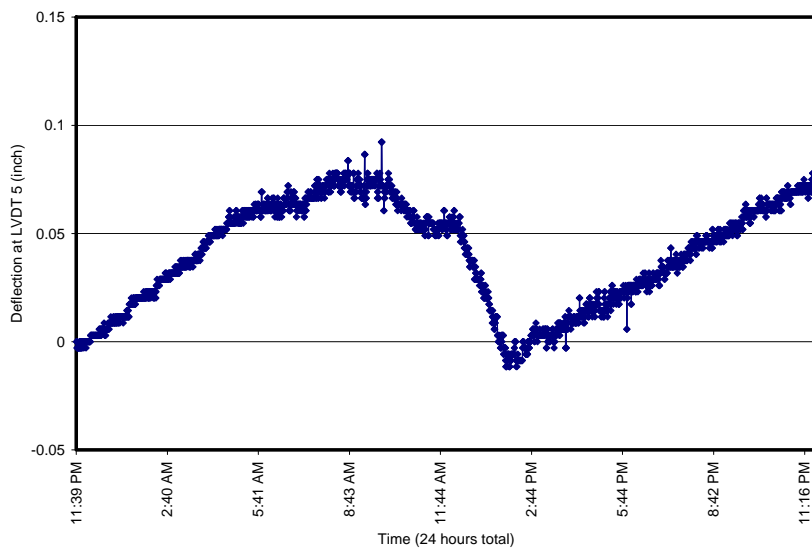


Figure 8.1.1. Thermal Deflection Observed by an LVDT-Taut-Wire Baseline System.

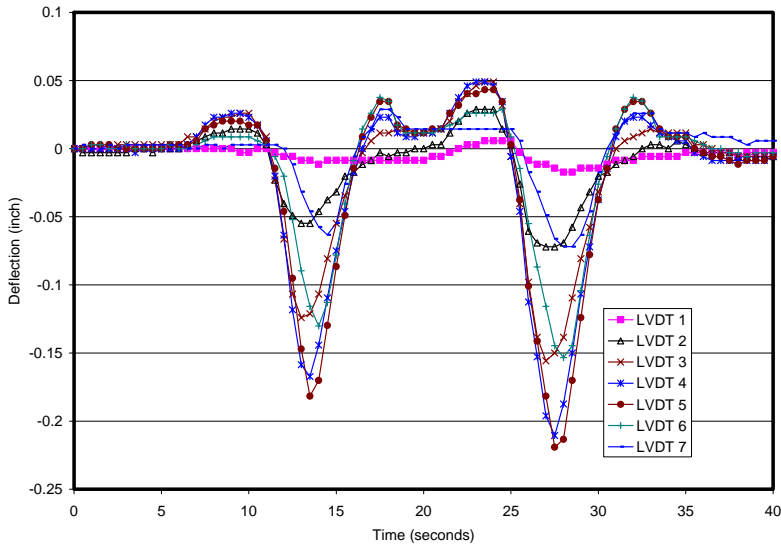


Figure 8.1.2. Traffic Loading Observed by an LVDT-Taut-Wire Baseline System.

8.1.3 Results: Strain Gauge Based C2D Methodology

A total of 12 electrical resistance based strain gauge devices were installed in a single span of the NHVV at six curvature measurement locations. A C2D Model consisting of two beam sections with a single node at mid span is currently under construction. Figure 8.1.3 shows data observed during a truck loading event. The data collected reveals that curvature measurement location 3 occurred at an inflection point so no significant strain change is observed. Also, a few of the six strain gauge devices mounted to the soffit of the top slab on the box-girder are near the neutral axis; they do not observe significant strain changes either. Both of these two observations are important to determining the final configuration of a C2D based deflection measurement system. If the intent is to measure traffic-induced deflections only, the low signal to noise ratio that exists at the inflection point or neutral axis locations may only serve to generate signal errors in the

calculation of the deflection. A location with a larger signal to noise ratio may lesson the overall noise.

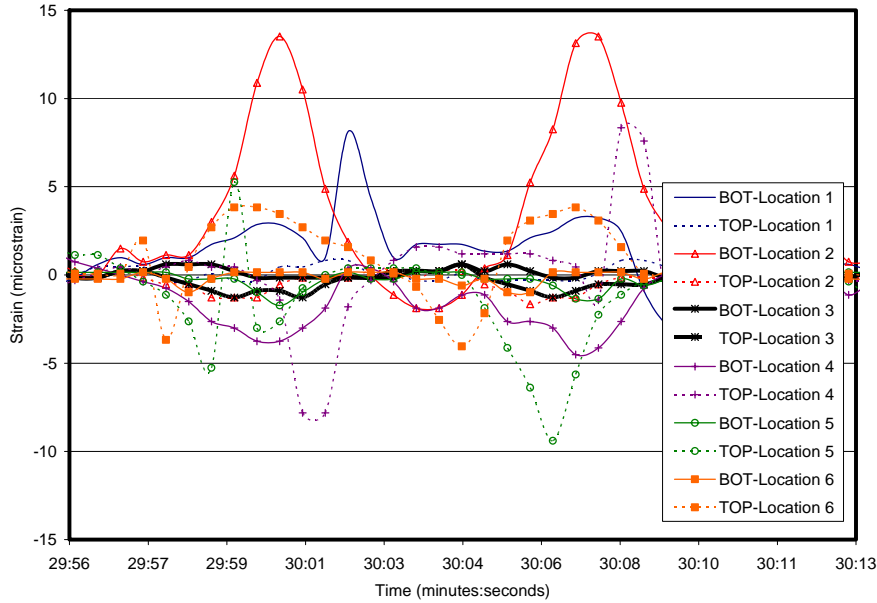


Figure 8.1.3. Strain Measurements from 1 m Long Gauges During Truck Loading

8.2 Kealakaha Stream Bridge Seismic Instrumentation

8.2.1 Background

This bridge was originally designed very similar to the NHVV. The method of construction was originally planned to be a segmental cast-in-place post-tensioned concrete box-girder bridge. The contractor who won the bid proposed a value engineered (VE) design to include friction pendulum style base-isolation at the top of the piers and abutments to save on foundation construction costs. This dramatically changes the requirements of the SHM system.

The purpose of the SHM system is to observe the seismic response of the new, long, three-span bridge. Short and long-term deflections will also be monitored. The instrumentation that will be used in the SHM system includes: accelerometers, fiber optic strain gauges for the C2D methodology, LVDTs, multiple LVDT-Taut-Wire baseline systems, pull wire displacement transducers, tiltmeters, and GPS stations. Other instrumentation systems yet to be developed may help to accommodate the change in structural system as well. The final data products for this SHM system includes a real-time web published report coupled with a database of observations from long-term and short-term phenomena. The recording system will be triggered to record seismic events at higher acquisition speeds.

8.2.2 LVDT-Taut-Wire Baseline System

Originally, three LVDT-Taut-Wire baseline systems were planned to measure the vertical deflection of each of the three spans along the bridge. The baselines would have been completely enclosed within the box section. However, the new design of the superstructure is a multi-cell box girder/pre-cast beam composite. Along the box girder section, each cell is much narrower than the original single box design. Since the superstructure is curved, this limits the straight line distance that the LVDT-Taut-Wire baseline can span without interfering with the webs of each cell. The planned single taut-wire spanning from pier to pier will not work without cutting through the web of either a pre-cast beam or a cell wall within the multi-cell box girder. The long middle span will now need three taut-wire baselines to fit within the curved superstructure. The detail of

the connections between the box girder section and the pre-cast beam section also restricts the placement of a single taut-wire baseline.

A total of five baselines need to be installed—complete with extra-baseline measurements that capture rigid body displacements of the ends of each of the baseline systems. In the original configuration an assumption of zero vertical displacement at the end of the baseline span was used to calculate the total displacement of the superstructure from the relative measurements observed by the LVDTs. Now, the relative measurements recorded from the LVDTs will be with respect to a point that is within the deflecting span. A new method to determine the relative vertical displacement of the dead end or live end of the baseline needs to be developed. The vertical deflection caused by the inverted pendulum base-isolation devices needs to be accounted for as well. Each support is subject to this movement. A system of pull-wire displacement transducers will be used to determine the three-dimensional motion of the superstructure with respect to the top of the piers and abutments. The investigators hope to design a system that is robust enough to identify any residual displacements that exist in a post earthquake condition.

8.2.3 C2D Methodology

The original design of the Kealakaha Stream Bridge was only expected to see about a 40 microstrain change at mid span under typical traffic loading. This was large enough such that the planned fiber optic strain gauges would produce a sufficient signal to noise ratio to measure curvatures at various locations. The noise characteristics and observations of

C2D error propagation discussed in chapters 5 and 6 will be incorporated into the final design. Constant beam section properties are an assumption of the C2D method, so, an exact solution was not possible for the original design of the system without a different form of the estimate curvature function. Alternate formulations are under consideration to obtain the best formulation to encompass the various expected loading conditions.

However, due to the new VE structural system, first a new finite element structural analysis needs to be performed to identify the new locations to place the strain gauges. The new design with its much more complex geometry, requires an additional, and likely multiple, curvature estimate formulations to be applied to the C2D algorithm. The fiber optic strain measurements used will need to be observed at many more locations to properly reflect the change in beam section properties between the box girder and pre-cast beam sections. The load sharing between the pre-cast beams will need to be accounted for more closely than the previous box girder design would have required. The instantaneous change in stiffness along the spans will alter mode shapes of the structure. The error analysis in this dissertation shows that the more curvature measurement locations incorporated into the C2D model, the larger the error away from the prescribed boundary conditions. If indeed the new structural system needs more curvature measurement locations to accurately determine the deflection of the superstructure, it may prove to be too difficult to obtain an accurate displacement configuration during dynamic events without a much faster acquisition speed and some data averaging techniques.

8.3 Salt Lake Boulevard – Halawa Stream Bridge: Shear Retrofit

8.3.1 *Background*

The Salt Lake Boulevard-Halawa Stream Bridge has multiple shear cracks in several of its beams. The retrofit process will include epoxy injection crack repair and two shear capacity upgrades. The Engineer of Record for the repair chooses to use a classic steel rod and plate shear retrofit technique at the most critical locations. A shear retrofit technique using carbon fiber reinforced polymer (CFRP) will be applied at other locations which are heavily loaded compared to their calculated capacity.

Since the CFRP technique is relatively new, a SHM program intended to monitor the structural health of the CFRP retrofit is underway. The phenomenon which will be measured is the strain level in the CFRP fabric. One of the possible failure modes that is of concern to the owner is the brittle sliding mode crack propagation that occurs between the concrete substrate and the CFRP during debonding. The concern is that this mode two sliding fracture type brittle failure will be induced by crack mouth opening displacements at existing shear cracks. This type of failure mode was investigated in the University of Hawaii's materials testing lab. It is thought that by observing strain in the CFRP at the region that is susceptible to crack formation, the initiation of debonding failure may be detectable.

8.3.2 *Planned Instrumentation*

The SHM system is designed to use fiber Bragg grating (FBG) fiber optic strain gauges to monitor the strain in the CFRP. The system will be designed and calibrated to observe

traffic induced straining of the material. It is hoped that a relationship between observed loading and possible deterioration of the retrofit can be detected—if failure begins.

This project is an excellent case study to observe all the SHM issues relating to the practical implementation of a real-time remote instrumentation project. The strain measurements require no heavy mathematics to analyze the current structural health. Because it is a relatively simple system, the budget is also small. At some time in the future, cracks may develop in the concrete near the retrofit. The economically designed Wheatstone bridge based crack gauges discussed in chapter 4 could be easily incorporated at that time for relatively little effort. This will provide another bit of information to help determine the cause of any deterioration in the structural health of the retrofit schemes used.

CHAPTER 9. SUMMARY AND CONCLUSIONS

In this age of computers and electronics, we become increasingly aware of all the new information we can collect about our surroundings. The medical industry has fully embraced the use of this technology to help diagnose problems with our health. Better diagnosis leads to appropriate and effective treatment when there is a problem. The result is that we are living longer, more productive lives. The structural engineering profession is only now beginning the steps toward the promise of extending the productive lives of our infrastructure using structural health monitoring (SHM).

The education of structural engineering professionals does not yet incorporate SHM system design into its curriculum. To help open the instrumentation world to engineers and scientists, an example of the process by which to design an economical crack gauge was discussed. While the technology used for that gauge is not new, it does provide an economical and robust alternative to other devices. The device has performed well during the Hanapepe River Bridge Load Test as discussed in Chapter 7.

The new contributions developed during the course of this research include: (1) a simple design process for an LVDT-Taut-Wire baseline system that measures vertical deflections on long and short span beams; and (2) a method by which to determine the expected error caused by real data for a strain based deflection monitoring algorithm (C2D Method). Both of these contributions will help to more quickly design such systems and have reasonable confidence of their performance before they are installed. Specific conclusions about the two systems are listed below.

The following conclusions about the LVDT-Taut-Wire baseline system and presented design process have been established.

- The proposed system is viable for monitoring static, diurnal, and traffic induced vertical deflections of beams.
- The system can work for both short- and long-span bridges.
- The initial sizing of the system can be accomplished by a design process using a simple “Rule of Thumb” procedure.
- An initial estimate of error can be determined or set during the design process.

The following conclusions about the C2D Method and presented analysis of the process have been established.

- Using a second degree polynomial to represent the curvature function in a beam provides excellent results when the applied loads conform to the exact solution: (1) point loads are applied at the nodes between (and / or at the ends of) beam sections; and (2) uniformly distributed loads act along the entire length of a beam section.
- Using a second degree polynomial for the curvature function can also produce good results in some cases even for non-conforming applied loads such that curvature measurement resolution is sufficient—with enough significant figures.
- Inadequate curvature measurement resolution can produce much larger error than non-conforming loading configurations, because: (1) more beam sections are affected,

and (2) the error is integrated twice over a longer span of the beam than a non-conforming load-induced curvature function in one beam section.

- Signal noise characterization is a useful tool to determine the expected range of error in a C2D modeled system.
- Displacement errors tend to increase with distance from prescribed boundary conditions within the C2D modeled beam.
- Data averaging techniques will likely improve the performance of the C2D method results from a dynamically acquired signal. This is necessary to effectively determine structural characteristics including: natural frequency, damping ratio, and mode shape.

Finally, the four SHM projects described in this dissertation will benefit from the analysis and results reported to date. Each project has different phenomena to be monitored; different combinations of instrumentation used; and different data products to be produced. It is important to continue the discussion of lessons learned in SHM successes and failures to advance the field by developing more easily available and useful tools for engineers and owners of infrastructure.

APPENDIX

A5.4	Matlab™ C2D Method Computer Program.....	233
A8.2	Crack Gauges: Supplementary Figures.....	245
A8.4	Truck Loading Series.....	251

A5.4 Matlab™ C2D Method Computer Program

This Matlab™ program is structured such that the main program performs function calls to the other program files. The dependency and function of each file is described below.

- *main.m* retrieves the input data from the input text file, it sends the data to the C2D() function. It saves the output data to the output file and sends the data to the function *plotter3d()*.
- *C2D.m* is the function that contains the algorithm for the C2D method. C2D.m prepares the data for the calculation of the curvature function coefficients a, b, and c—by calling the function *element_defl()*. Upon receiving the a, b, and c coefficients matrix, it calculates the rotation and displacements for the entire beam for all the time steps requested.
- *element_defl.m* is the function that is given the curvature and strain gauge location data and returns the a, b, and c coefficients matrix. It calls the function *Gauss()* to solve the linear system of equations for a, b, and c.
- *Gauss.m* is a general Gaussian elimination linear system of equations solver.
- *plotter3d.m* plots the output file array as a surface and contour plot of all the data versus time.
- *main_noise.m* retrieves the input data from the input file, then it augments that data with errors of a specified magnitude and sends the new data set to the C2D()

function. It saves the data with error to a new file per error level and plots the data.

The Programs are listed below in the following order: main.m, C2D.m, element_defl.m, Gauss.m, plotter3d.m, main_noise.m.

main.m

```
1  %get input from files
2  FILE='beam_raw';
3  INPUT_FILE=[FILE, '.txt'];
4
5  %get data from input file
6  IFA=dlmread(INPUT_FILE, '\t');
7
8  %get results (OFA) from C2D_Loop3 or C2D (curvature to displacement loop program)
9  %OFA=C2D_Loop3(IFA);
10 OFA=C2D(IFA);
11
12 % Save to output files.
13 OUTPUT_FILE=[INPUT_FILE, '_out', '.xls'];
14 dlmwrite(OUTPUT_FILE, OFA, '\t');
15
16 plotter3d(OFA);
```

C2D.m

```
1 function OFA = C2D(IFA)
2 % Author: Gaur Johnson
3 % Date: 11/22/05 modified 08/17/06
4 % Program: Strain to Curvature to Displacement eqn.
5 % Input: this function is passed the INPUT_FILE_ARRAY (here is is called IFA)
6 %     The format of the IFA is detailed in the metadata about the
7 %     Gscd program.
8 % Output: This function returns the OUTPUT_FILE_ARRAY (here is is called OFA)
9 %     This function also displays the displaced shapes on a Figure.
10 %     The OFA is an array: the first row of the array are the x
11 %     coordinates along the beam. The following rows are the
12 %     deflection values for each displaced shape calculated. Each
13 %     shape is in its own row. the code: OFA=[xplot;P4t];
14 %
15
16
17 % get number of sections (k is the number of sections)
18 k = IFA(1,1);
19
20 %Do is the displacement B.C. at node 0; Dk is the displacement B.C. at node k.
21 Do=0;Dk=0;% Do is the left hand vertical displacement, Dk is the right hand vertical displacement.
22
23 % Lk holds the lengths of each section of the beam.
24 Lk=zeros(k,1);
25 for i=1:k
26     Lk(i,1)=IFA(2,i);
27 end
28
29 % get gage locations
30 %xp (prime) is the left x coordinate of the sg.
31 %xpp (prime prime) is the right x coordinate of the sg.
32 %xppk and xpk are arrays that hold the relative x coordinate of the sg per
33 %each section.
34 xppk=zeros(k,3);
35 xpk=zeros(k,3);
36 left=1;
37 right=left+2;
38 for i=1:k
39     xppk(i,:) = IFA(4,left:right);
40     xpk(i,:) = IFA(3,left:right);
41     left = left+3;
42     right = left+2;
43 end
44
45 % get curvature data for all steps
46 dt = IFA(1,2); % dt is the count on the number of time steps
47 cvkt = zeros(k,3,dt);
48 Reldx = 10;
49
```

```

50
51 for step=1:dt
52 left=1;
53 right=left+2;
54 for i=1:k
55     cvkt(i,:,step)=IFA(step+4,left:right);
56     left = left+3;
57     right = left+2;
58 end
59 end
60
61 % cv is the measured curvature matrix.
62
63 colorvalue=['r' 'g' 'b' 'c' 'm' 'y' 'k' 'b'];
64 colorindex = 0;
65
66 %While still plotting deflected shapes
67 for step = 1:dt
68     cvk = cvkt(:, :, step);
69
70 % Determine the A, B, and C coefficients from the sg lengths
71 % and the measured strains(for each section 1 to k).
72 ABC=zeros(k,3);
73 for i=1:k
74     xpp=xppk(i,:);
75     xp=xpk(i,:);
76     cv=cvk(i,:);
77     %the "element_defl" function determines the A,B,&C coeff's given the
78     % relative x coordinate (the left and right end) of each sg and the
79     % measured strain at each gage location per section.
80     ABC(i,:)=element_defl(xpp,xp,cv);
81 end;
82
83 % DR contains the displacement and rotation constants as a result of integration
84 % to the 4th degree displacement equations.
85 DR=zeros(3,2);DR(1,1)=1/12;DR(2,1)=1/6;DR(3,1)=1/2;DR(1,2)=1/3;DR(2,2)=1/2;DR(3,2)=1;
86 Lak=Lk.^3; %length of section cubed for A coeff.
87 Lbk=Lk.^2; %length of section squared for B coeff.
88 Lck=Lk; %length of section for C coeff.
89
90
91 % double integration over Lk of second degree polynomial for each section
92 % (Not including B.C. which will determine alpha and beta later)
93 i_P2x=ABC;
94 i_P2x(:,1)=i_P2x(:,1).*Lak;
95 i_P2x(:,2)=i_P2x(:,2).*Lbk;
96 i_P2x(:,3)=i_P2x(:,3).*Lck;
97
98 ABC_DR=i_P2x*DR; % ABC_DR gives the monomials at Lk for the P4 (D=displacement eqn) and P3 (R ✓

```

```

=rotation eqn)
99 ABC_DR(:,1)=ABC_DR(:,1).*Lk; % this step completes the monomials at Lk for the P4 as noted on previous line
e.
100
101
102 % sum_ABC_D is the sum of the section cantilever displacements
103 % Dk is the right end B.C. Displacement
104 % Do is the left end B.C. Displacement
105 % sum_Lk is the total length of the beam
106 sum_ABC_RxLk=0;
107 sum_ABC_D=0;
108 sum_Lk=0;
109 for i=1:k
110     %sum the cantilever displacements for all sections. ABC terms only :
111     %all members of A,B,C monomials at Lk for P4 (displ).
112     sum_ABC_D=sum_ABC_D+ABC_DR(i,1);
113     %sum total length of beam
114     sum_Lk=sum_Lk+Lk(i,1);
115 end;
116
117 % determine alpha and beta by forcing continuity between sections
118 AB=zeros(k,2);
119
120 % initial rotation at left end of beam (so far so good)
121 sum_RxLarm=0;
122 for i=1:k
123     Larm=0;
124     for j=i+1:k
125         Larm=Larm+Lk(j,1);
126     end;
127     sum_RxLarm=(ABC_DR(i,2).*Larm)+sum_RxLarm;
128 end;
129 %AB(1,1)=0; % Cantilever Condition
130 AB(1,1)=(Dk-(sum_RxLarm+sum_ABC_D)-Do)/(sum_Lk); % Simple support at ends
131
132 %initial deflection at left end
133 AB(1,2)=Do;
134
135 % iterate the displacement and rotation B.C. for each section
136 for i=2:k
137     AB(i,1)=ABC_DR(i-1,2)+AB(i-1,1); % correct alpha
138     Ld=Lk(i-1,1); %length of previous section
139     AB(i,2)=ABC(i-1,1)*Ld.^4/12+ABC(i-1,2)*Ld.^3/6+ABC(i-1,3)*Ld.^2/2+AB(i-1,1)*Ld+AB(i-1,2);
140     %correct beta
141 end
142
143 % plotting of results and retaining equations
144
145 for i=1:k

```

```

146     x(i,:)=0:(Lk(i,1)/Reldx):Lk(i,1);
147     p4a(i,1)=(ABC(i,1))./12;
148     p4b(i,1)=(ABC(i,2))./6;
149     p4c(i,1)=(ABC(i,3))./2;
150     p4alpha(i,1)=(AB(i,1));
151     p4beta(i,1)=AB(i,2);
152     p3a(i,1)=(ABC(i,1))./3;
153     p3b(i,1)=(ABC(i,2))./2;
154     p3c(i,1)=(ABC(i,3));
155     p3alpha(i,1)=(AB(i,1));
156 end
157
158 %construct plotting data
159 for i=1:k
160     P2xk(i,:)=ABC(i,1)*x(i,:).^2+ ABC(i,2)*x(i,:) + ABC(i,3);
161     P3xk(i,:)=(p3a(i,1)*x(i,:).^3+p3b(i,1)*x(i,:).^2+p3c(i,1)*x(i,:)+p3alpha(i,1));
162     P4xk(i,:)=(p4a(i,1)*x(i,:).^4+p4b(i,1)*x(i,:).^3+p4c(i,1)*x(i,:).^2+p4alpha(i,1)*x(i,:)+p4beta(i,1));
163 end
164
165 %plot deflected shapes
166 xplot=x(1,:);
167 x_sum = Lk(1,1);
168 P2=P2xk(1,:);
169 P3=P3xk(1,:);
170 P4=P4xk(1,:);
171 for i=2:k
172     xplot=[xplot,x(i,:)+(x_sum*ones(1,Reldx+1))];
173     x_sum=x_sum+Lk(i,1);
174     P2=[P2,P2xk(i,:)];
175     P3=[P3,P3xk(i,:)];
176     P4=[P4,P4xk(i,:)];
177 end
178
179 P2t(step,:)=P2;
180 P3t(step,:)=P3;
181 P4t(step,:)=P4;
182
183 colorindex= colorindex +1;
184 if colorindex == 9
185     colorindex = 1;
186 end
187 figure(1)
188 plot(xplot,P2,colorvalue(colorindex))
189 hold on
190 figure(2)
191 plot(xplot,P3,colorvalue(colorindex))
192 hold on
193 figure(3)
194 plot(xplot,P4,colorvalue(colorindex))

```

```

195 hold on
196 end % End of While loop:
197
198 %% Save data to a txt tab delim file.
199 % OUTPUT_FILE_ARRAY OFA is the matrix that is written
200 % to the output file and the value returned by this
201 % function
202 OFA=[xplot;P4t]; % for 3d defl only plot and data
203 %OFA=[xplot;P4t;P3t;P2t]; % for 3d plot and data including angle of
204 % rotation and curvature
205
206
207 figure(1)
208 plot([0,sum_Lk],[0,0],'k')
209 % plot axes information and title
210 xlabel('Length of Beam = 236 inches')
211 ylabel('Curvature (1/in)')
212 title('Three Span Beam Curvature','FontSize',12)
213 hold off
214
215 figure(2)
216 plot([0,sum_Lk],[0,0],'k')
217 % plot axes information and title
218 xlabel('Length of Beam = 236 inches')
219 ylabel('Angle of Rotation (radians)')
220 title('Three Span Beam Angle of Rotation','FontSize',12)
221 hold off
222
223 figure(3)
224 plot([0,sum_Lk],[0,0],'k')
225 % plot axes information and title
226 xlabel('Length of Beam = 236 inches')
227 ylabel('Deflection of Beam (in)')
228 title('Three Span Beam Deflection','FontSize',12)
229 hold off

```

element_defl.m

```
1 function ABCj = element_defl(xppj,xpj,cvj)
2 % Author: Gaur Johnson
3 % Date: 11/22/05
4 % Program: element_defl.
5 % Inputs:
6 % -left and right x coordinates of start and end of 3 cells strain gages
7 % [curvature readings]--xppj[left] , xpj [right]
8 % -cvj is the curvature reading at cells from left to right
9 %
10 % Output:
11 % -coefficients A, B, C for second order polynomial, P2, approximation of
12 % section curvature.
13
14
15 % GCM is the gage length coefficient matrix.
16 GCM=zeros(3,3);
17
18 for k=1:3
19     GCM(k,1)=((xppj(k)^3-xpj(k)^3)/(3*(xppj(k)-xpj(k))));
20     GCM(k,2)=((xppj(k)^2-xpj(k)^2)/(2*(xppj(k)-xpj(k))));
21     GCM(k,3)=((xppj(k)-xpj(k))/(1*(xppj(k)-xpj(k))));
22 end;
23
24
25 ABCj= transpose(Gauss(GCM,cvj));
```

Gauss.m

```
1 function x = Gauss(A,btr)
2 %Source: This is a slight adaptation of code from
3 %[Fausett 1999, pg 84-85]
4 % Fausett, Laurene V. "Applied numerical analysis using MATLAB,"
5 % Upper Saddle River, New Jersey: Prentice-Hall, 1999.
6 %
7 %Solve Ax=b using gaussian elimination
8 % Inputs :
9 % A is the n-by-n coefficient matrix
10 % b is the n-by-k RHS matrix
11 %
12 %Output :
13 % x is the n-by-k solution matrix
14 %
15 b=transpose(btr);
16 [n,k1] = size(A); [n,k]=size(b); x = zeros(n,k);
17 for i=1:n-1
18     m=-A(i+1:n,i)/A(i,i);
19     A(i+1:n,:)=A(i+1:n,:)+m*A(i,:);
20     b(i+1:n,:)=b(i+1:n,:)+m*b(i,:);
21 end;
22 x(n,:)=b(n,:)/A(n,n);
23 for i=n-1:-1:1
24     x(i,:)=(b(i,:)-A(i,i+1:n)*x(i+1:n,:)) ./ A(i,i);
25 end
```

plotter3d.m

```
1 function plotter3d(OFA)
2
3 t_start=0.000;
4 dt=0.01;
5
6 xx=OFA(1,:);
7 y_points=size(OFA,1)-1;
8 yy=zeros(1,y_points);
9 for i=1:y_points
10     if i==1
11         yy(1,i)=t_start;
12     else
13         yy(1,i)=yy(1,(i-1))+dt;
14     end
15 end
16 zz=OFA(2:(y_points+1),:);
17
18 figure(4)
19 surf(xx,yy,zz)
20 figure(5)
21 contour(xx,yy,zz)
```

main_noise.m

```
1 % get input from files
2 FILE='beam';
3 INPUT_FILE=[FILE,'.txt'];
4 ERROR_MAG=10; % Magnitude of error also used in output file name.
5
6 % get data from input file
7 IFA=dlmread(INPUT_FILE,'\t');
8
9 % Determine number of cells (curvature readings) per displaced shape.
10 cells=IFA(1,1)*3;
11
12 % Determine number of steps (displaced shapes) in the Input_File.
13 steps=IFA(1,2);
14
15 % Determine magnitude of curvature error to induce.
16 error=ERROR_MAG/1000000;
17 IFA_error=IFA;
18
19 % Begin Loop that iterates through cells with error.
20 for i=1:cells
21     % Loop to apply error to each step
22     for j=1:steps
23         IFA_error(j+3,i)=IFA(j+3,i)+error;
24         if i~=1
25             IFA_error(j+3,i-1)=IFA(j+3,i-1); %reset previous cell to no error.
26         end
27     end
28
29     % get results (OFA) from C2D (curvature to displacement loop program)
30     OFA=C2D(IFA_error);
31
32     % append OFA to OFA_error.
33     if i==1
34         OFA_error=OFA; % Maybe add zero error case here by calling C2D_Loop3(IFA)
35     else
36         OFA_error=[OFA_error;OFA(2:steps+1,:)];
37     end
38
39 % Return or End Loop that iterates through cells with error.
40 end
41
42 % Determine number of plots and plot them
43 plots=size(OFA_error,1)-1;
44 xplot=OFA_error(1,:);
45 colorvalue=['r' 'g' 'b' 'c' 'm' 'y' 'k' 'b' 'k' 'y' 'm' 'c' 'b' 'g' 'r'];
46 colorindex = 1;
47 for i_p=1:plots
48     yplot=OFA_error(i_p+1,:);
49     plot(xplot,yplot,colorvalue(colorindex))
```

```
50 hold on
51 colorindex= colorindex +1;
52 if colorindex == 16
53     colorindex = 1;
54 end
55 end
56
57 % Save to output files.
58 OUTPUT_FILE=[INPUT_FILE,'_out_er_',num2str(ERROR_MAG),'.xls'];
59 dlmwrite(OUTPUT_FILE,OFA_error,'t');
60
```

A8.2 Crack Gauges: Supplementary Figures



Figure A8.2.17. Crack Gauges 1 (Left) and 2 Adjacent to Visual Crack Monitor 19 (Right), Shear Cracks.

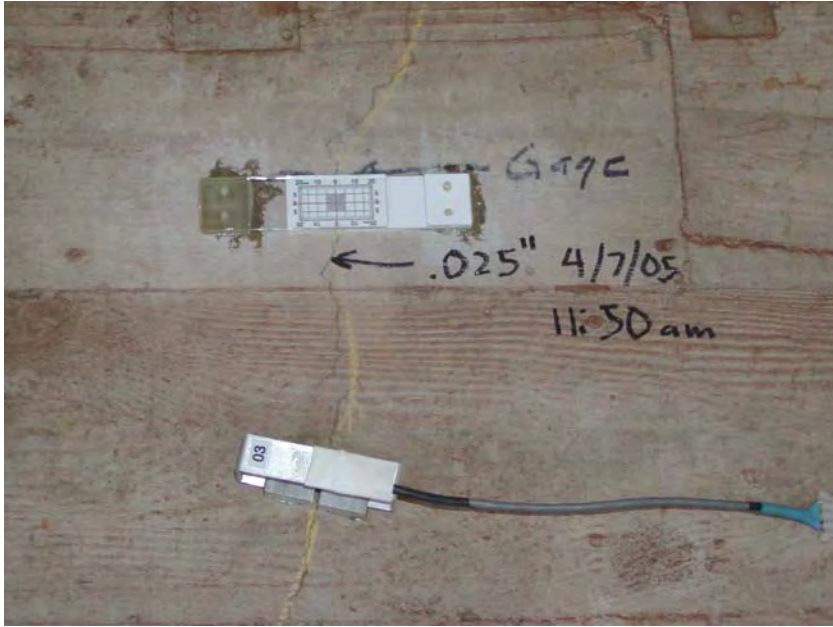


Figure A8.2.18. Crack Gauge 3 Adjacent to Visual Crack Monitor 11, Shear Crack.



Figure A8.2.19. Crack Gauge 4 Adjacent to Visual Crack Monitor 12, Flexural Crack.



Figure A8.2.20. Crack Gauge 5 Adjacent to Visual Crack Monitor 13., Flexural Crack.

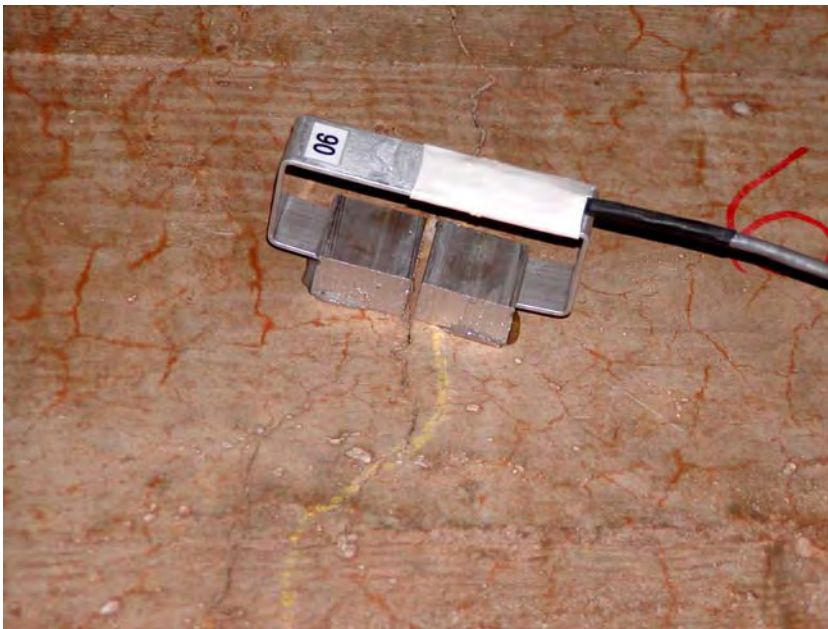


Figure A8.2.21. Crack Gauge 6, Shear Crack.

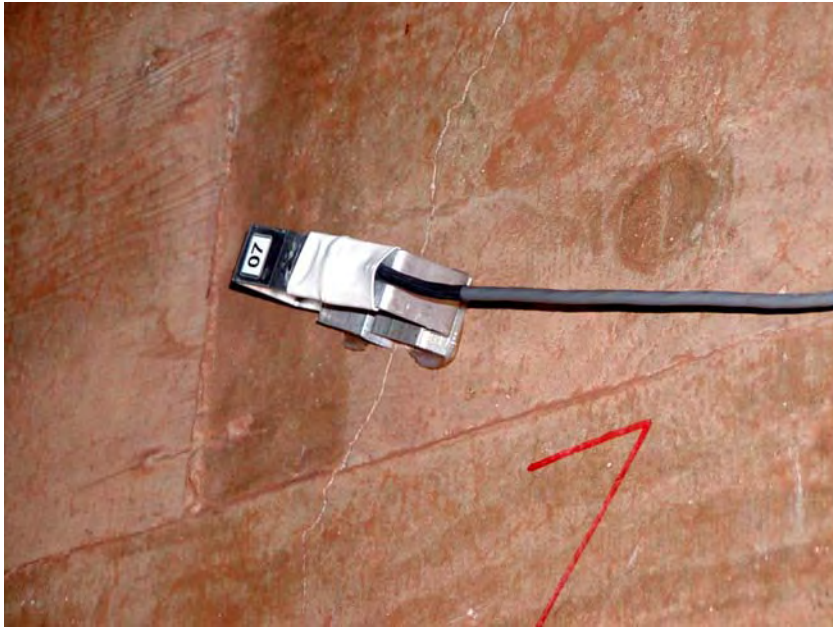


Figure A8.2.22. Crack Gauge 7, Shear Crack.

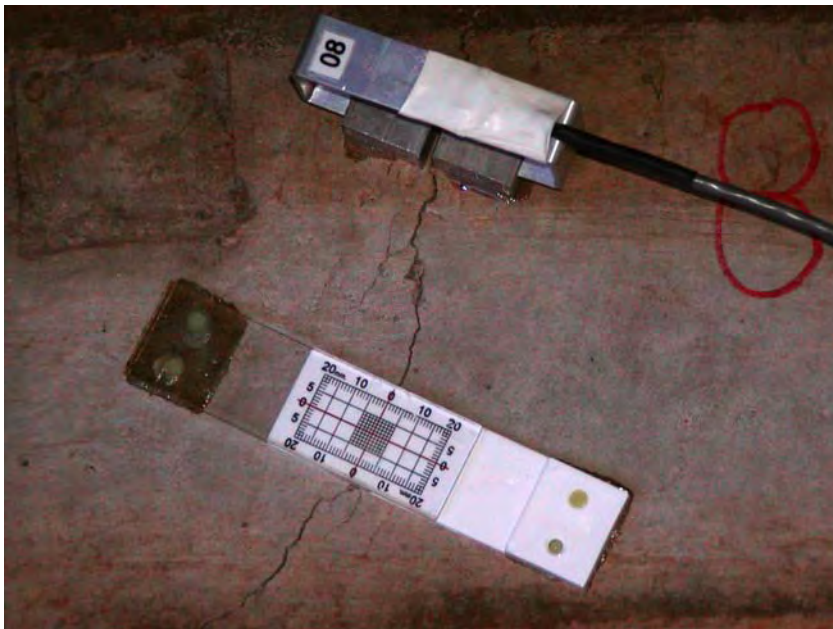


Figure A8.2.23. Crack Gauge 8 Adjacent to Visual Crack Monitor 2, Shear Crack.



Figure A8.2.24. Crack Gauge 9 Adjacent to Visual Crack Monitor 3, Shear Crack.

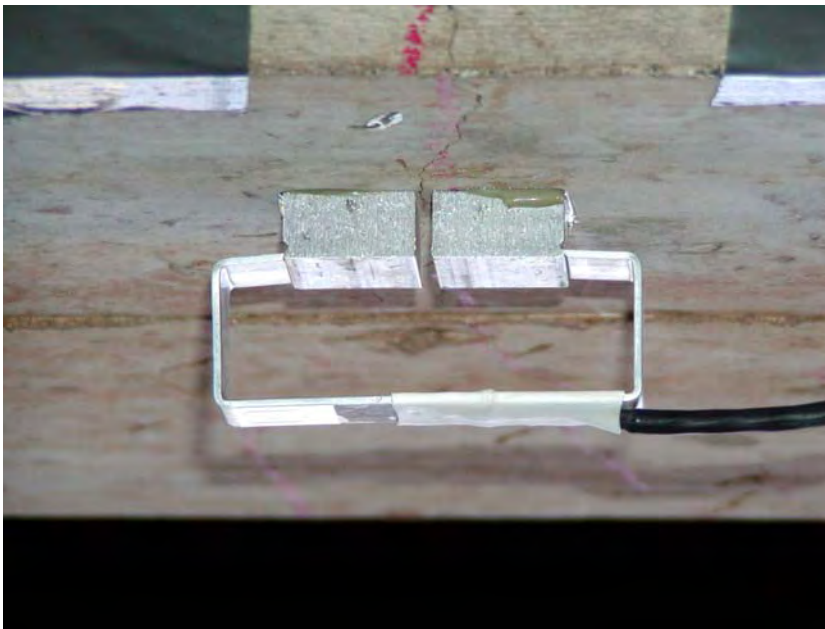


Figure A8.2.25. Crack Gauge 10 Adjacent to Visual Crack Monitor 12, Flexural Crack.

A8.4 Truck Loading Series

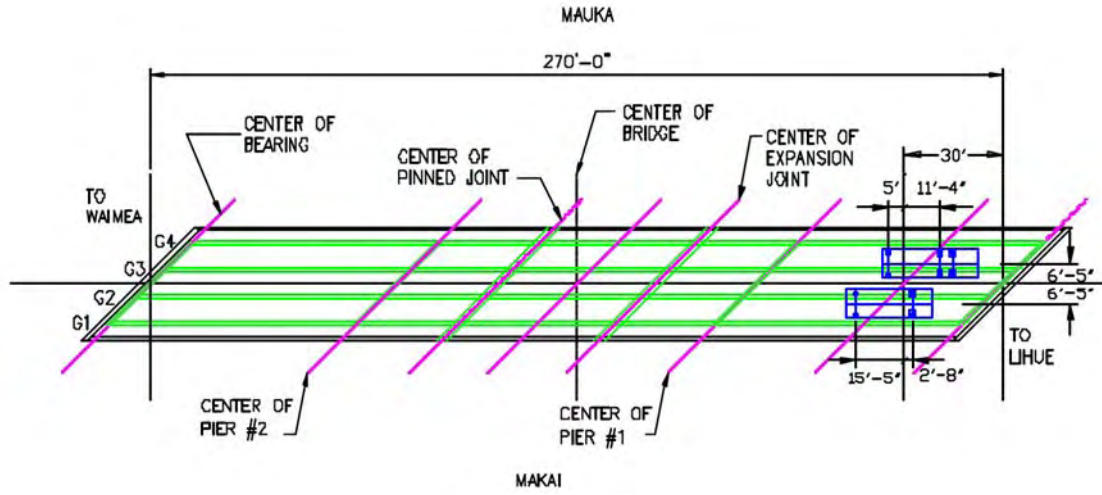


Figure A8.4.3. Load Series 1 – Location 1 (LS1-L1).

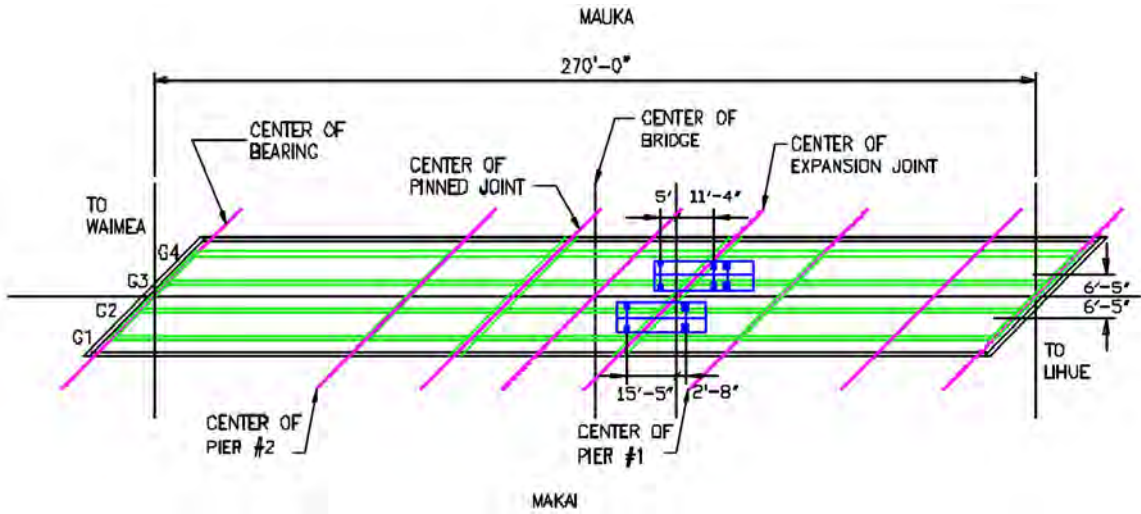


Figure A8.4.4. Load Series 1 – Location 2 (LS1-L2).

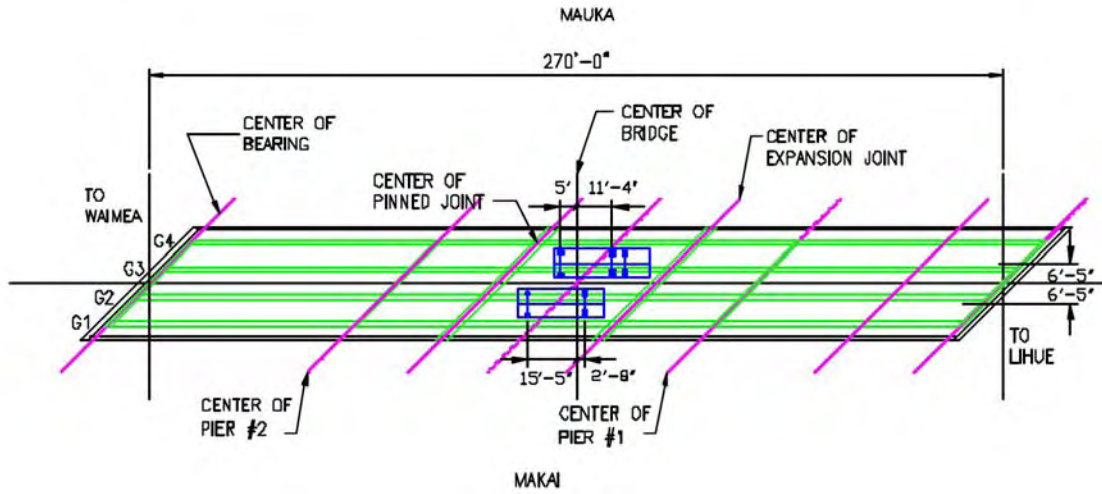


Figure A8.4.5. Load Series 1 – Location 4 (LS1-L4).

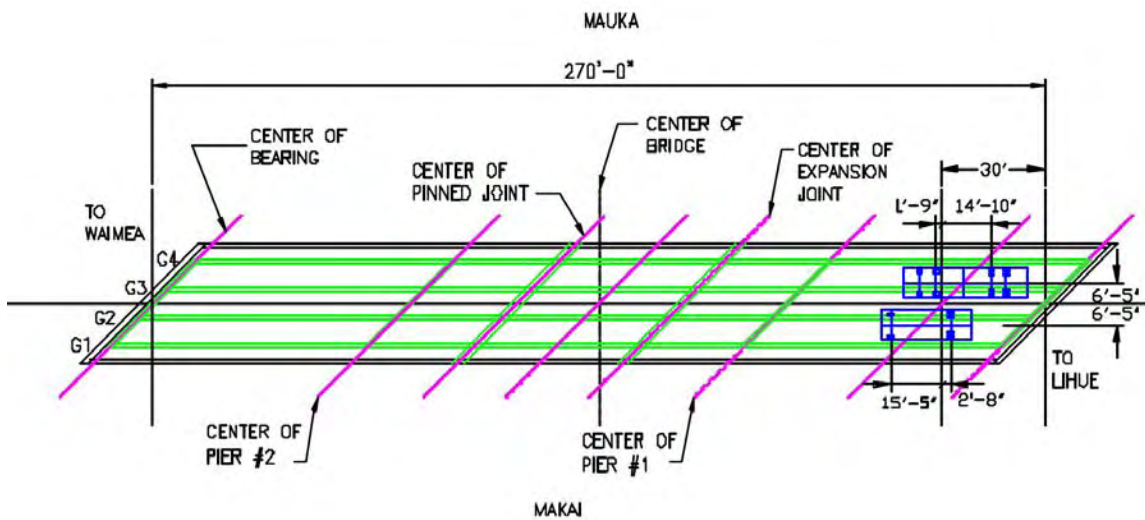


Figure A8.4.6. Load Series 2 – Location 1 (LS2-L1).

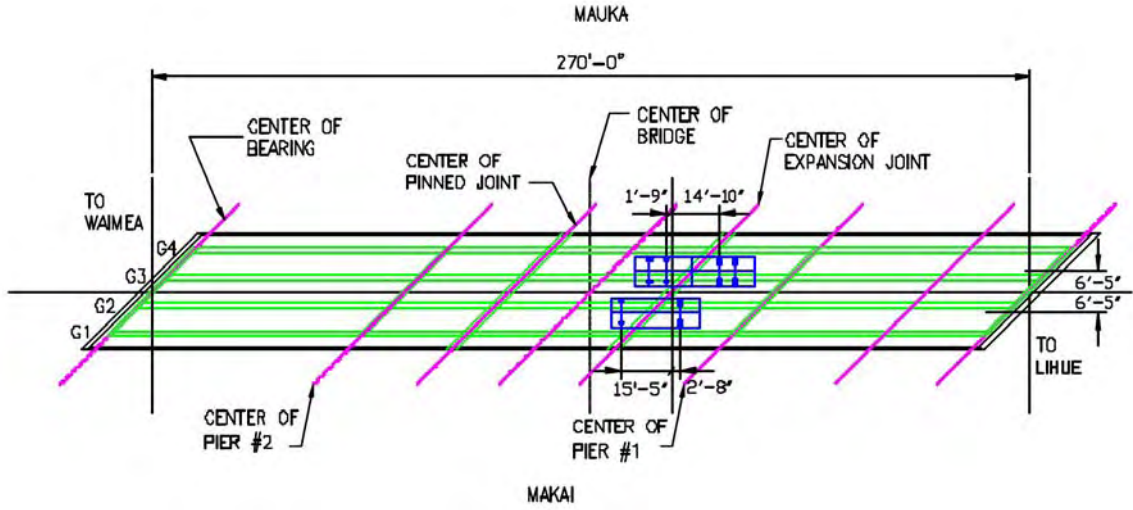


Figure A8.4.7. Load Series 2 – Location 2 (LS2-L2).

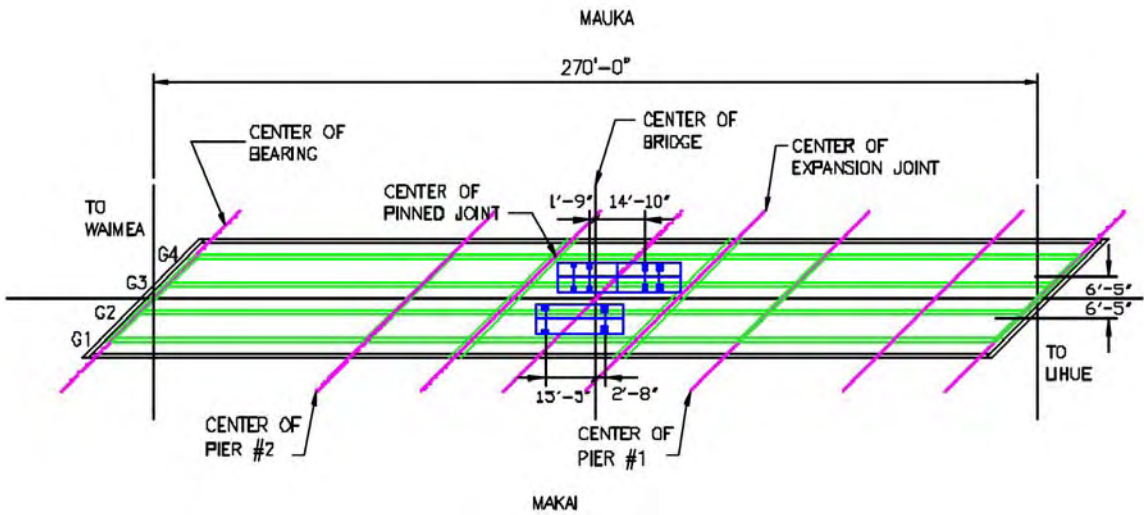


Figure A8.4.8. Load Series 2 – Location 4 (LS2-L4).

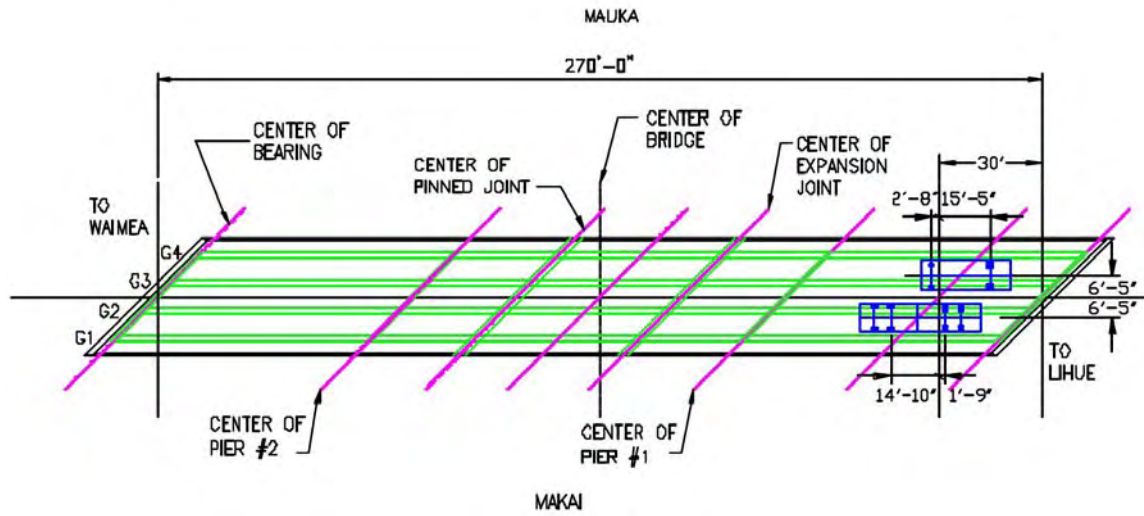


Figure A8.4.9. Load Series 3 – Location 1 (LS3-L1).

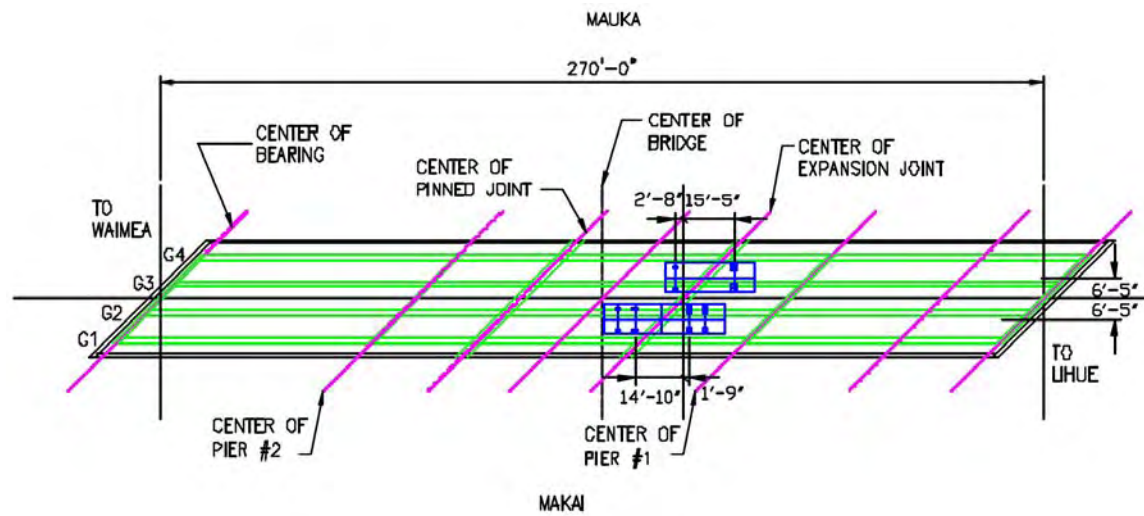


Figure A8.4.10. Load Series 3 – Location 2 (LS3-L2).

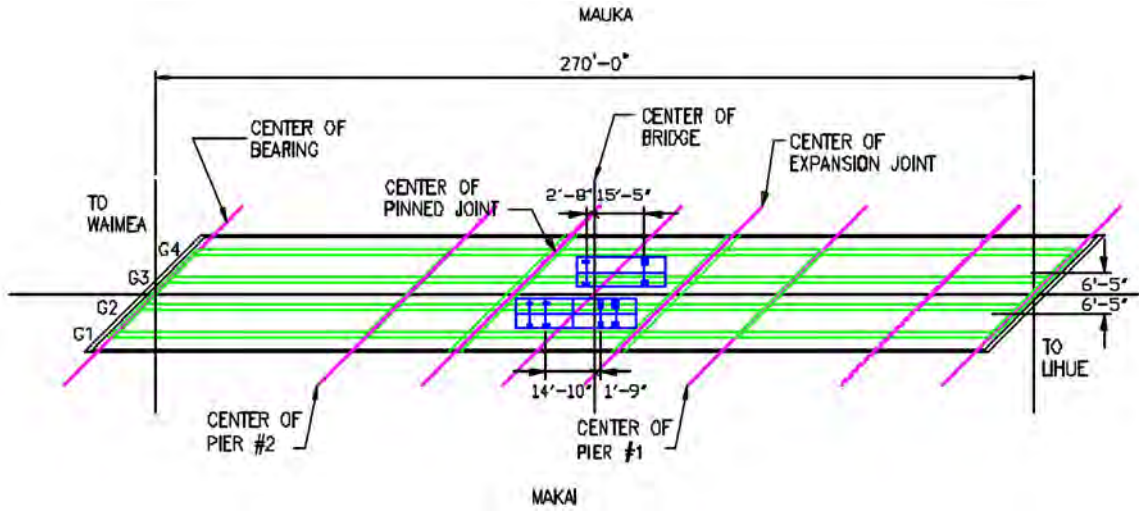


Figure A8.4.11. Load Series 3 – Location 4 (LS3-L4).

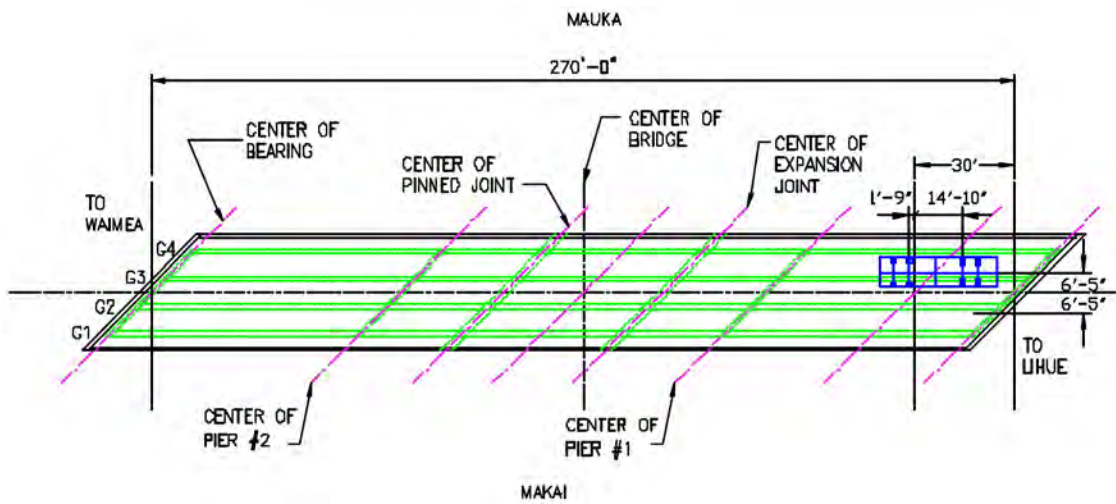


Figure A8.4.12. Load Series 4 – Location 1 (LS4-L1).

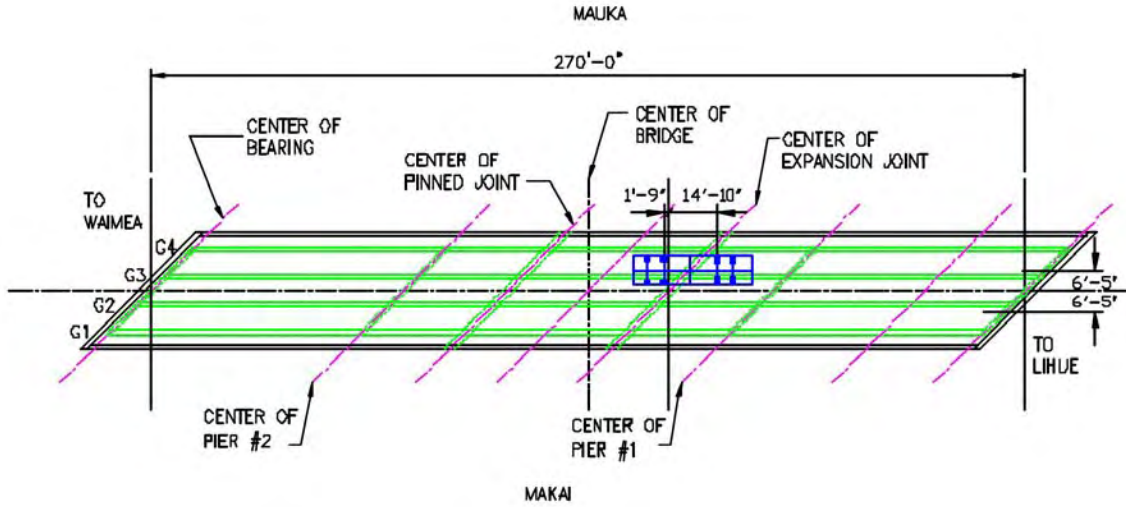


Figure A8.4.13. Load Series 4 - Location 2 (LS4-L2).

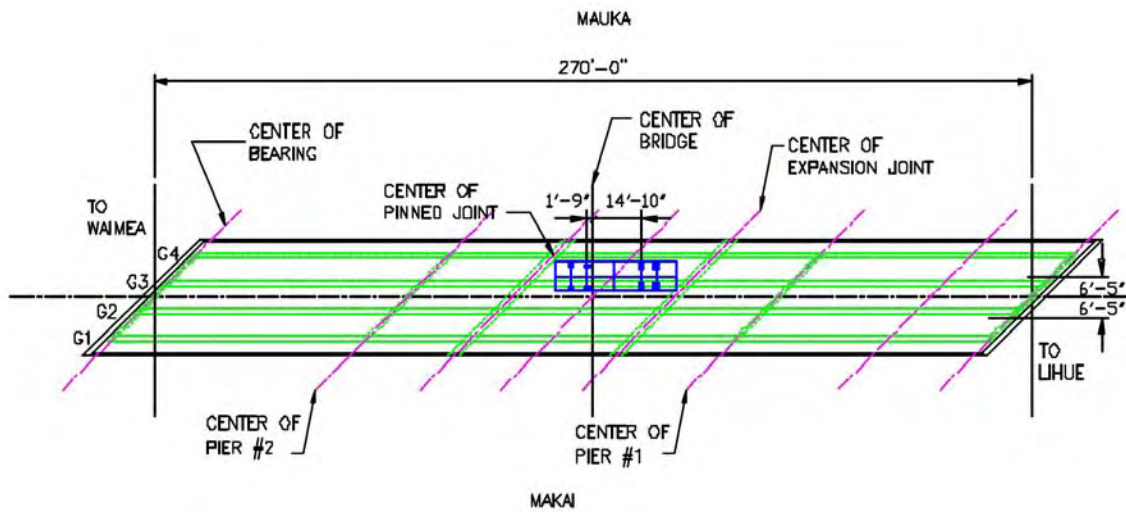


Figure A8.4.14. Load Series 4 - Location 4 (LS4-L4).

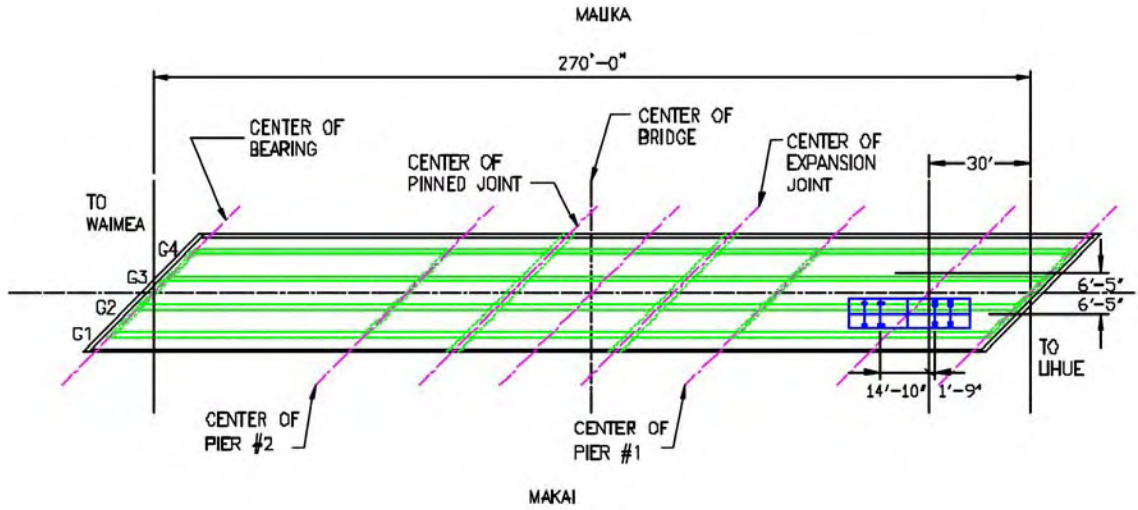


Figure A8.4.15. Load Series 5 – Location 1 (LS5-L1).

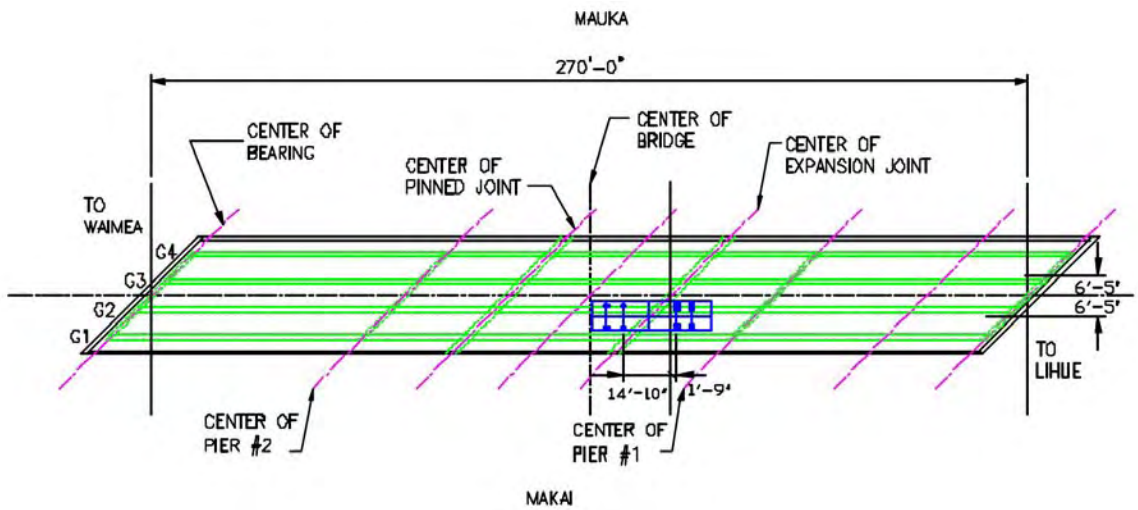


Figure A8.4.16. Load Series 5 – Location 2 (LS5-L2).

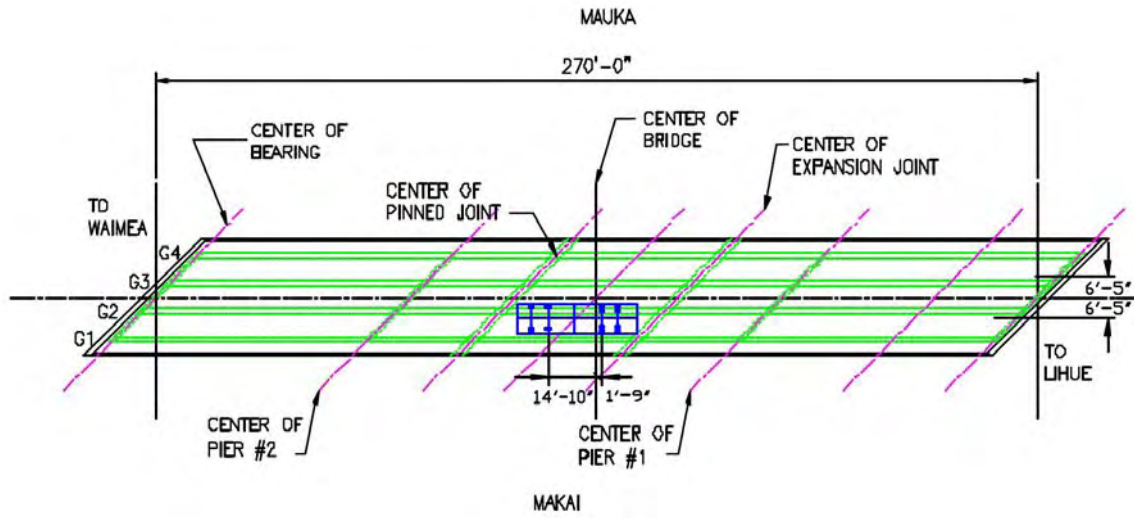


Figure A8.4.17. Load Series 5 – Location 4 (LS5-L4).

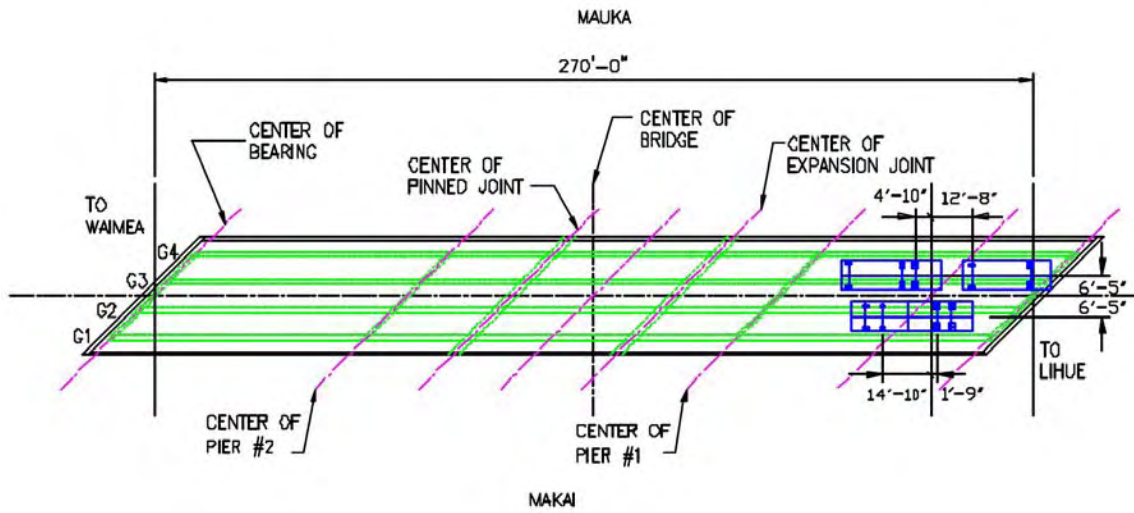


Figure A8.4.18. Load Series 6 – Location 1 (LS6-L1).

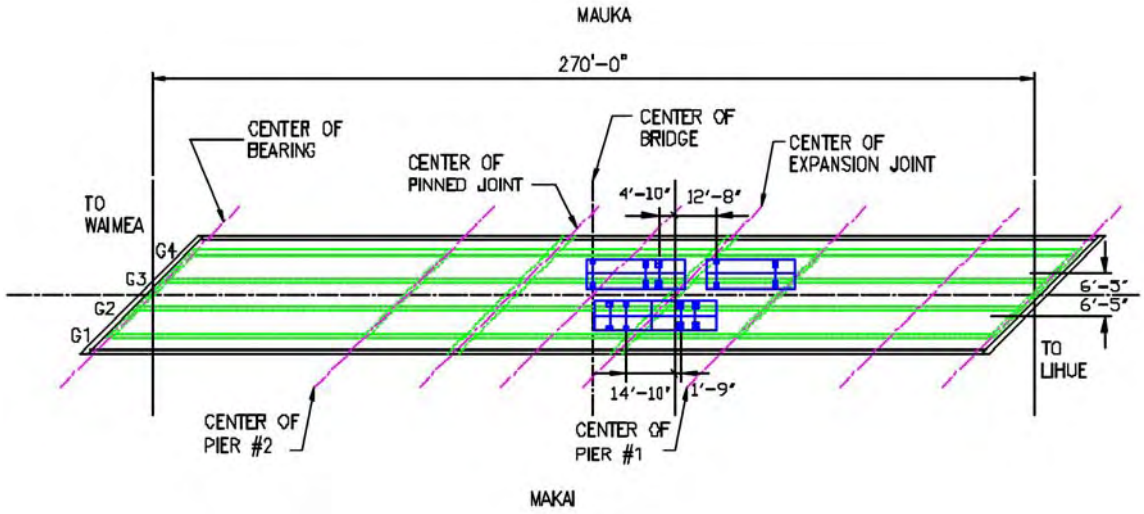


Figure A8.4.19. Load Series 6 – Location 2 (LS6-L2).

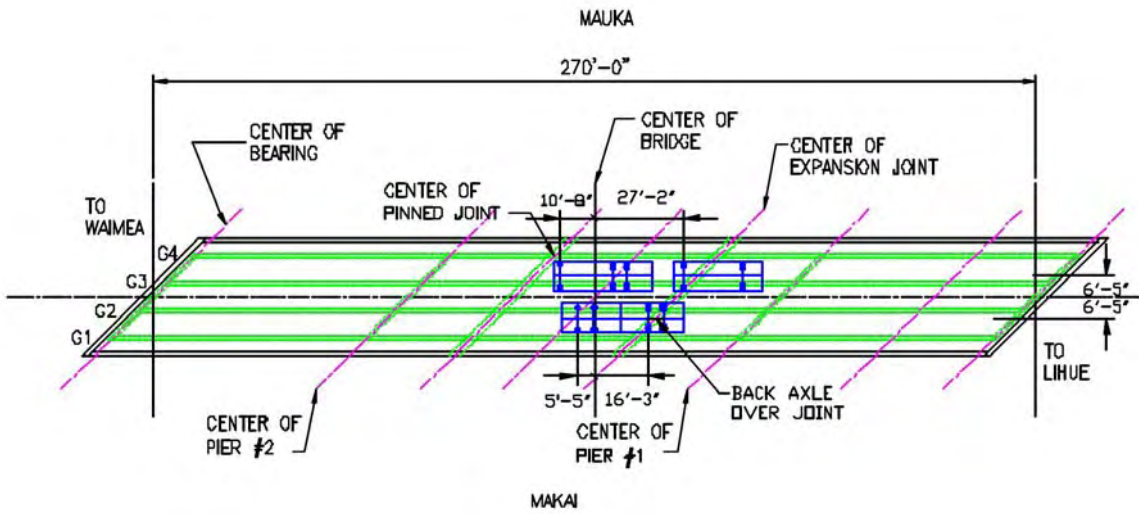


Figure A8.4.20. Load Series 6 – Location 3 (LS6-L3).

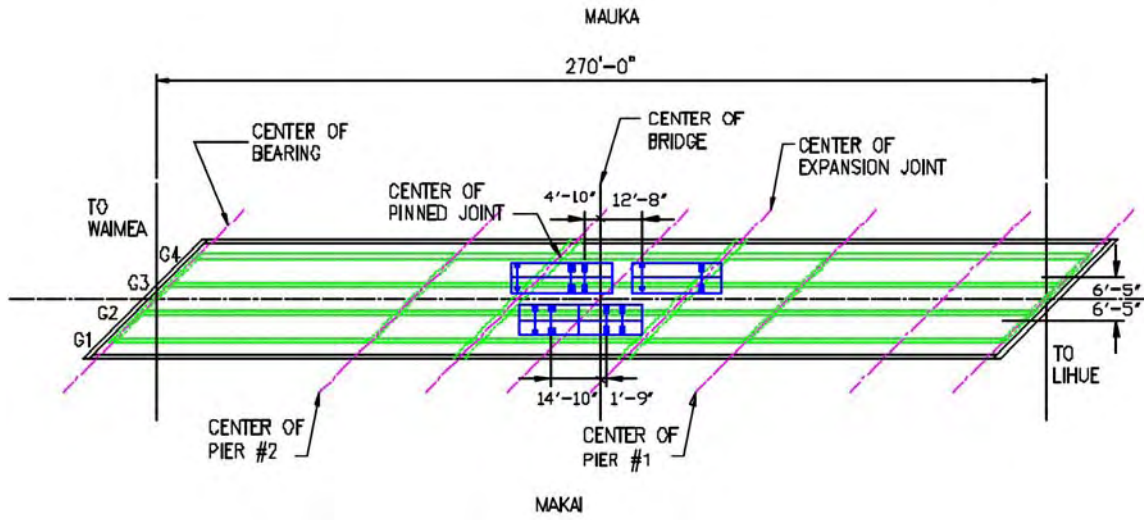


Figure A8.4.21. Load Series 6 – Location 4 (LS6-L4).

REFERENCES

- [Agapay & Robertson 2004] Agapay, Alison & Robertson, Ian N. “Test of Prestressed Concrete T-Beams Retrofitted for Shear and Flexure Using Carbon Fiber Reinforced Polymers,” Research Report UH/CEE/04-08, University of Hawaii, Honolulu, HI, USA, 268 p.
- [Aki & Robertson 2005] Aki, Kainoa D. & Robertson, Ian N. “Deflection Monitoring Systems in Static and Dynamic Conditions,” Research Report UHM/CEE/05-02, University of Hawaii, Honolulu, HI, 71 p.
- [Aktan et al. 2002] Aktan, A. E., Catbas, F. N., Grimmelsman, K.A., & Pervizpour, M. “Development of a Model Health Monitoring Guide for Major Bridges”, Drexel Intelligent Infrastructure and Transportation Safety Institute, Federal Highway Administration, Research and Development, Contract/Order No. DTFH61-01-P-00347, 270 p.
- [Aktan et al. 2003] Aktan, A. E., Catbas, F. N., Grimmelsman, K.A., & Pervizpour, M. “Development of a Model Health Monitoring Guide for Major Bridges,” Drexel Intelligent Infrastructure & Transportation Safety Institute, Drexel University, 2003, pg D3-D4.
- [Basu & Knickerbocker 2005] Basu, P. K. & Knickerbocker, D. J., “Behavior of Jointless High Performance Concrete Bridges,” Final Report Project Number TNSPR-

RES1162, State of Tennessee, DOT, USDOT, FHA, Vanderbilt University, Nashville, TN, USA.

[Bergmeister 2002] Bergmeister, Konrad., “Monitoring and Safety Evaluation of Existing Concrete Structures: State-of-the-Art Report”, fib Task Group 5.1, Final Draft.

[Bohnhoff et al. 1997] Bohnhoff, D. R., Chiou, W., & Hernandez, R., “Load Sharing in Nail-Laminated Assemblies Subjected to Bending Loads,” Presented at the August 10-14 1997 ASAE Annual International Meeting. Paper No. 974090. ASAE, St Joseph, MI USA, pg. 9.

[Chiareli 1999] Chiareli, Alessandra., Fiber Optics & Electronics Technology Center, 3M. Lecture Webpage: <http://www.ima.umn.edu/talks/workshops/9-9-10.99/chiareli/chiareli.pdf>.

[Cho et al. 2000] Cho, N., Kim, N., Jang, J., & Chang, S., “Estimation of deflection curve of bridges using fiber optic strain sensors,” Proc. SPIE Vol. 3988, pg. 339-348.

[Drexel 2006] Drexel University Website: http://repairfaq.ece.drexel.edu/sam/CORD/loet/course10_mod5/mod10-05.html.

[Fausett 1999] Fausett, L. V., Applied Numerical Analysis using Matlab®, Upper Saddle River, NJ: Prentice Hall, 596 p.

- [Ferreira et al. 2000] Ferreira, L. A., Araujo, F. M., Santos, J. L., & Farahi, F., “Simultaneous measurement of strain and temperature using interferometrically interrogated fiber Bragg grating sensors,” *Opt. Eng.*, Vol. 39, No. 8, August, pg. 2226-2234.
- [Fiso 2006] Fiso Technologies Inc. Website: <http://www.spie.org/web/oe/october/oct98/fiberop.html>
- [Fraden 2004] Fraden, J., ed. Handbook of Modern Sensors: Physics, Designs, and Applications, 3rd ed., New York: Springer.
- [Fung & Robertson 2003] Fung, S. S. Y., & Robertson, I. N. “Seismic Monitoring of Dynamic Bridge Deformations Using Strain Measurements,” Research Report UHM/CEE/03-02 University of Hawaii, Honolulu, HI, 112 p.
- [Hansen & Condon 1989] Hansen, Gladys, & Condon, Emmet, Denial of Disaster: The untold story and photographs of the San Francisco earthquake and fire of 1906, San Francisco: Cameron and Co. 160 p.
- [Harris & Piersol 2002] Harris, C. M. & Piersol, A. G., eds. Harris’ Shock and Vibration Handbook , 5th ed. New York: McGraw-Hill.
- [Henriksson et al. 1996] Henriksson, A., Sandgren, S., & Asseh, A., “Temperature insensitivity of a fiber optic Bragg grating sensor,” *Proc. SPIE* Vol. 2839, pg20-33

- [Hernandez et al. 2005] Hernandez, R., Green, D. W., Kretschmann, D. E., & Verrill, S. P. “Improved Utilization of Small-Diameter Ponderosa Pine in Glulam Timber,” Research Paper FPL-RP-625. Madison, WI: U.S. Department of Agriculture, Forest Service, Forest Products Laboratory, 38 p. (pg 10).
- [Inaudi et al. 1998] Inaudi, D., Vurpillot, S., Casanova, N., & Kronenberg, P., “Structural monitoring by curvature analysis using interferometric fiber optic sensors,” *Smart Mater. Struct.* 7, pg 199-208.
- [ISIS Canada 2001] ISIS Canada, “Guidelines for Structural Health Monitoring: Design Manual No. 2”, ISIS Canada Corporation, University of Manitoba, Winnipeg, Manitoba, Canada,. 127 p.
- [Land et al. 2003] Land, R., Murugesu, G., & Raghavendrachar, M., “Assessing Bridge Performance—When, What, How,” A Paper Presented to the 19th US-Japan Bridge Engineering Workshop, Session 7, October 28 2003, Public Works Research Institute, Tsukuba, Japan, pg 5-6.
- [Lee & Robertson 1995] Lee, Andre, and Robertson, Ian N., “Instrumentation and Long-Term Monitoring of the North Halawa Valley Viaduct,” Report UHM/CE/95-08, University of Hawaii, Honolulu, Hawaii.
- [Li & Robertson 2003] Li, X. and Robertson, I. N., “Long-Term Performance Predictions of the North Halawa Valley Viaduct,” Research Report UHM/CEE/03-04, University of Hawaii, Honolulu, Hawaii, 87p.

- [Lopez-Higuera 2005] Lopez-Higuera, J. M., Misas, C. J., Incera, A. Q., Cuenca, J. E.,
“Fiber optic civil structure monitoring,” *Optical Engineering*, Vol. 44, No. 4,
Paper 044401, April, 10 p.
- [Meltz 1996] Meltz, G., “Overview of Fiber Grating-Based Sensors,” *Proc. SPIE* Vol.
2838, pg. 2-22.
- [Mufti et al. 2005] Mufti, A. A., Bakht, B., Tadros, G., Horosko, A. T., & Sparks, G.,
“Are Civil Structural Engineers ‘Risk Averse’? Can Civionics Help?,” Report
printed in Sensing Issues in Civil Structural Health Monitoring, Ed. Farhad
Ansari. Dordrecht, Netherlands: Springer, pg 3-12.
- [Myers & Yang 2005] Myers, J., Yang, Y., “High Performance Concrete Bridge A6130-
Route 412 Pemiscot County, MO,” Report Number UTC R39, Center for
Infrastructure Engineering Studies/UTC Program, University of Missouri—Rolla,
Rolla, Missouri, pg 17, 65-66, 82.
- [Nawy 2000] Nawy, Edward G., Prestressed Concrete : a Fundamental Approach, 3rd ed.
Upper Saddle River, New Jersey: Prentice-Hall. 466 p.
- [NI 2000] National Instruments, SCXI™ - SCXI-1540 User manual: 8-Channel LVDT
Signal Conditioner, Austin, Texas: National Instruments, 70 p.
- [NI 2006] National Instruments Website: <http://www.ni.com>.

[NOAA 1972] NOAA (National Oceanic and Atmospheric Administration), 1972, “A study of earthquake losses in the San Francisco Bay Area - Data and Analysis,” A report prepared for the Office of Emergency Preparedness: U.S. Department of Commerce, 220 p.

[Norton 1989] Norton, H. N., Handbook of Transducers, Englewood Cliffs, NJ: Prentice Hall. 554 p.

[Rao et al. 2002] Rao, Y.J., Yuan, S.F., Zeng, X.K., Lian, D.K., Zhu, Y., Wang, Y.P., Huang, S.L., Liu, T.Y., Fernando, G.F., Zhang, L., & Bennion, I., “Simultaneous strain and temperature measurement of advanced 3-D braided composite materials using an improved EFPI/FBG system,” *Optics and Lasers in Engineering*, Vol. 38, pg 557-566.

[Ravet et al. 2005] Ravet, F., Zou, L., Bao, X., Chen, L., Huang, R.F., & Khoo, H. A., “Pipeline Buckling Detection by the Distributed Brillouin Sensor,” Report printed in Sensing Issues in Civil Structural Health Monitoring, Ed. Farhad Ansari. Dordrecht, Netherlands: Springer, pg. 515-524.

[Reasenbergs 2000] Reasenbergs, Paul. “1906 Marked the Dawn of the Scientific Revolution” U.S. Geological Survey, Earthquake Hazards Program Website: <http://quake.wr.usgs.gov/info/1906/revolution.html>. August 14.

- [Robertson & Ingham 1999] Robertson, Ian N. and Ingham, Tim., “Instrumentation of the North Halawa Valley Viaduct Oahu, Hawaii Final Report,” Funded by the Hawaii Department of Transportation and the U.S. Federal Highways Administration.
- [Robertson & Yoshimura 2004] Robertson, I. N. & Yoshimura, R. K., “North Halawa Valley Viaduct Load Test,” Research Report UHM/CEE/04-02, University of Hawaii, Honolulu, Hawaii. 227 p.
- [Robertson et al. 2005] Robertson, I. N., Johnson, G. P., and Wang, S., “Instrumentation Performance during Long-Term Bridge Monitoring,” Report printed in Sensing Issues in Civil Structural Health Monitoring, Ed. Farhad Ansari. Dordrecht, Netherlands: Springer, pg 331-340.
- [Salas 1995] Salas, S. L., Salas and Hille’s Calculus: One and Several Variables, 7th edition, Ed. Garret Etgen. New York: John Wiley & Sons Inc. pg 888.
- [Stanton et al. 2003] Stanton, J. F., Eberhard, M. O., & Barr, P. J., “A weighted-stretched-wire system for monitoring deflections,” *Engineering Structures* Vol. 25, pg. 347-357.
- [Techkor 2001] Techkor Instrumentation, Inc., “Technical Brief TB-31, LVDT Basics- An introduction to the Linear Variable Differential Transformer,” Middletown, PA, USA: Advanced Conversion Technology, Inc., 3 p.

[Trietily 1986] Trietily, H. L., Transducers in Mechanical and Electronic Design, New York: Marcel Dekker, Inc. 374 p.

[Virginia DOT 2006] Virginia Department of Transportation. “Virginia Test Method—20,” Virginia Test Methods. <http://www.virginiadot.org/business/resources/bu-mat-VTMs070704.pdf>. Accessed September 18, 2006.

[Vishay 2005] Vishay Micro-Measurments, “Strain Gage Thermal Output and Gage Factor Variation with Temperature Technical Note TN-504-1,” Vishay Document Number 11054, 13 p.

[Vishay 2006] Vishay Measurements Group Website: http://www.vishay.com/brands/measurements_group/guide/tn/tn504/504j.htm.

[Vurpillot et al 1998] Vurpillot, S., Krueger, G., Benouaich, D., Clement, D., Inaudi, D., “Vertical Deflection of a Pre-Stressed Concrete Bridge Obtained Using Deformation Sensors and Inclinometer Measurements,” ACI Structural Journal, Vol. 95, No. 5, September – October Issue, pg. 518-526.

[Wnuk 2005] Wnuk, V. P., Mendez, A., Ferguson, S., Graver, T., “Process for Mounting and Packaging of Fiber Bragg Grating Strain Sensors for use in Harsh Environment Applications,” Proc. SPIE Paper 5758-6. 8 p.

[Zepernick & Finger 2005] Zepernick, H. & Finger, A., Pseudo random Signal Processing: Theory and Application, San Francisco, CA, USA: John Wiley & Sons. 414 p.

[Zhu et al. 2003] Zhu, Y., Shum, P., Lu, C., Lacquet, M. B., Swart, P.L., Chtcherbakov, A. A., & Spammer, S. J., “Temperature insensitive measurements of static displacements using a fiber Bragg grating,” *Optics Express* Vol. 11, No. 16, August 11, pg. 1918-1924.